

Waveguide Architecture and Components for Photonic Vector Network Analysers

Wellenleiterarchitektur und Komponenten für photonische Vektornetzwerkanalysatoren

Zur Erlangung des akademischen Grades Doktor-Ingenieur (Dr.-Ing.)

Genehmigte Dissertation von Amlan kusum Mukherjee aus Bankura, WB, Indien

Tag der Einreichung: 13.10.2022, Tag der Prüfung: 20.01.2023

1. Gutachten: Prof. Dr. rer. nat. Sascha Preu

2. Gutachten: Univ. Prof. Mag. rer. nat. Dr. rer. nat. Karl Unterrainer

Darmstadt – D 17

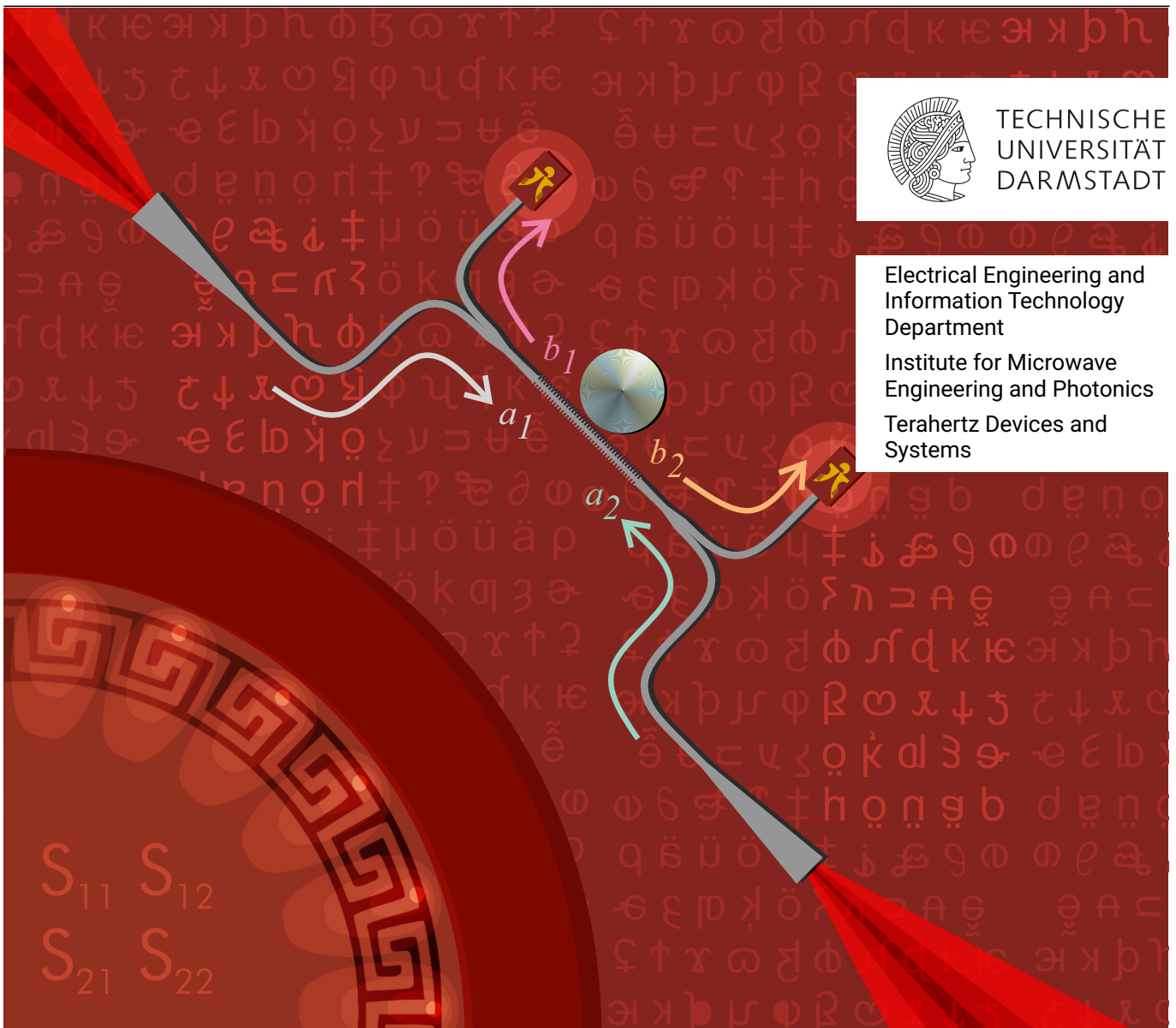


TECHNISCHE
UNIVERSITÄT
DARMSTADT

Electrical Engineering and
Information Technology
Department

Institute for Microwave
Engineering and Photonics

Terahertz Devices and
Systems



Waveguide Architecture and Components for Photonic Vector Network Analysers
Wellenleiterarchitektur und Komponenten für photonische Vektornetzwerkanalysatoren

Accepted doctoral thesis by Amlan kusum Mukherjee

1. Review: Prof. Dr. rer. nat. Sascha Preu
2. Review: Univ. Prof. Mag. rer. nat. Dr. rer. nat. Karl Unterrainer

Date of submission: 13.10.2022

Date of thesis defense: 20.01.2023

Darmstadt – D 17

Bitte zitieren Sie dieses Dokument als:

URN: urn:nbn:de:tuda-tuprints-233645

URL: <http://tuprints.ulb.tu-darmstadt.de/id/eprint/23364>

Dieses Dokument wird bereitgestellt von tuprints,

E-Publishing-Service der TU Darmstadt

<http://tuprints.ulb.tu-darmstadt.de>

tuprints@ulb.tu-darmstadt.de

Die Veröffentlichung steht unter folgender Creative Commons Lizenz:

Namensnennung – Weitergabe unter gleichen Bedingungen 4.0 International

<https://creativecommons.org/licenses/by-sa/4.0/>

This work is licensed under a Creative Commons License:

Attribution–ShareAlike 4.0 International

<https://creativecommons.org/licenses/by-sa/4.0/>

“Where the mind is without fear and the head is held high;
Where knowledge is free;
Where the world has not been broken up into fragments by narrow domestic walls;
Where words come out from the depth of truth;
Where tireless striving stretches its arms towards perfection;
Where the clear stream of reason has not lost its way into the dreary desert sand of dead habit;
Where the mind is led forward by thee into ever-widening thought and action -
Into that heaven of freedom, my Father, let my country awake.”

- Rabindranath Tagore, “*Gitanjali*”, 1912 (Orig. version: 1910, Bengali)

Abstract

In the past few decades, the Terahertz range (0.1 – 10 THz) has gained interest for its many applications in astronomy, non-destructive testing, imaging, security and many other fields. With the current availability of non-cryogenic, table-top Terahertz (THz) sources and receivers, THz systems with peak dynamic ranges between 120 – 140 dB have become commonplace due to their broad frequency coverages over a few octaves. However, there is a severe lack of affordable, broadband characterisation tools, like vector network analysers. Electronic systems in a hollow metallic waveguide configuration yet offer the largest dynamic range, however, they are comparatively narrowband. At least five different waveguide rectangular (WR)-configurations (*WR-1.5* to *WR-0.65*) are necessary for a frequency coverage between 0.5 – 1.5 THz, along with the corresponding frequency-extender modules, which become exponentially expensive with increasing operational frequency. A particularly costly component of an electronic system with on-chip measurement capability is the *ground-signal-ground* (G-S-G) probes that wear off and have to be regularly replaced. Therefore, free-space setups are implemented where possible. Traditionally employed optical components in free-space setups, such as lenses and parabolic mirrors, make THz systems bulky and create hurdles for miniaturisation and integration. For instance, a $10 \times 10 \mu\text{m}^2$ large active device needs an antenna and a silicon lens to operate in free-space configuration, which enlarges it by at least 6 orders of magnitude. In order to circumvent both the limitations of a hollow metal waveguide and the unhandiness of a free-space setup, we propose in this thesis a dielectric waveguide architecture and an integrated photoconductive receiver topology to manufacture a (semi-) integrated, broadband, continuous-wave vector network analyser driven by standard 1550 nm telecom lasers. Enhanced by digital post-processing techniques, the photonic vector network analyser (PVNA) features an operational bandwidth between 0.5 – 1.5 THz without the need of exchanging any bands.

The thesis first explores the applicability of free-space PVNAs in material characterisation and imaging at THz frequencies that will later serve as a benchmark for the integrated PVNA. For homogeneous, plane-parallel dielectric devices under test (DUTs), the measured scattering parameters (S-parameters) feature Fabry-Pérot oscillations. Fitting these oscillatory features allows the extraction of the physical thickness of the DUT with a precision of $\lambda/15,000$ and proves such high precision by visualising a Siemens star as thin as 50 nm using a bandwidth between 0.6 – 0.8 THz. For characterising multilayered samples, where calculation of analytical Fabry-Pérot functions is cumbersome, we propose scattering transfer parameter (T-parameter)-based modelling and vectorial optimisation algorithms and apply them in estimating the thickness and refractive index of each layer of a 5-layered distributed Bragg reflector (DBR) structure with $\sim 0.6\%$ error margin. The digital signal processing techniques demonstrably improve the operational bandwidth and dynamic range (DNR) of continuous-wave (CW) THz systems, such as the free-space PVNA, by $\sim 30\%$ and 20 dB, respectively, without any significant increase in the measurement time.

The waveguide architecture miniaturises the free-space PVNA by transforming the free-space THz beam to a guided one. The waveguides are highly-resistive float-zone silicon (HRFZ-Si)-based rectangular, dielectric structures with a $200 \times 50 \mu\text{m}^2$ cross-section. High density polyethylene (HDPE) or crystalline quartz (Qz) substrates provide mechanical stability to the waveguide and ease their

further integration with active devices, especially with Vivaldi antenna (VA)-coupled THz receivers manufactured in-house from erbium arsenide/indium (aluminium) gallium arsenide (ErAs:In(Al)GaAs) photoconductors. The single-mode bandwidths of the waveguides are between 0.45 – 0.7 THz and 0.5 – 0.75 THz when supported by HDPE and Qz substrates, respectively. We operate the waveguides in the overmoded regime, but suppress the generation of undesired higher-order modes (HOMs) at bends by using $\gtrsim 4$ mm bend radii for circular bends or $\gtrsim 2.3$ mm for sine-squared bends. The tapered structures for free-space in-coupling and quasi near-field out-coupling using VA-coupled active devices further suppress the excitation of HOMs. The coupling efficiency to VA-coupled receivers is 5 – 14 dB higher than free-space coupling between 0.4 – 1.05 THz. The operational bandwidth of the waveguides in their fundamental mode with free-space in-coupling and direct out-coupling is between 0.45 – 1.5 THz, where the upper boundary is solely given by the decreasing dynamic range (DNR) with increasing frequency. The VA-coupled THz receivers are only $0.23 \times 0.9 \times 0.03$ mm³ large and do not require silicon lenses to operate, easing integration to planar system-on-chip (SOC) architectures.

Finally, the thesis presents a (semi-) integrated 1.5-port PVNA using the waveguide architecture and VA-coupled, ErAs:In(Al)GaAs-based receivers. A commercial P-I-N diode-based THz source is used in the free-space configuration due to the unavailability of appropriate materials to fabricate powerful VA-coupled THz sources. Despite of the 10 – 13 dB in-coupling losses, the operational bandwidth of the PVNA extends between 0.5 – 1.5 THz, demonstrated by a characterised whispering gallery mode (WGM) resonator, where the entire HRFZ-Si structure is fabricated together. We successfully characterise a THz fibre Bragg grating and two cavity resonators using the PVNA setup between 0.45 – 1.2 THz, where the measured S-parameters match excellently with simulated models in CST® microwave studio. Furthermore, we demonstrate a coupling mechanism to rectangular hollow metallic (RHM) waveguides that enable on-chip measurements of integrated electronic circuits using commercially available wafer probes in G-S-G configuration between 0.45 – 1.1 THz, without changing any setup components. In closing, the thesis briefly discusses the current pitfalls of the 1.5-port architectures and the modifications necessary to assemble a 2-port PVNA.

Zusammenfassung

Aufgrund zahlreicher Anwendungsfelder, beispielsweise in der Astronomie, der Bildgebung bei zerstörungsfreien Testverfahren oder Sicherheitsanwendungen, nahm das Interesse am Terahertzbereich (0,1 – 10 THz) in den letzten Jahrzehnten stark zu. Mit der Verfügbarkeit von nicht-kryogenen kompakten Terahertz-(THz)-Quellen und -Empfängern sind THz-Systeme mit Spitzen-Dynamikbereichen zwischen 120 – 140 dB in vielen Laboren und ersten industriellen Umgebungen im Einsatz. Die Entwicklung der Terahertz-Technologie wird erschwert durch den Mangel an Breitband-Messgeräten, wie beispielsweise Netzwerkanalysatoren. Elektronische Systeme verfügen derzeit über den größten Dynamikbereich. Diese Systeme sind allerdings vergleichsweise schmalbandig. Für eine Frequenzabdeckung zwischen 0,5 – 1,5 THz sind mindestens fünf verschiedene WR-Wellenleiterkonfigurationen (*WR-1,5* bis *WR-0,65*) und die entsprechenden Frequenz-Extender erforderlich, die mit steigender Betriebsfrequenz exponentiell teurer werden. Insbesondere die für On-Chip-Anwendungen notwendigen Erde-Signal-Erde Messspitzen sind verschleißanfällig und damit sehr kostenintensiv. Aus diesem Grund werden häufig Freistrahlaufbauten verwendet. Die dort üblicherweise in Freistrahlaufbauten verwendeten sperrigen optischen Komponenten, wie Linsen und Parabolspiegel, verhindern deren Miniaturisierung und Integration. So benötigt ein $10\ \mu\text{m} \times 10\ \mu\text{m}$ großes aktives Bauteil eine Antenne und eine Siliziumlinse um in einer Freistrahlfunktion eingesetzt werden zu können. Im Vergleich zum aktiven Bauteil steigt der Platzbedarf um mindestens sechs Größenordnungen. Um die Schmalbandigkeit WR-gekoppelter elektronischer Systeme so wie die nachteilige Größe von Freiraumaufbauten zu umgehen, befasst sich diese Arbeit mit einer dielektrischen Wellenleiterarchitektur und einer integrierten photoleitenden Empfängertopologie. Auf deren Basis wird anschließend ein (halb-)integrierter breitbandiger Dauerstrich (CW)- Vektornetzwerkanalysator demonstriert, der mit Standard-1550 nm-Telekommunikationslasern betrieben wird. Durch digitale Nachbearbeitungstechniken verbessert, weist der photonische Vektornetzwerkanalysator (PVNA) eine Betriebsbandbreite zwischen 0,5 – 1,5 THz auf.

Zunächst wird die Anwendbarkeit der Freistrahlfunktions bei der Materialcharakterisierung und Bildgebung bei THz-Frequenzen untersucht, um Vergleichswerte der Performanzparameter für das integrierte System zu erhalten. Bei homogenen, planparallelen dielektrischen Messobjekten (DUTs) weisen die gemessenen Steuerparameter Fabry-Pérot-Oszillationen auf. Durch Fitten an Fabry-Pérot-Transmissions- und Reflexionsverläufen erhalten wir die physikalische Dicke des DUTs mit einer Genauigkeit von $\lambda/15\ 000$. Diese hohe Präzision verifizieren wir durch die Visualisierung eines „Siemens“-sterns von nur 50 nm Dicke unter Verwendung einer Bandbreite von 0,6 – 0,8 THz. Zur Charakterisierung mehrschichtiger Proben, bei denen die Berechnung analytischer Fabry-Pérot-Funktionen umständlich ist, stellen wir Transferparameter-basierte Modellierungs- und vektorielle Optimierungsalgorithmen vor und wenden sie anschließend bei der Schätzung der Dicke und des Brechungsindex der Schichten einer 5-schichtigen Bragg-Spiegel (DBR)-Struktur mit $\sim 0,6\%$ Fehlertoleranz an. Digitale Signalverarbeitungstechniken verbessern nachweislich die Betriebsbandbreite und den Dynamikbereich (DNR) von CW THz-Systemen, wie beispielsweise der Freistrahlfunktion, um $\sim 30\%$ bzw. 20 dB, ohne dass sich die Messzeit wesentlich verlängert.

Anschließend wird eine rechteckige, dielektrische Wellenleiterstruktur auf Basis von hochohmigem

Silizium (HRFZ-Si) mit einem Querschnitt von $200 \times 50 \mu\text{m}^2$ zur Miniaturisierung des Freistrah-PVNA entwickelt. Polyethylen hoher Dichte (HDPE)- oder Quarzkristall (Qz)-Substrate verleihen dem Wellenleiter mechanische Stabilität und erleichtern die weitere Integration mit aktiven Bauteilen, insbesondere mit Vivaldiantennen (VA)-gekoppelten THz-Empfängern, die aus ErAs:In(Al)GaAs-Photoleitern im Hause hergestellt werden. Die Single-Mode-Bandbreiten der Wellenleiter liegen zwischen $0,45 - 0,7$ THz und $0,5 - 0,75$ THz, wenn sie von HDPE- bzw. Qz-Substraten getragen werden. Wir betreiben die Wellenleiter in übermodiger Konfiguration, unterdrücken aber die Erzeugung der höheren Moden an Biegungen, indem wir $\gtrsim 4$ mm Biegeradien für kreisförmige Biegungen oder $\gtrsim 2,3$ mm für sinusförmige Biegungen verwenden. Die sich verjüngenden Strukturen für die Einkopplung in den freien Raum und die Quasi-Nahfeld-Auskopplung unter Verwendung von VA-gekoppelten aktiven Bauelementen unterdrücken die Anregung von höheren Wellentypen ebenfalls. Die Kopplungseffizienz zu VA-gekoppelten Empfängern ist im Frequenzbereich zwischen $0,4$ und $1,05$ THz $5 - 14$ dB höher als die Ankopplung mit einem Freistrah. Die Betriebsbandbreite der Wellenleiter in ihrem Grundmodus mit Freiraumeinkopplung und direkter Auskopplung liegt zwischen $0,45 - 1,5$ THz. Die obere Betriebsfrequenz ist lediglich um mit der Frequenz sinkenden Dynamikbereich geschuldet. Die VA-gekoppelten THz-Empfänger sind nur $0,23 \times 0,9 \times 0,03$ mm³ groß und benötigen keine Siliziumlinsen, was die Integration in planare On-Chip-System (SOC)-Architekturen erleichtert.

Zum Schluss wird in dieser Arbeit ein (halb-)integrierter 1,5-Port PVNA vorgestellt, der die Wellenleiterarchitektur und VA-gekoppelte, ErAs:In(Al)GaAs-basierte Empfänger nutzt. Eine handelsübliche P-I-N-Dioden-basierte THz-Quelle wird in der Freistrahkonfiguration verwendet, da keine geeigneten Materialien zur Herstellung leistungsfähiger THz-Quellen mit einer Vivaldi-Antenne zur Verfügung standen. Trotz der $10 - 13$ dB Einkopplungsverluste liegt die Betriebsbandbreite des PVNA zwischen $0,5 - 1,5$ THz, was durch die Charakterisierung eines Flüstergaleriemode (WGM)-Resonators, bei der die gesamte HRFZ-Si-Struktur in einem Schritt hergestellt wird, gezeigt wird. Wir haben ferner erfolgreich ein THz-Faser-Bragg-Gitter und zwei Hohlraumresonatoren unter Verwendung des modularen PVNA-Aufbaus zwischen $0,45 - 1,2$ THz charakterisiert, wobei die gemessenen S-Parameter hervorragend mit simulierten Modellen in CST® microwave studio übereinstimmen. Darüber hinaus demonstrieren wir einen Kopplungsmechanismus mit metallischen rechteckigen Hohlleitern, der On-Chip-Messungen integrierter elektronischer Schaltungen mit handelsüblichen Wafer-Proben zwischen $0,45 - 1,1$ THz ermöglicht, ohne dass eine Änderung der Setup-Komponenten erforderlich ist. Abschließend werden in dieser Arbeit kurz die derzeitigen Nachteile der 1,5-Port-Architekturen sowie die notwendigen Modifikationen für den Aufbau eines 2-Port-PVNA diskutiert.

Contents

1. Introduction	1
1.1. Motivation	2
1.1.1. Homodyne continuous-wave Terahertz systems	2
1.1.2. Vector network analysers	3
1.1.3. Photonic integrated circuits	6
1.2. Outline of the thesis	8
2. Theory	11
2.1. Dielectric waveguides	11
2.1.1. Marcatili's approximate solution	12
2.1.2. Waveguide modes	14
2.1.3. Mode excitation, mode conversion and radiation	17
2.1.4. Attenuation	19
2.1.5. Dispersion	19
2.2. Photomixing and photoconductors	20
2.2.1. Frequency-dependent roll-off	22
2.2.2. ErAs:In(Al)GaAs photoconductors	23
2.2.3. P-I-N Diodes	26
2.2.4. Photoconductors in PVNA	26
2.3. Antenna theory	27
2.3.1. Antenna characteristics	30
2.3.2. Frequency-independent antennas	30
3. Free-Space Photonic Vector Network Analysers	33
3.1. Architecture and calibration	33
3.2. Data post-processing	35
3.2.1. Implementation of digital filtering	36
3.2.2. Application in Spectroscopy	38
3.2.3. Application in PVNA	40
3.2.4. Advantages and limitations of post-processing	40
3.3. Applications of free-space PVNA	42
3.3.1. Characterisation of single-layered samples	42
3.3.2. Modelling of multilayered structures	47
3.3.3. Vectorial optimisation of multilayered models	49
3.3.4. Terahertz imaging	53
4. Passive Waveguide Components	61
4.1. Silicon-on-insulator waveguide architecture	61
4.2. Free-space measurement setup	63

4.3. Simulations	65
4.3.1. Bandwidth and multimode operation	66
4.3.2. Waveguide tapers	67
4.3.3. Waveguide bends	69
4.3.4. Propagation characteristics	73
4.3.5. Splitters and couplers	76
4.4. Fabrication	77
4.5. Characterisation	78
4.5.1. Transmission losses	79
4.5.2. Bend losses	79
4.5.3. Coupling losses	82
4.5.4. Dispersion	82
4.5.5. The splitter/coupler structure	84
4.5.6. Higher order modes and standing waves	85
5. Active Devices	89
5.1. Vivaldi antennas	90
5.1.1. Base design and endfire characteristics	90
5.1.2. Active devices with improved antennas	93
5.1.3. Fabrication	96
5.2. Characterisation	97
5.3. Comparison with free-space coupling	99
6. Semi-integrated THz PVNA	101
6.1. Data acquisition and software setup	102
6.2. 1.5-port setups	104
6.3. Whispering gallery mode resonator	106
6.4. Modular PVNA setup	108
6.4.1. Terahertz fibre Bragg grating	110
6.4.2. Cavity resonator	113
6.4.3. Dispersion in the waveguides	115
6.4.4. Necessary improvements for the modular PVNA	117
6.5. 2-port PVNA	117
6.6. Transitions to hollow metallic waveguides	117
7. Summary and Outlook	121
7.1. Synopsis	121
7.2. Outlook	123
A. Appendices	125
A.1. Lock-in detection	125
A.2. Performance of the vectorial error minimisation	126
A.3. Gaussian beam diameter	128
A.4. Characterisation of waveguide bends using modular PVNA	130
A.5. Deep reactive-ion etching	133
A.6. Photoconductor fabrication	136
A.7. Codes and application	138

Acronyms	157
List of Publications	159
Acknowledgements	161
Curriculum Vitae	163

1. Introduction

The frequency range between 0.1 – 10 THz is generally referred to as the THz range. Over the past five decades, a plethora of applications in the fields of astronomy [1], [2], spectroscopy [3], [4], imaging[5], [6], non-destructive testing[7], [8] etc. has been demonstrated using THz radiation. However, lack of powerful sources and low-noise receivers has impeded the commercial omnipresence of THz technologies and popularised the term “Terahertz-gap” in the scientific circles. This scarcity of active devices in the THz range stems primarily from two issues [9]: firstly, the mobility of the electrons at room temperature in conventional electronic active devices, such as transistors, are too low for the THz frequencies and secondly, the required photon energies are too small to engineer a band-gap for THz generation/detection in traditional photoconductive materials, such as silicon, germanium or indium gallium arsenide (InGaAs). Thus, sources and detectors in THz range are usually manufactured by up-converting radio frequency (RF) using electronic multiplier chains, down-converting optical frequencies by mixing lasers in a photoconductor or by engineering purely optical components such as quantum cascade lasers, molecular gas lasers etc. Extensive lists of THz active devices can be found elsewhere [10], [11]. A decade or two back, bulky, cryogenic THz devices and systems were commonplace. Nowadays, commercially available THz systems are equipped with powerful electronic and optoelectronic sources with up to milliwatts of emitted power [12]–[14]. Furthermore, sensitive table-top, non-cryogenic THz receivers have paved the way for THz systems featuring dynamic ranges (DNRs) between 120 – 140 dB [15], [16], albeit at the lower THz frequencies. Owing to the increased portability and modularity in recent years, THz systems are gaining commercial popularity in industrial and bio-medical imaging [17], [18], time-domain spectroscopy (TDS)-based breath-gas analysis [19], near-field microscopy and nanoscopy [20], [21], telecommunications [22], [23] etc. Nonetheless, most of the photonic THz systems are operated in free-space due to the lack of photonic integration platforms and characterisation equipments such as vector network analysers (VNAs), spectrum analysers, etc., whereas the electronic counterparts are only tunable by $\sim 50\%$ of its centre frequency compared to the few octaves of tunability of THz devices [24], [25] and are extremely expensive for frequencies above

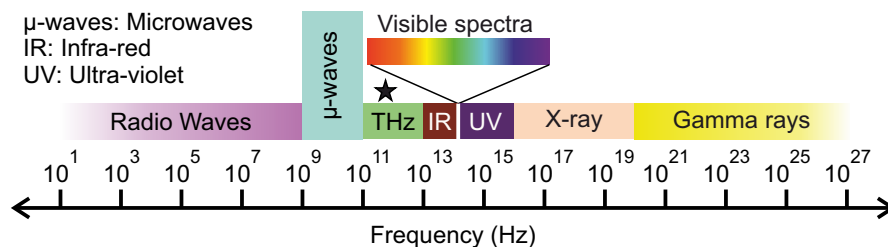


Figure 1.1.: The Terahertz (THz) range is located between the microwaves and the optical frequencies. The wavelength of THz radiation is between 0.03 – 3 mm and hence, it interacts with polar gas molecules, which leave spectroscopic signatures in the THz spectrum. Low photon energies (0.41 – 41 meV) make the THz radiation non-ionizing and, thus, less harmful for living tissues. The star represents the frequency range of interest for this thesis.

1 THz. The thesis aims to bridge this gap by demonstrating a broadband, (semi-)integrated photonic VNA, operational between 0.5 – 1.5 THz, using combination of optical and electrical components.

1.1. Motivation

Commonly used non-cryogenic, table-top THz systems are configured in homodyne or heterodyne fashion using either pulsed or continuous-wave (CW) lasers. On the one hand, commercially available pulsed systems are highly broadband featuring up to 6 THz bandwidths [26], however, they lack in spectral resolution. The CW systems, on the other hand, feature a frequency resolution on the order of 1 MHz [24], however, the frequency coverage is lower and systems are significantly slower compared to the pulsed variant. Nevertheless, Liebermeister *et al.* have recently demonstrated a photomixing based CW system with ~ 4 THz bandwidth with a scanning rate of ~ 68 Hz (also, 1.5 THz at 200 Hz) [27], with comparatively simple laser systems. Encouraged by these developments and future prospects, we work towards manufacturing a CW VNA operating in the THz range. In this thesis, we restrict ourselves only to homodyne CW measurement setups. A comprehensive list of alternative applications of terahertz CW systems can be found elsewhere [28]. Photomixing-based THz active devices, especially P-I-N diode based sources and erbium arsenide/indium (aluminium) gallium arsenide (ErAs:In(Al)GaAs)-based photoconductive receivers, constitute the demonstrated VNA system. Here, we introduce the homodyne photomixing CW setup in order to motivate the integrated CW photonic vector network analyser (PVNA) and we describe the active devices in detail in the following chapters.

1.1.1. Homodyne continuous-wave Terahertz systems

Traditionally CW photonic terahertz systems are set up in free-space configuration, i.e. the terahertz radiation emitted from the sources is collimated, focused and transmitted using optical mirrors and lenses in free-space before being detected by a receiver. Figure 1.2 shows the schematic of a typical CW free space setup we use in our experiments, consisting of a silicon lens-coupled, P-I-N diode-based THz source (Tx) developed by Toptica photonics/Fraunhofer Heinrich Hertz institute (HHI) and either a silicon lens coupled ErAs:In(Al)GaAs photoconductor-based THz receiver (Rx) fabricated in house [25] or a commercially available THz receiver from Toptica Photonics/Fraunhofer HHI. Both the THz source and receiver are excited using the same pair of 1550 nm distributed feedback (DFB) lasers, with a difference frequency in THz range (f_{THz}). The divergent emitted terahertz beam from Tx is first collimated using a 90° off-axis parabolic mirror (PM1). Two Polymethylpentene (TPX) lenses (L1 and L2) create an intermediate focal point F before collimating the beam again onto another 90° off-axis parabolic mirror (PM2), which finally converges the beam onto the Rx. In free-space setups, the Tx, PM1 and L1 constitute the transmitter module and similarly, L2, PM2 and Rx make up the receiver module. The detector current i_{THz} is proportional to the electric field of the incident terahertz radiation E_{THz} , reads [11]

$$i_{\text{THz}}(f_{\text{THz}}) \propto E_{\text{THz}} \cdot \cos\left(2\pi f_{\text{THz}} \frac{\Delta d_{\text{opt}}}{c_0} + \phi_0\right), \quad (1.1)$$

where c_0 is the speed of light in vacuum, ϕ_0 is a phase constant and Δd_{opt} is the optical path difference between the laser excitation and the incident THz beam on the receiver. Usually, the detector current varies between tens of picoamperes to ~ 100 nA. A low-noise transimpedance amplifier (TIA) amplifies detector current by an amplification factor of 10^6 and finally sends it to a lock-in amplifier (LIA) for lock-in detection.

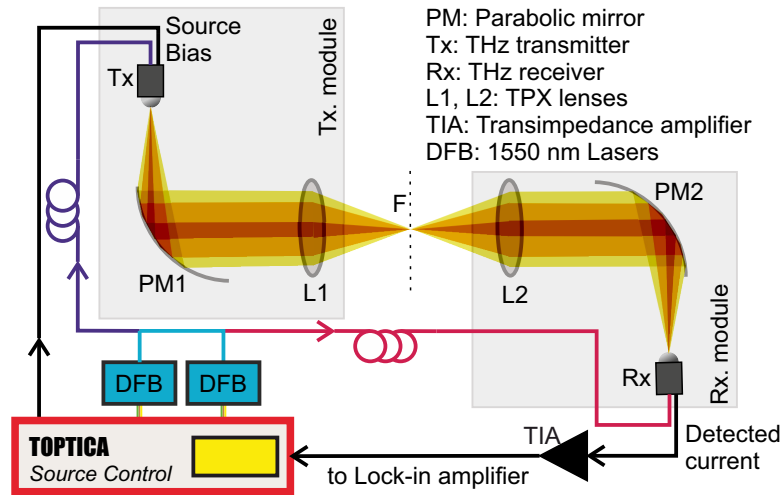


Figure 1.2.: Traditional free-space terahertz photonic setup using optical components, such as lenses and parabolic mirrors. The black lines show electrical connections. The violet and red lines are optical paths to the Tx and Rx respectively. Δd_{opt} is the optical path length difference between the red line and the free-space THz path along with the violet line. The LIA is located inside the source control unit.

The *Toptica source control* biases the Tx at a modulation frequency of either 12.2 kHz or 38.1 kHz for lock-in detection. The mathematical formulation of lock-in detection mechanism can be found in Appendix A.1. Since the same pair of DFB lasers drives both Tx and Rx, the detection mechanism is *homodyne*. This setup features an operational tuning range between 0 – 3.5 THz, with dynamic ranges > 100 dB at 0.1 THz and between 50 – 60 dB at 1 THz [24], [25]. The *Hilbert transform* of eqn. (1.1) results in the complex form of the detector current with a magnitude and a relative phase. If we now place any object in the free-space THz path, it will induce changes in the E_{THz} and Δd_{opt} , i.e., both the magnitude and phase of the detector current. These changes can be accurately measured and mapped back to the device properties such as refractive index (RI), thickness, material absorption or likewise, the scattering parameters (S-parameters), that we will introduce in the next subsection. Hence, such homodyne CW systems can be used to create a laser-driven material characterisation tool or a VNA, operating at THz frequencies.

1.1.2. Vector network analysers

At the higher end of the RF-band (20 kHz to 0.1 THz) and beyond, the size of the elements in electrical circuitry becomes comparable to the wavelength of operation. Here, the lumped element-assumption of constant voltages, currents and impedances across the entirety of an electrical component is inaccurate and circuit analyses at such frequencies require the consideration of the wave features through the electrical elements. This is also referred to as the analysis using the *distributed element model*. The traditional methods of circuit analysis using Z , Y , H and $ABCD$ parameters are unusable at RF frequencies. S-parameters provide an alternative way to characterise the distributed element model of electrical components. The S-parameters derive their name from the *optical scattering* phenomenon, where an electro-magnetic (EM) wave is partially transmitted and partially reflected when it experiences a change of wave-impedance in the propagating medium, usually induced by a change in RI.

Figure 1.3 shows the S-parameter-based characterisation scheme of a device under test (DUT) at

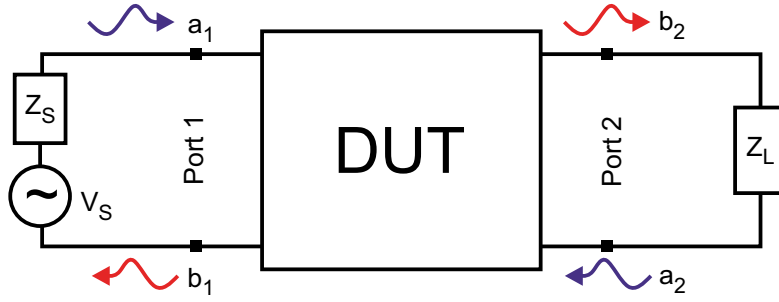


Figure 1.3.: Schematic of the 2-port architecture showing incident power wave, a_i , and reflected power wave, b_i , at port $i = 1, 2$.

frequencies where the *lumped element model* is inaccurate. The two-port DUT is connected to a RF source with known source impedance (Z_S) at one port and a known load (Z_L) at the other. The waves a_i and b_i are referred to as *power waves* [29], where the former is travelling towards the port i ($i = 1, 2$), whereas the latter travels away from the same port. Kurokawa explains the physical meaning of these power waves in greater detail in [30], where he defines them as

$$a_i = \frac{1}{2} \frac{V_i + Z_i I_i}{\sqrt{|\Re(Z_i)|}} \quad (1.2)$$

$$b_i = \frac{1}{2} \frac{V_i - Z_i^* I_i}{\sqrt{|\Re(Z_i)|}}, \quad (1.3)$$

where V_i , I_i and Z_i are the voltage, current and impedance across port i , respectively, and $[*]$ signifies the complex conjugate. Thus, these wave quantities are not a measure of electrical power, rather electric fields and have a unit of $W^{1/2}$. The S-parameters (S_{11} , S_{12} , S_{21} and S_{22}) define the relationship between the power waves at the two ports as

$$\begin{bmatrix} b_1 \\ b_2 \end{bmatrix} = \begin{bmatrix} S_{11} & S_{12} \\ S_{21} & S_{22} \end{bmatrix} \begin{bmatrix} a_1 \\ a_2 \end{bmatrix} \quad (1.4)$$

Thus, each of the S-parameters reads

$$S_{11} = \left. \frac{b_1}{a_1} \right|_{a_2=0} \quad S_{21} = \left. \frac{b_2}{a_1} \right|_{a_2=0} \quad S_{12} = \left. \frac{b_1}{a_2} \right|_{a_1=0} \quad S_{22} = \left. \frac{b_2}{a_2} \right|_{a_1=0}. \quad (1.5)$$

A perfectly conjugate-matched load at port i ensures a null a_i . S_{11} and S_{22} refer to the reflection coefficients at ports 1 and 2 respectively, whereas the parameters S_{12} and S_{21} refer to the transmission coefficient between ports $1 \rightarrow 2$ and $2 \rightarrow 1$, respectively. All the defined S-parameters are complex, i.e., they have an amplitude and an associated phase. Thus, the S_{ii} parameters give a measure of the input impedance/admittance of the DUT at either ports, return loss and voltage standing wave ratio (VSWR). The S_{ij} parameters measure gain or losses associated with the DUT, its insertion phase at either ports and the group delay induced by the DUT.

A VNA measures these complex S-parameters at RF frequencies for linear DUTs. Traditional VNAs are calibrated to a standardised non-reactive 50Ω impedance and can characterise one or multi-port DUTs between a few hertz and up to 53 GHz [31], featuring between 140 – 160 dB DNR. The bandwidth of the said systems can be extended up to 1 THz by employing multiple VNA extenders driven by several frequency multiplier units [14], [32]. The VNA extenders lower the DNR to ~ 80 dB at 1 THz.

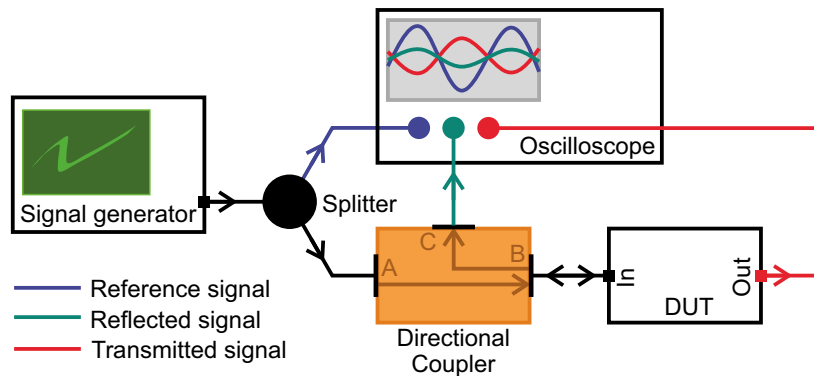


Figure 1.4.: A simplistic schematic of measurement in a VNA using a signal generator, a splitter, a directional coupler and an oscilloscope. The S-parameter-measurements of a linear DUT assumes it to be a black-box and give a measure of its input and output impedances. The calibration of a VNA ensures the extraction of amplitude and phase information very precisely.

Figure 1.4 shows a simplistic schematic of a VNA. The signal from a signal generator is split in two. The first part is fed to a oscilloscope and acts as a reference signal for the measurements. The second part is fed to the DUT via a directional coupler with ports A, B and C. Ideally, the coupling in direction $A \rightarrow B$, $B \rightarrow C$ and $C \rightarrow A$ is loss-less, whereas the coupling directions $C \rightarrow B$, $B \rightarrow A$ and $A \rightarrow C$ are isolated. Consequently, the reflected wave from input port of the DUT at port B is fully coupled to port C and then passed on to the oscilloscope. The oscilloscope also measures the output transmitted wave from the DUT. Once the phase change induced by the varying propagation path of the input signals at the scope is calibrated out, the ratio of reflected signal (green) to the reference signal (blue) measures the S_{ii} parameters, whereas the S_{ji} parameters ($i, j = 1, 2$) are given by the ratio between the transmitted (red) and the reference signal. The signal generator is swept over a frequency range of interest and the oscilloscope measures the complex S-parameters as a function of frequency. Another set of signal generator, splitter and directional coupler feeding the DUT from the *out* port enables the measurement of the other two S-parameters (S_{jj} and S_{ij}) and hence, the full set of four S-parameters fully describe the resistive and reactive features of the DUT. Here, we note that in electrically (or geometrically) symmetric DUTs $S_{11} = S_{22}$ and $S_{21} = S_{12}$ and hence, only the knowledge of S_{11} and S_{21} obtained by an uni-directional S-parameter measurement, as shown in Fig. 1.4, is sufficient for its full characterisation. Henceforth, we refer to the measurement schematic in Fig. 1.4 as 1.5-port measurements.

Photonic vector network analysers

Traditionally VNAs are driven by electrical sources and at higher RF, frequency extenders using rectangular hollow metallic (RHM) waveguides are employed. The RHM waveguides are only used in their fundamental modes and hence, at least five frequency extenders ($WR-1.5$ to $WR-0.65$) are necessary for a frequency coverage between $0.5 - 1.5$ THz [33]. This increases the system complexity and the associated costs for each VNA-extender increase exponentially with frequency. A promising solution to the bandwidth problems of electronic VNAs is replacing the electrical components by photonic counterparts and hence, the conception of photonic VNAs (PVNAs). Both CW and pulsed variants of THz systems are capable of acquiring both amplitude and phase information of the THz waves reaching the receiver. Faridi *et al.* has already demonstrated pulsed PVNA with a bandwidth

between 0.2 – 2 THz and a frequency resolution of 7.14 GHz [34], whereas the Fernandez Olvera *et al.* put forward a CW variant with a measurement bandwidth between 0.1 – 1 THz and a frequency resolution as low as 2 MHz [35].

Both the demonstrated PVNAs operate in free-space, i.e., a planar DUT is placed at the collimated part of the free-space THz beam, which usually has a Gaussian profile. The free-space wave propagates in the transverse electro-magnetic (TEM) mode. The directional coupler in Fig. 1.4 is implemented using two polarisers. The splitter is not used, rather the reference measurement is taken in an empty (DUT-less) setup. A pair of DFB lasers drives the two sets of THz sources and receivers. The two sources are modulated at two different intermediate frequency (IF) frequencies, and the receiver at port i receives the reflected signals at port i and transmitted signals from port j , separated temporally and in the IF. The post-detection mechanism uses two LIAs to segregate these two signals ($[a_1, b_2]/[a_2, b_1]$) at each of the receivers. Thus, the free-space PVNA setups are able to record the full set of S-parameters from the measured electric fields incident on the receivers. Only the CW variant of the free-space PVNA is in the scope of this thesis and we describe its architecture and applications in detail in chapter 3.

1.1.3. Photonic integrated circuits

The main motivation behind the work done in this thesis is to demonstrate **the applicability of a CW PVNA** as a broadband characterisation tool and to **miniaturise and integrate the CW PVNA** towards the development of a **scalable, chip-based THz-photonic integrated circuit (THz-PIC)** [36]. Integrated THz systems already exist, like their counterparts in the RF and microwave domains [37], [38] or in the near-infrared regime at the telecom bands. Integrated electronic systems use fundamental oscillators as sources at the lower end of the THz spectrum [39] and reach frequencies up to 1.5 THz [16] employing frequency multiplier-chains to generate higher harmonics. Both RHM waveguides with microstrip transitions and dielectric waveguide-based architectures [40]–[42] are utilised in these systems. Regardless of the high bandwidths offered by the waveguides, the lack of broadband transition to and from the active devices and lack of appropriate characterisation tools restrict the operability of such integrated systems within 10 – 50% of its centre frequency.

Electronic systems based on RHM waveguides feature the highest DNR (~ 80 dB or more) [32] amongst all the available THz systems working below 1 THz. Low-loss coplanar waveguides, along with their efficient transitions from microstrip lines (≤ 1 dB losses [43]) make such high DNR feasible. These transitions are necessary as Schottky diode-based frequency multipliers are typically fabricated with microstrip-based outputs [44]. Though highly efficient, these transitions are quite narrowband as they rely on wavelength-dependent field (mode) matching techniques, such as employing a quarter-wave stub to match impedances, using resonant filters and interference-based couplers or by simply placing the transition at a local field maximum. Beyond 1 THz, surface roughness of the metals introduce high scattering losses. *Skin effect* and alignment errors further reduce the transition efficiencies to the metallic waveguides. Additionally, probing mechanisms also decrease in size with reduced wavelengths and need additional support using rigid ceramics to prohibit mechanical failure and to prevent wear-off. Still, electronic VNAs are the state-of-the-art characterisation tool in the (lower) THz range.

Photonics-based THz systems are the most common alternatives to the electronic systems and are usually set up in a free-space configuration using optical components, such as lenses, mirrors, etc. These table-top, modular setups are ubiquitous in present-day THz research laboratories and extensively used in spectroscopy and material characterisation. However, these setups are huge due to the employed free-space optical components. The photoactive area of photoconductor used in [25] is only $\approx 10 \times 10 \mu\text{m}^2$, however, the broadband logarithmic-periodic antenna attached to it enabling its free-space operation increases the device size to $\approx 1 \text{ mm}^2$. Additionally, a hyper-hemispherical

silicon lens radius ≈ 6 mm is further attached to the antenna-coupled photoconductor to enhance the radiation efficiency [45]. In this instance, an active area of $100 \mu\text{m}^2$ increases by 6 orders of magnitude to facilitate its free-space operation. Fully packaged devices are much larger in size and the employed optical components in the setup (see Fig. 1.2) are even larger. The performance of free-space systems deteriorates due to the absorption by the humidity in air and often, nitrogen purging is necessary to maintain the purity of the measured spectra. A waveguide-based transmission architecture will reduce these external effects and will help in reducing the size of the THz sources and receivers significantly, as the propagating mode inside a dielectric waveguide is much smaller than in free-space. Additionally, the THz active devices are typically manufactured on high-permittivity dielectric materials, such as indium phosphide (InP) or InGaAs and the transitions to waveguides manufactured from low-loss, high-permittivity dielectric materials, such as highly-resistive float-zone silicon (HRFZ-Si), are easier to engineer. These reasons make dielectric waveguides apt and very lucrative for this use-case.

Despite featuring negligible conductive losses, a dielectric waveguide architecture has its own challenges. In theory, dielectric waveguides feature infinite bandwidth, however, their overmoded nature leads to mode conversion and radiation at the waveguide bends and abrupt discontinuities, very similar to their metallic counterparts. Additionally, the mode-field distribution and the wave-impedance are frequency dependent. Nonetheless, several research groups have demonstrated various dielectric waveguide-based THz systems and monolithic microwave integrated circuits (MMICs) in the past few years. Table 1.1 shows a non-extensive list.

Table 1.1.: List of demonstrated waveguide architectures and systems at THz frequencies from literature.

Systems	Bandwidth	Losses	References
Polymer-based Waveguides	> 1 THz	3 – 4 dB/cm	[46], [47]
Silicon-Germanium MMIC	0.11 – 0.17 THz	–	[48]
Integrated THz system (HRFZ-Si)	0.26 – 0.39 THz	–	[49]
Silicon-on-insulator (SoI) architecture	–	~ 1.6 dB/cm	[50]
Terahertz resonators (HRFZ-Si)	–	–	[51], [52]
Suspended HRFZ-Si waveguides	0.1 – 0.25 THz	0.4 – 1 dB/cm	[53]–[55]
Photonic-crystal-based waveguides	0.08 – 0.15 THz	0.05 – 1 dB/cm	[56]–[59]
Effective-medium-based waveguides	< 0.3 THz	0.05 – 1 dB/cm	[60]

Additionally, Amarloo *et al.* demonstrated an alternative HRFZ-Si-Cyclotene™ Advanced Electronic Resin (BCB)-crystalline quartz (Qz) platform [42] for lower THz frequencies. In comparison, RHM waveguides feature similar bandwidths and losses of around 1.3 – 1.9 dB/cm near 1 THz [33]. It is evident that most of the listed waveguide architectures are narrowband as they are usually associated with the electronic systems. Contrastingly, photonic THz systems feature bandwidth coverages over several octaves [61]–[64] and have comparable, or better DNR over 1 THz. These large frequency coverages are engineered either by pulsed femtosecond-lasers or by mixing of two 800 nm or 1550 nm CW lasers, differing by a desired THz frequency. The tuning happens in the optical domain, where the individual laser signals are narrowband ($\sim 5 - 6\%$ tunability). However, generation of a 1 THz signal requires only 0.5% tunability for the 1550 nm lasers. Additionally, free-space optical components, such as lenses and mirrors, are generally broadband, making transition and transport losses insignificant. However, photonics-based measurement and characterisation systems are yet to outperform their electronic counterparts in terms of the available DNR over the entire operational bandwidth.

This thesis proposes a waveguide-based platform to miniaturise the photonics-based THz systems to create photonic integrated circuits (PICs) at THz frequencies [36], with much larger bandwidths

than previously demonstrated. We demonstrate a mechanically rigid SoI architecture and characterise its key components like tapers, bends and splitters. The waveguides are manufactured from HRFZ-Si ($\epsilon_{r,Si} = 11.678 \pm 0.001$ [34], $\sigma_{Si} < 0.01$ S/m) and are supported by Qz ($\epsilon_{r,qz} = 4.52$ [65]) or high density polyethelene (HDPE) ($\epsilon_{r,PE} = 2.4$) substrates for rigidity and stability. The substrate also provides a platform for integration with active devices or incorporating DUTs. These materials, along with Teflon or Cyclo-Olefin Copolymer have the lowest known material losses in the THz range and feature comparatively low permittivity. We further put forward low-loss transitions between ErAs:In(Al)GaAs-based photoconductive receivers and the said waveguide architecture, facilitating integration of the active devices with the transmission medium. Finally, we demonstrate a (semi-) integrated PVNA with the waveguides and photoconductive receivers as a proof of concept, operational between 0.5 – 1.5 THz and characterise multiple dielectric THz circuit components like whispering gallery mode (WGM) resonators, cavity resonators and THz fibre Bragg grating structures to demonstrate its applicability as a broadband characterisation tool at THz frequencies.

1.2. Outline of the thesis

This thesis builds upon the already demonstrated free-space PVNA by Fernandez Olvera *et al.* [35] operational between 0.1 – 1 THz. Helped by digital signal processing, the proposed waveguide architecture and the directly-coupled active devices extend the operational bandwidth of the semi-integrated PVNA up to 1.5 THz, significantly beyond its free-space counterpart. The employed digital post-processing techniques suppress the measured out-of-band noise, extending the operational bandwidth of the PVNA by 30 – 50%.

Chapter 2 briefly describes the theoretical basics of dielectric waveguides, the photomixing technique and the antennas. The chapter helps to better understand the demonstrated waveguide architecture and antenna designs in integrated THz systems.

In **chapter 3**, we briefly introduce the free-space PVNA system and its calibration routines. We further show a few relevant applications of the free-space systems, namely:

- Thickness and RI estimation of single-layered, dielectric, low-loss materials in the THz range from the measured S-parameters.
- Material characterisation of multi-layered structures, wherein we introduce a modelling technique for multilayered structures using scattering transfer parameters (T-parameters) and a multi-parameter optimisation algorithm using a vectorial approach.
- Imaging of nanometric structures as small as 50 nm with a frequency scan ranging between 0.6 – 0.8 THz ($375 \mu\text{m} \leq \lambda \leq 500 \mu\text{m}$). The imaging algorithm fits the phase of the Fabry-Pérot oscillations recorded in the S_{21} parameter to estimate an optical thickness of the DUT. Another simpler, but less precise, imaging technique uses zero-padding to emulate a high-frequency scan and can resolve thicknesses up to 350 nm using as low as 10 GHz frequency scans.

This chapter also provides detailed descriptions of all the data-processing algorithms relevant for the PVNA applications and beyond. The imaging techniques are already published in [66], [67]. The data-processing techniques are submitted for publication [68] at the time of writing this thesis and a patent has been submitted to the German Patent Office (DPMA) [69].

Chapter 4 introduces the waveguide architecture, which transforms the free-space THz beam in [35] to a guided one. We demonstrate overmoded HRFZ-Si waveguides, featuring a $200 \times 50 \mu\text{m}^2$ cross-section and supported by either Qz or HDPE substrates. The single-mode bandwidth of the

waveguides with Qz substrate spans between 0.5 – 0.75 THz. The waveguide substrate is necessary for the robustness of the waveguide architecture, which enables further integration with active devices and improves the durability of the otherwise brittle silicon strips. Despite of the overmoded nature, we simulate waveguide bends, tapers and splitter structures that suppresses excitation of the higher order modes up to 1.5 THz. In this chapter, we also detail the fabrication process of the waveguides and characterise them using a modified version of the free-space THz system of Fig. 1.2. The contents of this chapter are published in [70], [71] and some of the chapter's plots are adapted from the aforementioned publications.

Chapter 5 shows a quasi-nearfield coupling scheme to the waveguides using an end-fire Vivaldi antenna (VA) attached to the ErAs:In(Al)GaAs-based photoconductive receivers. This direct-coupling mechanism reduces the coupling losses to the waveguides from 10 – 13 dB in free-space configuration to < 4 dB between 0.6 – 0.9 THz. The chapter details the designing, fabrication and characterisation processes of two different VA types which are extensively used in this thesis. The antenna designs and characterisations presented in this chapter are published in [72], whereas the direct coupling mechanism is reported in our publication [70].

In **chapter 6**, we show a prototypical architecture of a semi-integrated 1.5-port PVNA with a single THz transmitter (free-space) and two VA-coupled receivers to the HRFZ-Si waveguides. The 1.5-port PVNA suffices for a full characterisation of symmetric DUTs. Using the semi-integrated PVNA, we calculate the complex S-parameters of various dielectric DUTs, e.g., WGM resonators, waveguide-based filters and cavity resonators. Furthermore, we utilize the data-processing techniques from chapter 3 to reduce the measurement noise and extend the operational bandwidth of the PVNA till ~ 1.5 THz. We also look at the equivalent time-domain data to find sources of stray reflections in the DUTs or the waveguide setup. Additionally, the chapter demonstrates a coupling scheme between the RHM and the active device-coupled dielectric waveguides for characterising traditional metallic electronic integrated circuits using commercially available wafer probes. Finally, we propose the design of a fully integrated 2-port PVNA working between 0.5 – 1.5 THz.

Chapter 7 summarises the results of this thesis and suggests some improvements and/or alterations to enhance the robustness, accuracy and repeatability of the 1.5-port or 2-port PVNA architectures.

2. Theory

The two important components for an integrated PVNA architecture are the waveguides and antenna-coupled active devices driving the THz system. In this chapter, we present the basic theoretical background necessary to develop the device- and design-specific theories, presented in the latter chapters. First, we describe the basics of wave propagation through dielectric waveguides, the resulting mode characteristics and associated losses. In the latter half, we discuss the principles of THz generation using photomixing in ErAs:In(Al)GaAs photoconductors, which are used as receivers in the demonstrated PVNAs. We end the chapter delving into the basics of antenna theory and briefly introducing frequency-independent antennas.

2.1. Dielectric waveguides

The guided fields in a purely dielectric waveguide can extend to infinity and hence, are regarded as open surface-wave structures. The rectangular HRFZ-Si waveguides investigated in this thesis are no exception. We place the dielectric guides on insulating HDPE or Qz substrates for mechanical stability and integrability. The whole structure is anisotropic in the plane transverse to EM wave-propagation, i.e., the silicon waveguides have a dielectric medium at the bottom and are surrounded by air on all other sides. The propagation through these waveguides is of field-penetrable kind [73], where the EM fields at the design-frequencies reside considerably inside the silicon core. To better understand the behaviour of the EM waves inside the waveguide, we take a look at the set of conditions that the wave must fulfil whilst travelling through the guiding structure.

Propagation of EM waves in any medium is governed by the Maxwell's equations [74]

$$\vec{\nabla} \times \vec{E}(\vec{r}, t) = \frac{-\partial \vec{B}(\vec{r}, t)}{\partial t} \quad (2.1)$$

$$\vec{\nabla} \times \vec{H}(\vec{r}, t) = \vec{J}(\vec{r}, t) + \frac{\partial \vec{D}(\vec{r}, t)}{\partial t} \quad (2.2)$$

$$\vec{\nabla} \cdot \vec{B}(\vec{r}, t) = 0 \quad (2.3)$$

$$\vec{\nabla} \cdot \vec{D}(\vec{r}, t) = \rho(\vec{r}, t), \quad (2.4)$$

where \vec{r} and t are the displacement and time variables, respectively, $\vec{\nabla} = \hat{e}_x \partial / \partial x + \hat{e}_y \partial / \partial y + \hat{e}_z \partial / \partial z$ is the vector differential operator defined for the Cartesian coordinate system and \hat{e}_x , \hat{e}_y and \hat{e}_z are the unit vectors along x , y and z directions, respectively. \vec{E} and \vec{H} are the electric and magnetic field intensity vectors, $\vec{D} = \epsilon \vec{E}$ and $\vec{B} = \mu \vec{H}$ are the electric displacement and magnetic induction vectors, respectively, wherein ϵ stands for electrical permittivity and μ is the magnetic permeability of the medium. ρ is the electric charge density, which is null for any source-free dielectric media. $\vec{J} = \sigma \vec{E}$ is the current density in the medium, where σ is its electrical conductance. The time-averaged power transmitted by an EM wave through a surface area A is defined from the *Poynting's vector* as [75]

$$P = \left\langle \frac{1}{2} \text{Re} \left[\int_A \left\{ (\vec{E} \times \vec{H}^*) \cdot \hat{e}_n \right\} dA \right] \right\rangle_T, \quad (2.5)$$

where \hat{e}_n is unit vector normal to the area A , $[*]$ symbolises the complex conjugate and $\langle \cdot \rangle_T$ signifies time-averaging.

The parameters ϵ and μ represents macroscopic electric and magnetic properties of a medium and are functions of position for the non-isotropic media experienced by the guided wave. In vacuum, these parameters read as $\epsilon_0 = 8.854 \times 10^{-12}$ F/m and $\mu_0 = 4\pi \times 10^{-7}$ H/m. The aforementioned Maxwell's equations hold true for EM waves irrespective of spatial or temporal conditions. This, subsequently, engenders a set of *boundary conditions* that must be satisfied at source free ($\rho = 0$) and non-conducting ($\sigma = 0, \implies \vec{J} = 0$) media boundaries. The boundary conditions for dielectric waveguides can be summarised as follows:

1. The tangential components of \vec{E} and \vec{H} to the media boundaries must be continuous.
2. The normal components of \vec{B} and \vec{D} to the media boundaries must be continuous.

Detailed derivations can be found elsewhere [76]. The former condition is both necessary and sufficient, whereas second condition does not guarantee that all boundary conditions are satisfied [77].

Two further conditions must also be fulfilled for these rectangular dielectric waveguides. Firstly, the *radiation condition*, which states that the electric and magnetic field intensities must vanish at great distances from the waveguides, i.e. at $|\vec{r}| \rightarrow \infty$. Additionally, at greater distances, the EM wave must behave as a radially divergent travelling wave [78]. Secondly, the *edge condition* states that \vec{E} and \vec{H} field intensities may become infinitely large at sharp edges, however, the integrated energy density over a finite region in space must always be finite [79]. Considering these prerequisites, we bring forth an approximate analytical solution for the wave equations in the rectangular dielectric waveguides.

2.1.1. Marcatili's approximate solution

The primary assumption for Marcatili's approximate solution [80] is that the majority of the power flows through the core of the waveguide, i.e., through the silicon structures. Thus, boundary conditions are satisfied for most of the field distribution carrying majority of the power. Figure 2.1 shows the cross-section of the rectangular waveguide transverse to the direction of wave propagation, which we assume to be along z -axis. The core waveguide structure has permittivity and permeability of ϵ_1 and μ_1 , respectively, whereas the corresponding values for supporting substrate underneath are ϵ_2 and μ_2 . All other sides are surrounded by air and feature the vacuum permittivity and permeability. The total power flowing in the shaded corner region should be finite to satisfy the edge conditions. Only a miniscule fraction of power flows in this region [81] and hence, the approximate solution ignores the fields in these shaded areas. Further, the fields outside the waveguide structure are evanescent in nature, satisfying the aforementioned radiation condition.

The modes propagating through the dielectric waveguide are hybrid, i.e., the components of both E and H fields are present along z direction. Two different mode families can exist in such structures [82]: the one, where most the electric field is polarised along the x -direction, henceforth referred to as E_{nm}^x modes and the other, where the electric field predominantly points in y -direction, referred to as E_{nm}^y modes. Mode subscripts n and m refer to the number of field extrema in the corresponding mode field distribution along the x and y axes, respectively. Practically, E_y can be approximated to be 0 for all E_{nm}^x modes and similarly, $H_y \approx 0$ for all E_{nm}^y modes [80], where, the field component R_k refers to the component of R field along k -direction. Additionally, both electric and magnetic modal fields form closed loops [81], and consequently, E_y and H_x can be neglected for all the E_{nm}^x family. Similarly, H_y and E_x are negligible for all E_{nm}^y modes.

To derive the mode field distribution for individual components of E_{nm}^y modes, we consider all the propagating mode fields to be of the form $f(u, v) \cdot \exp\{j(\omega t - \beta z)\}$ [73], where u and v are orthogonal

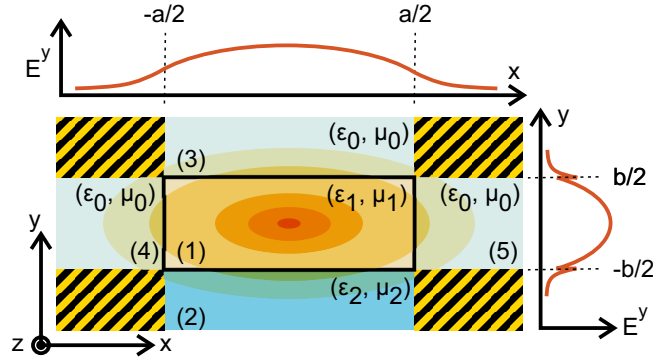


Figure 2.1.: Schematic of the cross-section of a rectangular dielectric waveguide of dimension $a \times b$ shows 5 regions of interest marked by the numbers in parenthesis. The shaded corner regions are excluded from the derivation of the analytical solution. The graphs (red) on top and to the right show the electric field distribution along x and y axis respectively.

coordinates, $\omega = 2\pi f$ is the angular frequency, wherein f denotes actual frequency and β is the phase constant of the travelling wave in z -direction. The individual field components are time-harmonic. Accordingly, the Maxwell's equations (2.1 – 2.4) can be reformulated in their time-harmonic form for a source-free, non-conducting medium ($\rho = 0$ and $\sigma = 0$) as

$$\vec{\nabla} \times \vec{E}(\vec{r}, t) = -j\omega\vec{B} \quad (2.6)$$

$$\vec{\nabla} \times \vec{H}(\vec{r}, t) = j\omega\vec{D} \quad (2.7)$$

$$\vec{\nabla} \cdot \vec{B}(\vec{r}, t) = 0 \quad (2.8)$$

$$\vec{\nabla} \cdot \vec{D}(\vec{r}, t) = 0. \quad (2.9)$$

Substituting $H_y = 0$ in the time-harmonic Maxwell's equations for a homogeneous medium with permittivity ϵ and permeability μ , the amplitudes of all the field components of the E_{nm}^y mode read [80]

$$H_x = -\frac{1}{j\omega\mu} \left[\frac{\partial E_z}{\partial y} + j\beta E_y \right] \quad (2.10)$$

$$H_y = -\frac{1}{j\omega\mu} \left[-\frac{\partial E_z}{\partial x} - j\beta E_x \right] = 0 \quad (2.11)$$

$$H_z = -\frac{1}{j\omega\mu} \left[-\frac{\partial E_y}{\partial x} - \frac{\partial E_x}{\partial y} \right] \quad (2.12)$$

$$E_x = \frac{1}{j\omega\epsilon} \frac{\partial H_z}{\partial y} \quad (2.13)$$

$$E_y = -\frac{1}{j\omega\epsilon} \frac{\partial H_z}{\partial x} + \frac{\beta}{\omega\epsilon} H_x \quad (2.14)$$

$$E_z = \frac{1}{j\omega\epsilon} \frac{\partial H_x}{\partial y}. \quad (2.15)$$

The spatio-temporal phase variation for all of the above components along the direction of propagation is $\exp\{j(\omega t - \beta z)\}$. The individual field components of E_{nm}^y modes must also satisfy the wave equation

$c^2 \nabla^2 \Psi = -\partial^2 \Psi / \partial t^2$, and hence,

$$\nabla^2 E_{x,y,z} + k^2 E_{x,y,z} = 0 \quad (2.16)$$

$$\nabla^2 H_{x,y,z} + k^2 H_{x,y,z} = 0, \quad (2.17)$$

where $k = \omega \sqrt{\mu \epsilon}$ is the wavenumber of the guided mode. Manipulating equations (2.10 – 2.15) and assuming the y -dependence of all fields to be $\exp(\pm j k_y y)$, i.e., the components have a sinusoidal spatial dependence in y -direction, we can write all the field components in terms of the dominant E_y component as [80],

$$H_x = -\left(\frac{k^2}{k^2 - k_y^2}\right) \frac{\beta}{\omega \mu} E_y \quad (2.18)$$

$$H_y = 0 \quad (2.19)$$

$$H_z = -\left(\frac{k^2}{k^2 - k_y^2}\right) \frac{1}{j \omega \mu} \frac{\partial E_y}{\partial x} \quad (2.20)$$

$$E_x = \left(\frac{1}{k^2 - k_y^2}\right) \frac{\partial^2 E_y}{\partial x \partial y} \quad (2.21)$$

$$E_z = -\left(\frac{j}{k^2 - k_y^2}\right) \beta \frac{\partial E_y}{\partial y}. \quad (2.22)$$

The solutions for all the field components for E_{nm}^x modes are obtained from equations (2.18 – 2.21) by interchanging magnetic field and electric field components and replacing ϵ by $-\mu$ [81].

2.1.2. Waveguide modes

Prior to calculating waveguide modes, we consider Marcatili's approximation, which results in $n_1/n_2 - 1 \ll 1$ and $n_1/n_0 - 1 \ll 1$, where $n_i = \sqrt{\epsilon_i}$ is the RI of the medium. This also means both k_x and k_y are $\ll k_z$. The predominant component E_y for E_{nm}^y modes can be obtained by solving equations (2.16). For media 1, 2 and air (designated as medium 0), the values of E_y read [81]

$$E_y^{(1)} = C_1 \cos(k_{x1}[x + x_0]) \cos(k_{y1}y + y_0) \quad (2.23)$$

$$E_y^{(2)} = C_2 \cos(k_{x2}[x + x_0]) \exp(-j k_{y2}y) \quad (2.24)$$

$$E_y^{(3)} = C_3 \cos(k_{y0}[y + y_0]) \exp(-j k_{x0}x) \quad (2.25)$$

$$E_y^{(4)} = C_4 \cos(k_{x0}[y + x_0]) \exp(-j k_{y0}y) \quad (2.26)$$

$$E_y^{(5)} = C_5 \cos(k_{y0}[y + y_0]) \exp(-j k_{x0}x), \quad (2.27)$$

where the field superscripts (1) – (5) correspond to the transverse sections labelled in Fig. 2.1 and

$$k_{xq}^2 + k_{yq}^2 + \beta^2 = k^2 = \omega^2 \mu_q \epsilon_q, \quad (2.28)$$

where, subscript $q = 0, 1, 2$ identifies the medium. All C_i are arbitrary constants and x_0 and y_0 are coordinates of the field maxima/minima in medium 1, i.e., the silicon waveguide. We note that eqn. (2.28) can be reformulated for medium 1 as

$$\beta = \sqrt{(\omega^2 \mu_1 \epsilon_1) - k_{x1}^2 - k_{y1}^2}. \quad (2.29)$$

The phase constant β must be real for all propagating modes. An imaginary β leads to an exponential damping of all the field components as a function of z and the wave does not propagate.

Recalling the boundary conditions for the horizontal air-silicon interface above the waveguide at $y = b/2$, the tangential electric and magnetic field components should be continuous, ergo $H_x^{(1)} = H_x^{(3)}$ and $E_z^{(1)} = E_z^{(3)}$. Satisfying these conditions results in

$$k_{x1} = k_{x0} = k_x \quad (2.30)$$

and consequently,

$$C_1 \cos \left(k_{y1} \left[\frac{b}{2} + y_0 \right] \right) = \frac{k_3^2}{k_1^2} C_2 \exp(-jk_{y0}b/2) \quad (2.31)$$

$$C_1 \sin \left(k_{y1} \left[\frac{b}{2} + y_0 \right] \right) = \frac{k_3^2}{k_1^2} C_2 \exp(-jk_{y0}b/2) \quad (2.32)$$

The non-trivial solution of equations (2.31) and (2.32) leads to [81]

$$\tan \left(k_{y1} \left[\frac{b}{2} + y_0 \right] \right) = j \frac{\epsilon_1 k_{y0}}{\epsilon_0 k_{y1}}. \quad (2.33)$$

Similarly for matching boundary conditions at $y = -b/2$, we get

$$\tan \left(k_{y1} \left[\frac{b}{2} - y_0 \right] \right) = j \frac{\epsilon_1 k_{y2}}{\epsilon_2 k_{y1}}, \quad (2.34)$$

where $k_{x1} = k_{x2} = k_x$. Pursuing similar strategy for vertical interfaces at $x = \pm a/2$, two more dispersion relations are obtained as follows:

$$\tan \left(k_x \left[\frac{a}{2} \pm x_0 \right] \right) = j \frac{k_{x0}}{k_x}, \quad (2.35)$$

and similarly $k_{y1} = k_{y0} = k_y$. Equations (2.33 – 2.35) can be rewritten as [81]

$$\tan \left(k_y \left[\frac{b}{2} \pm y_0 \right] - \frac{m\pi}{2} \right) = -j \frac{\epsilon_{2,4}}{\epsilon_1} \frac{k_y}{|k_{y2,y0}|} \quad (2.36)$$

$$\tan \left(k_x \left[\frac{a}{2} \pm x_0 \right] - \frac{n\pi}{2} \right) = \frac{k_x}{|k_{x0}|}. \quad (2.37)$$

Equation (2.37) implies $x_0 = 0$, i.e., the maxima and minima are symmetrically placed within the guiding structure since the media to the left and right of the waveguide are identical. Simplifying equations (2.36) and (2.37) results in two transcendental propagating mode equations

$$k_y b = m\pi - \tan^{-1} \left(\frac{\epsilon_2}{\epsilon_1} \frac{k_y}{\sqrt{k_1^2 - k_2^2 - k_y^2}} \right) - \tan^{-1} \left(\frac{\epsilon_0}{\epsilon_1} \frac{k_y}{\sqrt{k_1^2 - k_0^2 - k_y^2}} \right) \quad (2.38)$$

$$k_x a = n\pi - \tan^{-1} \left(\frac{k_x}{\sqrt{k_1^2 - k_0^2 - k_x^2}} \right) - \tan^{-1} \left(\frac{k_y}{\sqrt{k_1^2 - k_0^2 - k_x^2}} \right), \quad (2.39)$$

where n and m are arbitrary integers signifying the mode number of the propagating waves through the waveguide. The values for k_x and k_y are obtained by solving the above transcendental equations. The phase constant of the travelling waveguide reads as [80]

$$\beta = \frac{1}{a} \left[(k_1 a)^2 - (k_x a)^2 - \left(k_y b \cdot \frac{a}{b} \right)^2 \right]^{1/2}, \quad (2.40)$$

where $k_1 = \omega\sqrt{\epsilon_1\mu_1}$. Likewise, the transcendental equations for E_{nm}^x modes read as

$$k'_x a = n\pi - \tan^{-1}\left(\frac{\epsilon_0}{\epsilon_1} \frac{k'_x}{\sqrt{k_1^2 - k_0^2 - k_x'^2}}\right) - \tan^{-1}\left(\frac{\epsilon_0}{\epsilon_1} \frac{k'_x}{\sqrt{k_1^2 - k_0^2 - k_x'^2}}\right) \quad (2.41)$$

$$k'_y b = m\pi - \tan^{-1}\left(\frac{k'_y}{\sqrt{k_1^2 - k_0^2 - k_y'^2}}\right) - \tan^{-1}\left(\frac{k'_y}{\sqrt{k_1^2 - k_0^2 - k_y'^2}}\right), \quad (2.42)$$

where the prime represents the dispersion relations for E_{nm}^x modes. The corresponding phase constant is given by

$$\beta' = \frac{1}{a} \left[(k_1 a)^2 - (k'_x a)^2 - \left(k'_y b \cdot \frac{a}{b} \right)^2 \right]^{1/2}. \quad (2.43)$$

Furthermore, the phase velocity of the propagating mode is defined as $v_p = \omega/\beta$ and the corresponding group velocity by $v_g = \partial\omega/\partial\beta$.

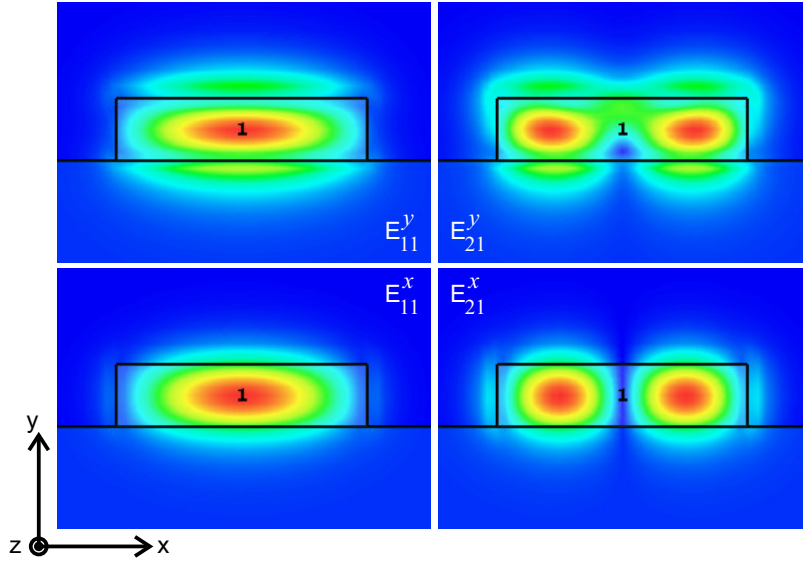


Figure 2.2.: Simulated port modes in CST® microwave studio show the distribution of the electric field intensity of the propagating wave in the transverse plane. The black rectangular enclosure is the cross-section of the waveguide, supported by a substrate underneath (here, HDPE). The "1" in the image shows the port number at which these simulation snapshots are taken. These simulated frequency is 1 THz.

Figure 2.2 shows the simulated absolute values of the electric field intensities for the first two E_{nm}^y and E_{nm}^x respectively. The black rectangle outlines the waveguide cross-section. The field discontinuities for E_{nm}^y at the top and bottom boundaries are clearly visible, likewise at the vertical boundaries in the case of E_{nm}^x modes. The plots also clearly show the asymmetric location of the field maxima along the vertical axis due to the difference of permittivity of the media atop and beneath the guiding structure. The maxima is symmetrically located along x -direction. We demonstrate the dispersion relations of these waveguide modes in chapter 4, where we characterise these waveguides relevant to this thesis.

Marcatili's solution provides approximate estimations of two important propagation characteristics

[80]. Firstly, the $1/e$ field penetration depth along the x -direction in media 0 and 2 reads

$$d_{0,(2)}^{x \rightarrow} = \frac{1}{|k_{x0,(x2)}|} = \frac{1}{([\pi/Q_{0,(2)}^{x \rightarrow}]^2 - k_x^2)^{1/2}}, \quad (2.44)$$

and similarly for y -direction is calculated as,

$$d_0^{y \rightarrow} = \frac{1}{|k_{y0}|} = \frac{1}{([\pi/Q_0^{y \rightarrow}]^2 - k_y^2)^{1/2}}, \quad (2.45)$$

where λ is free-space wavelength of the propagating wave and Q for both axes reads

$$Q_{0,(2)} = \frac{\lambda}{\sqrt{\epsilon_1 - \epsilon_{0,(2)}}}. \quad (2.46)$$

The parameter Q defines the maximum dimension of the waveguide, along either axes, which can only support the fundamental mode [80]. If $a > Q_0$, the waveguide will be overmoded along x -direction and similarly $b < \min(Q_0, Q_2)$ would ensure only one mode along the vertical direction. In chapter 4, we use these criteria to determine preliminary dimensions of the HRFZ-Si waveguides. Generally, the transverse electric field of the propagating wave in an open wave structure can be expressed as the sum of all guided and radiating orthogonal modes, which therefore means that the modal power for each guided and radiating mode are independent and additive [83].

The waveguide modes can also be calculated analytically or quasi-analytically employing other methods, such as beam propagation method [84], circular harmonics method [85] etc., which are more accurate but also tedious. Alternatively, improved semi-analytical methods for high-index contrast waveguides, such as ours, can be found in the works of Westerveld *et al.* [86]. Here, Marcatili's approximation, i.e., n_1 is minimally larger than n_0 and n_2 , is no longer a necessary assumption for the solution. Nevertheless, the Marcatili's approximate method provides a basic understanding of the wave propagation in the dielectric waveguides and hence, is a good starting point for further numerical analysis. In this thesis, we conduct numerical simulations using CST Microwave Studio® to design and analyse the waveguide structures.

2.1.3. Mode excitation, mode conversion and radiation

Arguably, the easiest and an efficient way to excite guided modes in a waveguide is to illuminate it with an incident wave or a beam at one of its longitudinal end-facets [87]. The most efficient way to calculate the excited mode (or sum of modes) in the guide is by using Green's functions [75]. However, we describe a more intuitive approach presented by C. Yeh and F. I. Shimabukuro [73]. Fulfilling the orthogonality relations between the waveguide modes (only valid for lossless or slightly lossy propagation), the transverse electric field of the guided wave, designated by the subscript t , can be expressed as [73]

$$E_t(x, y) = \sum_p A_p E_{tp}^{(g)}(x, y), \quad (2.47)$$

i.e., as the sum of the transverse electric fields of orthogonal guided modes $E_{tp}^{(g)}$, multiplied by a coefficient A_p . Assuming a normal incidence on the waveguide facet for simplicity, the power coupled to the p^{th} guided mode P_p is calculated as the mode-overlap between the field distribution of the

incident beam $E_t^{(inc)}$ and the field distribution of the respective mode. Hence,

$$\begin{aligned} P_p &= (1 - \eta_{ref}) \frac{1}{2} |A_p|^2 \\ &= (1 - \eta_{ref}) \frac{\epsilon_1}{2\mu_0} \text{Re} \left[\iint \vec{E}_t^{(inc)} \cdot \vec{E}_{tp}^{(g)} dx dy \right], \end{aligned} \quad (2.48)$$

where, η_{ref} is the fraction of power reflected from the waveguide facet due to the mismatch of wave impedances, the transverse mode field $\vec{E}_{tp}^{(g)}$ is normalised for unit incident power, such that

$$\sqrt{\frac{\epsilon_0}{\mu_0}} \iint \left| \vec{E}_{tp}^{(g)} \right|^2 dx dy = 1 \text{ W.}$$

We excite the waveguides demonstrated in this thesis by a free-space circularly symmetrical Gaussian beam, where the electric field distribution can be expressed as

$$\vec{E}^{(inc)} = E_0 \exp \left[- \left(\frac{x^2 + y^2}{2w^2} \right) \right] \hat{e}_x, \quad (2.49)$$

where w is beam radius and E_0 is the normalised amplitude. Hence, substituting $E^{(inc)}$ from eqn. (2.49) in (2.48), total coupled power to the guided mode can be estimated. However, due the discontinuities in the transverse electric fields of the guided mode, the coupled power can only be numerically evaluated. Other efficient ways of exciting waveguides using efficient transitions from rectangular metallic waveguides are out of the scope of this thesis and can be found elsewhere [88]–[90].

Coupled mode theory [89] states that any waveguide cross-section supports finite guided modes and a continuous spectrum of radiating modes [73]. Any lack of uniformity in the wave-propagation path can lead to inter-modal coupling, resulting in multimodal propagation in the waveguides. Examples of non-uniformity can be bends and corners in waveguide structures, scattering centres due to surface irregularities, dimensional variation or interface roughness. In practice, power in the radiating modes can be considered lost and hence, power coupling from a guided mode to radiating modes is always undesired. Obvious exceptions are the waveguide-based leaky-wave antennas, which are designed to radiate. On the contrary, intermodal coupling between guided modes can be beneficial to reduce dispersion in the waveguides [73]. The guided higher frequencies propagate at a slower speed than the lower frequency components and can be transported in higher-order modes (HOMs) until the propagation delays between the frequency components are appropriately compensated. The inter-modal coupling coefficient can be calculated using the spatial overlap integral among the two modes at the location of the non-uniformity. The power coupling coefficient is defined as

$$C_{p \leftrightarrow q} = \frac{\left| \iint \vec{E}_p(x, y) \cdot \vec{E}_q^*(x, y) dx dy \right|^2}{\iint |\vec{E}_p(x, y)|^2 dx dy \cdot \iint |\vec{E}_q(x, y)|^2 dx dy}, \quad (2.50)$$

where \vec{E}_p and \vec{E}_q are the electric field distribution of the two inter-coupled modes. Note that, in straight lossless or slightly lossy waveguide sections, the modes are orthogonal and consequently, the numerator of eqn. (2.50) is 0. $C_{p \leftrightarrow q}$ is only be non-zero when the modes are spatially shifted along the $x - y$ -plane, usually induced by the aforementioned waveguide perturbations. Equation (2.50) is a more generalised form of eqn. (2.48). This relation is extremely handy while designing waveguide bends, especially for offset circular bends [91] or bends with non-constant radius of curvature [92], where the expected $C_{p \leftrightarrow q}$ can be minimised by changing the waveguide offset or the curvature functional.

2.1.4. Attenuation

Up until now, we derived the mode characteristics for lossless wave propagation in perfect dielectrics. The relevant boundary conditions and orthogonality relations can also be extended for slightly lossy media. The propagating waves undergo power dissipation as Joules heat in media with a finite electrical conductivity [76]. This time averaged heat dissipation P_d within a volume V_d can be calculated from the *Poynting's vector* as,

$$P_d = \left\langle \frac{1}{2} \text{Re} \left[\int_{V_d} \sigma \vec{E} \cdot \vec{E}^* dV \right] \right\rangle_T. \quad (2.51)$$

The permittivity of imperfect dielectrics is complex and usually described as $\epsilon = \epsilon' - j\epsilon''$, where ϵ' is its real part and $\epsilon'' = \sigma/\omega$ is the imaginary component. Consequently, the propagation constant is represented in complex form as

$$\gamma_p = \alpha_p + j\beta_p, \quad (2.52)$$

where α_p is the field attenuation constant for the p -th mode and β_p is the corresponding phase constant defined in equations (2.40) and (2.43). The spatio-temporal variation of the field components along the direction of propagation changes to $\exp(j\omega t - \gamma_p z)$.

For slightly lossy media, such as the ones used in this thesis, the power loss in the waveguides and corresponding attenuation constant can be calculated using perturbation techniques [93]. It essentially considers an exponential power decrement as function of the propagation distance, which is later multiplied to a loss-less transmission scenario to obtain the solutions for the lossy case. For single mode propagation through the waveguides, this translates to,

$$\bar{P}^{(p)}(z) = \bar{P}_0^{(p)} e^{-2\alpha_p z}, \quad (2.53)$$

where $\bar{P}_0^{(p)}$ is the time-averaged input power coupled to the p th mode, $\bar{P}^{(p)}(z)$ is the time-averaged power after a propagation distance of z . Assuming that no intermodal power exchange occurs, i.e., the cross-sectional area of the mode remains identical over z , the average power dissipation per unit length in eqn. (2.51) must be equal to

$$\bar{P}_d^{(p)} = -\frac{\partial \bar{P}^{(p)}(z)}{\partial z} = 2\alpha_p \bar{P}^{(p)}. \quad (2.54)$$

Thus, using equations (2.5) and (2.54), the attenuation constant for p th mode can be calculated to,

$$\alpha_p = \frac{\bar{P}_d^{(p)}}{2\bar{P}^{(p)}} = \frac{\sigma/2 \int \int \vec{E}^{(p)}(x, y) \cdot \vec{E}^{(p)*}(x, y) dx dy}{\text{Re}[\int \int (\vec{E}_t^{(p)}(x, y)) \times \vec{H}_t^{(p)*}(x, y)] \cdot \hat{e}_z dx dy}, \quad (2.55)$$

We note that the α_p for unidirectional single mode propagation is a constant. Derivations pertaining to attenuation constant for multimode propagation can be found in the works of Imbriale *et al.* [94].

2.1.5. Dispersion

Dispersion in the dielectric waveguides is critical for their use in communication systems or in pulsed operations [34]. Equations (2.44) and (2.45) show that the penetration depth of the propagating transverse fields into surrounding media is inversely proportional to frequency. Hence, as the frequency increases, the modal power tends to concentrate in the high refractive index region (e.g. silicon).

Consequently effective permittivity of the mode increases non-linearly with frequency, which results in the dispersive behaviour of the waveguides. The modal dispersion factor for mode p is quantified as [95],

$$D^{(p)} = \frac{2\pi c_0}{\lambda^2} \frac{\partial^2 \beta^{(p)}}{\partial \omega^2} = \frac{f^2}{2\pi c_0} \frac{\partial^2 \beta^{(p)}}{\partial f^2}, \quad (2.56)$$

where $\beta^{(p)}$ is the corresponding modal phase constant and $\partial^2 \beta^{(p)} / \partial \omega^2$ is the derivative of group velocity of the propagating mode. D is also called the *pulse broadening factor*. The effect of waveguide dispersion for CW operation is insignificant and hence, dispersion compensation techniques are not investigated in the scope of this thesis.

2.2. Photomixing and photoconductors

Any THz system requires active devices, namely THz sources and receivers, to drive the system. A photoconductor is a highly resistive piece of semiconductor, whose conductivity can be modulated by an applied laser signal. Photomixing is an effective way of THz generation using these photoconductive switches, wherein the optical signals of two lasers are mixed and subsequently down-converted to generate currents oscillating at THz frequencies. Two lasers with electric fields $\vec{E}_1(t)$ and $\vec{E}_2(t)$ and having a frequency separation of f_{THz} are mixed inside a photoconductor. For simplicity, we consider that the lasers are polarised in the same direction and their corresponding electric field amplitudes are equal. Their time-harmonic scalar electric fields read

$$E_1(t) = E_0 \cdot \exp(-j2\pi f_L t) \quad (2.57)$$

$$E_2(t) = E_0 \cdot \exp(-j2\pi [f_L + f_{\text{THz}}]t + \phi), \quad (2.58)$$

where, E_0 is the amplitude of the electric field, ϕ is the relative phase difference between the lasers and $f_L \gg f_{\text{THz}}$. A more generalised consideration can be found elsewhere [96], however, under the aforementioned proposition, maximum THz photocurrent is generated [11]. The charge carrier concentration in the photoconductive material is proportional to the intensity of the incident laser signal I_L , where

$$\begin{aligned} I_L(t) &\propto |E_{\text{total}}(t)|^2 = |E_1(t) + E_2(t)|^2 \\ &= |E_0 \cdot \{\exp(-j2\pi f_L t) + \exp(-j2\pi [f_L + f_{\text{THz}}]t + \phi)\}|^2 \\ &= 2E_0^2 \cdot \{1 + \cos(2\pi f_{\text{THz}}t + \phi)\} \end{aligned}$$

With I_0 as its amplitude, the time varying intensity of the incident laser signal reads

$$I_L(t) = I_0 \cdot \{1 + \cos(2\pi f_{\text{THz}}t + \phi)\}. \quad (2.59)$$

$I_L(t)$ is proportional to the time-varying laser power $P_L(t)$. When a voltage is applied across the electrodes attached to the photoconductors, the extracted *photocurrent* oscillates depending on the changing charge carrier density in the photoconductor. Assuming all the laser power is absorbed and all electron-hole pairs efficiently separated by the applied bias, the total photocurrent generated in the ideal photoconductor is calculated as [11]

$$i_{\text{THz}}(t) = \frac{eP_L(t)}{hf_L} = \frac{eP_0}{hf_L} \cdot \{1 + \cos(2\pi f_{\text{THz}}t + \phi)\}, \quad (2.60)$$

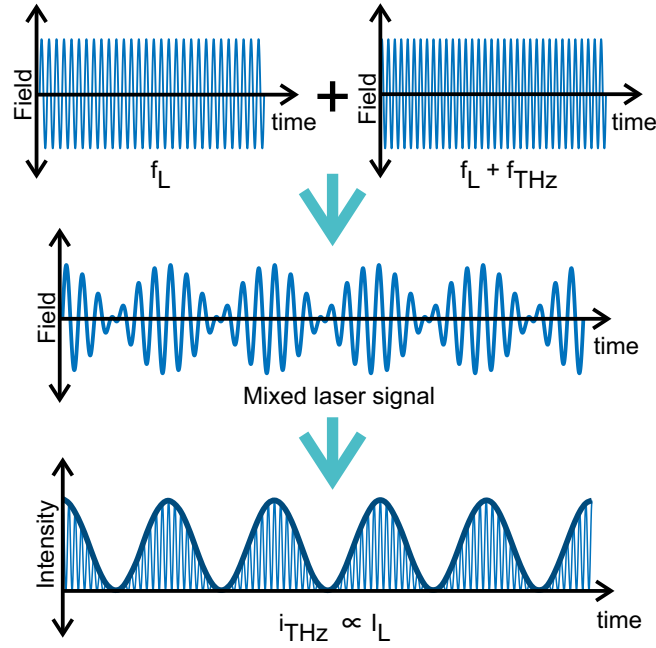


Figure 2.3.: Plots show the mathematical representation of the photomixing process of two lasers signals.

where, $P_0 \propto I_0$, h is the Planck's constant and e is the charge of an electron. The generated photocurrent has a frequency-independent direct current (DC) component and a frequency-dependent alternating current (AC) component, which constitute the THz current. In real photoconductors, in addition to the *roll-offs* discussed in the following section, the applied bias is not sufficient to separate all the generated electron-hole pairs. Hence, the generated THz photocurrent is lower than the ideal case described by eqn. (2.60). The DC component in real photoconductors usually depend on frequency, as the absorption coefficient of the photoconductors varies with frequency. Figure 2.3 shows a schematic of the photomixing process. The time-averaged envelope of the intensity, responsible for the generation of the electron-hole pairs in the photoconductor, varies at THz frequencies.

The photoconductors are usually attached to antennas to radiate the THz photocurrent into free-space or other passive components such as waveguides, lenses, etc. When used as receivers, the photoconductors are not externally biased but the incident THz field on the attached antenna induces a bias voltage across the electrodes of the photoconductors. The resulting ideal current density j in the device reads

$$j(t) = N_{e,h}(t)e\mu_{e,h}E(t), \quad (2.61)$$

where $\mu_{e,h}$ is the average mobility of the charge-carriers, $N_{e,h}(t) \propto \cos(2\pi f_{\text{THz}}t)$ is the charge carrier density in the photoconductor and E is the scalar electric field in the device, which is proportional to the THz bias voltage across the electrodes. Thus, the product of the two varying THz components leads to an ideal receiver current of

$$\begin{aligned} i_{rx}(t) &= \int j(t)\partial A \propto \frac{eI_0}{hf_L} \cos(2\pi f_{\text{THz}}t + \phi) \cdot E_{\text{THz}} \cos(2\pi f_{\text{THz}}t + \phi + \psi) \\ &= i_0[\cos(\psi) + \cos(4\pi f_{\text{THz}}t + 2\phi + \psi)], \end{aligned} \quad (2.62)$$

where A is cross-sectional area through which the charge-carriers flow, $i_0 \propto E_{\text{THz}}$ is the amplitude of the generated photocurrent, wherein E_{THz} is the received THz electric field at the antenna. $\psi =$

$2\pi f_{\text{THz}} \cdot \Delta d_{\text{opt}}/c_0$ is the phase difference between the two mixed THz components at the receiver resulting from an optical path length difference of Δd_{opt} in the setup and c_0 is the speed of light in vacuum. Subsequently, the high frequency component of the photoconductor is filtered out and the low frequency component is measured as the receiver response, which contains both the amplitude and phase information of the detected THz waves.

In the scope of this thesis, we used ErAs:In(Al)GaAs-based photoconductors as they are engineered specifically for 1550 nm operation, i.e., compatible with widely available and cost-effective telecom lasers. We primarily used them as receivers in the PVNA architecture, both in the free-space and integrated versions. A broad-side log-periodic antenna is coupled to the photoconductor for free-space operation. Detailed description of the such devices can be found in the works of Fernandez Olvera *et al.* [25], [97]. In this thesis, we fabricated and used end-fire VA-coupled photoconductors in the integrated PVNA, to couple in THz power from waveguides, which is described in further details in chapter 5.

2.2.1. Frequency-dependent roll-off

Figure 2.4 shows the equivalent circuit diagram of an antenna-coupled photoconductor with a DC resistance $R_{pc} \geq 10 \text{ k}\Omega$ under illumination. Like any other semiconductor-based electrical component, photoconductors too have associated parasitic capacitances, primarily stemming from the metal electrodes required to extract the generated photocurrent. For a distance of d_{elec} between two electrodes and an effective permittivity of ϵ_{eff} , the device capacitance C_{pc} reads [11]

$$C_{pc} = \frac{\epsilon_{eff} A_{elec}}{d_{elec}}, \quad (2.63)$$

where A_{elec} is the cross-sectional area of the electrodes. For planar metallic capacitors atop a semiconductor, the field lines between the electrodes are non-linear and hence, ϵ_{eff} is a function of absolute material permittivity, width of the electrodes and the gap between them. The electrode structure of the photoconductive receivers specific to this thesis is detailed in the next section, where eqn. (2.69) gives the exact value of ϵ_{eff} . Along with the device capacitance, the attached antenna adds additional resistance ($R_{pc} \gg R_A \sim 100 \Omega$) to the photoconductor circuitry and thus, the photocurrent undergoes a frequency dependent *RC roll-off*, where the roll-off coefficient can be expressed as [11]

$$\eta_{RC} = \frac{1}{1 + (2\pi R_A C_{pc} f_{\text{THz}})^2}. \quad (2.64)$$

At very high frequencies, i.e., when $2\pi R_A C_{pc} f_{\text{THz}} \gg 1$, the photocurrent extracted from the photoconductive receiver decreases by a factor of f_{THz}^2 , thus limiting the high frequency performance of such devices. A larger gap between the electrodes (d_{elec}) reduces the parasitic capacitance of the photoconductor and consequently, improves the *RC roll-off*. However, the transit time τ_{tr} of the charge-carriers between the electrodes increases, which adversely affects the THz photocurrent. Simply put, individual charge-carriers contributing to the current are generated at different locations on the photoconductor and travel non-identical distances to reach the electrodes. Ergo, their current contributions have different phases. If these phase differences exceed $\pi/2$, then the current contribution does not add up constructively, resulting in a reduced net THz photocurrent in the photoconductor. This phenomenon is called *transit time roll-off*. In order to prevent destructive interference, photoconductive materials used in CW operation are engineered to have very short carrier lifetime [98], [99], ideally shorter than the inverse of the target frequency. The carrier lifetime is typically shortened by the introduction of *trap-states* [99], which act as recombination centres for the electron-hole pairs.

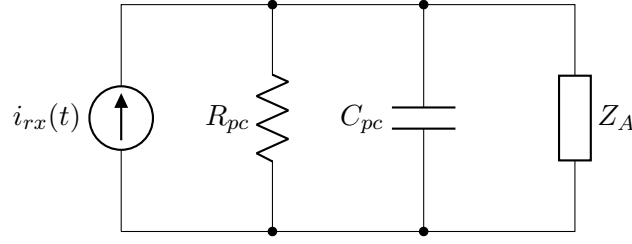


Figure 2.4.: Equivalent circuit of an antenna-coupled photoconductor. R_{pc} and C_{pc} are the resistance and the capacitance of the photoconductor, respectively and $Z_A = R_A + jX_A$ is the antenna impedance, where X_A is the reactance of the antenna.

In real photoconductors, only a fraction of all photo-generated electron-hole pairs contribute towards the photocurrent, the rest recombine before reaching the electrodes. The number of available charge-carriers decreases exponentially with time due to recombination. With τ_{rec} as the *recombination time* of the photoconductive material, the average photocurrent over the *transit time* τ_{tr} can be calculated from eqn. (2.60) as [100]

$$\begin{aligned} i_{THz}(t) &= \frac{1}{\tau_{tr}} \int_0^{\infty} i_0^{ideal} \cdot \{1 + \cos(2\pi f_{THz}t + \phi)\} \exp(-t/\tau_{rec}) dt \\ &= i_0^{ideal} \frac{\tau_{rec}}{\tau_{tr}} \left[1 + \frac{\sin(2\pi f_{THz}t + \phi)}{\sqrt{1 + (2\pi f_{THz}\tau_{rec})^2}} \right], \end{aligned} \quad (2.65)$$

where $i_0^{ideal} = eP_0/hf_L$ is the ideal photocurrent. The factor $\tau_{rec}/\tau_{tr} \ll 1$ is called photoconductive gain g , which affects both the DC and the THz photocurrent identically. This brings forth the *lifetime roll off* factor of the THz photocurrent as [100]

$$\eta_{LT} = \frac{1}{1 + (2\pi\tau_{rec}f_{THz})^2}. \quad (2.66)$$

It is evident from eqn. (2.66) that a smaller τ_{rec} improves the lifetime roll-off, however, it negatively affects the carrier mobility of the photoconductor, and subsequently the generated photocurrent. Thus, engineering photoconductors for CW operation is an optimisation between the advantages of short carrier lifetime and the resulting reduced carrier mobility. ErAs:In(Al)GaAs material show excellent results in this regard. The periodic stacking of InGaAs and InAlAs helps to maintain a higher carrier mobility and the localised semi-metallic ErAs depositions creates recombination centres to maintain a low carrier lifetime.

2.2.2. ErAs:In(Al)GaAs photoconductors

Apart from desired high carrier mobility and low carrier lifetime, there are two further requirements for a good photoconductive mixer working as a detector at THz frequencies [25]. Firstly, the material should be highly absorptive at the laser wavelengths, i.e., the conversion efficiency of the laser intensity to charge carrier density should be high. This mostly requires materials which undergo inter-band absorption for the employed telecom laser wavelengths, and thus a bandgap smaller than 0.8 eV [101]–[103]. Secondly, the device resistance R_{PC} must be high, even under illumination, to reduce the noise floor of the device. The noise current in photoconductors are predominantly thermal in origin [25] and reads

$$I_N = \sqrt{4k_B T \Delta f / R_{PC}}, \quad (2.67)$$

where k_B is the Boltzmann constant, T is the absolute temperature and Δf is the equivalent noise bandwidth of the measurement system (e.g., LIA). Noise equivalent power (NEP) is a measure of the lowest detectable power by the photoconductive receiver over an unit measurement bandwidth ($\Delta f = 1$ Hz) and is expressed as [104]

$$NEP(f) = \frac{8k_B T}{\eta_{THz}^{eff} \eta_{LT}(f) \eta_{RC}(f)} \frac{R_{PC}}{R_A(f)}, \quad (2.68)$$

where R_A is the resistance of the attached antenna, η_{RC} and η_{LT} are the frequency-dependent RC and lifetime roll-offs, respectively and η_{THz}^{eff} incorporates all other non-idealities of the photoconductor, such as laser-alignment errors, different DC and THz mobility of the charge-carriers, etc. Additionally, high device resistances reduce the current flowing in the photoconductor, therefore reducing the heating related performance depreciations (e.g. reduced mobility due to phonon scattering, faster device ageing, etc.) [11] of the receiver. Typical values of desired dark resistance and resistance under laser illumination are ~ 1 M Ω and ~ 10 k Ω , respectively. The ErAs:In(Al)GaAs material system is engineered to suffice the four aforementioned requirements.

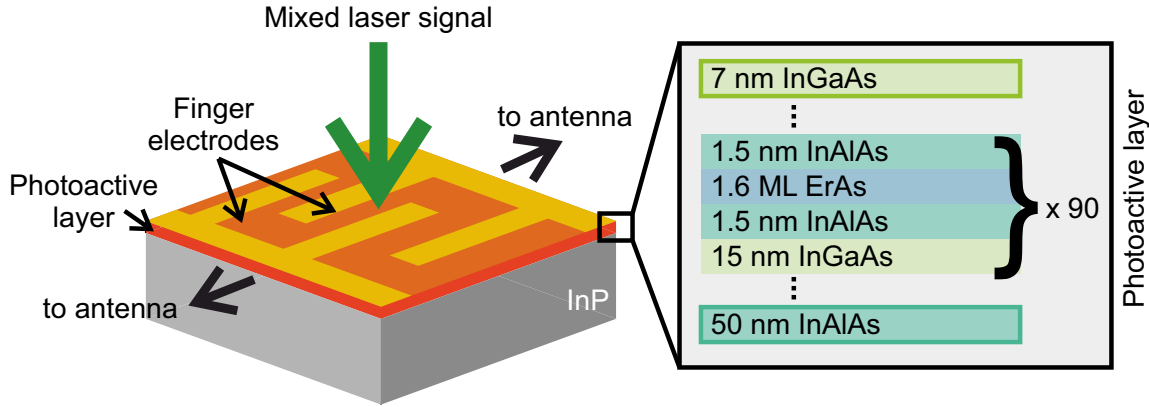


Figure 2.5.: Schematic shows a photomixing device with detailed layer structure of an exemplary photoactive region. The (internal) material label is 160229A.

Figure 2.5 shows a schematic of an exemplary ErAs:In(Al)GaAs photoconductor used in this thesis as THz receivers for CW operation. The gold electrodes deposited atop the photoconductor resemble interlocked fingers and the motivation behind is discussed later. The photoactive area (orange) is a periodic crystalline stack of alternating nanometric InGaAs and ErAs:InAlAs layers, also referred to as *super-lattice* structure and is grown on InP substrate. The charge carriers are generated and transported in the absorbing InGaAs layers, which feature a high electron mobility along with high laser absorption at 1550 nm. The ErAs trapping centres are deposited inside or next to thin InAlAs layers, so that the tunnelling probability of the charge carriers travelling in InGaAs layer to the recombination sites is elevated. 90 repetitions of the layers, in order, form the super-lattice structure. The engineered super-lattice structure physically decouples the carrier mobility from the carrier recombination time as the carriers recombine in a different layer than the layer they traverse. However, the necessary tunnelling for recombination increases the carrier lifetime compared to structures where ErAs is deposited in bulk InGaAs. The super-lattice structure also results in slightly lowered absorption coefficient, compared to bulk InGaAs. Regardless, the ErAs:In(Al)GaAs super-lattice provides a good compromise between short carrier lifetime, high dark resistance and high carrier mobility [11]. A deeper dive into the material specifications, the recombination phenomenon and the relevant analytical formulations can be

found elsewhere [11], [98], [99]. For the photoconductor used in this thesis, the dark and illuminated resistances are $\sim 0.4 \text{ M}\Omega$ and $\sim 15 \text{ k}\Omega$, respectively. Furthermore, the photoconductors feature a recombination time $\tau_{rec} = 2.27 \pm 0.15 \text{ ps}$ [105] and carrier mobility of $800 \pm 70 \text{ cm}^2/\text{V}\cdot\text{s}$ [106].

A smaller carrier lifetime reduces the distance travelled by the photo-generated charge carriers. To compensate this, the collection area electrodes of the electrodes is enlarged, i.e., transit path of the charge carrier is shortened, resulting in the apparent finger-like structures. The corresponding capacitance of the photoconductor can be calculated using eqn. (2.63), where the effective permittivity of the structures becomes [11]

$$\epsilon_{eff} = \frac{K(k)}{K(k')}(\epsilon_0 + \epsilon_{pc}), \quad (2.69)$$

where, ϵ_{pc} is the absolute permittivity of the photoconductive material, $k = \tan^2(\pi w_E / \{4[w_E + w_G]\})$, $k' = \sqrt{1 - k^2}$ and $K(k) = \int_0^{\pi/2} (1 - k^2 \sin^2 \theta)^{-1/2} d\theta$ and w_E and w_G are width of the individual finger electrodes and gap between two consecutive ones, respectively. The effective gap between electrodes is $d_{elec} = w_E + w_G$. In essence, finger structures increase the device capacitance as the gap between the electrodes decreases, and consequently worsens the RC roll-off, however, the charge collection efficiency, i.e., the photoconductive gain, significantly increases. We note that, the fingers structures, due to their proximity, have a very high electric field density between them and can only be used for CW operation, where the laser power is roughly constant over time and is in the order of a few milliwatts. For pulsed operation the laser energy is temporally concentrated. These devices saturate and even, undergoes electrical and thermal breakdown, as the significantly powerful laser pulse generates a surge of photocurrent which, in turn, generates excessive heat in the device. Hence, unstructured photoconductive gaps are typically used in pulsed operation [102].

Besides, these finger structures affect the incoming laser signal in two further ways. Firstly, the metallic fingers acts as a polarisation filter for the incident laser, and thus maximum optical power is transmitted to the photoactive material when the laser is polarised perpendicular to the direction of the fingers, i.e. along y-axis for the finger electrodes shown in Fig. 2.6(a). The finger electrodes of the photoconductive active devices shown here are $1.5 \text{ }\mu\text{m}$ wide (w_E) and are separated by $2 \text{ }\mu\text{m}$ (w_G). This results in the total photoactive area of $12 \times 10 \text{ }\mu\text{m}^2$.

Secondly, these electrodes cast a shadow on the photoactive area and therefore, the laser spot needs to be positioned appropriately on the active area for maximum carrier generation. Two Gaussian laser spots with diameters of $4.34 \text{ }\mu\text{m}$ and $7.26 \text{ }\mu\text{m}$, respectively, are considered to find the optimal incidence position on the photoactive area. Considering an electron drift velocity $v_d^{e^-} \approx 10^5 \text{ m/s}$ and the recombination time of $\tau_{rec} = 2.27 \times 10^{-12} \text{ s}$, the distance travelled by an electron before recombination is $v_d^{e^-} \times \tau_{rec} \approx 227 \text{ nm}$. In other words, only the electrons generated 223 nm around the finger electrodes are absorbed and contributes to the total photocurrent. The phase difference between these collected charge carriers are insignificant as $\tau_{rec} \ll \tau_{tr}$ and an additive contribution is assumed. Figures in 2.6(b) and (c) show the fraction of generated photoelectrons contributing to photocurrent for different positions of the center of the Gaussian laser spot incident on $x - y$ plane. The figures show for a tighter laser spot in 2.6(b), the fluctuations of photocurrent due to the incidence-position of the laser is higher than a larger laser spot in 2.6(c), however the maximum photocurrent is $\approx 25\%$ more for a tighter laser focus.

The log-periodic antenna-coupled, ErAs:In(Al)GaAs-based photoconductive receivers, developed in-house, are comparable to commercially available table-top non-cryogenic THz receivers [107]. The photoconductors feature a NEP = 1.8 fW/Hz at 0.188 THz . A THz system constituting ErAs:In(Al)GaAs-based photoconductive source and receiver has an operational bandwidth up to 3.65 THz and DNRs of 52 dB and 31.7 dB at 1 and 2 THz , respectively [25], despite the fact that the active devices only

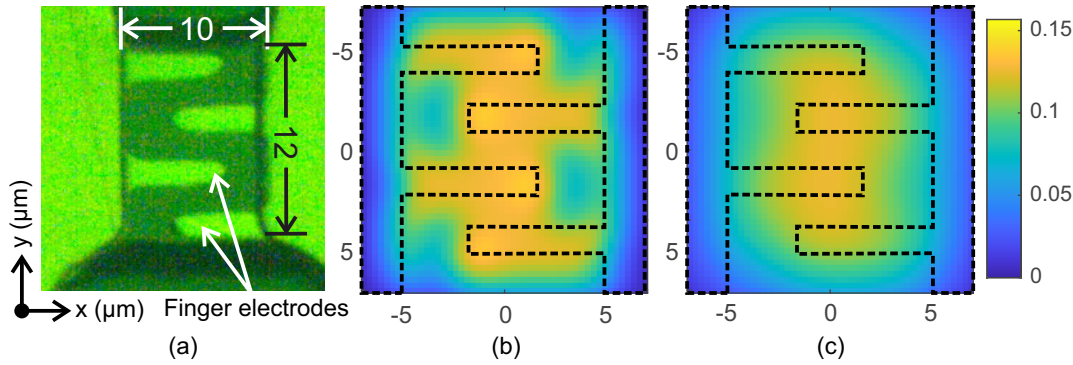


Figure 2.6.: Micrograph in (a) shows the finger electrodes atop the active region of the ErAs:In(Al)GaAs photoconductor. Graphs in (b) and (c) show the analytically calculated THz photocurrent as a function of the incidence position of the Gaussian beam atop the active area. The laser spot-sizes for (b) and (c) are $4.34 \mu\text{m}$ and $7.26 \mu\text{m}$, respectively. The dotted lines in the plots show the boundaries of the finger electrodes. Due to the small carrier lifetime, high photocurrents are generated when the laser is incident very close to or on top of a finger-electrode. The plots assume that the photoactive area is not optically saturated.

absorb $\sim 50\%$ available laser power [11], with additionally reduced carrier collection due to the low lifetime of the charge carriers. An increment in the super-lattice stack depth improves laser absorption, however, only logarithmically. Theoretically, more a smaller gap between the finger-electrodes will improve charge carrier collection, however, photolithographic limitations and increase of parasitic capacitances [11] make such configurations impractical. However, we note that, Turan *et al.* have very recently demonstrated plasmonics-enhanced THz detector performance for nanometric gaps between finger structures [108].

2.2.3. P-I-N Diodes

In photoconductors, the generated electron-hole pairs under illumination need an external bias to be separated and constructively contribute to the photocurrent. This technique is inefficient as many charge carriers recombine before reaching the electrodes. An alternative photomixing device is a P-I-N diode, which has a built-in potential gradient between the positively and the negatively doped sides. Due to the internal potential gradient, the electrons and holes readily start moving right after generation towards the *p-side* and the *n-side*, respectively, and a photocurrent is generated in the diode without necessitating any additional external bias. However, the P-I-N diodes usually operate in reverse-biased condition generate higher photocurrents. The photoconductive gain of P-I-N diodes is close to unity due to minimal recombination losses and hence, they make excellent THz sources. Like photoconductors, P-I-N diodes also suffer from *RC* and *transit time roll-offs*. Since we only used a commercially available P-I-N diode from Toptica photonics/Fraunhofer HHI as source, its working principle and characteristics are beyond the scope of this thesis and can be found elsewhere [11], [100], [109].

2.2.4. Photoconductors in PVNA

Photoconductive receivers are well-suited to be used in PVNA architectures because they measure THz electric field, rather than its power. We only detect the DC component of the receiver photocurrent

given in eqn. (2.62). Considering the *roll-offs* from section 2.2.1, the detected receiver current reads

$$i_{Rx} = i_0^{ideal} g \sqrt{\eta_{RC} \eta_{LT}} \cos(\psi) = i_0(f_{THz}), \quad (2.70)$$

where i_0^{ideal} is the photocurrent in an ideal photoconductor, g is the photoconductive gain, η_{RC} and η_{LT} are the *RC* and *lifetime roll-offs*, respectively. Thus, the DC detector current is a function of THz frequency owing to the roll-off factors. The homodyne setup in Fig. 1.2 acts as an interferometer with unbalanced arms, where the receiver current i_{homoo} can be written from eqn. (2.62) as [96]

$$i_{homoo}(f_{THz}) = i_0(f_{THz}) \cdot \cos(k_0 \Delta d_{opt}), \quad (2.71)$$

where $k_0 = 2\pi f_{THz}/c_0$ is the wavenumber at f_{THz} for free-space propagation and i_0 is proportional to the incident THz field on the receiver. The Hilbert transform of i_{homoo} calculates the complex receiver current [110] as

$$\underline{i}_{homoo}(f_{THz}) = i_0(f_{THz}) \cdot \exp(jk_0 \Delta d_{opt}). \quad (2.72)$$

When a dielectric DUT of complex RI \underline{n}_s and thickness d_s is introduced in the THz path, an identical thickness of the free-space THz path is shortened, along with the absorption-induced losses, reflections and scattering, which change the incident THz field on the receiver. Consequently, the receiver current changes to

$$\underline{i}'_{homoo}(f_{THz}) = i'_0(f_{THz}) \cdot \exp(jk_0[\Delta d_{opt} - d_s]) \cdot \exp(jk_0 n_s d_s), \quad (2.73)$$

where $i'_0(f_{THz}) = i_0(f_{THz}) \times \underline{H}_{DUT}(f_{THz})$ and \underline{H}_{DUT} is the frequency-dependent complex transfer function of the dielectric DUT, which incorporates all the changes induced on the transmitted electric field by the DUT, owing to its material and geometric properties. The transfer function can be quantified in complex form by dividing eqn. (2.73) by (2.72) as

$$\begin{aligned} \underline{T}_{meas}(f_{THz}) &= \frac{i'_{Rx}(f_{THz})}{i_{Rx}(f_{THz})} \\ &= \frac{i'_0(f_{THz})}{i_0(f_{THz})} \cdot \exp(jk_0 n_s d_s) \exp(-jk_0 d) \\ &= \underline{H}_{DUT}(f_{THz}) \cdot e^{-jk_0 d}. \end{aligned} \quad (2.74)$$

$$(2.75)$$

The reflection coefficient of the substrate can also be calculated using similar tactics. A system comprised of these photoconductive mixers is capable of measuring complex transmission and reflection coefficients, and therefore, can be essentially utilised as a VNA working at THz frequencies powered by photonic components. In chapter 3, we take a look at the free-space PVNA architecture in greater details. In the following chapters, we elaborate on miniaturisation and integration strategies and techniques of the free-space PVNA architecture using these antenna-coupled photoconductors and HRFZ-Si waveguides to create integrated PVNA as system-on-chips (SOCs).

2.3. Antenna theory

Antennas are an essential and ubiquitous component for optoelectronic THz devices, used to transfer the generated current in THz sources to the transmission media and conversely, to couple in THz power from the transmission media into receivers [45]. From Maxwell's equations, we can derive that the

radiated field from an antenna can be uniquely determined by the electric field vector tangent to any surface enclosing the antenna [111]. The radiated field from an antenna can be approximated in polar coordinates as the Taylor-series

$$\vec{E}_{rad}(r, \theta, \phi, f, t) \approx \vec{E}_0(\theta, \phi) \left[\frac{a_1(\theta, \phi, f, t)}{r} + \frac{a_2(r, \theta, \phi, f, t)}{r^2} + \frac{a_3(r, \theta, \phi, f, t)}{r^3} + \dots \right], \quad (2.76)$$

where \vec{E}_0 is the electric field tangential to a surface enclosing the antenna at $r \rightarrow 0$ and a_i are the spatio-temporally varying normalised field coefficients. The time-harmonic phase of the electric field varies as $\exp[j(\omega t - \vec{k} \cdot \vec{r})]$, where $\omega = 2\pi f$ is the angular frequency and \vec{k} is the wave-vector pointing towards the direction of propagation of the wave. $|\vec{k}| = (\omega \sqrt{\epsilon/\epsilon_0})/c_0$, where c_0 is the vacuum speed of light and ϵ is the complex permittivity of the propagating medium.

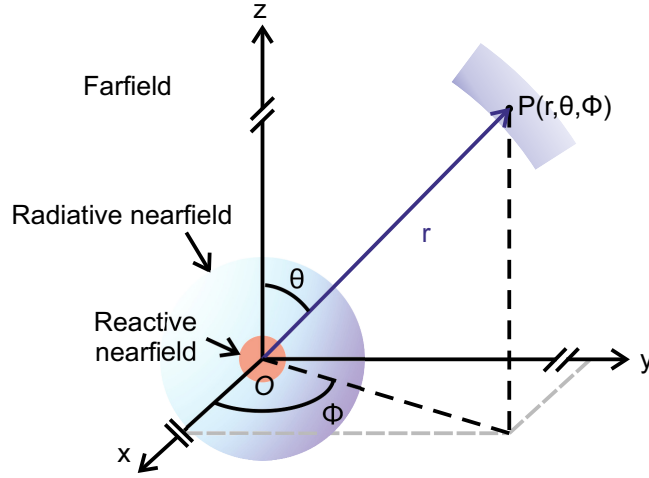


Figure 2.7.: Schematic shows the reactive nearfield, the radiative nearfield and the farfield regions surrounding an antenna placed at the origin O , assumed as a point source for simplicity. The point P is located in the farfield region of the antenna.

Equation (2.76) divides the space around the radiating antenna into three approximate regions. Firstly, the *reactive nearfield*, where the reactive components field dominate and rapidly decay with distance ($\propto 1/r^3$ or higher). Generally, the boundary of the reactive nearfield extends up to $\lambda/2\pi$ [112], where λ is the effective operating wavelength. Beyond this, the radiating field dominates. The region where the radiating fields dominate can be further divided into two and hence, the second region of interest is called the *radiative nearfield*. In this region, the angular distribution of the radiated energy is a function of the distance from the antenna. Finally, in the *farfield* region, the angular distribution of the radiated field becomes independent of the distance from the antenna [113] and can be expressed as a function of only θ and ϕ , where $0 \leq \theta \leq \pi$ and $-\pi \leq \phi \leq \pi$. The boundary between the radiating nearfield and the farfield is at $r = 2D^2/\lambda$, where D is the largest dimension of the antenna aperture [114]. The schematic in Fig. 2.7 shows the various regions around an antenna, located at the origin O . Here, we will primarily restrict ourselves to the farfield of the antenna denoted by the point P , where the antenna can be approximated as a point source with a specific normalised angular field distribution $C(\theta, \phi)$. The farfield radiation pattern is approximated as,

$$E_{ff}(r, \theta, \phi) \approx \frac{E_0}{r} C(\theta, \phi) \cdot \sin \theta \exp(j[\omega t - kr]). \quad (2.77)$$

The power in the farfield decays proportional to $1/r^2$. Here, we note two important results. Firstly, eqn. (2.77) shows a bijective relation between $E_{ff}(r, \theta, \phi)$ and $C(\theta, \phi)$. Any electric field distribution

in the antenna farfield would generate the corresponding unique normalised field distribution around the origin and correspondingly, the unique current distribution in the antenna element. This is known as the *reciprocity theorem*, i.e., the relation between the current distribution in the antenna element and its farfield radiation pattern is reciprocal. Secondly, antennas satisfy the *radiation condition*, i.e., the EM field intensities vanish at greater distances.

The term $C(\theta, \phi)$ in eqn. 2.77 for antennas with large apertures is calculated as the integral of the field distribution over the entire aperture. D. Paris showed that the farfield pattern is a function of the aperture field distribution as [115]

$$\vec{E}(r, \theta, \phi) = \frac{-jk}{4\pi} \int_A \hat{e}_r \times \left[\{\hat{e}_n \times \vec{E}'(\theta, \phi)\} - \sqrt{\frac{\mu}{\epsilon}} \{\hat{e}_r \times \hat{e}_n \times \vec{H}'(\theta, \phi)\} \right] \frac{e^{-jkr}}{r} da \quad (2.78)$$

$$\vec{H}(r, \theta, \phi) = \frac{-jk}{4\pi} \int_A \hat{e}_r \times \left[\{\hat{e}_n \times \vec{H}'(\theta, \phi)\} - \sqrt{\frac{\epsilon}{\mu}} \{\hat{e}_r \times \hat{e}_n \times \vec{E}'(\theta, \phi)\} \right] \frac{e^{-jkr}}{r} da, \quad (2.79)$$

where, \vec{E} (\vec{H}) is the farfield electric (magnetic) field vector, \hat{e}_r is the unit vector towards the farfield point (r, θ, ϕ) , \hat{e}_n is the normal vector to the antenna aperture A and \vec{E}' (\vec{H}') is the electric (magnetic) field distribution at the antenna aperture. Equations (2.78) and (2.79) only hold under the following assumptions:

1. The field intensities have harmonic time variations.
2. The medium surrounding the antenna is linear, homogeneous, isotropic and source-free.
3. There are no tangential field intensities over the surface area outside the aperture.
4. The point (r, θ, ϕ) is in the farfield of the antenna, i.e., $r \gg \lambda/2\pi$.

Additionally, considering the planar antenna aperture situated on the $z = 0$ plane, the operational wavelength is of the same order of magnitude as the aperture and the EM field confined within the antenna aperture [116], a scalar formulation for field intensities at farfield can be derived from equations (2.78) and (2.79) as [115],

$$E(r, \theta, \phi) = \frac{j}{\lambda r} e^{-jkr} \iint \underline{E}(x, y) \exp \left[jk \sin \theta (x \cos \phi + y \sin \phi) \right] dx dy, \quad (2.80)$$

where $\underline{E}(x, y)$ is the complex nearfield electric field distribution at the aperture, represented in the Cartesian coordinate system. The farfield field intensities are in spherical coordinates. The two-dimensional Fourier transform relationship between the nearfield distribution and the farfield pattern is apparent from eqn. (2.80) [114], [116]. Thus, many farfield characteristics can be intuitively estimated from the shape of the antenna aperture and its corresponding EM field distribution. For example, the farfield distribution of a square antenna aperture with uniformly intense EM fields is a *sinc* function of θ and ϕ , with the main lobe being normal to the aperture in the direction of the wave propagation. The angular main lobe width decreases as the size of the uniformly illuminated aperture increases but the side lobes also increase. Signal processing techniques, especially the relations between various window functions and their corresponding frequency responses, can be used to shape the antenna farfield by varying the EM field distribution at the aperture. We note here that an extremely narrow antenna main lobe (pencil-beam) is indeed possible with huge apertures respective to the radiating wavelength, e.g. in parabolic reflector antennas, nevertheless generating a uniform illumination over an aperture larger than $\sim \lambda/10$ is cumbersome. Tapered aperture illumination, phase differences of the field intensities between the centre and the outskirts of the aperture etc., limit the main-lobe width as the aperture size increases [117].

2.3.1. Antenna characteristics

A few important farfield characteristic parameters of an antenna are as follows [112]:

- *Radiation efficiency* η_{rad} is the ratio of radiated power by the antenna P_{rad} to the power accepted by the antenna.
- *Directivity* $D(\theta, \phi)$ is defined as the potential of an antenna to concentrate power in a particular angular direction (θ, ϕ) . It reads as the ratio of the radiation intensity in any particular angular direction to the average radiation intensity given by $P_{rad}/4\pi$, i.e., an isotropic radiator. Unless otherwise specified, the antenna directivity, expressed in decibels, refers to its maximum directivity. Alternatively, the directivity is expressed as [117]

$$D_{max} \approx 4\pi \frac{(180/\pi)^2}{\theta_E \cdot \theta_H}, \quad (2.81)$$

where θ_E and θ_H are the angular 3-dB bandwidth of the main lobe in *degrees*. Hence, the narrower the main-lobe width, the larger the antenna directivity.

- *Antenna gain* is the product of its directivity and radiation efficiency, i.e., $G(\theta, \phi) = \eta_{rad}D(\theta, \phi)$. For loss-less antennas where $\eta_{rad} = 1$, antenna gain and directivity are identical.
- *Effective aperture* $A_{eff}(\theta, \phi)$ of an antenna is its equivalent absorption area, when used a receiver. The effective antenna aperture is related to the antenna gain as $A_{eff} = G(\theta, \phi) \times \lambda^2/4\pi$.
- *Aperture efficiency* η_a is the ratio of the effective aperture to the physical aperture A_{phy} of the antenna. It is usually a product of multiple factors such as spillover efficiency, effective illumination of the aperture, phase errors, polarisation efficiency etc. [117]. Analytically, the maximum antenna gain and directivity can be related to its physical aperture as

$$G = \frac{4\pi}{\lambda^2} A_{eff} = \frac{4\pi}{\lambda^2} \eta_a A_{phy} \quad (2.82)$$

$$D = \frac{4\pi}{\lambda^2} \frac{\eta_a}{\eta_{rad}} A_{phy}. \quad (2.83)$$

Detailed derivations of these antenna parameters can be found elsewhere [112], [117]. Equations (2.82) and (2.83) show that antenna gain is proportional to physical aperture. However, A_{phy} cannot be indefinitely increased to increase the antenna gain as large phase errors significantly reduce the aperture efficiency. Lowering the operating wavelength of the antenna also has the same effect. However, η_a remains unaltered if the ratio A_{phy}/λ^2 is kept unchanged [111]. In other words, the characteristic antenna parameters are unchanged if the antenna dimensions are altered proportionally to the operating wavelength (inversely to the operating frequency). This idea forms the basis for designing frequency-independent antennas.

2.3.2. Frequency-independent antennas

Unlike the narrow-band resonant antennas, which are only operable over a small bandwidth around their resonance frequency, frequency-independent antennas are well suited for broadband operation. One way to design frequency-independent antennas is to determine the antenna shape by the angles [111], rather than by absolute lengths. This ensures an unchanged shape of the antenna with respect

to the scaling of its dimensions. Thus, the antenna retains its radiation characteristics over a large bandwidth. This is called the *angle principle*. Mathematically, the angle principle reads

$$Kr(\varphi) = r(\varphi + C), \quad (2.84)$$

where $r(\varphi)$ is the radius of the antenna and scales as a function of the polar angle φ .

The second principle condition for frequency-independent operation, namely, the *truncation principle*, states that the total current in the antenna must approach zero with increasing distance from the antenna-feed and that the pattern of the finite antenna structure reaches a limiting form with increasing frequency [111]. Thus, a frequency-independent antenna is a truncated version of an infinitely large antenna designed following the angle principle. A significant consequence of the truncation principle is that, if designed appropriately, the field pattern of a frequency-independent antenna is zero in all directions that the infinite-structure would occupy.

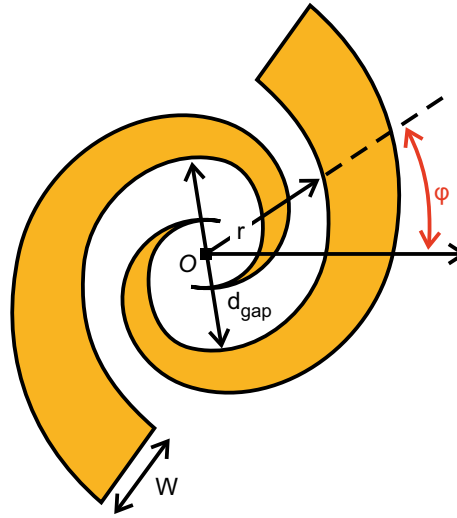


Figure 2.8.: Representation of a frequency-independent log-spiral antenna. The width of the antenna blades W also increases with the distance from the centre r . The distance between the antenna electrodes changes as $d_{gap} = 2 \times r$.

Figure 2.8 shows an example of a frequency-independent log-spiral antenna. Here, the distance of structure from centre O increases as $r(\varphi) = r_0 \exp(a\varphi)$, where r_0 is a constant and $a = 1/K \cdot dK/dC$ (see eqn. (2.84)), i.e., independent of φ [111]. The antenna thus satisfies the angle principle. As frequencies increase, r decreases eventually converging to the origin O , hence, satisfying the truncation principle and consequently, the farfield of the log-spiral antennas along the antenna plane is null. We extensively use frequency-independent antennas in this thesis. The ErAs:In(Al)GaAs photoconductors are coupled to log-periodic antennas for free space operation and VAs are employed in the integrated PVNA architecture [70], both of which show frequency-independence within their designed operational frequency range. Detailed free-space operation of the log-periodic antenna-coupled photoconductors can be found in [45]. We discuss the design and analysis of VAs in detail, along with waveguide coupling mechanisms, in chapter 5.

3. Free-Space Photonic Vector Network Analysers

A free-space PVNA utilises a THz beam, usually guided by optical components (lenses, mirrors, etc.), to measure the complex S-parameters of any DUT placed in its free-space THz path. The first broadband two-port free-space VNA functioning in the THz range, demonstrated by Faridi *et al.* [34], was based on a pulsed THz system and it features an operational bandwidth of > 3 THz. The first CW variant was demonstrated by Fernandez *et al.* [35] functioning between 0.1 – 1 THz. Despite its large frequency coverage, the pulsed PVNA featured a comparatively low frequency resolution of 7 – 8 GHz. In contrast, the frequency resolution of the CW PVNA is in the order of a few megahertz, which is usually limited by the tuning capabilities and the stability of the employed DFB lasers. This enables the CW variant to precisely characterise narrowband features, which otherwise could not be resolved in the pulsed PVNA. Additionally, CW PVNAs are better suited for the characterisation of non-linear DUTs like transistors, mixers, etc. as only a single frequency component is used at a time for measurement [35]. In this chapter, we describe a free-space CW PVNA and its applications in details. Firstly, we briefly discuss its architecture, define S-parameters for such a system and its calibration mechanism. We then discuss some data processing techniques to reduce noise in the measured data, which have the potential to further increase the operational bandwidth of the PVNA, or alternatively, any homodyne CW system. Finally, we demonstrate multiple applications of PVNA in material characterisation using Fabry-Pérot oscillations generated in the single and multilayered DUTs. We subsequently develop two algorithms for RI and thickness estimation from the Fabry-Pérot features. We further image nanometric structures using complex S-parameters.

3.1. Architecture and calibration

Figure 3.1 shows the schematic of a free-space PVNA, which is essentially an extension of the free-space THz setup shown in Fig. 1.2. Two PIN-diode-based transmitters ($Tx1$, $Tx2$) are used as sources at the two ports of the VNA and two ErAs:In(Al)GaAs-based antenna-coupled receivers ($Rx1$, $Rx2$) [25]

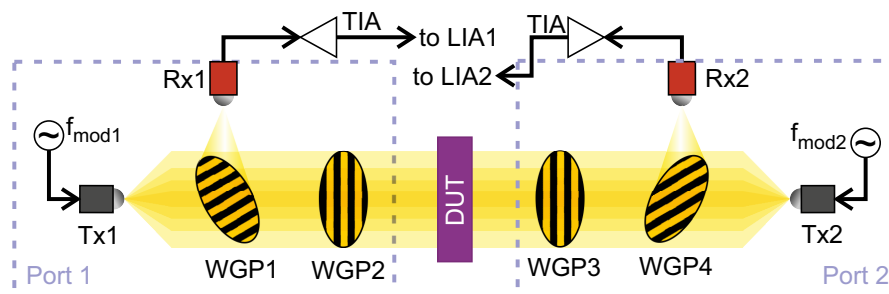


Figure 3.1.: Schematic of a free-space 2-port PVNA. The receivers $Rx1$ and $Rx2$ simultaneously receive the signals from both the transmitter, however are later demodulated at different modulation frequencies.

are used for measuring transmitted and reflected fields through and from the DUT, originating from the individual sources. The THz beam is collimated using lenses and parabolic mirrors which are not explicitly shown here. The DUT is placed in the collimated part of the beam and thus, the estimated S-parameters are a spatial average over the whole sample area. Two sets of two polarisers are set up such that they behave as broadband beam-splitters and steer a part of the THz beam towards the receivers. Each receiver output is amplified via a TIA before being sent to a LIA for lock-in detection. All the active devices at the PVNA ports are driven simultaneously using the same set of DFB lasers. An Erbium-doped fibre amplifier (EDFA) is also employed to increase the optical power before it is split 4 : 1 to power the aforementioned active devices.

As discussed in section 2.2, the detected current at the photoconductive receivers is proportional to the incident THz field. Thus, the S-parameters of a free-space VNA can be written in terms of transmission and reflection measurements of the DUT as

$$S_{11} = \frac{I_1}{\hat{I}_{1,Rx}} \Big|_{Tx2=off} \quad (3.1)$$

$$S_{21} = \frac{I_2}{\hat{I}_{1,Tx}} \Big|_{Tx2=off} \quad (3.2)$$

$$S_{12} = \frac{I_1}{\hat{I}_{2,Tx}} \Big|_{Tx1=off} \quad (3.3)$$

$$S_{22} = \frac{I_2}{\hat{I}_{2,Rx}} \Big|_{Tx1=off}, \quad (3.4)$$

where I_i is the frequency-dependent THz current at receiver $Rx(i)$ and $\hat{I}_{i,Tx}$ and $\hat{I}_{i,Rx}$ are the reference currents in transmission and reflection, respectively, measured in $Rx(i)$ during system calibration. i denotes the port number of the VNA. A standard TTN-calibration routine [118], which is well-suited for free-space systems, is employed. This calibration technique determines the reference phase change of the VNA with very high precision, whereas the reference amplitude is considered trivial. For transmission measurements, a DUT-less straight signal path between the transmitter and the receiver is established, and the detected THz field is considered as reference. For reflection measurements, a gold mirror is placed at the position of the DUT to mimic an electrical short at the calibration plane and the resulting reflection in the setup is measured. It is extremely critical to place the gold mirror very precisely at the position of the DUT. Notably, the measured phase of the S-parameters are relative to the measured phase difference during the PVNA calibration, rather than its absolute value. This difference between the relative and absolute phase is, ideally, a constant value over the measurement frequencies. A detailed description of the calibration kit for this free-space PVNA can be found elsewhere [35].

Unlike traditional electronic VNAs, the free-space PVNA can perform simultaneous measurements of the two ports by using different modulation IFs at the transmitters. Each receiver receives signals from both transmitters, however, separated in the frequency domain by the difference in the modulation frequencies and in the time-domain, by the corresponding distances from each transmitter. In LIAs, the received signals are demodulated at the individual modulation frequencies to segregate the signals received from $Tx1$ and $Tx2$. The cross-talk between the two modulation frequencies is minimized using appropriate frequency spacing and bandpass filtering [34], [35]. However, the non-trivial reflections between the polarisers and other optical components of the VNA architecture cannot be completely calibrated out and behave as coloured noise in the measured data. In general, the coloured noise components can be removed from the transmission measurements (S_{12} , S_{21}), as all the noise components arrive at the receiver with a greater delay than the main signal. However, in reflection measurements, the noise components can temporally overlap the non-trivial reflected signal from the

DUT and thus, the measured S_{11} and S_{22} parameters usually feature a lower signal-to-noise ratio (SNR). In the next section, we introduce data post-processing techniques using digital filters to significantly suppress the said setup-related white and coloured noise components, thereby improving the overall DNR and operational bandwidth of the free-space PVNA.

3.2. Data post-processing

Typically, DNR of all CW systems suffer from roll-offs obeying a power law of frequency (e.g. f^4) [96], [119]. Consequently, the detected signal at the receiver becomes indistinguishable from the noise floor at higher terahertz frequencies. The detection mechanism and the post-detection electronics contribute to this noise, thus, limiting the maximum operational frequency of any THz system. To reduce the noise, LIAs are typically employed which averages the measured signal over an integration time period, τ . This results in proportional increment of the measurement time in homodyne systems and a quadratic increment in case where direct detectors are employed. For instance, meaningful data can be extracted from a scan over 1 THz in the commercial homodyne CW system [24], with a 50 MHz frequency step, using 3 ms integration time within a minute for frequencies below 2 THz. To conduct scans above 2 THz, τ must be ≥ 300 ms and a scan of similar frequency coverage will take nearly 2 hours. The frequency of the DFB lasers drifts significantly on such long time-scales. Alternatively, this noise can be reduced during post-processing with digital filters. The data quality of the post-processed data is similar to that of unfiltered measurements taken 100 times longer τ . Applications of digital post-processing in CW terahertz spectroscopy, conducted around water vapour absorption resonances between 1.6 – 2.4 THz and the free-space PVNA are demonstrated in this section.

The receiver current I_{Rx} is typically of the order of a few nano-amperes down to a few pico-amperes. The noisy demodulated detector current I_{det} can be written from eqn. (2.62) as

$$I_{det}(f) = I_{Rx}(f) \cos \left[\frac{2\pi f \Delta d_{opt}}{c_0} \right] + I_N(f, f_{IF}), \quad (3.5)$$

where c_0 is the vacuum speed of light, Δd_{opt} is the optical path length difference between the laser and the incident THz signal at the receiver and $I_N(f, f_{IF})$ is the noise current constituting IF noise sources and clutters originating in the THz path. The former can be approximated as white noise generated primarily from the electrical device resistances of the receiver, the TIA and the LIA. This Johnson-Nyquist noise power reads

$$N = \sigma_N^2 \cdot ENBW = k_B \cdot T \cdot ENBW, \quad (3.6)$$

where σ_N^2 is the noise power density, T is the absolute temperature, k_B the Boltzmann constant and $ENBW$ is the equivalent noise bandwidth (ENBW). The ENBW of a lock-in amplifier is b/τ , wherein τ is the aforementioned integration time and b depends on the transition band roll-off of the equivalent low pass operation of the lock-in and usually in the order of 1/2. Thus, the noise power scales inversely with τ . An increment of the lock-in integration time by an order of magnitude consequently improves the DNR by 10 dB (c.f. Fig. 3.3(a)). However, this also results in an order of magnitude increase of the total measurement time. For integrated terahertz applications which require high system DNR but fast measurements, like PVNA [35], [62], noise reduction by increasing τ is unrealistic. Moreover, the clutters in the setup, stemming from the reflections and stray radiations, are coloured and remain unaffected by the lock-in integration time. Both these noise sources can be reduced by digital filters in post processing, with miniscule increment of data-processing time.

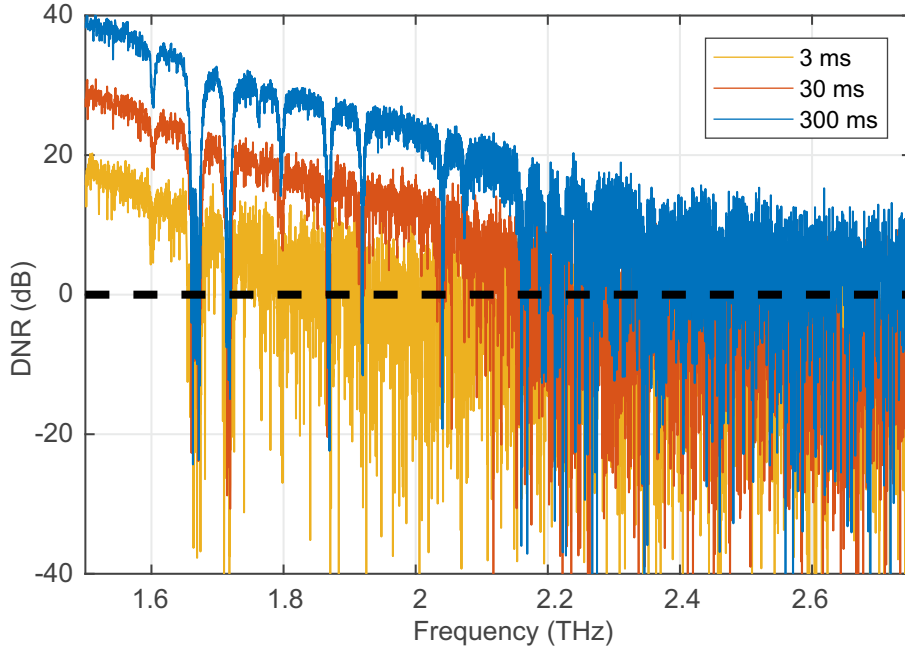


Figure 3.2.: Measured DNR of a commercial CW system with integration times 3, 30 and 300 ms between 1.5 – 2.7 THz. A 10-fold increment in integration time increases the system DNR by 10 dB. The CW system can be operated up to 1.8 and up to 2.4 THz with $\tau = 3$ ms and 300 ms, respectively. Adapted from [68].

3.2.1. Implementation of digital filtering

The `filtfilt` function in Matlab™ [120] implements an anti-causal zero-phase filtering technique, i.e., the phase is not distorted in the filtering process [121]. Hence, implementation of both finite impulse response (FIR) and infinite impulse response (IIR) filters preserves the phase information of the signal. The filter is implemented using `design` and `fdesign` functions of Matlab™. The centre frequency is dynamically calculated from the measured signal and a bandwidth is chosen to maximise noise reduction with minimal loss of information content of the signal, along with a 60 dB stop-band attenuation and 0.01 dB of pass band ripple. For any such filter with a 3-dB bandwidth Δf normalised to the sampling frequency f_s as $\Delta f_{norm} = \Delta f / f_s$, the residual white noise power after filtering is $N_{filt} \approx N \times \Delta f_{norm}$. This results in an estimated DNR improvement due to filtering, in dB, of

$$\Delta DNR \approx 10 \log_{10} \left(\frac{N}{N_{filt}} \right) = -10 \log_{10}(\Delta f_{norm}). \quad (3.7)$$

Frequency scans having band-limited spectroscopic features, for e.g., absorption lines, undergo spectral broadening and smoothing due to filtering, as a part of their infinite temporal response is cut short. Numerical investigations reveal that the band-limited features are only minimally broadened if the 3-dB bandwidth of the spectral features is thrice as large as the 3-dB width of the envelope of the filter impulse response. For simplicity, assuming the pass-band of the filter to be a *rect* function, a lower limit of Δf_{norm} to avoid spectral broadening can be calculated to

$$\Delta f_{norm} \geq 2.67 \frac{f_{reso}}{\Delta f_{spec}}, \quad (3.8)$$

where f_{reso} is the resolution of the frequency scan, which is usually in the range of a few MHz to a few 10 MHz and Δf_{spec} is the 3-dB line-width of the spectral resonance. For example, the 3-dB line-width of waterline in ambient conditions at 1.671 THz is ≈ 5.90 GHz [122]. Thus a maximum DNR improvement without noteworthy broadening of this particular spectral feature can be calculated from eqn. (3.7) and (3.8) to be 16.45 dB for a 50 MHz scan resolution. However, for $f_{reso} = 10$ MHz, the corresponding DNR improvement increases to ≈ 23 dB. For finitely-long temporal signals (e.g., inverse Fourier transform (IFT) of a frequency-domain measurement with no band-limited features such as absorption lines), no spectral broadening occurs if the equivalent time-window is larger than the maximum pulse delay in the time-domain signal. Furthermore, the filter function is purely analytical. Theoretically, this spectral broadening can be compensated by deconvolution of the filtered data by the filter impulse response.

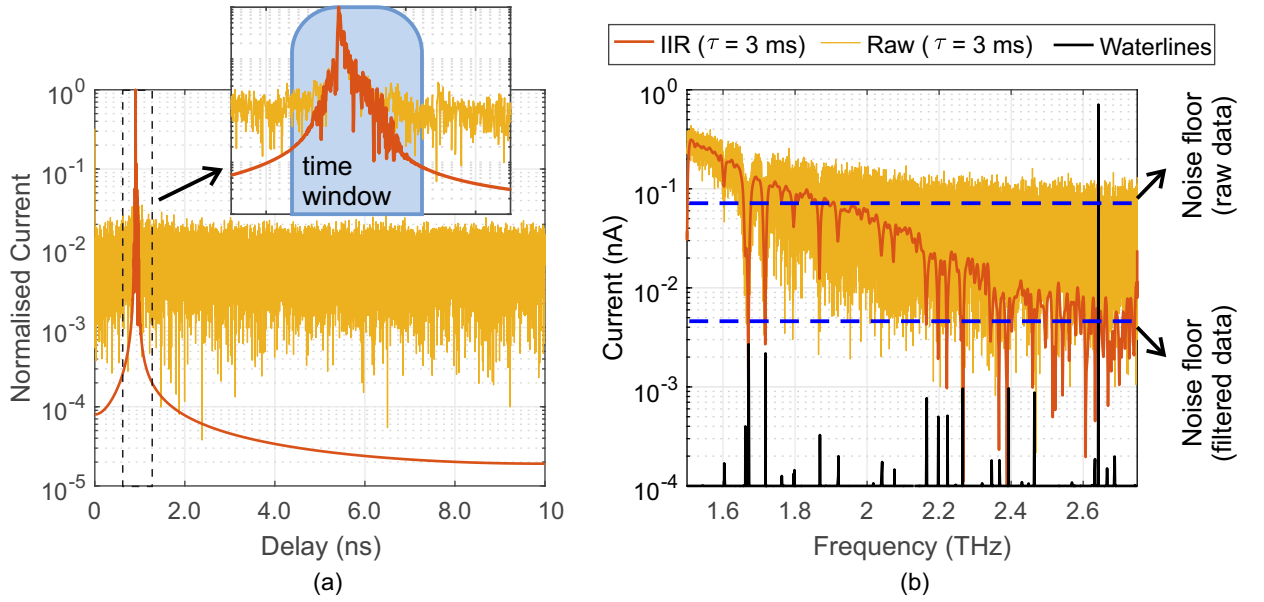


Figure 3.3.: (a) The windowing operation on the measured time-domain removes temporally delayed noise and clutter from the raw data shown in yellow. The designed time-window depicted in the inset is centred at a delay of 0.9 ns and spans over 0.1 ns. (b) Increased operational bandwidth of the measured data with $\tau = 3$ ms by filtering to ~ 2.5 THz, comparable to the scan with $\tau = 300$ ms shown in Fig. 3.2. Adapted from [68].

In Fig. 3.3, we filter the data-set measured with $\tau = 3$ ms of Fig. 3.2 using an IIR filter of order 10 with $\Delta f_{norm} = 0.01$. The envelope of the detected signal, expressed by eqn. (3.5), carries the spectral information, which is modulated by the phase difference in homodyne setup. The detected signal in the time-domain translates to a pulse occurring at a delay $\Delta d_{opt}/c_0$, shown in 3.3(a). Reflections in the setup, that give rise to the clutter, occur at different path lengths and can be simply filtered out by windowing in the time-domain, corresponding to band-pass filtering of the frequency scan. Figure 3.3(b) shows the corresponding filtered signal (red), where the spectral features of the atmospheric moisture become prominent till ≈ 2.5 THz, which are otherwise undecipherable above ≈ 1.9 THz in the unfiltered data (yellow). Waterlines from the HITRAN database [122] are also added for reference. The noise floor data-set reduces by an order of magnitude due to filtering and consequently, its DNR improves by 20 dB.

The additional post-processing times including filter implementation and filtering of a data set of

$\approx 41,600$ samples is in the order of tenths of a second with Matlab™ running on a 64-bit windows 10 PC with 8 gigabytes of RAM and a 4-Core Intel® Core™ i7-7700 CPU. Implementing the filtering algorithms in “C” or “Python” should be faster. Field programmable gate arrays (FPGAs) can further improve performance, however, with reduced adaptability.

3.2.2. Application in Spectroscopy

Spectroscopic fingerprints at ambient conditions are band-limited and typically have resonance peaks with Δf_{spec} on the order of a few GHz. We investigate waterlines as a representative spectroscopic data-set to compare resonances in the raw data-set measured with $\tau = 300$ ms (*UF300*) to a filtered data-set measured with $\tau = 3$ ms (*FILT3*). An 10th order IIR filter is employed as before with $\Delta f_{norm} \approx 0.01$. Figures 3.4(a)-(d) show four different waterlines at 1.671, 1.797, 2.042 and 2.345 THz, respectively. *FILT3* nicely replicate the resonance features of *UF300* till at least ~ 2 THz. Even above that, in Fig 3.4(d), the filtering technique allows to visualize resonances which are indiscernible in *UF300*. An ideal envelope spectrum estimated using the HITRAN database [122] for a temperature of 291 K and a $\approx 30\%$ relative humidity at 1 atm pressure is added to the plots for reference. The Lorentzian shape and peak-position of *FILT3* match excellently with the absorption spectrum calculated from HITRAN database.

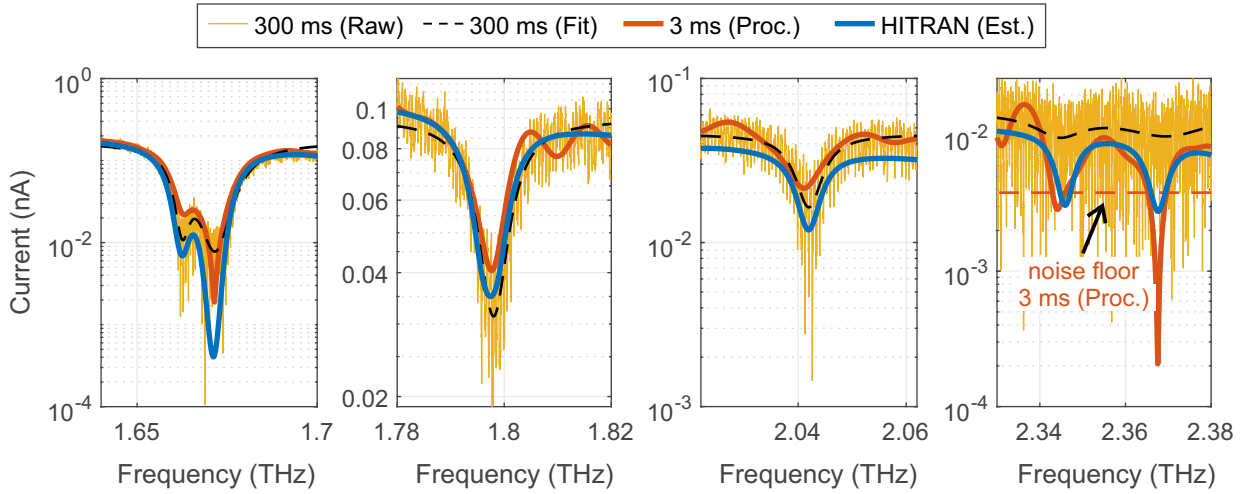


Figure 3.4.: (a)-(d) shows a comparison between raw data measured with $\tau = 300$ ms and filtered data acquired with $\tau = 3$ ms for four water absorption lines at frequencies 1.671, 1.869, 2.169 and 2.366 THz respectively. The dashed black curve shows a fit for the raw data obtained with $\tau = 300$ ms. Water absorption lines from the HITRAN database are added in blue. The humidity level of 30% is estimated from the average height of the peaks. Adapted from [68].

Table 3.1 tabulates the quality factors (Q-factors) for unfiltered and filtered data measured with $\tau = 3, 30$ and 300 ms. The noisy raw data is fit to a Lorentzian function to accurately estimate their Q-factors [123]. The resulting Q-factors of the filtered data-set with $\tau = 3$ ms is comparable or higher than the unfiltered data-set measured with $\tau = 300$ ms. Filter data show Q-factors close to those calculated from the HITRAN database, particularly, in cases, where the raw data peaks are not distinctly resolvable because of their vicinity to the noise floor. The systematic lag between set and actual frequency in the CW system has been calibrated out.

Table 3.1.: Comparison of measured Q-factors of resonances caused by water vapour between 1.6 – 2.4 THz for both raw (unfiltered) and filtered (IIR) data-sets measured with $\tau = 3, 30, \text{ and } 300$ ms. Q-factors estimated from the HITRAN data [122] are also added for reference. Adapted from [68].

Integration time (ms)	Data type	Frequency (THz)				
		1.671	1.797	2.042	2.345	2.367
3	raw	119.47	263.44	–	–	–
30	raw	163.38	302.86	428.48	–	–
300	raw	143.68	263.64	336.07	169.09	93.64
3	IIR	228.17	266.41	232.44	428.60	718.96
30	IIR	223.30	260.21	323.41	428.40	424.34
300	IIR	240.39	275.83	322.64	457.31	401.12
–	HITRAN	263.87	287.83	407.26	491.66	430.23

We calculate the absorption coefficients for water vapour $\alpha_{H_2O}(f)$ from the HITRAN dataset for aforementioned experimental conditions. Using the Lambert-Beer law and assuming a Lorentzian line-shape of the absorption lines, the expected detector current $I_{HT}(f)$ reads

$$I_{HT}(f) = I_0(f) \cdot \exp[-\alpha_{H_2O}(f)d] \quad (3.9)$$

where $d = 28$ cm is the total free-space path of the THz beam in the setup and $I_0(f)$ is the frequency-dependent envelope estimated from the roll-off of the filtered detector current measured with $\tau = 300$ ms. Figure 3.5 shows a comparison between expected detector current featuring waterlines calculated and a filtered dataset measured with $\tau = 300$ ms. The filtered data-set matches excellently

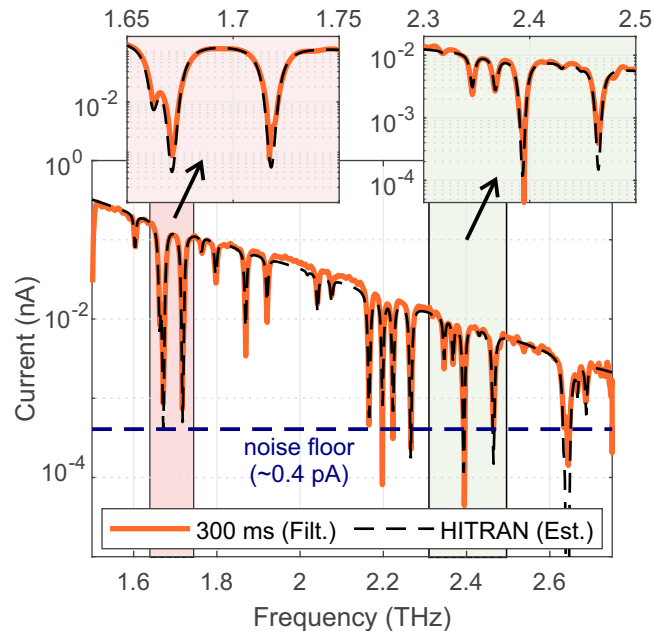


Figure 3.5.: Comparison between the filtered data set measured with $\tau = 300$ ms and waterlines analytically calculated from the HITRAN database. Insets show frequency bands 1.65 – 1.75 THz and 2.3 – 2.5 THz in greater details. Adapted from [68].

with the THz spectrum calculated from the HITRAN database after correcting the frequency-offset. The waterlines become visible up to the maximum measurable frequency of the *Terascan* system [24] of 2.75 THz. The noise floor of the filtered data is at ≈ 0.4 pA, which is approximately an order of magnitude lower than the thermal noise floor of the photoconductor. An additional advantage of the spectroscopic measurements is that the resonances are usually characterised from the amplitude data, whereas, the phase information is usually ignored. Thus, even non-zero-phase filtering using IIR filters can produce accurate results.

3.2.3. Application in PVNA

As a PVNA measures complex S-parameters, it requires strict preservation of the phase information. Here, IIR filters implemented without the zero-phase filtering technique will produce erroneous results. In contrast, FIR filters have a linear-phase response and are better for preserving phase information. We use a 220 μm thick Qz wafer as an exemplary DUT in the free-space PVNA. Plots in Fig. 3.6(a) show the measured $|S_{21}|$ and $|S_{11}|$ parameters of the quartz wafer. The filtered coefficients match the theoretical value nicely and thus, increase the fitting accuracy of the employed estimation algorithm. Figure 3.6(b) shows the time-domain pulse of the unfiltered reflected current at the PVNA port. Two distinct peaks in stray reflections *R1* originate from the two polarisers in the setup (c.f. Fig. 3.1) and appear prior to the reflected signal from DUT. *R2* are the remnants of multiple reflections occurring between the DUT and the polarisers, which appear after the reflected signal from the DUT. These stray reflections are usually correlated to the signal components and constitute the coloured noise component in the measured data. Filtering removes these unwanted, systematic sources of clutter, which cannot be suppressed by increasing the integration time. Thus the band-pass filter (BPF) is crucial for measuring S-parameters in PVNAs.

3.2.4. Advantages and limitations of post-processing

Equation (3.7) states that narrower Δf_{norm} increases the system DNR. However, the appropriate filter bandwidth depends on the type of application, frequency resolution and scanning bandwidth. In contrast to small Δf_{norm} utilised in spectroscopic measurements, too narrow bandwidth can attenuate the multiple Fabry-Pérot reflections occurring in planar dielectric DUTs (e.g. quartz plate, distributed Bragg reflectors). Since phase information is essential, FIR filters are well suited for PVNA applications, whereas IIR filters can be used in spectroscopy for their lower order in general. Additionally, broader pass bands increase the filter order of IIR filters significantly. We note that the phase-zero filtering technique is important to remove phase distortion and delays induced by the filtering processing. For hardware implementation, however, the standard filtering architectures (direct form I and II) are simpler and in such cases, IIR filters should only be utilised where phase information is unnecessary.

Noise reduction by averaging over N samples is equivalent to a low-pass FIR filter, where all of its filter coefficients are the same. Thus, the resulting impulse response is a *sinc* function, which features with high pass-band ripple and a high main side-lobe (4% of the main peak, i.e., ≈ 26.5 dB suppression). A low-pass filter (LPF) with different filter coefficients of the same order can be implemented to have a much lower pass-band ripple and a side-band suppression up to 60 dB. Hence, an appropriately designed LPFs performs much better than the commonly employed averaging filters [124]. BPFs attenuate the out-of-band noise even further. Down-sampling after using an anti-aliasing filter also significantly reduces measured noise power, however spectral resolution is also reduced by the downsampling factor. Alternatively, wavelet-based filtering techniques notably improve the system DNR but spectral features are attenuated at higher THz frequencies, where the DNR of the measured data is already too low.

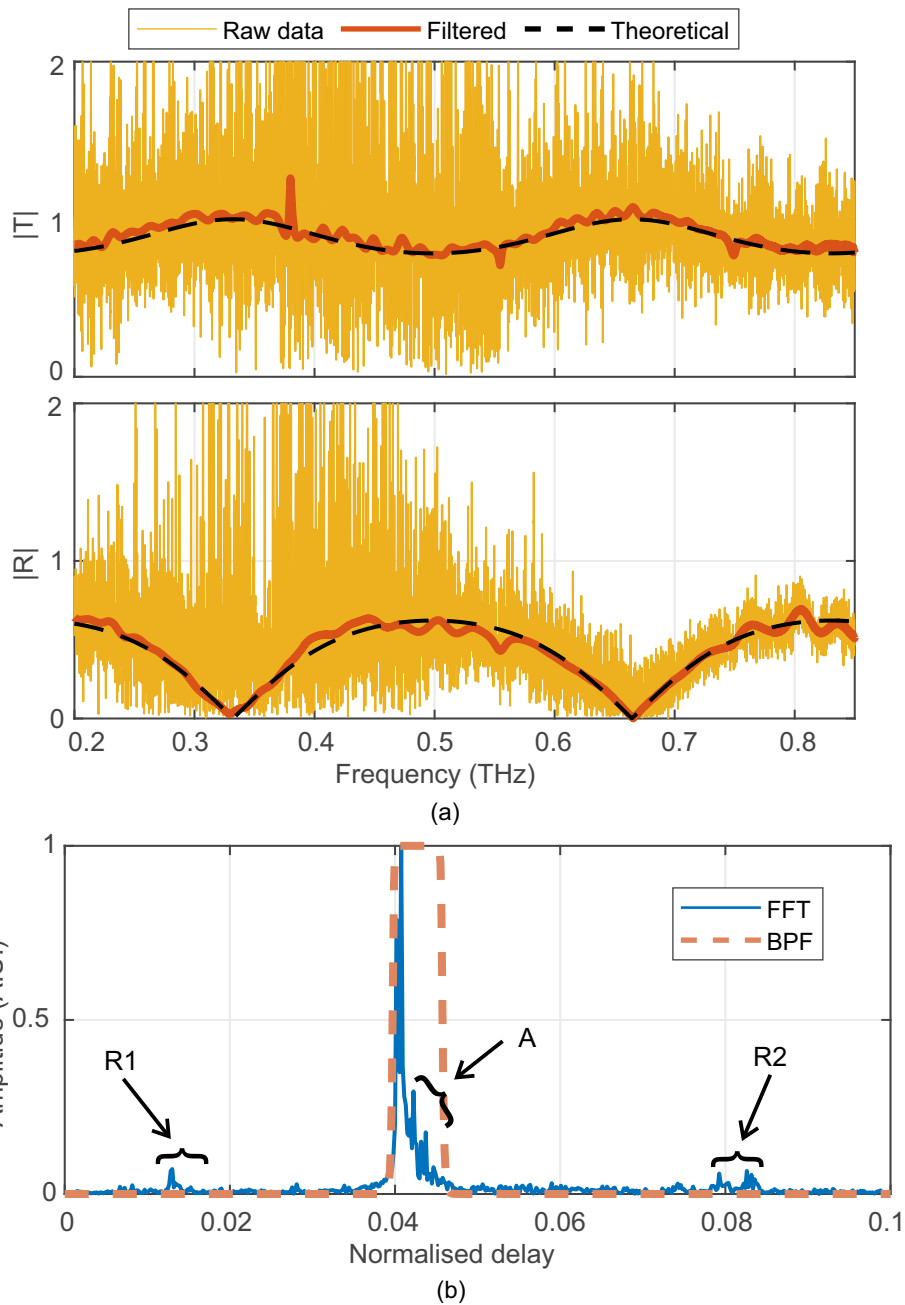


Figure 3.6.: (a) Comparison between the measured raw data, its filtered form and theoretically expected values of transmission and reflection coefficients of a $220 \pm 5 \mu\text{m}$ thick crystalline quartz plate. The filtered spectra excellently match the theoretical prediction. (b) The raw detector current is filtered using the equivalent window function generated by the IIR filter. Unwanted correlated reflections from the components in the measurement setup come both before and after the main signal. Adapted from [68].

In summary, digital BPFs in post-processing significantly improves the system performance for homodyne CW THz systems by reducing the measurement time and increasing the operational bandwidth [69] of the THz system. Noise can be further suppressed, even adaptively, with Wiener filters [125].

Auto-regressive-moving-average (ARMA) modelling, prediction filtering can further improve the system performance, however at the cost of implementation complexity. These post-processing techniques, in combination with faster hardware [27], can enable high speed THz systems suitable for industrial needs. We have submitted a patent application to the German Patent Office (DPMA) pertaining to the Bandwidth extension of homodyne CW system using digital signal processing [69]. Throughout this thesis, we extensively utilise digital post-processing techniques to improve operational bandwidth of the PVNAs by reducing the measured noise and by rejecting stray reflections from the setup.

3.3. Applications of free-space PVNA

Free-space VNAs find their application in material characterisation, imaging and non-destructive testing of mostly planar DUTs [34], [35]. The PVNAs can also be employed for device characterisation in an antenna-coupled measurement scheme, where the power is delivered to the DUT via transmission lines [126], [127]. In the following section, we demonstrate a few applications of the CW PVNA primarily involving single-layered and multi-layered planar DUTs, placed transversely in the free-space THz path. The DUTs are geometrically symmetric and hence, the S-parameter symmetry holds, i.e., $S_{12} = S_{21}$ and $S_{11} = S_{22}$.

3.3.1. Characterisation of single-layered samples

Material characterisation involves the accurate estimation of thickness and complex RI of any DUT. Traditionally, broadband time-domain systems are used to perform time-of-flight measurements to estimate these material parameters, where the measurement precision usually improves with increasing bandwidth. Contrastingly, Fabry-Pérot oscillations inside a planar, homogeneous, dielectric cavity provide a more precise way to find these characteristic sample parameters. The planar DUT is placed in the collimated part of the free-space THz beam as shown in Fig. 3.1. Both the transmitted and reflected THz waves through and from the DUT contain Fabry-Pérot oscillatory features. The complex transmission (T_{FP}) and reflection (R_{FP}) coefficients obtained from the Fabry-Pérot oscillations are expressed as [128]

$$\begin{aligned} T_{FP} &= \frac{(1 - R) \cdot \exp(-jk_0 \underline{n} d_{phy})}{1 - R \cdot \exp(-2jk_0 \underline{n} d_{phy})} \\ &= \frac{1 - R}{\sqrt{1 + R^2 - 2R \cos(2k_0 \underline{n} d_{phy})}} \exp \left[j \tan^{-1} \left(-\frac{1 + R}{1 - R} \tan(k_0 \underline{n} d_{phy}) \right) \right] \end{aligned} \quad (3.10)$$

$$\begin{aligned} R_{FP} &= -\sqrt{R} + \frac{\sqrt{R}(1 - R) \cdot \exp(2jk_0 \underline{n} d_{phy})}{1 - R \cdot \exp(2jk_0 \underline{n} d_{phy})} \\ &= \frac{2\sqrt{R} \sin(k_0 \underline{n} d_{phy})}{\sqrt{1 + R^2 - 2R \cos(2k_0 \underline{n} d_{phy})}} \exp \left[j \tan^{-1} \left(\frac{1 - R}{1 + R} \frac{1}{\tan(k_0 \underline{n} d_{phy})} \right) \right], \end{aligned} \quad (3.11)$$

where $k_0 = 2\pi f / c_0$ is the wavenumber of the travelling THz wave in free-space, wherein f is the THz frequency, c_0 is the speed of light in vacuum, $\underline{n} = n + j\kappa$ is the complex RI of the DUT, where n is the real part of the RI and κ is the extinction coefficient and d_{phy} is its average physical thickness. R is the power reflection coefficient calculated as the ratio $|(n - 1)/(n + 1)|^2$. Thus, the material characteristics of the DUT can be extracted from its S-parameters, where S_{11} and S_{21} corresponds to R_{FP} and $T_{FP} \cdot e^{-jk_0 d_{phy}}$, respectively (c.f. eqn. (2.75)). For low-loss dielectrics, i.e., $n \gg \kappa$, the finesse of the Fabry-Pérot oscillations depends only on the real part of the RI of the sample, whereas

the periodicity of oscillations depend on its optical thickness ($d_{phy} \times n$). In principle, both n and d_{phy} can be estimated from any one of the measured complex S-parameter, however, both S_{11} and S_{21} parameters are used to improve the estimation accuracy by reducing the effect of the coloured noise occurring in the setup.

Estimation using S-parameter amplitudes

In free-space VNAs, the accuracy of the measured S-parameter phases highly depends on the quality of calibration employed prior to the measurement. In comparison, the magnitudes of the S-parameters are less affected by the calibration errors. Hence, we use only the magnitudes of S_{11} and S_{21} to develop the first material characterisation algorithm.

Dividing the magnitude of S_{11} (R_{FP}) by S_{21} (T_{FP}) from equations (3.11) and (3.10), we get

$$\left| \frac{S_{11}}{S_{21}} \right| = \left| \frac{R_{FP}}{T_{FP}} \right| = \frac{2\sqrt{R}}{1-R} \cdot \sin(k_0 n d_{phy}). \quad (3.12)$$

We then fit eqn. (3.12) to a function $F_{fit}(f) = A \sin(mf + \phi)$ in order to estimate the reflection coefficient

$$\hat{R} = \frac{\sqrt{A^2 + 1} - 1}{\sqrt{A^2 + 1} + 1} \quad (3.13)$$

Similarly, the optical thickness of the sample \hat{d}_{opt} is estimated as

$$\hat{d}_{opt} = \hat{n} \times \hat{d}_{phy} = \frac{mc_0}{2\pi}. \quad (3.14)$$

The estimate of RI is first calculated from the value of \hat{R} in eqn. (3.13) as $\hat{n} = (1 + \sqrt{\hat{R}})/(1 - \sqrt{\hat{R}})$ and inserted into eqn. (3.14) to calculate the value of \hat{d}_{phy} from the estimated optical thickness.

Noise in measured S-parameter-amplitudes mainly stems from the thermal white noise of the receiver and coloured noise generated from the stray reflections in the setup, while contributions of the post-detection electronics are usually negligible. The division in eqn. (3.12) results in the addition of the noise power in the reference and the DUT measurements. This eventually results in increased fitting errors. The following error minimisation steps are iteratively employed to reduce the overall effect of additive noise on the fitting:

1. First, we filter the ratio $|S_{11}/S_{21}|$ using a BPF to remove temporally out-of-band noise component (c.f. section 3.2). Since S_{21} is less prone to noise than S_{11} , a frequency-dependent offset is subtracted from $|S_{11}|$ such that $|S_{11}|^2 + |S_{21}|^2 = 1$.
2. The filtered and adjusted $|S_{11}/S_{21}|$ is then fit to eqn. (3.12) using a non-linear least square algorithm to obtain initial estimates of RI \hat{n} , and geometrical thickness \hat{d}_{phy} . Norm-2 distance between the estimated and measured S-parameters quantifies the error. We note here that a very narrow pass-band of the employed BPF in the previous step will result in an increased fitting error, as a small variance in fitting data can lead to statistical underfitting [129].
3. Then, we iteratively minimise the error using the following steps until the error minima is found or we complete a pre-defined maximum number of iterations.

- a) The optical thickness of the DUT (d_{opt}) is recalculated using autocorrelation function of $|S_{11}/S_{21}|$, and new estimates for RI and geometrical thickness are calculated as:

$$n_{new} = d_{opt}/\hat{d}_{phy},$$

$$d_{new} = d_{opt}/\hat{n}.$$

We use autocorrelation here to reduce the remaining in-band additive zero-mean white noise components after filtering. The new estimates replace the current estimates, i.e., $\hat{n} = n_{new}$ and $\hat{d}_{phy} = d_{new}$ only if they feature a lower error than the current value.

- b) Subsequently, we probe errors in four equidistant neighbouring points from (\hat{n}, \hat{d}_{phy}) on n - d plane and update current thickness and RI estimates to avoid getting stuck in a local error minima, until current set of estimates has the lowest error among its neighbours. The distance between these neighbouring points is 10 times the desired measurement accuracy.
- c) Finally, a 1-D steepest gradient descent algorithm finds the minimum error for \hat{n} and \hat{d}_{phy} , individually and the current estimates are updated.

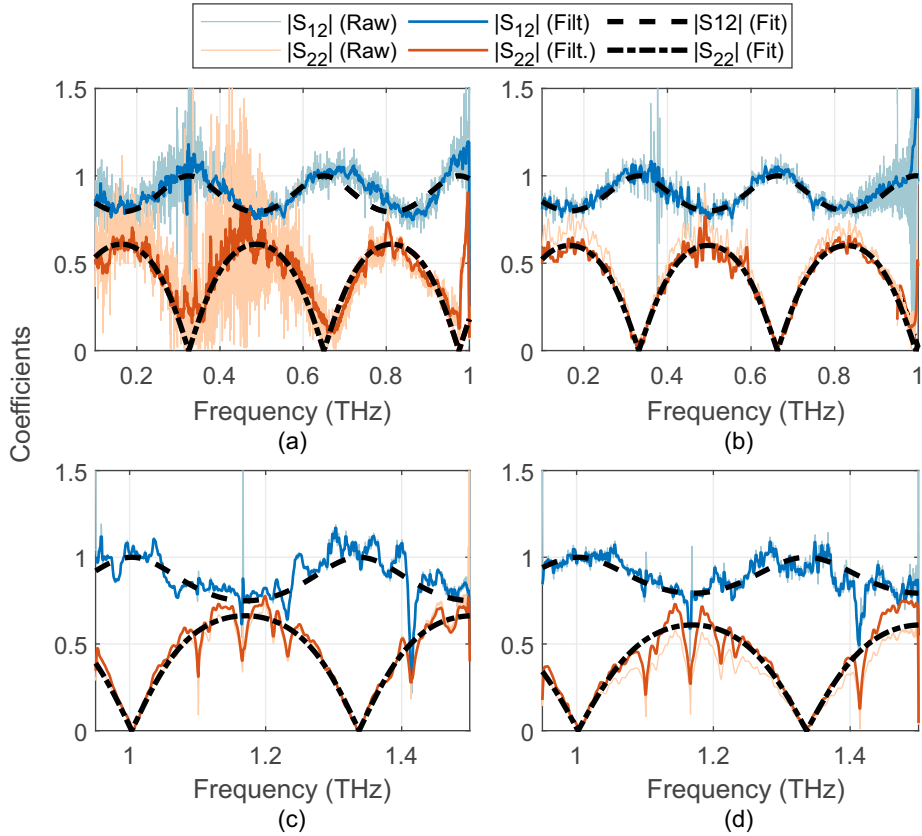


Figure 3.7.: Plots (a) and (b) show the measured, filtered and fitted S-parameters for ports 1 and 2 respectively between 0.1 – 1 THz. Plots in (c) and (d) are measured between 0.9 – 1.5 THz, where the fitting algorithm is inaccurate due to the presence of many waterlines.

The plots in Fig. 3.7 show the measured complex S-parameters of a nominally $220 \pm 5 \mu\text{m}$ thick crystalline quartz plate ($n_{qz} \approx 2.093$ [130]) for different frequency ranges at both the VNA ports. The estimated thickness and RI values for the corresponding plots are tabulated in Table 3.2. The

Table 3.2.: RI and thickness estimates of a $220 \pm 5 \mu\text{m}$ thick *z-cut* Qz wafer ($n_{qz} = 2.093$ [130]) from measured S-parameters shown in plots of Fig. 3.7. The port number signifies the active transmitter during measurements.

Fig.	Port	Frequency (THz)	\hat{n}	Thickness (μm)		Relative errors		
				\hat{d}_{phy}	\hat{d}_{opt}	\hat{n}	\hat{d}_{phy}	\hat{d}_{opt}
(a)	1	0.10 – 1.0	1.928	232.57	448.40	0.077	0.057	0.025
(b)	2	0.10 – 1.0	2.005	225.51	452.15	0.041	0.025	0.017
(c)	1	0.95 – 1.5	2.220	201.97	448.37	0.062	0.082	0.025
(d)	2	0.95 – 1.5	2.031	220.96	448.77	0.028	0.004	0.024

relative estimation errors for RIs, optical and physical thicknesses are also mentioned therein. The estimation errors are high for Fig. 3.7(a), where the measured S_{11} parameter is significantly noisy and has standing waves despite of data-filtering. Additionally, the measurements conducted between frequencies 0.9 – 1.5 THz have higher estimation errors due the presence of many water absorption lines. These can be suppressed by conducting the measurements in a nitrogen-flooded chamber and thus, the operational bandwidth of the PVNA can be extended further. Between 0.1 – 1 THz, we estimate the DUT thickness as 232.57 and 225.51 μm at ports 1 and 2, respectively, compared to the 220 μm nominal thickness. The precision of thickness measurements is 13.1 μm . The estimated RIs at the respective ports are 1.928 and 2.005 at ports 1 and 2, respectively, compared to the literature value of 2.09. The precision of the estimated RI is 0.12. We note that the error in measured optical thickness is always $< 3\%$ for all the measurements. This hints to the fact that the error in the estimation of the reflection coefficient, and subsequently, RI, makes the estimation of physical thickness significantly erroneous as they are not mutually independent. Direct estimations of RI and d_{phy} can decouple the errors, however, the fitting algorithm becomes inaccurate as their product dictates the fundamental feature of the Fabry-Pérot oscillations.

Characterisation using S-parameter phases

The phase of the measured S-parameters also oscillates with a periodicity proportional to Δd_{opt} and can be similarly fitted to the analytical Fabry-Pérot phase to extract the material characteristics of the DUT. The phase of the measured reflection S-parameters has discontinuities (c.f. eqn. (3.11)), which makes it significantly difficult to fit. The phase of the transmission S-parameters is continuous and is utilised for determination of RI and thickness of the dielectric sample. The phase can be reformulated from (3.10) as [66]

$$\begin{aligned} \angle S_{21} = \angle T_{FP} - k_0 d_{phy} &= \tan^{-1} \left[\frac{R \sin(2k_0 \underline{n} d_{phy})}{1 - R \cos(2k_0 \underline{n} d_{phy})} \right] + k_0 \underline{n} d_{phy} \\ &= \tan^{-1} \left[\frac{R \sin(2\pi f \underline{n} d_{phy} / c_0)}{1 - R \cos(2\pi f \underline{n} d_{phy} / c_0)} \right] + \frac{2\pi \underline{n} d_{phy}}{c_0} f. \end{aligned} \quad (3.15)$$

For low loss dielectrics, where $\underline{n} \rightarrow n$, the slope of the linear component is proportional to the optical thickness of the DUT, and the free spectral range (FSR) of the sinusoidal component, $c_0/2nd_{phy}$, is also inversely proportional to the optical thickness. The finesse of the phase oscillation increases with increasing RI. In this case, we take optical thickness ($\hat{d}_{opt} = n \times d_{phy}$) and reflection coefficient (\hat{R}) as

parameters to determine the fitting function $P_{fit}(f)$, which reads as

$$P_{fit}(f) = \tan^{-1} \left[\frac{\hat{R} \sin(2\pi\hat{d}_{opt}/c_0 \cdot f)}{1 - \hat{R} \cos(2\pi\hat{d}_{opt}/c_0 \cdot f)} \right] + \frac{2\pi\hat{d}_{opt}}{c_0} f + a_0, \quad (3.16)$$

where, a_0 is a constant required to counteract the phase-offset in the measured S_{21} , as it contains the relative, rather than absolute, phase information. Here too, the material RI n is first calculated from \hat{R} as $(1 - \sqrt{\hat{R}})/(1 + \sqrt{\hat{R}})$ and then is divided from estimated optical thickness to get an estimate of the physical thickness of the DUT.

The phase-noise in the measured S-parameters stems from the random frequency drifts of the DFB lasers used to drive the active devices in the PVNA. The drift-induced noise can be reduced by increasing the coherence between the THz signal reaching the receiver and the THz beat-node generated by the lasers. An added additional optical path of the laser-signal to the receiver becomes necessary to compensate for the total optical path-length of the THz signal between the transmitter and the receiver.

The optical thickness estimation error from the phase of the transmission S-parameters, in general, reads as [66]

$$\hat{d}_{err} = \Delta d_{opt} \frac{\partial f_L}{f_{scan}}, \quad (3.17)$$

where, Δd_{opt} is the optical path length difference between the laser signal and the received THz signal at the receiver, ∂f_L is the frequency drift of the DFB lasers and f_{scan} is frequency scan range of the PVNA measurements. Plots in Fig. 3.8 show the variation of standard deviations in the estimated optical thicknesses, physical thicknesses and RIs of a $520 \pm 5 \mu\text{m}$ thick HRFZ-Si wafer as a function of Δd_{opt} . As expected, the standard deviation of phase-based estimates increases with Δd_{opt} as the signals at the receiver become more incoherent. Additionally, the standard deviation of the estimates from the S-parameter amplitudes also shows reduction in estimation errors with increased coherence. This indicates that the measured noise is not purely thermal for S-parameter amplitudes. The optical thickness precision, i.e., its standard deviation, reduces to 70 nm with a $\Delta d_{opt} = 2.4 \text{ cm}$ for a scan range of 0.6 – 0.8 THz, which is as small as $\lambda/6000$ at the centre frequency. The reduction in the measured standard deviation saturates for very small Δd_{opt} as fitness inaccuracies become non-trivial.

Figure 3.8(a) shows that the measured deviation in optical thickness calculated from the S-parameter-phases is significantly lower than when estimated from their amplitudes. However, plots in Fig. 3.8(c) show that the estimated RI is comparable for both the cases. Hence, the physical thickness is more precisely estimated from the phase information. Furthermore, the frequency drift of the DFB lasers is calculated from the data points in Fig. 3.8(a) and eqn. (3.17) to be $209 \pm 50 \text{ kHz}$, which is in good agreement with the technical specifications of the lasers.

The estimation precision of the RI and d_{phy} in phase-based estimation are in the order of 0.14% and 0.07% respectively, whereas for amplitude-based estimation they are around 6%. Thus, phase-based material characterisation is significantly more precise than the amplitude-based method. Besides, both the implemented algorithms lack extraction of complex RI as a function of frequency. Such features are already available for a pulsed PVNA [34] and can be easily implemented for the CW case too. An obvious drawback of material characterisation using Fabry-Pérot features is that the fitting accuracy depends on the f_{scan} with respect to the optical thickness of the DUT, i.e, precisely on the ratio $r = 2d_{opt}f_{scan}/c_0$. Fitting accuracy significantly decreases if the ratio becomes $r < 2$. Simply put, very thin samples must feature a high RI or vice versa. In such cases, zero-padded time-of-flight-based estimates can be more precise. An example imaging application using this technique is demonstrated later in this chapter.

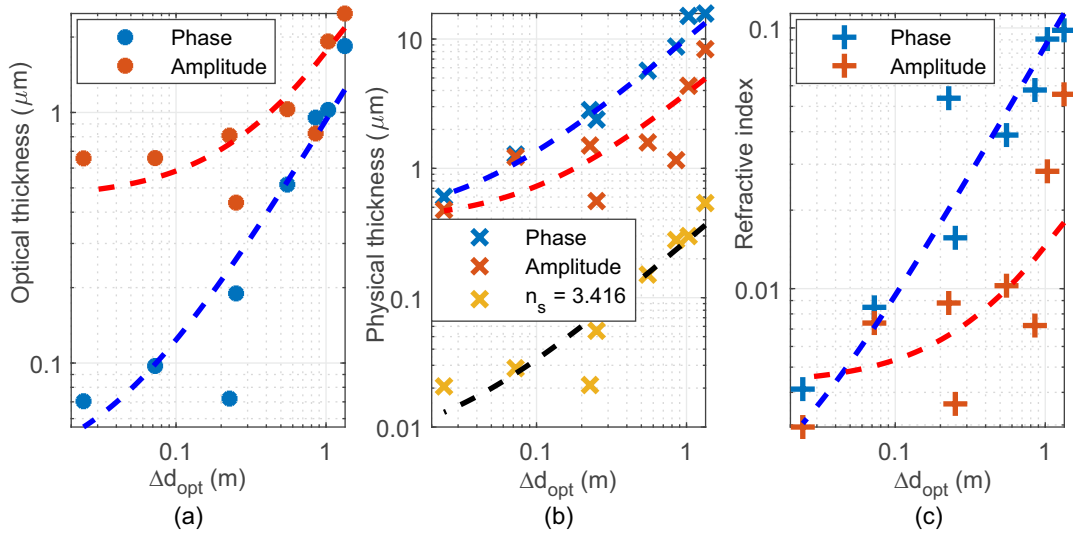


Figure 3.8.: Plots in (a), (b) and (c) show the measured standard deviation as a function of the total optical path-length difference at the receiver for optical thickness, physical thickness and refractive index, respectively. The standard deviation is measured over 25 measurements of the same pixel on the DUT. The dashed lines act as a guide for the eye. Standard deviations decrease with decreasing Δd_{opt} for all the estimates from the Fabry-Pérot magnitude and phases. Adapted from [66].

3.3.2. Modelling of multilayered structures

We demonstrate that the estimation of the material characteristics of single-layered dielectric DUTs from the Fabry-Pérot oscillations is very precise. However, for multilayered structures, the corresponding analytical Fabry-Pérot equations become increasingly complex with the number of layers and consequently, extremely tedious to evaluate, even with the aid of the well known optical transfer matrix method [131]. Alternatively, an estimate of the S-parameters of multilayered DUTs can be numerically obtained using T-parameters [132] calculated from the S-parameters of individual layers. In this section, the modelling methodology of multilayered structures is briefly discussed.

The S-parameter matrix of a single layered DUT, S_{l1} , can be written as

$$S_{l1} = \begin{bmatrix} R_{FP} & T_{FP} \cdot e^{-jk_0 d_{phy}} \\ T_{FP} \cdot e^{-jk_0 d_{phy}} & R_{FP} \end{bmatrix}, \quad (3.18)$$

where T_{FP} and R_{FP} are the complex field transmission and reflection coefficients calculated from (3.10) and (3.11) from the estimated RI and thickness of the individual layer. Figure 3.9 shows a multilayered DUT, which can be alternatively considered as a cascaded structure of multiple single layered structures. Subsequently, the overall S-parameters of the multilayered DUT can be calculated by multiplying T-parameters of individual layers obtained from their scattering matrices and finally, reevaluating the overall S-parameters back from the T-parameter-product. The scattering matrix relates the reflected power wave at each port to the transmitted power waves into each port (c.f. eqn. (1.4)). However, in cascaded models shown in Fig. 3.9, the output power waves of an individual layer acts as the input power waves of the consecutive layer, thus expressing the power waves in terms of input and output is beneficial in this scenario. The transfer matrix (T-matrix) relates the power waves as

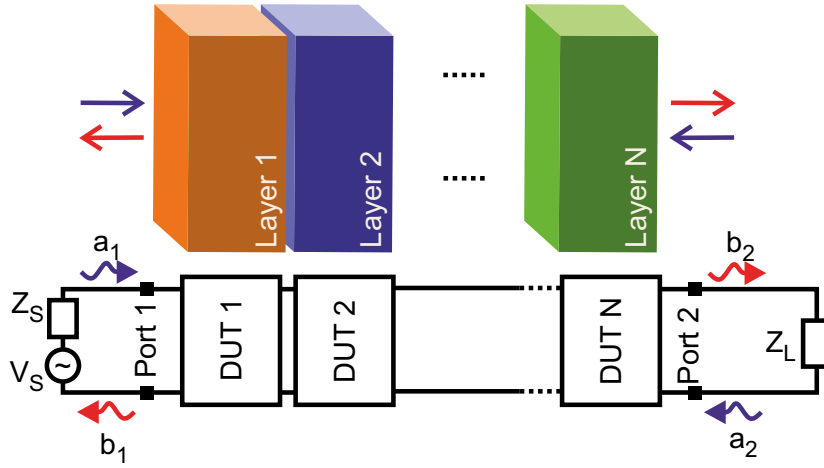


Figure 3.9.: Schematic of a multilayered DUT. The multilayered structure can be considered as a cascade of multiple single layer structures.

$$\begin{bmatrix} b_1 \\ a_1 \end{bmatrix} = \begin{bmatrix} T_{11} & T_{12} \\ T_{21} & T_{22} \end{bmatrix} \times \begin{bmatrix} a_2 \\ b_2 \end{bmatrix}, \quad (3.19)$$

where the subscripts of the power waves a and b represent the two ports when each layer is individually characterised using the VNA. Individual parameters of T-matrix can be defined in conjunction with the S-parameters as

$$T_{11} = \frac{-\det([S])}{S_{21}} \quad T_{12} = \frac{S_{11}}{S_{21}} \quad T_{21} = \frac{1}{-S_{22}} \quad T_{22} = \frac{1}{S_{21}}, \quad (3.20)$$

where $\det(\cdot)$ calculates the determinant of a matrix. For multilayered DUT, the T-matrices of individual layers ($[T_i]$) are multiplied to find the total T-matrix for the multilayered structure, $[T_{total}]$

$$[T_{total}] = \prod_{i=1}^N [T_i]. \quad (3.21)$$

The S-parameters of DUT are finally calculated back from $[T_{total}]$ using the following relations:

$$S_{11} = \frac{T_{12}}{T_{22}} \quad S_{12} = \frac{\det([T_{total}])}{T_{22}} \quad S_{21} = \frac{1}{T_{22}} \quad S_{22} = \frac{-T_{21}}{T_{22}}. \quad (3.22)$$

This analytical modelling technique fails for multilayered structures with perfectly reflecting layers, i.e., with perfect electric conductors, as S_{21} for the said layer is null and all the parameters of the T-matrix become undefined. To circumvent this issue, a very small value for S_{21} can be assumed to get an approximate analytical model. We also note that it is not necessary to assume individual layers to be symmetric, i.e., $S_{11} = S_{22}$ and $S_{12} = S_{21}$, to generate this multilayered model. If the full set of S-parameters for any individual layer is available, the corresponding T-matrix can be calculated using equations in (3.20) and cascaded with other layers using equation (3.21).

3.3.3. Vectorial optimisation of multilayered models

Multilayer modelling, in conjunction with a multidimensional parameter optimisation, can be used for the estimation of individual layer characteristics from the measured S-parameters of multilayered planar structures. This is done by finding the best fit between the measured data and an assumed multilayered model. A vectorial implementation similar to Nelder-Mead simplex algorithm (NMA) for minima finding [133] is developed in the course of this thesis to optimise characteristic parameters of individual layers in a multilayered DUT. A simplistic explanation using two optimisation parameters, x and y is visualised in Fig. 3.10(a). In a three-dimensional space, x and y axes indicate the parameters to be optimised and the vertical z -axis indicates the error between measured and estimated S-parameters. For a specific set of S-parameters, a single error minima is assumed at (x_{min}, y_{min}) . A triangular ABC plane is created by any three points on this imaginary error plane, where point C is calculated to have the minimum error. The area vector is then calculated at C as the cross-product between \vec{AC} and \vec{BC} , which is normal to the plane of the triangle. The orientation of the area vector represents the tilt of ABC on the error plane and its projection on the $x - y$ plane indicates the direction of lower error. A new point is calculated from C by adding a predetermined displacement factor to the unit vector in the direction of projection, which replaces the previous point of maximum error to create a new triangular plane. This process is iteratively followed using adaptive displacement vectors to reach the minimum of the error plane. The movement of the triangular plane is analogous to a ball rolling in the gravitational plane, represented here by the error plane.

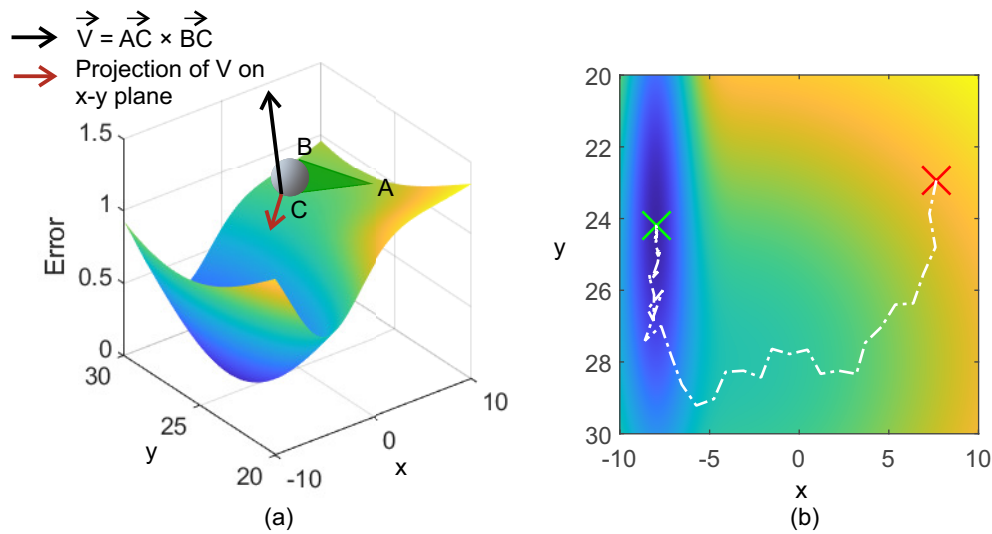


Figure 3.10.: (a) The minima-seeker point is modelled as a ball placed on a gravitational plane represented by the error plane. The minima-seeker point always moves towards the projection of vector \vec{V} on $x - y$ plane. (b) The traced movement of the simulated seeker-point over a simulated error plane. The red cross represents the starting point and the green cross marks where the seeker point reaches at the end of the minimisation process, which is the error minimum.

Fig. 3.10(b) shows an optimisation trace of a minima seeker point which adaptively moves from a random location of the red cross to the position of minimum error indicated by the green cross. The movement of the seeker point is completely heuristic, i.e., the point has no a-priori information about the entire error plane. The direction of movement is determined only by the errors of three points of the $\triangle ABC$. This, at times, can result in parameters being optimised to a local minimum. In such cases, the

optimisation must be restarted from another starting point. The two-parameter optimisation is further generalised for N parameters, where the calculation of area vector using cross-product is substituted by wedge product [134], commonly employed in Grassmann algebra [135]. The displacement vectors are adaptively updated following an additive increase and multiplicative decrease algorithm [136], used for congestion control in Transfer control protocol (TCP) networks.

The optimisation algorithm

The vectorial optimisation algorithm optimises a model with N degrees of freedom, henceforth referred to as parameters, by minimising its Norm-2 distance from the measured data. Figure 3.11 shows the flow-diagram for two parameter optimisation process. For the more generalised case, we list the steps for optimising N parameters simultaneously. The algorithm takes three $N \times 1$ arrays as inputs for an N -parameter optimisation, namely upper and lower limits of the N optimisation parameters and their resolution accuracy of estimates, in order.

1. In the initialisation step, the algorithm computes three parameters:
 - a) an initial displacement value D ,
 - b) a running displacement threshold, $D_{th} = D/2$ and
 - c) the minimum threshold displacement D_{min} .
2. We chose $N + 1$ points on the N -dimensional plane created by the input bounds of the optimisation parameters. For example, assuming two optimisation parameters x and y , the three initial point vectors are set to (x_{max}, y_{max}) , $(x_{max}, y_{max} - \Delta y_{lim}/4)$ and $(x_{max} - \Delta x_{lim}/4, y_{max})$, where Δx_{lim} and Δy_{lim} are the optimisation span for parameters x and y respectively. Each point represents a set of parameters describing the analytical model. We set the $N + 1^{\text{th}}$ dimension of each point as the error between the measured data and the analytical model. P_{set} is a matrix of order $(N + 1) \times (N + 1)$ containing the $N + 1$ points.
3. Iterative optimisation continues until either D_{th} becomes less than D_{min} , i.e. expected optimisation accuracy for the parameters is attained or maximum number of iterations is reached.
 - a) We determine \vec{P}_{min} as the point with minimum error in P_{set} .
 - b) N line vectors $(\vec{V}_1, \vec{V}_2, \dots, \vec{V}_N)$ join other N points to the \vec{P}_{min} .
 - c) The wedge product \vec{V}_p of all N vectors at \vec{P}_{min} is calculated as

$$\vec{V}_p = \begin{vmatrix} \hat{e}_1 & \hat{e}_2 & \dots & \hat{e}_{N+1} \\ V_{1,1} & V_{1,2} & \dots & V_{1,N+1} \\ V_{2,1} & V_{2,2} & \dots & V_{2,N+1} \\ \dots & \dots & \dots & \dots \\ V_{N,1} & V_{N,2} & \dots & V_{N,N+1} \end{vmatrix}, \quad (3.23)$$

where \hat{e}_i is the unit vector in i -th dimension, $|M|$ is denotes the determinant of the matrix M , $V_{j,k}$ is the component in k -th dimension for j -th vector. For $N = 2$, eqn. (3.23) is the cross-product of \vec{V}_1 and \vec{V}_2 .

- d) The projection of \vec{V}_p on the N -dimensional plane formed by the optimisation parameters $(\vec{V}_{p,N})$ indicates the direction of lower Norm-2 error. A new point vector \vec{P}_{new} is estimated as $\vec{P}_{min} + D \cdot \hat{V}_{p,N}$, where $\hat{V}_{p,N}$ is the unit vector along $\vec{V}_{p,N}$.

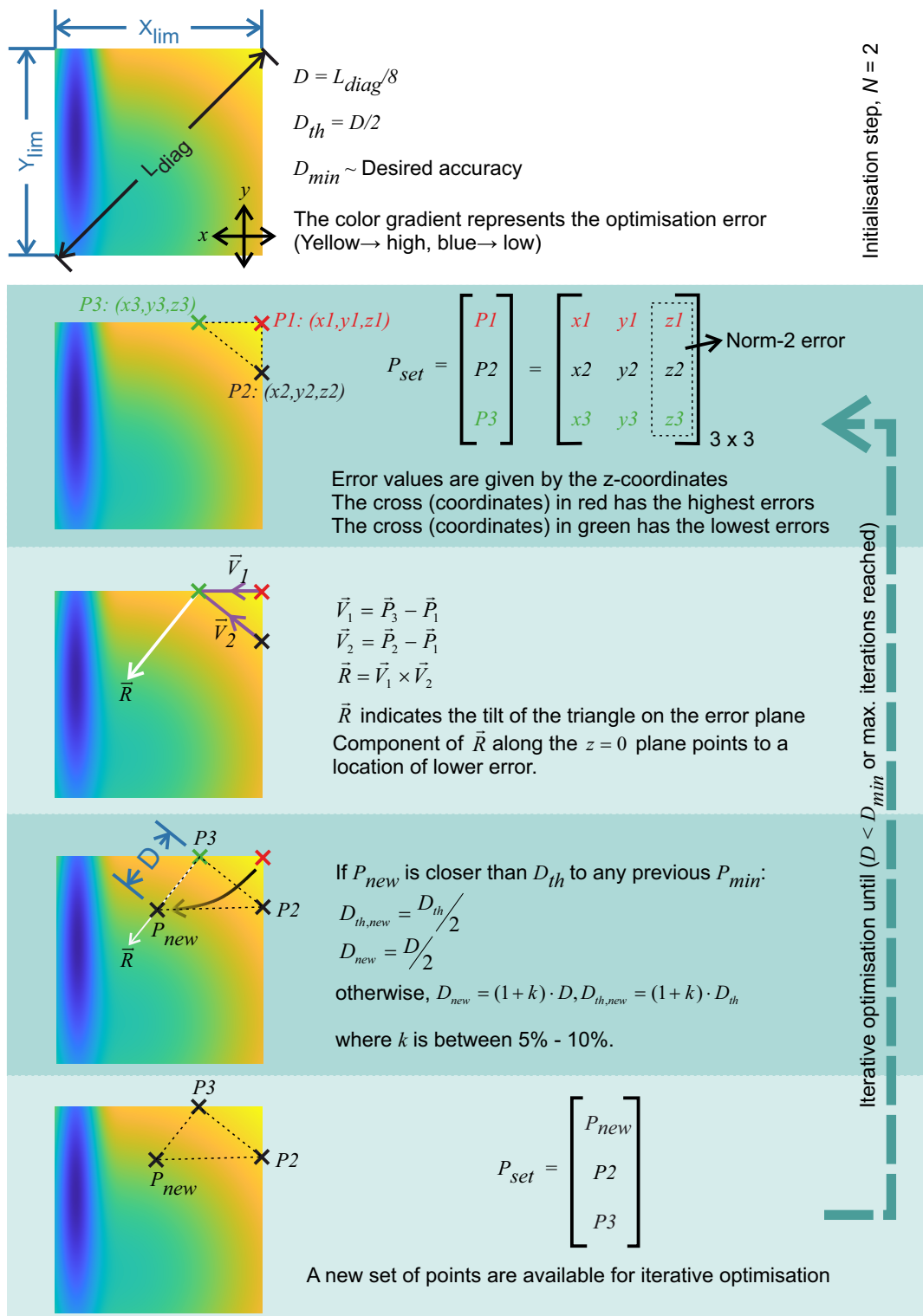


Figure 3.11.: A flowchart of the optimisation algorithm for the 2-D case. The optimisation parameters are x and y . The colour gradient in the background represents the error between the modelled and the measured gradient values, where the deeper the blue, the lower is the error.

- e) If \vec{P}_{new} exceeds the limits along any dimensions, it is reflected inside the limiting bounds along those dimensions. This keeps the optimisation algorithm within its limits.
- f) \vec{P}_{new} then replaces the point vector with maximum error in P_{set} .
- g) D and D_{th} are additively increased in each iteration. However, when $|\vec{P}_{new} - \vec{P}_{min}| < D_{th}$ or the distance of current \vec{P}_{new} from a previously calculated \vec{P}_{new} is less than D_{th} , they are multiplicatively decreased. The multiplicative decrease helps in accurately finding the error minimum, whereas, the additive increase maintains an optimal displacement rate to reach the minimum faster.

4. The final P_{new} is returned as the optimal point with minimum error when the iteration ends.

The optimisation time depends on the complexity of the error calculating function and expected accuracy of the fitting parameters, and hence, number of iterations. Additionally, better optimisation results are obtained when individual parameter limits are either normalised or are scaled to the same order of magnitude, such that optimisation of one parameter does not outweigh the others. Next, we use this vectorial optimisation technique to accurately model individual layers of a planar 5-layered distributed Bragg reflector (DBR).

Characterisation of a DBR

The DBR is constructed using 3 layers of HRFZ-Si, each $525 \pm 5 \mu\text{m}$ thick, separated by air-gaps created by $\approx 120 \mu\text{m}$ thick glass spacers glued using a cyanoacrylate-based adhesive (e.g. SuperGLUE™). The measured magnitude and phase of the transmission and reflection coefficients obtained from S-parameters are plotted in Fig. 3.12. The dotted black lines show the numerically obtained values for the same using multilayer modelling, in conjunction with the vectorial optimisation algorithm. The thicknesses of individual layers are optimised, with an estimation accuracy of 200 nm, assuming the refractive indices of air and HRFZ-Si to be 1 and 3.416, respectively.

Table 3.3.: Estimated individual layer thicknesses of the DBR. The layer thicknesses are in microns.

Data set	Si	Air	Si	Air	Si	Residual Error
Only $ S_{11} $	528.10	131.88	526.65	140.72	523.52	16.89
Only $ S_{21} $	527.04	124.37	528.20	129.60	526.29	10.20
$ S_{11} + S_{21} $	527.93	136.18	526.66	146.57	522.68	8.50 + 16.60

The estimated thicknesses of individual layer are tabulated in Table 3.3. Three cases are considered, where in the first two, the thicknesses are estimated just from the $|S_{11}|$ and $|S_{21}|$ parameters respectively, and the third one estimates from both the S-parameters simultaneously. The estimated thicknesses of HRFZ-Si are well within the error range of their physical measurements. The air-gaps are larger than $120 \mu\text{m}$, as a $5 - 10 \mu\text{m}$ thick layer of cyanoacrylate glue is expected at each facet of glass spacers. Also unsurprisingly, the residual error of the third estimation is much lower than that of the former two, as both the S-parameters offer more information than any of them individually.

A caveat of estimating symmetric multilayered structures using the vectorial optimisation technique is that the order of the layers can be reversed depending on the starting point of the optimisation. This occurs simply because $|S_{21}| = |S_{12}|$ and $|S_{11}| = |S_{22}|$, i.e., there is no distinction in S-parameter-magnitudes between N layers stacked in order $1 \rightarrow N$ or $N \rightarrow 1$ in the numerically estimated S-parameters from the model. Consequently, there are always two positions where the Norm-2 error between the simulated and measured S-parameters are minimal and both solutions are valid. If

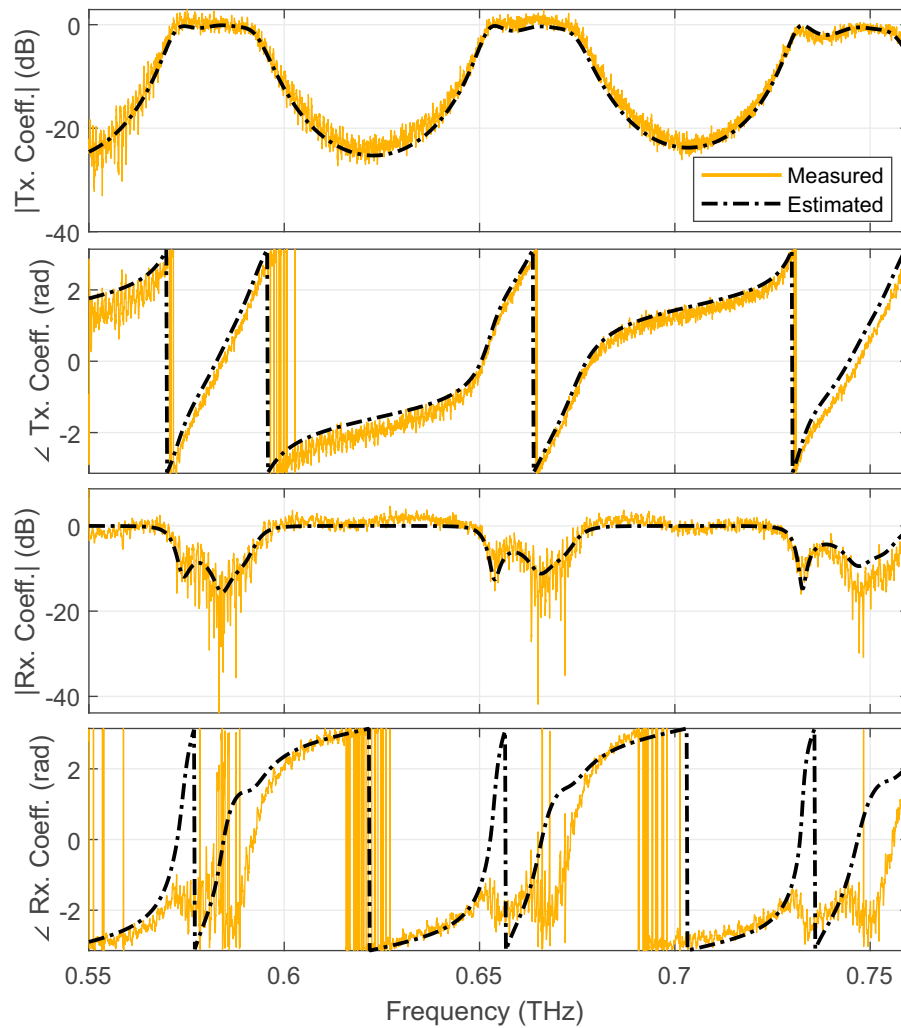


Figure 3.12.: Plots show the measured S-parameters of a DBR between 550–765 GHz. The black dotted line shows the best-fit multilayered model to the measured data obtained using vectorial optimisation. The optimisation limits for individual silicon layers are between 500 – 550 μm and for the air-gaps between 100 – 150 μm . The free-space VNA measures relative phase of the DUT and hence, there is a offset between the estimated and measured phases in the second and fourth graph.

S-parameter-phases are also considered in calculating the Norm-2 error, this ambiguity can be resolved, however, the phase-offset between the modelled and the measured phases must be corrected beforehand, along with potential phase alterations arising due to misalignment of the DUT. Appendix A.2 contains further performance comparisons between the vectorial optimisation and the Matlab™ implementation of Nelder-Mead algorithms and more examples of the thickness estimation of multilayered thin films.

3.3.4. Terahertz imaging

The amplitude and phase information of the S-parameters can be further utilized for surface imaging of nanometric structures using THz waves. Multiple HRFZ-Si samples with varying surface structure heights between 50 nm to 10 μm are demonstrably imaged in this thesis using the free-space PVNA.

The images of the structured DUT surface are reconstructed utilising only the S_{21} parameter in two distinct ways, namely from estimated time-of-flight data and evaluating the Fabry-Pérot phase changes. The frequency range of measurement is set to 0.6 – 0.8 THz to have a considerable system DNR of ~ 30 dB.

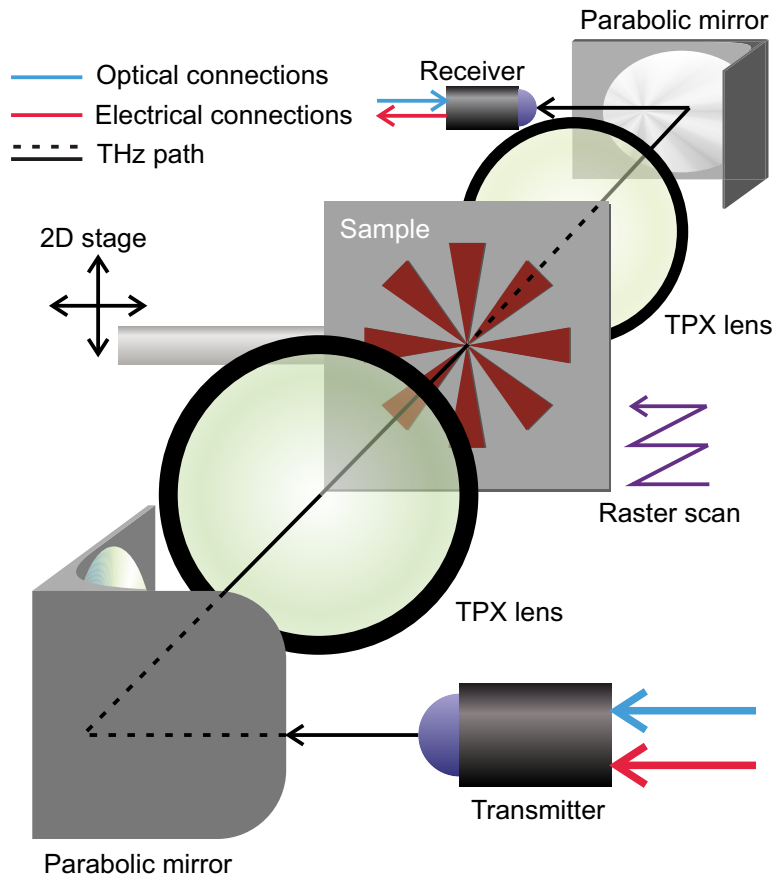


Figure 3.13.: Measurements setup for 2-D imaging in transmission geometry. Adapted from [67] ©2022 IEEE.

Fig. 3.13 shows a schematic of the CW imaging setup, which is a modification of the PVNA schematic depicted in Fig. 3.1. The polarisers are removed here as only S_{21} is the parameter of interest. The DUT is mounted on a two-dimensional motorised stage for conducting single-pixel raster-scan and is placed between two TPX lenses which focuses the THz beam on to the sample. The radius of the THz beam spot on the sample is $\approx 550 \mu\text{m}$ at 0.8 THz. Frequency sweeps are carried out between 0.6 – 0.8 THz for each position of the raster scan, referred henceforth as pixels, with a frequency resolution of 50 MHz. A total area of $25 \times 25 \text{ mm}^2$ is scanned. The pixels are separated from each other by a distance of 0.5 mm, thus resulting in a total of 2,601 pixels.

Imaging from time-of-flight estimates

Using Nyquist criterion, a frequency scan of 200 GHz allows for a temporal resolution of 5 ps, corresponding to an optical thickness resolution of 1.5 mm. To record smaller thickness changes, a frequency scan over a larger bandwidth is necessary, which is constrained by the operational bandwidth of the PVNA and the measurement time. However, if smaller frequency scans are first windowed

and then, zero-padded before calculating the IFT, its measurement bandwidth increases artificially, and consequently, the temporal resolution of equivalent time-domain pulse. Thus, more accurate thickness estimates can be obtained. Figure 3.14 shows an example image of a $10\ \mu\text{m}$ Siemens star ($d_{opt} \approx 34\ \mu\text{m}$) etched on a $520\ \mu\text{m}$ thick HRFZ-Si wafer. Figure 3.14(a) has the usual optical thickness resolution of $1.5\ \text{mm}$ and hence, the Siemens star is not visible. In Fig. 3.14(d), as the frequency scan is elongated by a factor of 50 using zero-padding, the resolution of the corresponding IFT reduces to $30\ \mu\text{m}$ and the relative thickness differences of the HRFZ-Si wafer becomes decipherable and the Siemens star becomes visible.

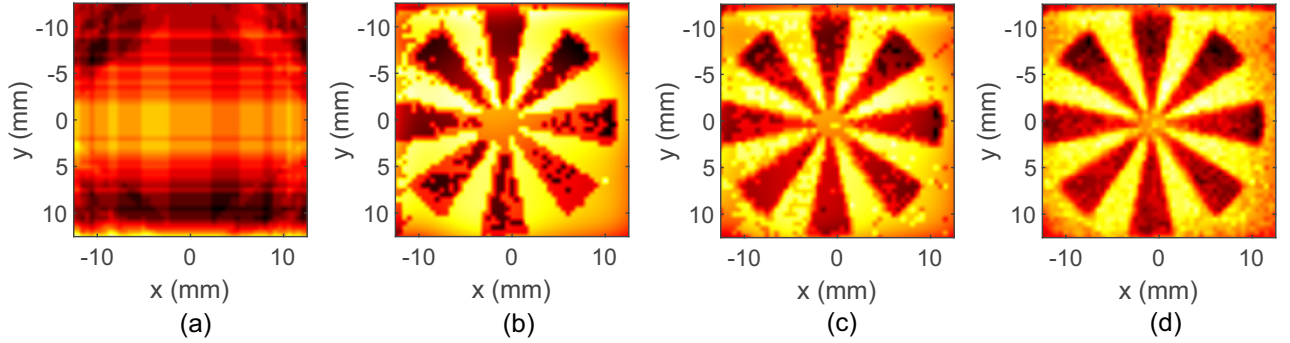


Figure 3.14.: The series of images show measurements of a $10\ \mu\text{m}$ deep Siemens star etched on a $525\ \mu\text{m}$ thick HRFZ-Si wafer. Figures (a - d) show the image enhancement by enhancing the delay resolution by a factor of 1, 10, 20 and 50, respectively, by zero-padding of the scan data. Adapted from [67] ©2022 IEEE.

Surprisingly, the image of the star can also be reproduced using order 10 and 20 zero-padding (c.f. Fig. 3.14(b) and (c)), where the thickness resolutions are $150\ \mu\text{m}$ and $75\ \mu\text{m}$ respectively, i.e., 2 – 5 times higher than the optical thickness of the star. This happens coincidentally as the two peaks of the equivalent pulses arising from $520\ \mu\text{m}$ silicon and its $\approx 486\ \mu\text{m}$ etched area resides in separate Fourier transform bins. In other words, due to the discrete nature of the data, the two peaks approximate to two different thickness values separated by the aforementioned resolutions. This phenomenon indicates that if the zero-padding order is changed incrementally, surface images can be reconstructed for structures much smaller than the thickness resolution defined by the Fourier limit.

To test the limits of this zero-padding enhanced thickness resolution technique, we further image a HRFZ-Si sample with silicon nitride (SiN) of thicknesses of $350\ \text{nm}$ (corresponding to an optical thickness of $714\ \text{nm}$ [66] respectively) deposited atop using chemical vapour deposition. A zero-padding order of 2000 is used to reconstruct the image. Additional image extraction and enhancement steps are necessary to evaluate these nanometric structures for two reasons. Primarily, the thickness of a polished wafer is not uniform throughout and has a surface warping of about $4 - 5\ \mu\text{m}$ [66]. This overshadows the Siemens star, which is thinner by a factor of 10. Secondly, the frequency of the DFB lasers drift (∂f_L) during the lengthy raster scan altering the measured Δd_{opt} over a set of consecutive pixels. The error induced by the surface warping for the host wafer is significantly larger than the one induced by the latter and hence, is corrected from the estimated sample thicknesses before correcting for the errors induced by the laser drifts.

Fig. 3.15 shows the detailed image extraction process for such nanometric structures. The height estimations of the $350\ \text{nm}$ DUT using zero-padding followed by peak-finding of the equivalent time-domain pulse are plotted as functions of the scanning distances in horizontal (x) and vertical (z) axes in Fig. 3.15(a). The star is not visible here. We then calculate the warping plane of the silicon wafer by

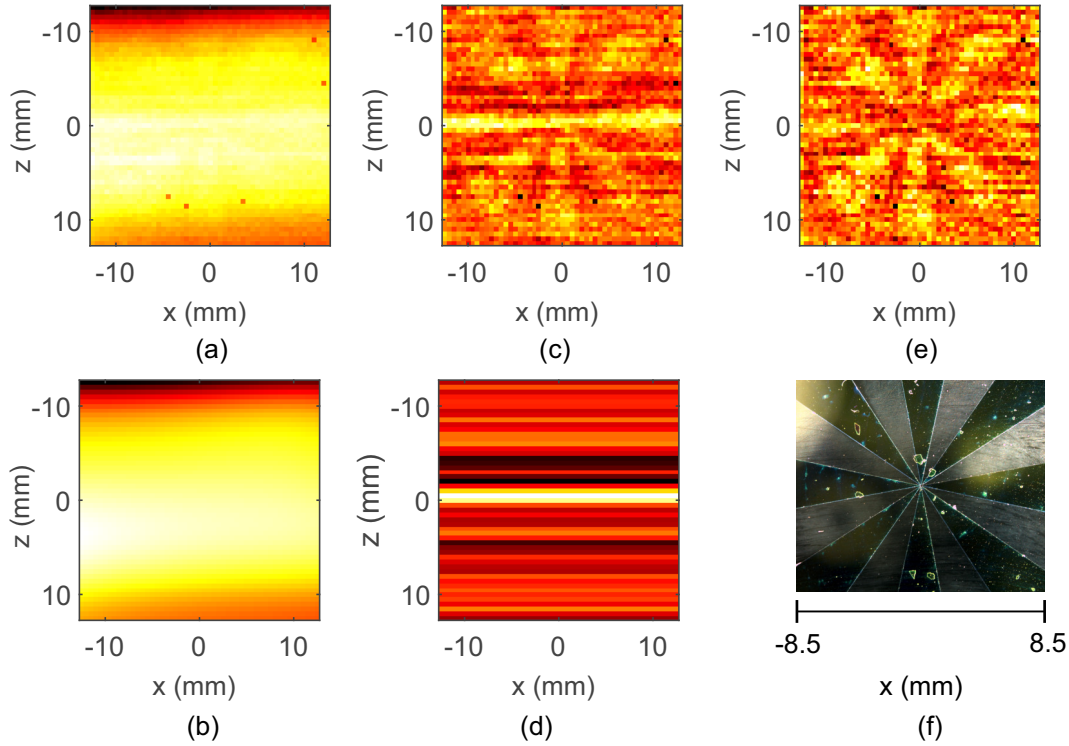


Figure 3.15.: (a)-(e) show the image processing steps of the measured 350 nm SiN deposition into $520 \pm 5 \mu\text{m}$ thick HRFZ-Si wafer. (f) shows the corresponding optical micrograph. Adapted from [67] ©2022 IEEE.

fitting a fifth order plane representing the localised 2-D mean of 3.15(a) as functions of x and z , shown in Fig. 3.15(b). The warping plane is subsequently subtracted from Fig. 3.15(a) to obtain Fig. 3.15(c), in which the 350 nm high structure is discernible but is still affected by the apparent horizontal lines of localised noise. These horizontal artefacts are the laser drifts. These artefacts are considerably, but not completely, reduced by calculating the mean for each horizontal line scan (c.f. Fig. 3.15(d)) and subtracting it from Fig. 3.15(c) to obtain Fig. 3.15(e). With additional contrast enhancement, the star-structure becomes clearly visible. For comparison, a microscopic image of the DUT is added in Fig. 3.15(f). Therefore, an important limiting factor for imaging is the stochastic phase drifts of the DFB lasers which add noise to the image.

An exemplary 2000-order zero-padding, in this case, increases the number of sample to be processed to $\sim 8 \times 10^6$. This significantly increases the computation effort for such nanometric structures. However, since the only significant data-point of the equivalent time-domain pulse is the position of its maxima, down-sampling of the frequency scan can be carried out before its IFT, which decreases the computational load. A 10-fold down-sampling of the frequency sweep reduces the evaluation time by an order of magnitude, without any significant loss of image quality [67]. We note that, an additional low-pass filter is essential before down-sampling to remove aliasing effects.

Figure 3.16(a) shows the THz image of a $10 \pm 5 \mu\text{m}$ thick *Cling wrap* ($d_{opt} \approx 16 \mu\text{m}$) attached to a metal reflector with a $40 \pm 5 \mu\text{m}$ thick adhesive tape ($d_{opt} \approx 64 \mu\text{m}$). Both the wrap and the adhesive tape are manufactured from Polyvinyl Chloride (PVC) ($n_{pvc} = 1.63$, absorption $\approx 86 \text{ dB/cm}$ [34]). We scanned the DUT in reflection geometry between 0.6 – 0.8 THz and used a 100-order zero-padding to generate the THz image. The optical image is added for comparison in Fig. 3.16(b). The adhesive

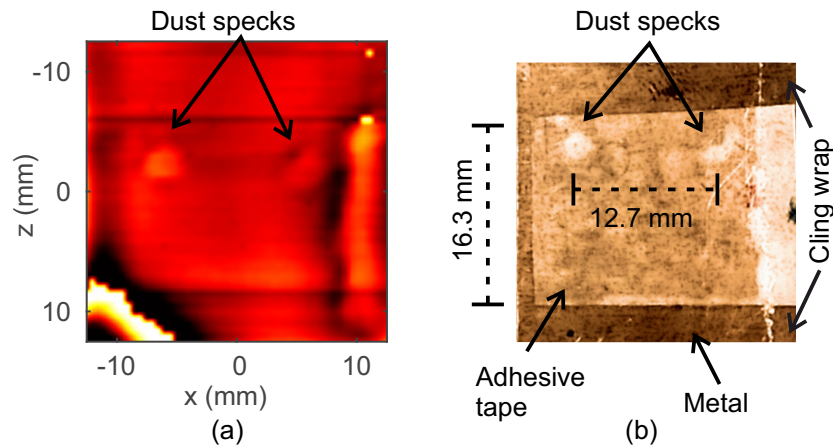


Figure 3.16.: The THz (a) and optical (b) images of $10 \pm 5 \mu\text{m}$ thick Cling wrap stuck on a metallic plate with a $40 \pm 5 \mu\text{m}$ thick adhesive tape. Adapted from [67]. ©2022 IEEE.

tape is clearly visible in the THz image, along with two dust-specks stuck underneath at a distance of 12.7 mm apart. On a closer inspection, we also see the edge of the *Cling wrap* at the top-right corner of the THz image and below the adhesive tape. This demonstrates an absolute optical thickness resolution of $\sim \lambda/15$, which can be further enhanced using higher order zero-padding. In contrast to the Fabry-Pérot-based thickness estimations, the time-of-flight measurements with enhanced resolution can visualize thin-films of low RI, absorptive materials, without any necessary thick, high RI substrate.

Zero-padding does not add additional information in the equivalent time domain signal. As a result, zero-padded IFT cannot distinguish between the reflections from the multiple interfaces between very thin layers in a multi-layered samples, if they are not already distinguishable in the non-zero-padded IFT. Thus, the estimated optical thickness of thin structures such as 350 nm SiN layer is the mean thickness of the HRFZ-Si substrate with and without SiN depositions. An approximate deposition thickness can be estimated from accurate knowledge of the host-wafer thickness and RI of the deposited layer. This can be easily estimated using the phase information of the S_{21} parameter at a reference location on the host wafer where no other structures are present.

Imaging from Fabry-Pérot phase fitting

The DUT is a $510 \pm 5 \mu\text{m}$ thick HRFZ-Si wafer with a 240 nm thick of SiN deposited using chemical vapour deposition (CVD) in form of a similar $25 \times 25 \text{ mm}^2$ large Siemens star. The optical-thickness of the DUT at each of these measurement points is evaluated from the phase of the S_{21} parameter, as it is less erroneous compared to thickness evaluation based on amplitude of the Fabry-Pérot oscillations. Since the deposited SiN layer is very thin with respect to the silicon substrate, the measurement error induced by assuming the DUT to be only surface-structured silicon is negligible. Fitting the phase of the measured S_{21} parameters to eqn. (3.16), an optical thickness map of the DUT is obtained. The physical thickness of the DUT is estimated considering a constant RI of silicon, i.e., $n_{\text{Si}} = 3.416$, obtained from the single layer characterisation by Fabry-Pérot phase-fitting described in section 3.3.1.

Figure 3.17(a) shows the estimated 2-D height profile of the DUT, i.e., HRFZ-Si with 240 nm of deposited SiN on top. The seemingly planar silicon surface has a warping of $\approx 4 \mu\text{m}$ and hence, the 240 nm high Siemens star is invisible in the image. As demonstrated earlier, the mean surface warping is calculated by fitting the entire height-map to a fifth order plane function, shown in Fig. 3.17(b), and is subtracted from the raw height-profile of Fig. 3.17(a). The Siemens star is revealed in Fig. 3.17(c).

Figure 3.17(d) shows the geometrical height measured as function of displacement along y -axis at $x = 8$ mm, indicated by the white arrow in Fig. 3.17(c). The height profile follows the expected values for the Siemens star shown by the dashed black line. Furthermore, the average optical thickness of the star is calculated to 490 ± 160 nm, corresponding to a RI of 2.04 ± 0.19 [66]. The evaluated RI of SiN is lower than the literature value of 2.75 [137] of its crystalline variant at infra-red frequencies, which is expected as the SiN deposited using CVD is usually amorphous.

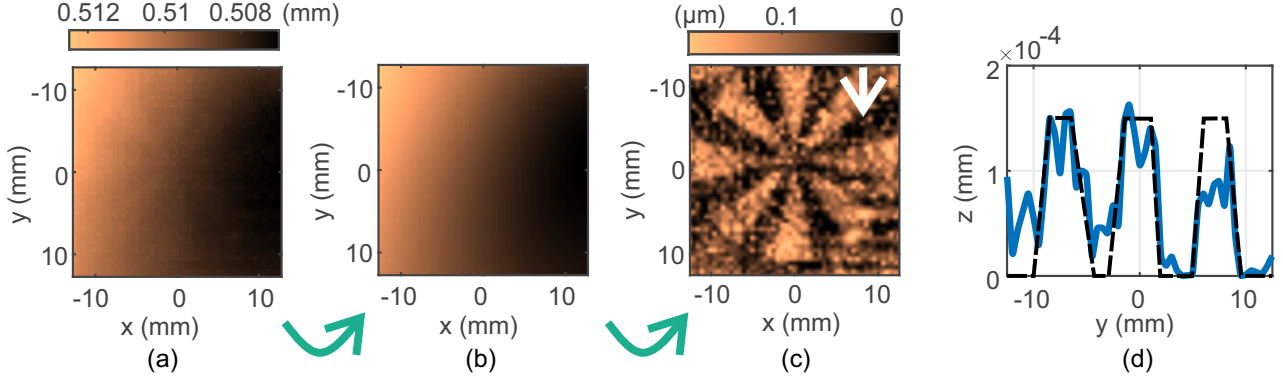


Figure 3.17.: Measurements of nanometric SiN Siemens stars deposited on a silicon wafer. (a) Recorded Terahertz image. (b) Warping of the silicon wafer. (c) THz image of the 240 nm thick SiN Siemens star after subtracting the warping of the silicon wafer and image enhancement. (d) Actual height profile of the column indicated by the white arrow in (b). Adapted from [66].

The THz-imaging system utilizing the Fabry-Pérot pattern in the phase of the S_{21} parameter can be similarly employed to image an extreme range of thickness differences, from as small as $\lambda/7500$ to $\lambda/10000$ to as high as 10λ [66]. However, the scan window should be at least larger than a complete Fabry-Pérot oscillation period to attain good fitting accuracy during thickness estimation. Therefore, the presence of the HRFZ-Si substrate is important in case of measuring thin films to increase the absolute cavity length and proportionally decrease the oscillation period of the induced Fabry-Pérot resonator. Each individual scanned point is evaluated independently and the random drifts of the DFB lasers occur at a slower rate than the total scanning time per point, rather than the total scanning time of the sample (~ 22 s). The slow phase drifts of the DFB lasers do not affect the measurement noise considerably. With all aforementioned conditions fulfilled, the theoretical minimum thickness resolution achievable in such a free-space VNA is given by [66],

$$\Delta h_{FP} = \frac{1}{\eta_{fit}} \cdot \frac{n_{si} d_{si}}{n_{obj}} \cdot \frac{\delta f_L}{f_{scan}}, \quad (3.24)$$

where, d_{si} is the physical thickness of the host silicon wafer, η_{fit} is a measure of the fitting efficiency, n_{obj} is the RI of the deposited thin-film material, δf_L is the frequency stability of the DFB lasers during one frequency sweep, which in this case is previously calculated to 209 ± 50 kHz and f_{scan} is the scanning bandwidth. The height resolution of this system is ≈ 22 nm [66], which is comparable to the minimum reported thickness resolution obtained by far-field thickness measurement systems, generally employing pulsed-lasers featuring at least 10 – 20 times higher bandwidths [27], [138]. We prove this by imaging a 50 nm thick silicon carbide (SiC) star deposited on 510 μm thick HRFZ-Si substrate in Fig. 3.18(a). The star-pattern is clearly visible in the THz image, however, the image is noisier than Fig. 3.17(c), which indicates that we are close to the measurement limit. Figure 3.18(b) shows the

estimated height profile of the line marked by the green arrow in Fig. 3.18(a). A optical micrograph is presented in Fig. 3.18(c).

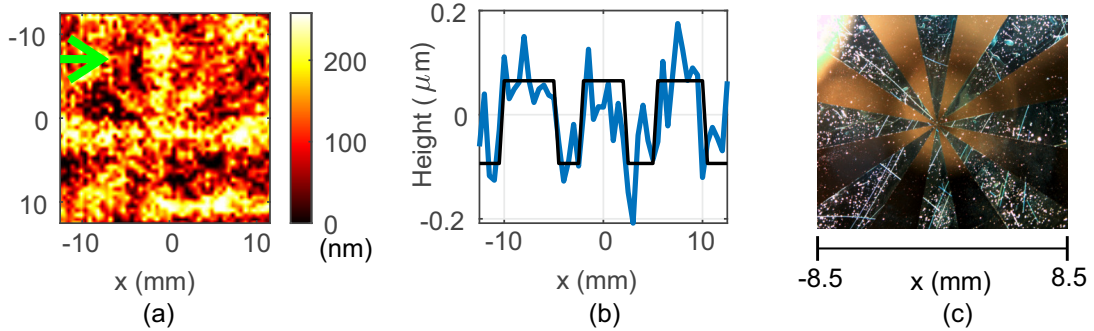


Figure 3.18.: Measurements of nanometric SiC Siemens stars deposited on a silicon wafer. (a) Terahertz image of the 50 nm thick SiC Siemens star after subtracting the warping of the silicon wafer and image enhancement. (d) Actual height profile of the line indicated by the green arrow in (a). (c) shows an optical micrograph of the DUT with the Siemens star. Adapted from [66].

To summarise, we demonstrated two imaging techniques, namely, by measuring the time-of-flight data and fitting Fabry-Pérot phase to the measured S_{21} parameter acquired from a 200 GHz frequency scan with the PVNA. Nanometric depositions on HRFZ-Si wafer are successfully imaged using a bandwidth of mere 200 GHz between 0.6 – 0.8 THz. The clarity of Fabry-Pérot based images are significantly higher than that of the zero-padding based technique. However, the zero-padded-imaging technique circumvents three hurdles of Fabry-Pérot-based imaging. Firstly, the image quality is independent of the sample thickness as it does not necessitate full Fabry-Pérot oscillation periods for the data-fitting. Secondly, since IFT is significantly faster than fitting, the data evaluation for thicknesses higher than a few microns is considerably faster, and comparable for nanometric structures if additional down-sampling is employed. And lastly, the maxima-locator technique is not influenced by the measurement noise, given the homodyne fringes are discernible in the frequency sweeps. This happens because the overall measurement noise is redistributed over a hugely increased number of samples and it does not induce a location shift of the peak-maxima.

The zero-padded-imaging technique is limited to single layered samples and has a worse depth resolution of $d_{opt} \approx 500$ nm compared to Fabry-Pérot based estimations, which is about an order of magnitude worse. Furthermore, unlike Fabry-Pérot based imaging, the individual pixel estimates are not independent of the overall frequency drift of the DFB lasers. A single pixel scan takes about 20 s, thus a total raster scan runs over ~ 12 hours. These laser drifts are significant in this time scale and add additional noise to the image. The deterministic part of the noise, i.e., the gradual changes in the laser frequency, can be calibrated out but the stochastic components cannot be easily removed.

4. Passive Waveguide Components

The miniaturisation of the free-space PVNA requires a waveguide architecture to transform the free-space THz beam into a guided one. The transmission media in Fig. 3.1 is redesigned using dielectric waveguides, which do not necessitate bulky optical components, such as TPX lenses, parabolic mirrors or polarisers. Even the silicon lenses of the active devices, necessary for their free-space operation, can be discarded. We note here that due to the unavailability of suitable material to manufacture THz transmitters in-house, we use a commercial, free-space P-I-N diode-based transmitter from *Fraunhofer Heinrich Hertz Institute/Toptica photonics AG*. Hence, the miniaturised PVNAs are not yet fully integrated and waveguides are thus designed to incorporate free-space in-coupling of THz power. The THz receivers in the semi-integrated PVNA are based on ErAs:In(Al)GaAs photoconductors (see section 2.2.2) and are elaborately discussed in chapter 5. In this chapter, we focus on the passive waveguide components. The contents of this chapter are published in [70], [71] and some of the chapter's plots are adapted from the aforementioned publications.

4.1. Silicon-on-insulator waveguide architecture

The rectangular waveguides are fabricated using HRFZ-Si ($\epsilon_{r,Si} = 11.67$ [34], resistivity > 10 k Ω -cm [139]), chosen due to their extremely low material losses at THz frequencies and considerably high permittivity, and consequently, high mode-confinement inside the guiding silicon. Figure 4.1(a) illustrates a rectangular HRFZ-Si waveguide mounted on a low-loss, lower RI substrate. We use Qz and HDPE as substrates in this work as they are known to have lowest losses in the THz regime and feature considerable low RIs. As the guided wave in open-waveguide structures extends into the surrounding media with its evanescent field components, an effective RI of the guided mode is calculated as integral of the local power across the mode profile weighted by the local RIs. Even though the dielectric guiding structure theoretically offers an infinite single-mode bandwidth, the propagation constant of the guided mode (see eqn. (2.43)) becomes imaginary at lower frequencies for inhomogeneous surrounding media. This introduces a lower cut-off frequency for the waveguide modes. Put in other words, if the effective RI of the guided mode n_g becomes lower than the RI of the substrate, the propagating wave leaks into the higher-RI substrate and is not guided further. This usually happens at lower frequencies when the sufficiently large evanescent field in air reduces the effective RIs of the waveguide modes below the RI of the substrate.

Simulation snapshots in Fig. 4.2 show the electric field propagation through the designed waveguides, supported by a Qz substrate ($n_{qz} = \sqrt{\epsilon_{r,qz}} \approx 2.12$ [34]). At $f \leq 0.5$ THz, the n_g of the fundamental E_{11}^x mode is lower than n_{qz} , which causes a part of the propagating wave to leak towards the substrate and this sets a lower cut-off for the fundamental mode. The HDPE substrate ($n_{PE} \approx 1.55$) reduces this lower cut-off frequency to ≈ 0.451 THz. With increasing frequency, as the guided mode gets more strongly confined within the HRFZ-Si structure, the substrate leakage becomes negligible and the transmission losses depend only on the material properties.

The modes supported by the waveguides are based on the number of possible maxima/minima along the cross-section of the travelling wave. Since the wave outside the guiding silicon is evanescent, the

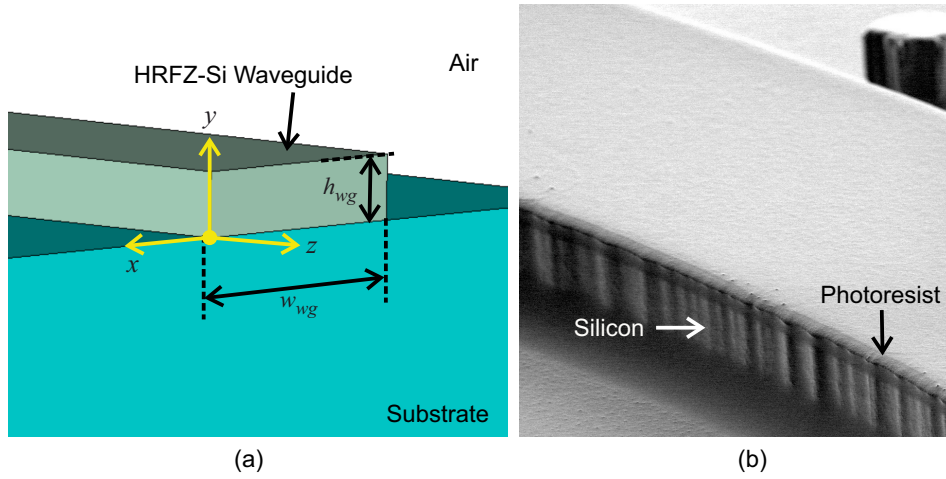


Figure 4.1.: (a) Schematic representation of the planar waveguide architecture where the HRFZ-Si guiding structure is supported by either a Qz or a HDPE substrate. (b) A scanning electron microscope (SEM) image of the etched silicon waveguide with some residual photoresist atop. The etched walls of the waveguides have a longitudinal roughness in the order of ~ 100 nm, whereas the vertical periodic undulations caused by the deep reactive-ion etching (DRIE) process are between 7 – 10 nm. Adapted from [70].

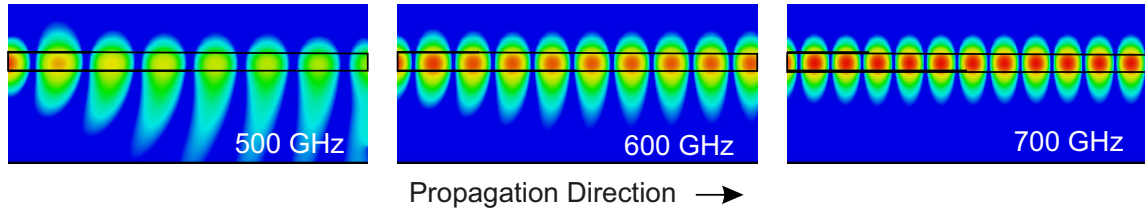


Figure 4.2.: Simulations of the guided fundamental mode at frequencies 0.5, 0.6 and 0.7 THz. The black rectangular structure represents the waveguide. At 0.5 THz, the wave significantly leaks into the Qz substrate. At 0.7 THz, the substrate leakage becomes negligible and the guided fundamental mode is strongly confined within the HRFZ-Si guide. Adapted from [70].

extrema are only feasible in the cross-section of the guiding dielectric $h_{wg} \times w_{wg}$. Additionally, eqn. (2.46) gives an estimate of the largest waveguide dimensions to support only fundamental mode as

$$\begin{aligned}
 Q_{x,(y)} &= \frac{\lambda}{\sqrt{\epsilon_1 - \epsilon_{0,(2)}}} \\
 &= \frac{c_0}{f^{\text{THz}} \sqrt{\epsilon_{r,\text{Si}} - \epsilon_{r,\text{eff}}}},
 \end{aligned} \tag{4.1}$$

where c_0 is the speed of light in vacuum and $\epsilon_{r,\text{eff}}$ is the effective relative permittivity of waveguide surroundings. We aim for a waveguide architecture which is operable over several octaves (0.5 – 2 THz) to complement broad bandwidth of the THz active devices. This inevitably leads to overmoded waveguides. We design the HRFZ-Si waveguides such that they support only a single maximum along its height for the entire frequency range 0.5 – 2 THz. This is necessary to prevent mode conversion along the vertical dimension of waveguide as it cannot be later rectified owing to the planar waveguide architecture. Thus, we need to ensure that the height of the waveguide h_{wg} is smaller than Q_y . Using

$f_{\text{THz}} = 2$ THz and $\epsilon_{r,sur} = (\epsilon_{r,air} + \epsilon_{r,Qz})/2 \approx 2.76$ in eqn. (4.1), we get $Q_y = 50.23$ μm . Subsequently, setting the waveguide height $h_{wg} = 50$ μm in CST® microwave studio, we optimise the width w_{wg} of the silicon waveguide such that the lower 3-dB cut-off frequency of the waveguide is 0.5 THz. The final waveguide dimensions obtained from the numerical simulations are 200×50 μm^2 . We note that the HDPE substrate reduces Q_y to 47.5 μm . In this case, the 200×50 μm^2 waveguides support only one vertical mode till ≈ 1.90 THz.

As closed-form analytical solutions are not available for open waveguide structures, numerical simulations are necessary to estimate the propagation characteristics of the guided wave through dielectric waveguides. However, to have an intuitive understanding of the wave guidance and, subsequently, the reasonableness of the simulation results, we must reflect back on the orthogonality of the propagating modes in a waveguide and the corresponding *coupled-mode theory* (see section 2.1.3). In essence, inter-modal power coupling between the guided and radiating modes are triggered by waveguide perturbations, like curvature, tapers, etc. Power coupled to the radiating modes is lost, whereas, the guided modes carry power through the waveguide length. Since, the waveguide architecture is planar with (ideally) no perturbations along the vertical axis (y -axis), mode conversions, neither to guided-modes nor to the radiating modes, are expected during propagation. Assuming the wave inside the waveguide is propagating in the positive z -direction and a higher mode-confinement in the guiding HRFZ-Si, we can approximate the electric field distribution for the modes along the lateral x -axis as [140]

$$\begin{aligned} E_p(x) &= \cos(k_{x,p}x) \quad \forall p = 2n \text{ and} \\ E_p(x) &= \sin(k_{x,p}x) \quad \forall p = 2n + 1, \end{aligned} \quad (4.2)$$

where, $k_x = (p+1)\pi/w_{wg}$ and n is an integer. This approximation is true at higher operating frequencies at which the evanescent fields along the lateral axis can be neglected. At lower guided frequencies, the effective waveguide width to calculate k_x must be slightly larger than w_{wg} . Furthermore, the electric field of even modes follows $E_p(x) = E_p(-x)$ and hence, are called *symmetric modes*, whereas the electric field of the odd modes are *anti-symmetric* as $E_p(x) = -E_p(-x)$. The electric field intensity of any pq^{th} propagating mode from equations (2.23 - 2.27) and (4.2) approximates as

$$E_{pq}^x(x, y, z, t) = C_{pq} E_p(x) E_q(y) \exp(\gamma z - j\omega t), \quad (4.3)$$

where γ is the complex propagation constant (cf. eqn. (2.52)) and C_{pq} is the coupling coefficient signifying the fraction of power coupled to pq^{th} mode. $E_q(y)$ stays invariant throughout the whole waveguide. The lateral perturbations in the guide essentially alter the coupling coefficients C_{pq} of the guided as well as radiating modes as inter-modal coupling occurs.

4.2. Free-space measurement setup

Figure 4.3(a) shows the schematic of the modified free-space THz setup to characterise the waveguides. All waveguides feature a 90° bend to minimise the line-of-sight coupling between the THz source and the receiver. The end-facets of the waveguides are placed at the foci of the TPX lenses ($L1$ and $L2$). Similar to the free-space PVNA, the transmission coefficient is calculated by referencing to a measurement without waveguide, where the transmitter and receiver modules face each other (cf. Fig. 1.2). Since, the detector current is proportional to the incident THz field, the total transmission loss in the system L_{tot} (in decibels) equates to

$$L_{tot,dB} = 20 \log_{10} \left(\left| \frac{I_{wg}}{I_{ref}} \right| \right), \quad (4.4)$$

where, I_{wg} is the measured detector current with a waveguide in the setup and I_{ref} is reference detector current. The total measured loss is an accumulation of the coupling losses to the waveguides, guiding losses through the waveguides and material losses in the waveguides. We will elaborate upon each of these losses as we progress through this chapter.

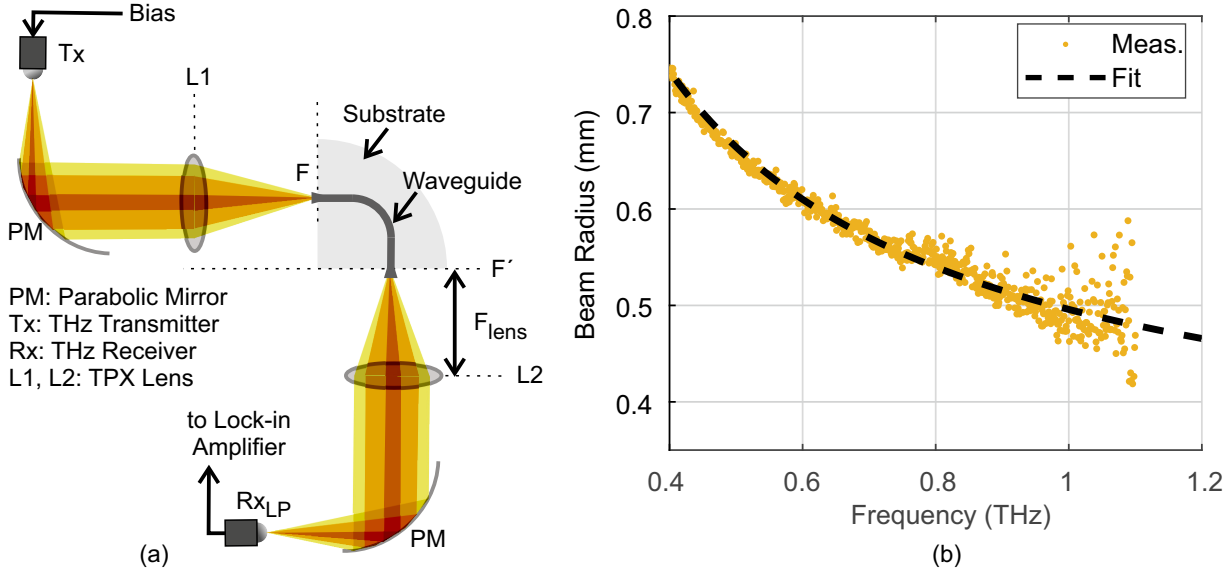


Figure 4.3.: (a) Free space measurement setup for the waveguides. The waveguides are supported by either Qz or HDPE substrate. (b) Measured beam radius of the free-space Gaussian THz beam at F and F' . Adapted from [70].

The free-space THz beam in the setup approximately has a Gaussian profile [45]. The $1/e^2$ -diameter of the beam at its focus dictates the extent of mode-matching at waveguide end-facets and consequently, the amount of power coupled to the waveguides. The *knife-edge* technique is commonly employed to measure Gaussian beam profiles [141], however, we took advantage of an iris diaphragm (circular aperture with adjustable radius) to estimate the same. Assuming the beam is propagating in positive z -direction, the fraction of total power transmitted through the iris aperture reads as [142]

$$T_{iris}(z) = 1 - \exp \left[- \frac{2\rho_{iris}^2}{\rho_g^2(z)} \right], \quad (4.5)$$

where ρ_{iris} is the radius of the circular iris-aperture and $\rho_g(z) = \rho_{g0} \sqrt{1 + (z/z_R)^2}$ is the radius of the Gaussian beam profile at a distance z from its focus, where its radius is ρ_{g0} and $z_R = \pi\rho_{g0}^2/\lambda$ is the Rayleigh length of the Gaussian beam. Keeping the diameter of the aperture unchanged, we place the iris longitudinally at three different locations along the z -axis between $L1$ and F and measure the transmitted power. Using eqn. (4.5) and the corresponding relative displacements of the iris, we calculate the frequency-dependent estimates of the beam diameter at the focus F in Fig. 4.3(b). Detailed calculations are in Appendix A.3. The estimated beam radius fits excellently to the expected frequency-dependent Gaussian spot-size reduction for the given set of optical components, such as parabolic mirrors and TPX lenses, in the setup.

4.3. Simulations

We use CST® microwave studio to simulate the waveguide characteristics throughout this chapter. In simulations, a Gaussian beam excites the waveguides, mimicking the measurement setup of Fig. 4.3(a). The beam radius is $\rho_{g0} \approx 660 \mu\text{m}$ at 0.5 THz and $\approx 500 \mu\text{m}$ at 1 THz (see Fig. 4.3(b)). Figure 4.4 shows the complete simulation schematic. The horizontally polarised electric field of the THz beam excites only E_{pq}^x modes in the waveguide, E_{11}^x being the fundamental mode, with E_{21}^x and E_{31}^x are the principle higher order modes. The coupling coefficient to E_{21}^x mode, C_{21} , is significantly lower than C_{11} and C_{31} as the mode requires a null along the $x = 0$ plane. The simulated waveguide structure is divided into four regions, demarcated by the locations A, B, C and D. Four transparent (non-absorbing) waveguide ports are placed at the aforementioned locations to monitor the guided EM fields. We use the transient solver with lowered mesh-count in the simulations for a significantly shorter simulation time compared to the frequency-domain solver. However, the latter is more accurate, especially the edges of the simulated bandwidth.

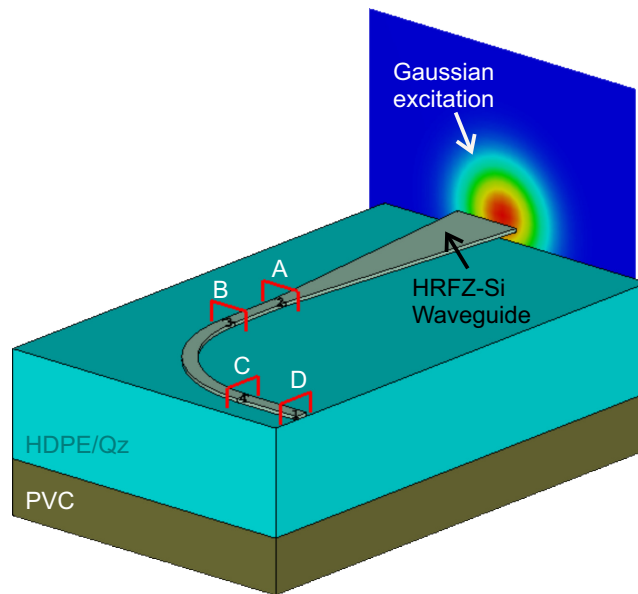


Figure 4.4.: Simulation schematic for the entire waveguide structure excited by a free-space Gaussian beam with horizontally polarised electric field and a beam radius $\rho_g \approx 660 \mu\text{m}$ at 0.5 THz. Waveguide ports at locations A, B, C and D are non-absorbing ports, used to monitor the EM fields at their corresponding positions. The simulation structure has open boundaries such that no reflections occur at the edges of the simulated structure. The HRFZ-Si waveguide is placed atop either a HDPE or a Qz substrate and is supported by a PVC layer underneath.

The waveguide section between the Gaussian beam and A is tapered, which mimics a horn antenna and is necessary to couple power into the waveguide. The sections AB and CD are straight guiding structures and give an estimate for the transmission loss in waveguide. A 90° bend between BC is essential to prevent line-of-sight coupling from the free-space beam to the active devices and is an integral part of designing passive waveguides structures as splitters, 3-dB couplers, etc. The waveguide port located at D is orthogonal to the Gaussian excitation and estimates the total travelling power in the waveguide. Next, we simulate and optimise the waveguide tapers and bends, to obtain their complete

set of S-parameters. The transmission characteristics of any substantially complex waveguide structure can be evaluated by cascading these primary structures, by multiplying their individual T-parameters to obtain the overall S-parameters.

4.3.1. Bandwidth and multimode operation

The 200 μm width of the waveguides are much larger than Q_x calculated from eqn. (4.1) at higher design frequencies and hence, the HRFZ-Si waveguides support multiple modes along its width. Simulations also concur this behaviour. Figure 4.5 shows the dispersion diagram of the designed waveguides. The dashed black line shows the propagation constant of the wave in free-space and the red-line shows the same in bulk Qz. A mode is only guided if its propagation constant is larger than that of a plane wave travelling in the bulk substrate. In other words, the lower cut-off frequency of the guided modes is the frequency at which the dispersion line of the waveguide mode crosses the same of the substrate. Below this frequency, the power propagating in the modes readily couples to the radiating modes and is lost.

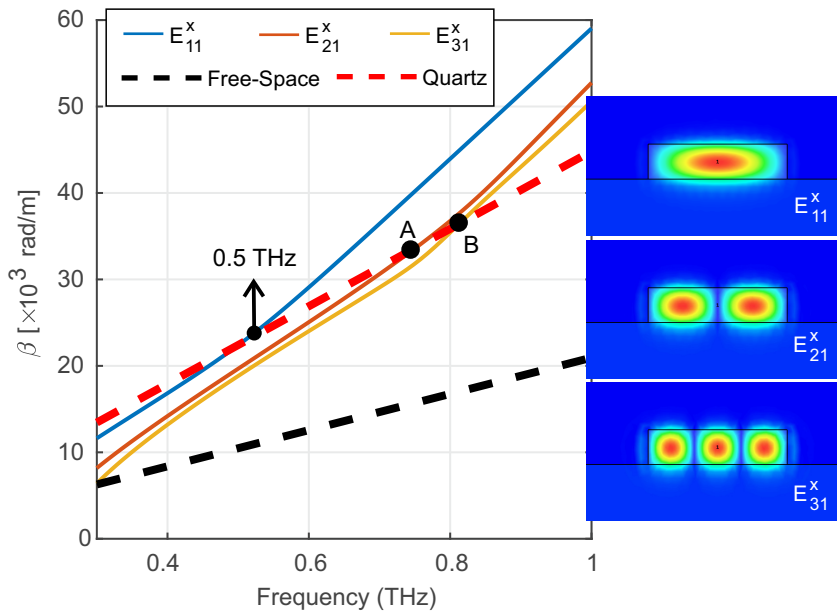


Figure 4.5.: Simulated dispersion diagram of the designed HRFZ-Si waveguides supported by Qz shows the propagation constant of the first three E_{pq}^x modes. The corresponding transverse electric field distribution is shown in the inset. The propagation constants of E_{21}^x and E_{31}^x modes crosses the dispersion line of the Qz substrate at points A and B, respectively. The propagation constants of E_{21}^x and E_{31}^x modes are smaller than the fundamental mode and they propagate at higher velocities through the waveguide. Adapted from [70].

We define the bandwidth of waveguides as the frequency band between the lower cut-off frequency of the fundamental mode and that of the first higher order mode. However, for open-waveguide structures with inhomogeneous surrounding media, such as the one presented in this thesis, the travelling power couples from the guided mode to the radiating mode throughout the whole frequency range of operation. This can be intuitively understood by the higher phase velocity of the propagating mode in air than in the substrate, which results in a forward-inclined wavefront of the propagating mode, resulting in radiation into the substrate. With increasing frequency, the mode becomes more

confined within the high-permittivity HRFZ-Si structure and this leakage loss significantly decreases. Therefore, in addition to material losses, the fundamental mode loses power due to substrate leakage even above its lower cut-off frequency.

The *single-mode bandwidth* of the designed waveguides is the frequency range within which only the fundamental mode (E_{11}^x) is guided. The dispersion characteristics of the guided modes in Fig. 4.5 shows that the single-mode bandwidth of the waveguides with Qz substrate is 0.5 – 0.75 THz [70]. Using a HDPE substrate changes the single-mode bandwidth to $\sim 0.45 - 0.7$ THz. This is comparable to the state-of-the-art RHM *WR-1.5* waveguides designed for the same bandwidth [33]. Above 0.75 THz, the waveguide structures support multimode propagation. The *coupled mode theory* states that, when multiple modes propagate simultaneously in a waveguide, the modes exchange the total guided power among themselves as a sinusoidal function of [140]

1. the propagation-distance normalised to the guided wavelength, and
2. the phase-mismatch between the propagating modes.

This results in standing-wave-like oscillatory patterns in the detected signal of field-detectors (sensitive to the mode-field distribution), such as the ErAs:In(Al)GaAs-based photoconductors. However, with appropriate excitation and transition structures, such as waveguide bends, splitters, etc., the excitation of HOMs can be significantly suppressed and these waveguides can be essentially operated in their fundamental mode over a much larger bandwidth, which we will henceforth refer to as their *operational bandwidth*. In practical electronic systems, it is extremely difficult to employ the RHM waveguides in their overmoded regime as selective mode excitation from electronic sources, like commonly used Schottky-diode based multipliers, is almost impossible. Thus, at least five different RHM waveguides (*WR-1.5* to *WR-0.65*) are necessary to measure the bandwidth 0.5 – 1.5 THz. This is expensive and impractical in designing broadband PVNAs. We note that Mitrofanov *et al.* have demonstrated broadband, overmoded operation of dielectric-lined circular metallic waveguides in THz range [143], [144], however, a free-space pulsed THz transmitter was used to excite the waveguides, in a setup similar to Fig. 4.3. We will see later in this chapter that the designed HRFZ-Si waveguides have an operational bandwidth of at least 0.5 – 1.5 THz and therefore, are suitable for designing integrated broadband THz systems.

4.3.2. Waveguide tapers

Waveguide tapers are smooth transitions between two different widths or heights [140]. In this thesis, we will restrict ourselves only to lateral tapers as the vertical tapers are cumbersome or highly expensive to fabricate with fabrication techniques used in this thesis. Coupled mode theory says that such structural perturbations will lead to power inter-coupling between various guided and radiated modes in the waveguide dictated by the cross-coupling coefficients formulated in eqn. (2.50), also known as the overlap integral of two modal distributions. For slowly varying structures, where the waveguide width only adiabatically changes for a Δz change in longitudinal distance, the mode profiles before and after the Δz section is almost identical and hence, the overlap integral is ≈ 1 . Thus, gentle tapers suppress mode coupling to the radiating modes and are called *non-radiating* tapers. Alternatively, drastic change in waveguide width leads to mode conversion, where propagating modes before the taper loses its power to another guided or radiating mode. Thus, these are tapers of *radiating* kind. Dielectric rod waveguides (DRWs) are an example of the radiating taper, which significantly couples the guided power from the waveguide to the radiating modes, thus, acting as a radiating element similar to leaky-wave antennas. In general, non-radiating tapers are better for designing waveguide transitions, whereas, radiating ones are good as antennas or mode-convertors.

Out-coupling to free-space Gaussian beam

In the measurement setup, the $1/e^2$ -diameter of the free-space Gaussian beam is orders of magnitude larger than the waveguide cross-section and hence, some transition structures are necessary to increase the in-coupling efficiency. Figure 4.6 shows two possible solutions to the coupling problem. A narrowing taper in Fig. 4.6(a) is radiating and acts as an unidimensional DRW antenna to couple-in THz power into the waveguides. Similar to the leaky-wave antennas, the taper radiates different frequencies at different points on the taper and thus, a good mode-overlap with the Gaussian beam is difficult to achieve over a large bandwidth. In this work, we use the broadening, non-radiating tapers depicted in Fig. 4.6(b). The idea behind is to excite the fundamental mode in the 1 mm-wide end-facet of the taper and adiabatically transform the mode to the fundamental mode inside the waveguide. The broadened taper acts a horn antenna and its gain increases proportionally to the aperture size when

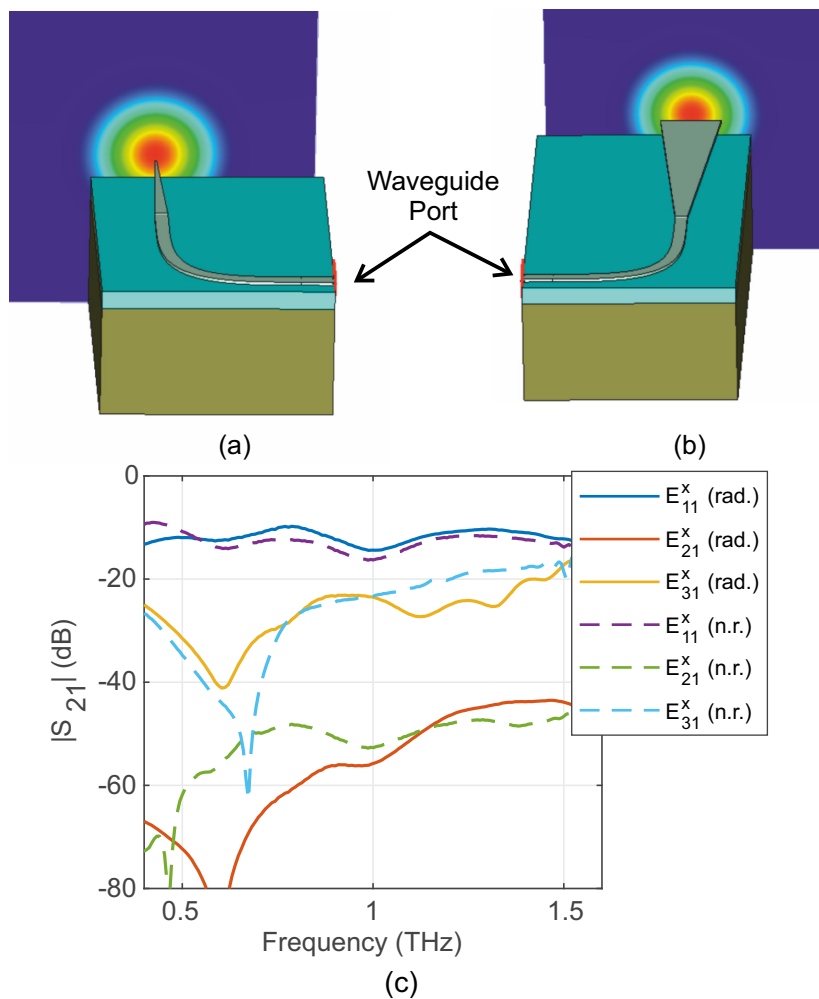


Figure 4.6.: (a) Narrowing, radiating (rad.) waveguide taper excited by a free-space Gaussian beam with a beam radius ρ_g . The width at the end of the 1 mm-long taper is $20 \mu\text{m}$. (b) A broadened, non-radiating (n.r.) waveguide taper used extensively with the designed waveguides to in-couple power. The final width of the taper is 1 mm and it is 4 mm long. (c) Comparison of the simulated power coupled to the first three horizontal modes for the tapers in (a) and (b).

the aperture efficiency is assumed unchanged (see eqn. (2.82)). The adiabatic taper helps to maintain an uniform phase-front at the radiating waveguide aperture and consequently, increases the aperture efficiency.

Figure 4.6(c) shows the power coupled to the first three horizontal modes for both the radiating (rad.) and non-radiating (n.r.) tapers. The radiating tapers show 1 – 2 dB higher coupling efficiency to the fundamental mode over the whole frequency range. Additionally, it suppresses power coupled to the E_{31}^x mode by $\approx 6 - 8$ dB above 1 THz. Without any loss of generality, we can treat the waveguide tapers as transmitting structures due to the antenna reciprocity theorem (see section 2.3). The effective permittivity of the radiating tapers in Fig. 4.6(a) is much lower than that of the propagating mode. At the point of radiation, the permittivity lowers so much that the guiding structure cannot sustain the mode any more and the power is radiated. This significantly reduces reflection at the point of radiation. Whereas, the non-radiating tapers, due to their broadened HRFZ-Si structure, have a larger permittivity mismatch at the radiating facet. This causes a reflection, and consequently, a reduced coupling efficiency to the free-space Gaussian beam. However, broadened end-tapers are easier to fabricate and to handle than waveguides with narrowed tips and hence, are used as the coupling structures of choice. Additional cylindrical lenses can be employed to turn the circular Gaussian beam to a cylindrical one for a better mode-matching at the tapered waveguide aperture. Alternatively, silicon lenses can be used at the waveguide end-facet to improve the coupling efficiency, however, both the approaches are counterproductive to the final goal of miniaturisation and integration of the free-space PVNA components.

4.3.3. Waveguide bends

An analytical solution to the waveguide bends requires solving the wave equations of section 2.1 in cylindrical coordinates (r, y, ϕ) . The solution involves numerical calculations of Bessel functions with large and complex indices [145]. Instead, we will use conformal transformation [146] and maintain the same shape of the Helmholtz equations of the guided modes in the transformed coordinate system (u, y, ϕ) as it is in the Cartesian coordinates (x, y, z) . Simply speaking, the lateral field distributions

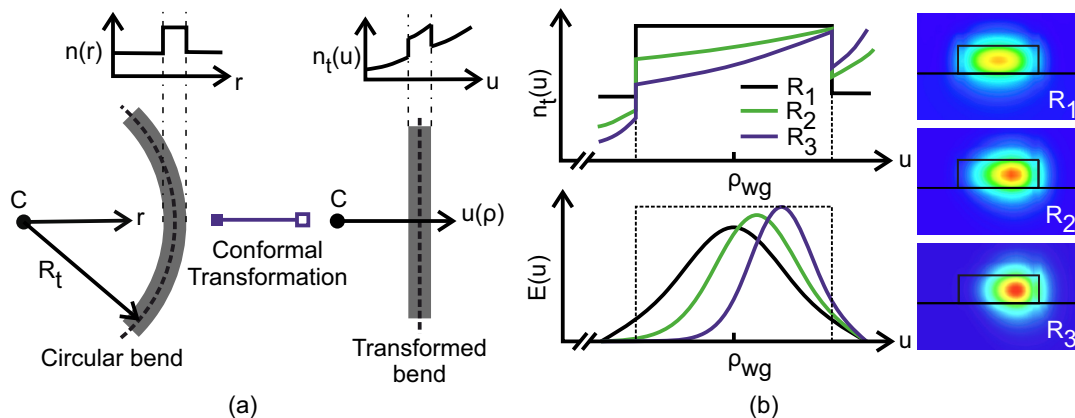


Figure 4.7.: (a) Conformal transformation changes the waveguide bend into an equivalent straight waveguide section. The transformed RI is an exponential function of the transformed lateral distance. (b) The smaller the radius of curvature (ROC), the more the mode maximum is shift outwards. The simulations in the inset confirm this phenomenon. Adapted from [70].

of eqn. (4.2) after transformation will vary sinusoidally with u , however, the term $k_{u,p}$ increases exponentially with u . Figure 4.7(a) shows the transform of a circular waveguide bend to an equivalent straight waveguide schematically. After transformation, the RI profile $n(x)$ of the bend with local ROC ρ_{wg} becomes

$$n_t(u) = n(r) \exp\left(\frac{u}{\rho_{wg}}\right), \quad (4.6)$$

where $u = \rho_{wg} \ln(r/\rho_{wg})$ is the transformed radial distance r . We can make two important inferences about the propagating mode in a bend from the conformal transformation technique:

- Firstly, at certain radial distance ρ_{lim} , the transformed RI $n_t(u)$ becomes larger than the effective RI of the guided mode. All the guided power carried by the evanescent fields beyond this point gradually leaks into the radiation modes in the high- n_t region [147]. In other words, the guided power in the bent section of the waveguide gradually radiates away from the centre of the bend. This makes the waveguide bends inherently lossy. With higher mode confinement or lower ROCs, this radiation loss can be substantially suppressed.
- Secondly, the mode is most strongly guided at the position of highest transformed RI. This shifts the mode profile towards the outer rim of the waveguide bend [140]. Figure 4.7(b) illustrates such a shift of electric field intensity ($E(u)$) of the E_{11}^x mode along the waveguide cross-section for three different ROCs $R_1 \gg R_2 > R_3$. The simulated field distribution in the insets corroborates this phenomenon.

The outward-shifted mode profile introduces two further losses in the bends, namely mode-mismatch between the straight and the bent sections leading to inter-modal coupling losses and increased surface scattering losses at the outer rim of the waveguide bend. The losses due to mode-mismatch is proportional to ρ_{wg}^{-2} [148]. The waveguides are fabricated using DRIE and the waveguide walls feature an average surface roughness in the order of ~ 100 nm. These perturbations lead to increased surface scattering, proportional to the fraction of the propagating power which interacts with the waveguide walls and roughness variance of the walls [149]. We simulate in CST® microwave studio to optimise these waveguide bends to have a small ROC, yet minimal radiation and mode-conversion losses.

Circular bends

Circular bends are the simplest to design. Bends with different ROCs simulated in CST® microwave studio reveal that 2 mm bend radius suppresses mode conversion by 20 dB till ≈ 1.2 THz, where as a 4 mm radius suppresses it further till ≈ 1.6 THz. The radiation losses mostly occur at the lower frequencies where evanescent field associated with the guided wave is significant. Simulations in Fig. 4.8 show the wave propagation in fundamental mode through a bend with ROC of 2 mm. The substrate is Qz. We see significant power leakage at 0.6 THz away from the centre of the bend, but also into the substrate due to its higher permittivity. As the frequency increases to 1 THz, these radiation losses become negligible.

Since, the mode maxima shifts towards the outer rim of the waveguide as frequency increases, the propensity of power coupling to the higher order modes is larger at higher frequencies. Unlike waveguide tapers, this power interchange happens between two successive E_{pq}^x and $E_{(p+1)q}^x$ modes. Thus, using the coupled mode theory and assuming only fundamental mode propagating before the waveguide bend, the mode at the bend can be expressed as a linear combination of the first two straight waveguide modes [148], [150]. An outward offset of the straight waveguide section to compensate

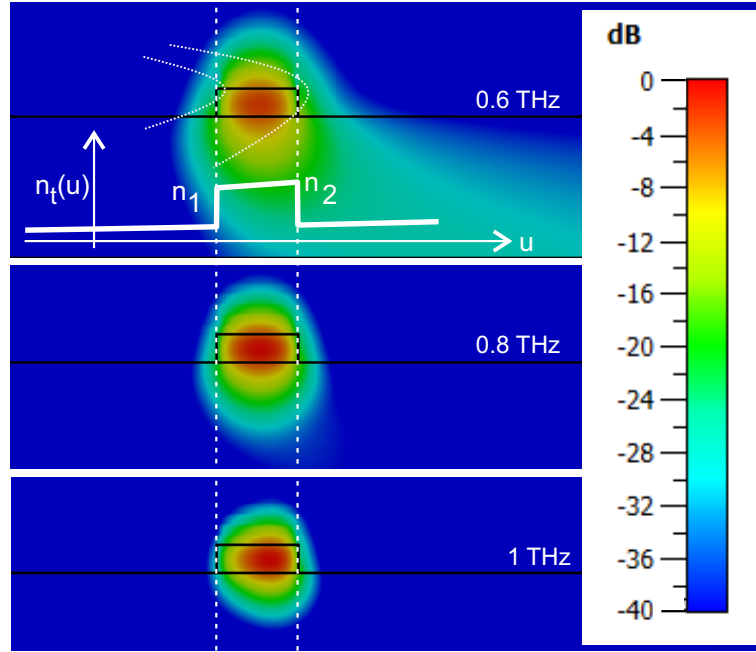


Figure 4.8.: Simulated transverse mode profile of the guided fundamental mode at 0.6, 0.8 and 1 THz. Adapted from [70].

the outward-shifted mode-profile of the bend increases the mode overlap between the bend and the straight waveguide modes, thus decreasing inter-modal coupling [91]. However, an offset is only useful for narrowband waveguides with bandwidths a fraction of their centre frequency. An alternative broadband solution is to design bends with non-constant ROC.

Non-circular bends

Gradual and slow perturbations suppresses mode conversions. So instead of transforming a straight waveguide (ROC $\rightarrow \infty$) abruptly into a bent structure with finite ROC, the local bend radius can be gradually decreased and later increased to design the waveguide bends. In this thesis we use a sine-squared function to model the 90° bend (see Fig. 4.9(d)). The curvature, in cylindrical coordinates, reads

$$r(\phi) = A \times \sin^2\left(\frac{\phi}{A}\right), \quad (4.7)$$

where $\phi = A \times [-\pi/4, \pi/4]$ and $A = 2\sqrt{2}\tilde{\rho}_{wg}/\pi$ is a scaling parameter to adjust the effective radius of the non-circular 90° bend $\tilde{\rho}_{wg} = L_c/\sqrt{2}$, wherein L_c is the length of a line connecting the two ends of the bend. The local curvature κ of the bend reads [151]

$$\kappa(\phi) = \frac{1}{\rho_{wg}(\phi)} = \frac{|d^2r/d\phi^2|}{[1 + (dr/d\phi)^2]^{3/2}} \quad (4.8)$$

which for the sine-squared bend in eqn. (4.7) reads

$$\kappa(\phi) = \frac{2}{A} \frac{|\cos(2\phi/A)|}{\sqrt{[1 + \sin^2(2\phi/A)]^3}}. \quad (4.9)$$

Here κ is a non-linear function of ϕ . Numerical analysis of constant, linear, non-linear, trapezoidal, and offset-circular dependence of κ on ϕ shows minimum mode-conversion losses for the non-linear $\kappa - \phi$ dependence [92] and hence, the sine-squared curvature is apt to design the waveguide bends. The length of the curvature is numerically calculated as [152]

$$l_{\sin^2} = \int_{-A\pi/4}^{A\pi/4} \sqrt{1 + \sin^2(2\phi/A)} d\phi. \quad (4.10)$$

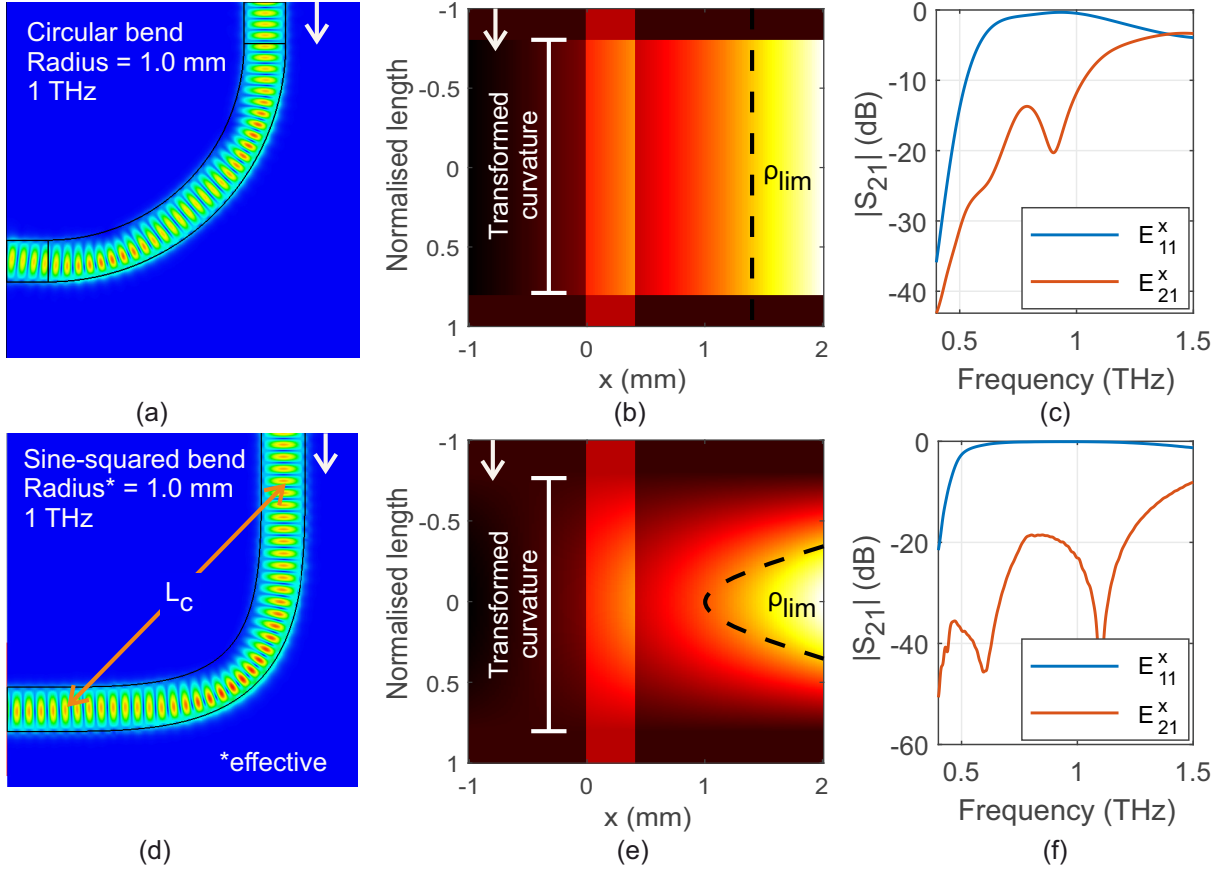


Figure 4.9.: (a) and (d) show the simulated electric field propagation through a circular and sine-squared bend, respectively, with $\tilde{\rho}_g = 1$ mm. (b) and (e) show the conformal transformed refractive index distribution for circular and sine-squared bends, respectively. The dashed black line depicts ρ_{lim} , beyond which the transformed RI is greater than the RI of the propagating mode. The power travelling on the right of the ρ_{lim} line is radiated. (c) and (f) show the simulated $|S_{21}|$ parameters for the E_{11}^x and E_{21}^x modes for the circular and sine-squared bends. E_{21}^x mode carries equal power as the fundamental mode in the circular bend above 1.4 THz, whereas it is suppressed by > 10 dB for the sine-squared bend.

Simulations in Fig. 4.9(a) and (d) show the mode propagation in circular and sine-squared waveguide bends with an effective bend radius of 1 mm. Unlike the circular bend, the mode in sine-squared bend depicted in 4.9(d) uniformly deforms to an outward-shifted bend mode, before gradually reverting to the fundamental mode of the straight section. We note that the radiation losses (and surface scattering

losses) near the position of maximum curvature in the sine-squared bend is higher than the circular bend, however, the losses are incurred over a smaller propagation distance. Heat-maps in Fig. 4.9(b) and (e) show the conformal transformed RI distribution encountered by a guided wave while moving from a straight section to a bent one. On the one hand, the severe RI jump at the beginning and the end of the curvature for the circular bends leads to significant mode-conversions. Furthermore, the propagating power beyond the ρ_{lim} line is constantly radiated out of the guided mode. On the other hand, the sine-squared bend shows gradual and subtle changes in RI over the whole curvature and hence, both mode conversion and radiation losses are significantly smaller. Transmission coefficients in plots 4.9(c) and (f) show significantly lower mode conversion for the sine-squared bend. If the effective bend radius of the sine-squared bend is increased to ≈ 2.3 mm, the power coupled to E_{21}^x mode stay below -20 dB over the frequency range of $0.4 - 2$ THz.

4.3.4. Propagation characteristics

We now stitch together all the simulation results, and their corresponding inferences, to have a behavioural overview of the propagating wave in the HRFZ-Si waveguides. Plots in Fig. 4.10 show the evolution of the first three guided E_{pq}^x modes through the transparent ports at A , B , C and D . The waveguide curvature between BC is a circular bend with $ROC = 2$ mm. First, we use a Qz substrate for the simulations. The straight waveguide sections AB and CD are 1 mm long. The in-coupling tapered structure is 4 mm long and its end-facet is 1 mm wide. The transient solver is inaccurate at the band-edges as it simulates over a finite time-window, resulting in large side-lobes of the equivalent BPF (see section 3.2). Thus, we only limit ourselves to the frequency characteristics between $0.5 - 1.5$ THz of the simulations.

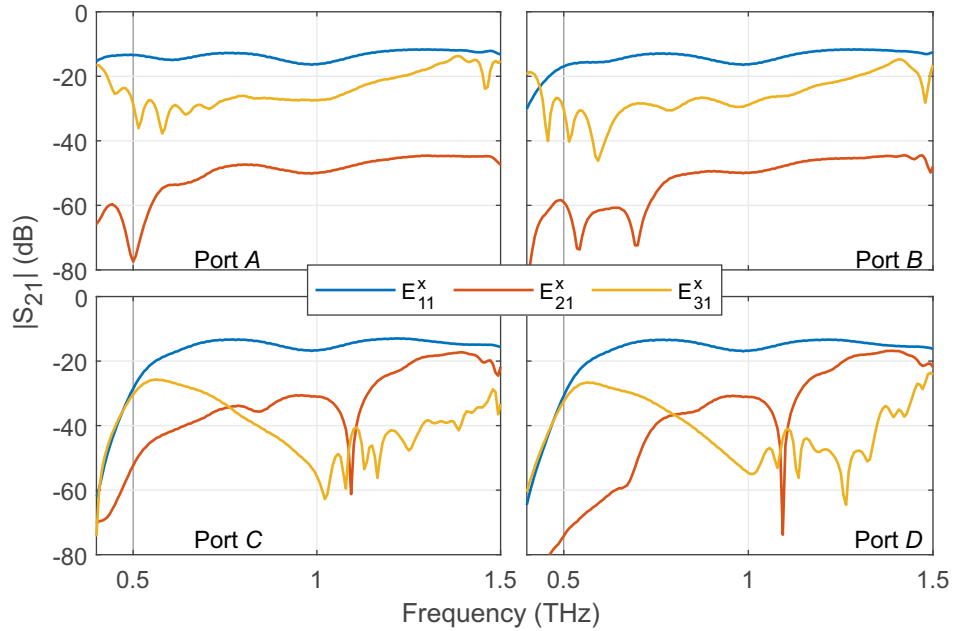


Figure 4.10.: Simulated transmission coefficient ($|S_{21}|$) of first three horizontal modes E_{11}^x , E_{21}^x and E_{31}^x with respect to the total power of the Gaussian beam at locations A , B , C and D . The simulated waveguides has Qz as substrate.

At the base of the waveguide taper A , we observe ~ -15 dB coupling efficiency of the Gaussian beam to the fundamental mode over the entire bandwidth under examination. Significant power is also

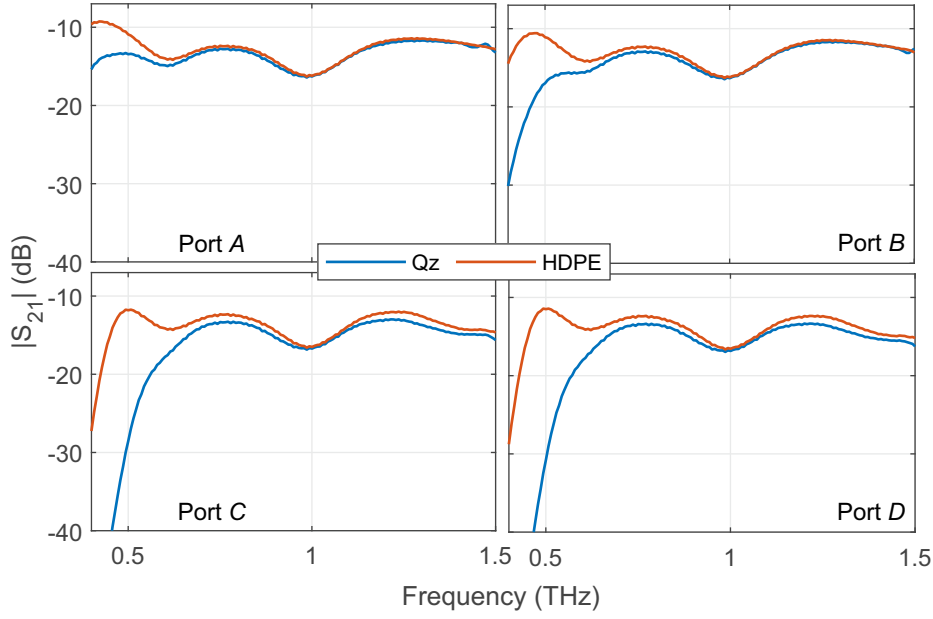


Figure 4.11.: Comparison of the simulated transmission coefficients of the E_{11}^x mode between substrates HDPE and Qz.

coupled to E_{31}^x mode at frequencies > 1.2 THz. As expected, the power coupled to the anti-symmetric E_{21}^x mode is at least 40 dB smaller than the fundamental mode. The straight section AB attenuates the E_{11}^x mode significantly below the cut-off frequency of 0.5 THz. The port at C shows significant increase in power coupled to E_{21}^x mode throughout the whole frequency range, whereas E_{31}^x mode significantly loses power. Above frequency 1.4 THz, a significant fraction of power from E_{11}^x mode is also coupled into the E_{21}^x mode due to the circular curvature at the bend. All modes undergo some attenuation in the straight section CD . Thus, the simulated waveguides are essentially operational in fundamental mode between 0.5 – 1.2 THz.

Plots in Fig. 4.11 shows a comparative transmission characteristics of the guided wave when the waveguides are supported by HDPE and Qz substrates. The port at A shows a higher coupling efficiency to E_{11}^x mode at lower frequencies due to the reduced effective permittivity of the propagating mode. At higher frequencies, the mode is fully confined within the $1000 \times 50 \mu\text{m}^2$ waveguide aperture and thus, the in-coupling efficiency does not significantly change. Modes at location B show lower attenuation in the case of HDPE substrate, as the lower cut-off frequency of E_{11}^x is ≈ 50 GHz lower than with Qz substrate. The bent-section BC remains practically unchanged irrespective of the waveguide substrate. The overall attenuation of the fundamental mode at D is lower for HDPE substrate than Qz, especially between 0.5 – 0.6 THz.

Figure 4.12(a) shows the power transmission between the Gaussian excitation and E_{11}^x mode at the end of the in-coupling taper, additionally through the sections AB , BC and CD for fundamental mode in the waveguides supported by HDPE substrate. The most significant losses (10 – 15 dB) occur at the in-coupling position. The other waveguide sections show negligible losses between 0.5 – 1.5 THz, with an exception of the circular bend above 1.2 THz, which leads to mode conversion to E_{21}^x . Figure 4.12(b) shows a comparison of the transmission efficiencies of the fundamental mode for Qz and HDPE substrates. Here too, the waveguide bend shows significantly higher losses for Qz substrate at lower frequencies, same for the attenuation in the straight sections.

Finally, to mitigate the inter-mode coupling at the waveguide bends, we employ a non-uniform,

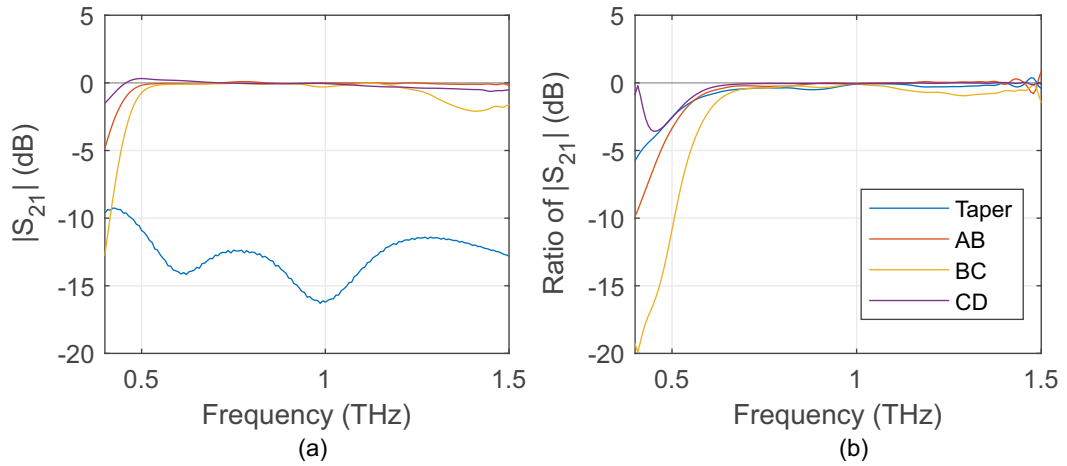


Figure 4.12.: (a) Simulated transmission coefficient through the individual waveguide sections shown in Fig. 4.4. The waveguides are supported by HDPE substrate and have circular bends. (b) Comparison of simulated losses between HDPE and Qz substrates. The ordinate shows the ratio of the simulated $|S_{21}|$ parameters between waveguides supported by Qz and HDPE substrates for each individual waveguide sections. HDPE substrate shows lower losses over the entire simulation frequency, especially at the lower end of the spectrum. Above 1.4 THz, the inaccuracies of the simulated band edges are amplified due the division of the S-parameters. The legend corresponds to both the plots (a) and (b).

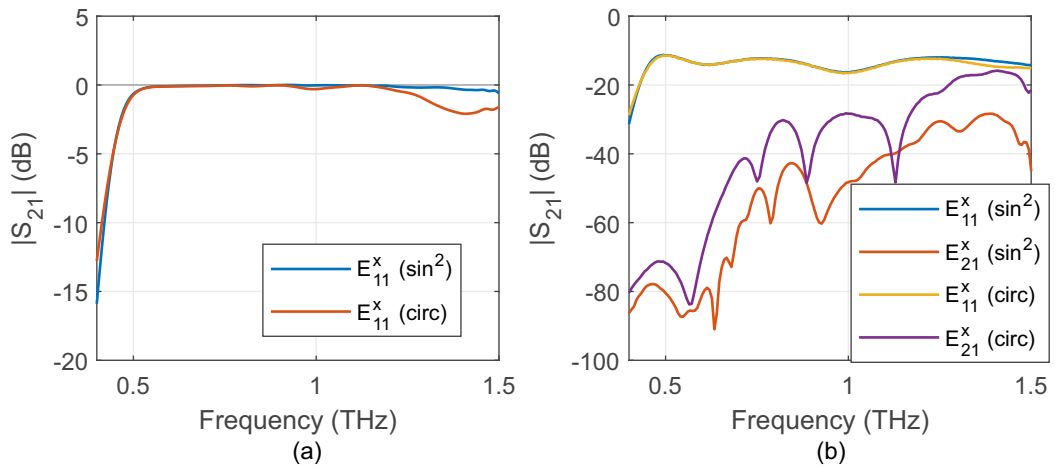


Figure 4.13.: (a) Comparison of the simulated transmission coefficient of E_{11}^x mode through circular and sine-squared 90° bends in segment BC. The bend radius for both the curvatures is 2 mm. HDPE substrate supports the waveguides. (b) Simulated E_{11}^x and E_{21}^x modes at location D. Sine-square bends suppress higher order mode generation significantly, thus extending the operational bandwidth of the waveguides to 0.5 – 1.5 THz.

sine-squared bend with identical effective bend radius as the circular bend. HDPE is used a substrate. Plot in Fig. 4.13(a) shows the transmission coefficient of E_{11}^x mode through BC. The power is not lost anymore above > 1.2 THz and the mode-conversion at the bend is suppressed until ≈ 1.5 THz. Figure 4.13(b) plots the simulated E_{11}^x and E_{21}^x modes for both the bend types at location D. For sine-squared

bend, the E_{21}^x mode is ≈ 20 dB smaller than the fundamental mode over the whole frequency range of 0.5 – 1.5 THz. Power coupled to higher order modes are even smaller. Thus, the operational bandwidth of the simulated waveguides is extended till 1.5 THz, albeit using an HDPE substrate and a non-uniform waveguide bend.

4.3.5. Splitters and couplers

Splitter/coupler structures are essential components in the 2-port PVNA architecture. The polariser based splitters in the free-space PVNA (see Fig. 3.1) are replaced by waveguide splitters in the integrated version. For narrowband systems, a multitude of splitter and coupler structures, like multimode interference (MMI) coupler, rat-race coupler, etc., are available in the literature, which use the interference of the propagating wave to split the power. However broadband solutions for bandwidths spanning over multiple octaves are hard to come by as interference-based methods cannot be applied. A wavelength-independent MMI coupler was reported by Maese-Novo *et al.* [153] based on sub-wavelength grating structures, but the bandwidth coverage is much lower than a complete octave. Only symmetric geometrical Y-shaped splitters feature an uniform broadband splitting ratio. Ideally, the designed splitters must have a 3-dB power splitting ratio into their two outputs. The output arms of the splitter should also feature very high isolation between them, ideally higher than 30 dB.

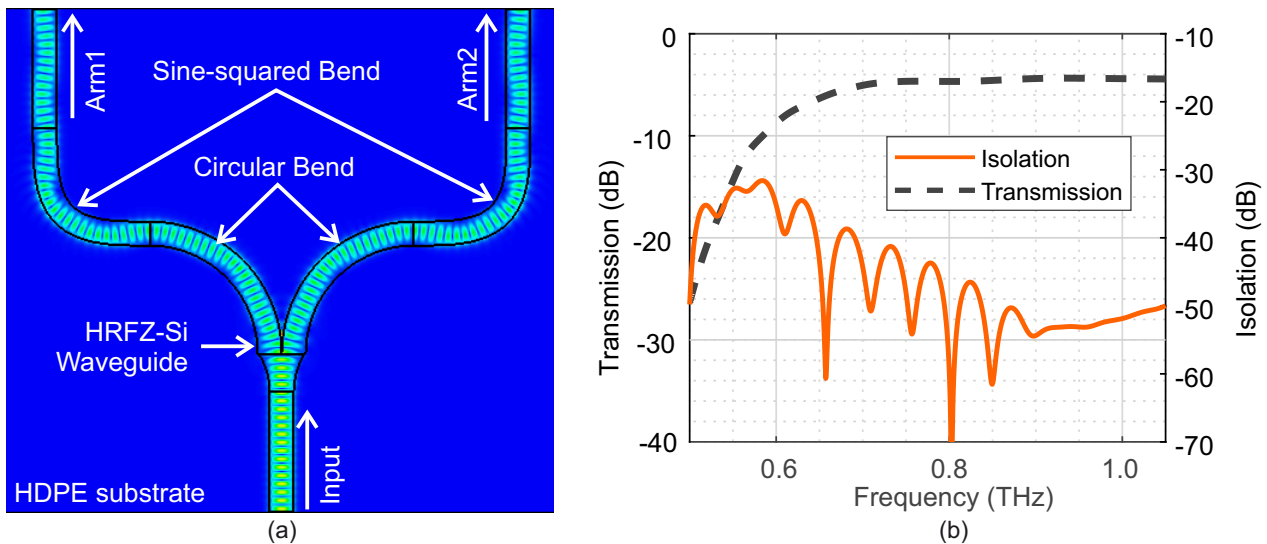


Figure 4.14.: (a) Simulated electric field propagation through a splitter structure at 1 THz. Mode mismatch is apparent at the junction of the circular and sine-squared bends. (b) Plot shows the simulated transmission between the input port and both the output arms. The isolation between *Arm1* and *Arm2* is minimum at 0.5 THz (≈ -30 dB). Adapted from [70].

Figure 4.14(a) shows one of the few simulated splitter designs. The designed structure uses a non-radiating taper to widen the HRFZ-Si waveguide from 200 μm to 400 μm to accommodate two symmetric S-shaped bends. These bends carry power to the two splitter outputs *Arm1* and *Arm2*. The bent section attached to the taper has a circular curvature so that the mode shift in the bend better matches the centrally located mode maxima of the taper. The second part of the bend is sine-squared to prevent further mode-conversions at higher frequencies. In contrast, an S-section with two sine-squared bends will have severe mode-mismatch at the splitting point, whereas two circular bends will result in mode-mismatch when the radius of the curvature flips from ρ_{wg} to $-\rho_{wg}$ in the middle of the S-section.

Nevertheless, the plot in Fig. 4.14(b) shows the simulated the insertion loss is ≈ 4 dB for both the output arms and the isolation is > 30 dB between them. At frequencies < 0.7 THz, significant power is lost due to radiation, predominantly at the junction between the taper and splitter arms. Also, the modal characteristics are distorted at the transition between the circular and the sine-squared bends. In hindsight, an offset attachment between the circular and the sine-squared curvature could have improved the mode overlap, however, offset-junctions always excites undesired reflected modes, especially at lower frequencies. Due to the structural symmetry and the reciprocity theorem, the splitter can also be used as a 3-dB coupler.

4.4. Fabrication

We fabricate the simulated waveguide structures out of 50 μm -thick double-side-polished HRFZ-Si wafers using either DRIE or laser ablation using a femtosecond laser. Even though HDPE is the preferable substrate for the waveguides, it is neither well-suited for the DRIE nor for laser ablation owing to its bad thermal conductivity and a relatively low melting point of ≈ 80 °C. Figure 4.15(a) shows a burnt HDPE substrate after the DRIE process. A 525 μm -thick Qz is instead used as the substrate during fabrication and the HRFZ-Si wafer is glued on the substrate wafer with a 5 – 9 μm thick layer of ethylcyanoacrylate adhesive, also commonly known as SuperGLUE™. Post fabrication, the adhesive layer is removed using Acetone, detaching the waveguide structures from the Qz underneath. These waveguides are subsequently manually transferred atop a HDPE substrate.

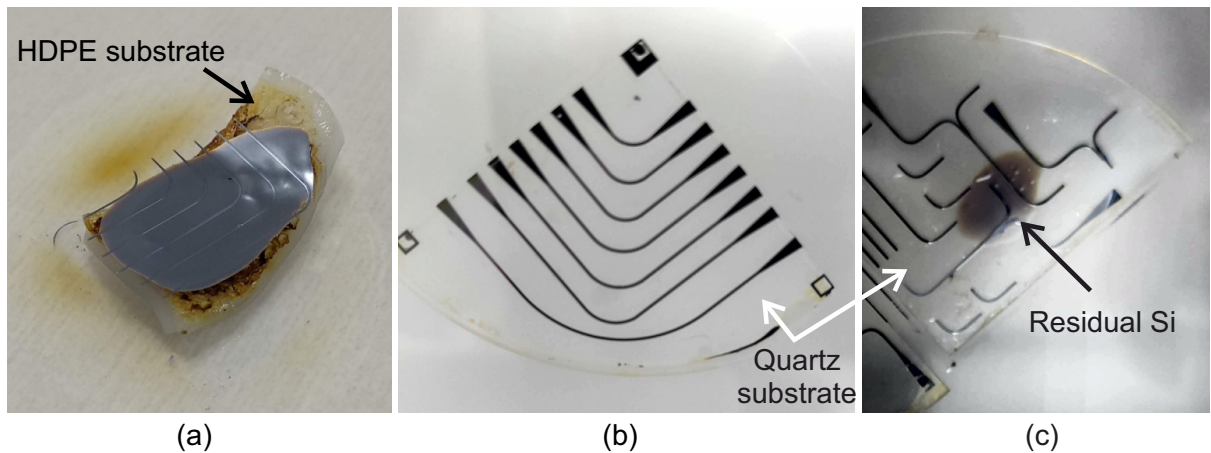


Figure 4.15.: Snapshots of the DRIE process. (a) A burnt HDPE substrate after etching. (b) A set of fabricated waveguides on Qz substrate. (c) Areas of residual silicon as a result of bad thermal contact with the substrate, most likely due to a bubble in the adhesive layer between HRFZ-Si and Qz.

The silicon wafers are etched at the Max Planck Institute for the Science of Light (MPL) in Erlangen Germany. First, a lithographically defined hard mask (~ 4 μm -thick hard-baked AZ® nLoF 2035) is created on top of the sample (HRFZ-Si wafer atop Qz substrate). The sample is then mounted on a larger 4-inch Alumina (AlOx) wafer using Fomblin® oil as the wafer clamp of the etching chamber is only suited for 4-inch wafers. The DRIE processes of silicon, also referred to as Bosch Process, involves repetitive deposition and etching cycles using inductively coupled plasmas (ICPs) of C_4F_8 and SF_6 . The chamber temperature whilst processing is maintained at -10 °C, wherein the cooling is done using a stream of liquefied nitrogen underneath the AlOx wafer. Figure 4.15(b) shows a set of etched

waveguides fabricated using this process. The etching selectivity of silicon is substantially higher than the hard-baked AZ® nLof 2035, such that a 2.9 μm layer of photoresist is sufficient for a 50 μm deep etch (≈ 4.5 μm photoresist for 180 μm thick silicon wafers). The etching rate is significantly slower if the silicon wafer is not cooled. Figure 4.15(c) shows an incompletely etched area of silicon resulting from bad heat dissipation, probably caused by a residual air bubble in the adhesive layer between the silicon and Qz substrate. Figure 4.15(c) also shows some of the fabricated structures, such as a splitter with a tapered arm for free-space in-coupling, waveguide bends, etc., that we later assemble to make the integrated PVNA. Detailed processing steps, along with process parameters are in Appendix A.5.

3-D Micromac UG, based in Chemnitz, Germany carried out the Laser ablation process. The difference between the two processes is the roughness of the waveguide side-walls. The side-wall roughness of the etched samples along the longitudinal direction (z -direction) is determined by the edge-roughness of the photolithographic hard-mask, which is a few hundreds of nanometres (see Fig. 4.1(b)). The vertical undulations resulting from repetitive etching and deposition cycles are in the order of a few tens of nanometres and are dependent on the duration of the etching and deposition steps. In contrast, side-wall roughness in all directions can be as low as tens of nanometres for laser ablation. Decreasing the ablating laser's power results in relatively smooth side-walls. Additionally, maintaining the stability of ablation process is easier than long DRIE runs (for e.g. etching ~ 200 μm thick silicon wafers). Apart from being inexpensive, etching a 50 μm HRFZ-Si wafer takes about half an hour, compared to ≈ 7 hours needed for laser ablation. Thus, we use DRIE as the preferred method of fabrication.

4.5. Characterisation

The fabricated waveguide structures are characterised using the homodyne CW setup depicted in Fig. 4.3(a). We calculate the transmission characteristics with respect to a reference measurement in the standard free-space CW setup (c.f. Fig. 1.2), where we assume that no transmission losses occur between the source and the receiver above 0.2 THz. Dividing by reference measurement also subdues setup related artefacts, such as standing waves at the silicon lenses or stray reflections arising from slightly misaligned optical components. The waveguides are only characterised between 0.4 – 1.05 THz due to the lack of DNR in the setup of Fig. 4.3(a) beyond these frequencies. We assumed a perfect alignment of the Gaussian beam to the in-coupling port of the waveguide during simulations, it is however extremely difficult to realise in practical setups. Additionally, we did not consider the losses caused by the cyanoacrylate adhesive layer between the waveguides and the substrate or the surface roughness of the waveguide walls in the simulated model. We therefore expect some deviation of the measured waveguide characteristics from the simulated values.

All the characterised waveguides in this section feature a 90° bend with various ROCs, have different lengths, but feature two non-radiating tapers of length 4 mm and an end-facet broadened to 1 mm. Figure 4.15(b) shows an exemplary set of waveguides supported by Qz substrate. Total losses measured in the setup using eqn. (4.4) have three principle components, namely coupling losses, radiation and mode-conversion losses at the bends and material losses throughout the guiding structure. Thus, eqn. (4.4) can be reformulated as

$$\begin{aligned}
 L_{tot,dB} &= 20 \log_{10}(|I_{wg}/I_{ref}|) \\
 &= 20 \log_{10}(|\eta_c^2 \eta_{tx} \eta_{90^\circ} I_{ref}/I_{ref}|) \\
 &= 40 \log_{10}(\eta_c) + 20 \log_{10}(\eta_{90^\circ}) - \alpha_E l_{wg} \cdot 20 \log_{10}(e),
 \end{aligned} \tag{4.11}$$

where $\eta_{tx} = \exp(-\alpha l_{wg})$ is the total material loss coefficient in a waveguide of length l_{wg} , α_E is the field attenuation constant, η_{90° is loss coefficient of the 90° bends and η_c is the coupling efficiency at

individual waveguide end-facets. To segregate individual losses, we calculate the material losses in transmission first, then the bend losses and finally get an estimate of the in-coupling losses. Note that the parameters, η_c^2 , α_E and η_{90° are frequency-dependent. Additionally, we ignore the scattering losses induced by surface roughness of the waveguides ($< 0.01\lambda_{THz}$ digs/sleeks) as they are insignificant compared to the three aforementioned propagation losses.

4.5.1. Transmission losses

As the mode confinement increases with increasing frequency, the attenuation constant of the guided mode approximates to a plane wave travelling through a purely dielectric, homogenous HRFZ-Si medium with a conductance of σ_{si} . Despite of having low material losses, at low design frequencies the propagating mode readily couples to the radiative modes with similar spatial field distribution and propagation constants at waveguide perturbations and power is lost. We measure the transmission losses using multiple waveguides with varying lengths but identical ROC, similar to the cut-back technique used for optical fibres [154]. The power absorption coefficient ($\alpha_{pow} = 2 \times \alpha_E$) is calculated using two waveguides with same ROC and coupling tapers but of lengths l_1 and l_2 as:

$$\alpha_{pow} = -\frac{2}{l_1 - l_2} \ln \left(\frac{I_1}{I_2} \right), \quad (4.12)$$

where I_1 and I_2 are the measured current at the receiver passing through the respective waveguides in the setup.

Six waveguides supported by Qz substrates, with ROC= 2 mm and lengths l_{wg} varying between 15 – 35 mm are characterized. Figure 4.16 shows an excellent agreement between the measured α_{pow} and the simulated values from sections *AB* and *CD* in Fig. 4.4. The discrepancies arise only below 0.47 THz, i.e., below the lower cut-off frequency of the fundamental mode. α_{pow} decreases from ≈ 8 dB/cm to 0.4 dB/cm between 0.5 – 0.65 THz. The oscillatory features above 0.9 THz can be attributed to standing waves in the waveguide cavity and the mode beating between the E_{11}^x and E_{21}^x modes [148] at the waveguide bend. Later in this chapter, we try to differentiate between these two phenomena, however, a clear distinction from just the transmission characteristics is impossible. The ethyl-cyanoacrylate adhesive ($\epsilon_r = 2.72$, $\tan \delta = 0.067$ at 1 THz [155], $\alpha_{pow} \approx 23 \text{ cm}^{-1}$) increases the measured absorption coefficient, especially at lower THz frequencies, where a significant amount of the guided power travels in the evanescent fields below the guiding structures. Using alternative, low-loss adhesives, for e.g., BCB or UV-Glue, instead of SuperGLUE™ can reduce this undesired, excess loss [42].

4.5.2. Bend losses

First, we characterize waveguides of length $l_{wg} = 19.14$ mm with circular curvatures to confirm the minimum bend radius required for broadband operation. The propagation through waveguides with bend radii of 1 (Q1), 2 (Q2), and 4 mm (Q4), placed on quartz, are compared. Since the waveguides are equally long, the total transmission losses only differ due to their bend radii. Figure 4.17 shows the total measured transmission losses for these waveguides. Total losses in a waveguide with larger ROC= 5 mm (Q5, $l_{wg} = 22.71$ mm) are also plotted for comparison.

The waveguide Q1 with ROC = 1 mm has 3 – 5 dB higher losses over the measured frequency range than the rest. This is expected as both the radiation and mode conversion losses are higher for a smaller bend radius. Q2, Q4 and Q5 have similar losses between 0.55 – 0.9 THz, indicating negligible power is lost due to radiation. At frequencies > 0.9 THz, we start seeing the onset of mode/conversion losses

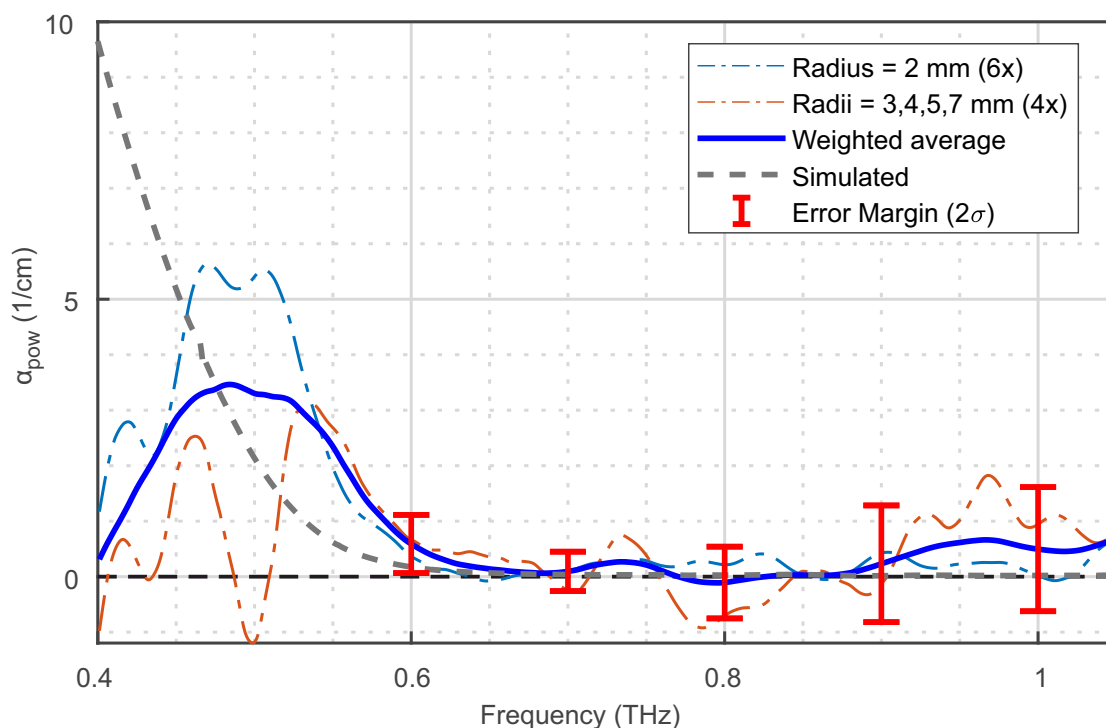


Figure 4.16.: Measured power absorption coefficient in cm^{-1} for the HRFZ-Si waveguides on Qz substrate. The weighted average data shows good agreement with the simulated data between 0.6 – 0.9 THz. At higher frequencies, possible mode conversions and standing waves deteriorate the data quality, however, the simulated absorption coefficient is within the $2 \times \sigma$ error margin of the measured values. Adapted from [70].

in Q2 (ROC= 2 mm) as the total losses increase with respect to waveguides with larger bend radii. Compared to the simulations, the measured total losses in Q2 are higher and the onset of coupling losses in Q2 occur at a lower frequency. The increased surface scattering due to the sidewall roughness can explain these losses, however, a more significant contributor is the adhesive between HRFZ-Si waveguide and Qz. Measured losses in waveguides with ROC between 6 – 10 mm show similar losses as Q4 and Q5. Thus, a 4 mm bend-radius is sufficient to have minimal radiation and mode-coupling losses at the circular bends.

We now place Q1 atop a HDPE substrate, measure the transmission losses and plot it in Fig. 4.17. Two interesting observations are as follows:

1. The lower cut-off frequency decreases to ≈ 0.45 THz due to the lower permittivity of HDPE. This is also evident in the simulations (see Fig. 4.11).
2. The total transmission losses are reduced by 5 – 7 dB compared to the waveguides on Qz over the whole frequency range. This is unexpected as the simulations predict only ~ 1 dB improvement. The SuperGLUE™ between the waveguides and the Qz substrate is 5 – 9 μm thick, whereas the waveguides are fixed on HDPE substrate using minimal SuperGLUE™. It emphasises that the excess loss in Qz-supported waveguides stems from the ethylcyanoacrylate adhesive, which is highly absorptive at THz frequencies.

We leap-frog here a bit and characterise the waveguides featuring sine-squared bends using a different receiver configuration, discussed later in chapter 5. The total losses of this new configuration

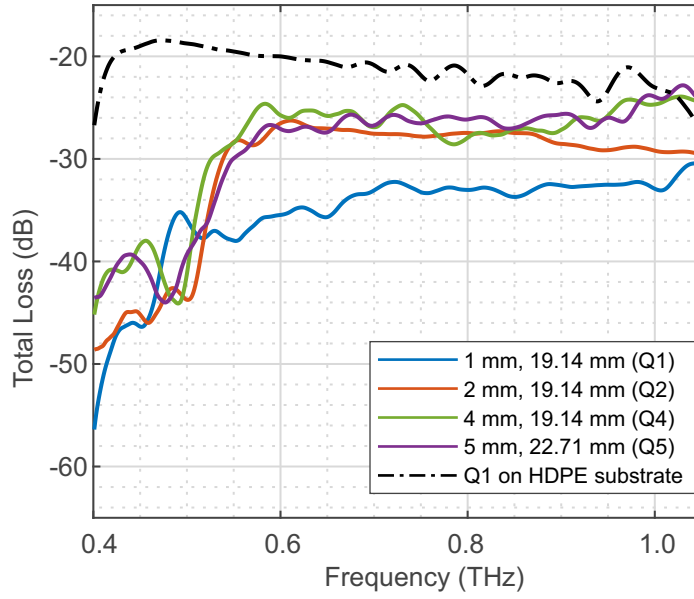


Figure 4.17.: Measured total transmission losses in waveguides with various bend radii between 1 – 5 mm supported by Qz substrate. A 19.14 mm long waveguide with ROC= 1 mm on HDPE substrate (dashed-dotted line) show significantly lower transmission losses than the waveguides on Qz.

is significantly lower than the free-space coupling case and the transmission characteristics look different than in Fig. 4.17. Figure 4.18 shows total transmission of three waveguides with sine-squared bends $H1$ ($A = 0.78$ mm, $l_{wg} = 16.63$ mm), $H2$ ($A = 1.54$ mm, $l_{wg} = 24.69$ mm) and $H3$ ($A = 2.35$ mm, $l_{wg} = 31.26$ mm) placed on HDPE substrate. Higher transmission losses for larger waveguide lengths is especially emphasised at lower frequencies. Above 0.9 THz, $H1$ starts showing $\approx 5 - 10$ dB mode coupling losses.

The purple plot compares the total losses in $H2$ and a waveguide with circular bend $C1$, but the same effective bend radius and waveguide length and in-coupling taper, measured with the directly coupled receiver. The excess losses in circular bend are ≈ 4 dB compared to the sine-squared curvature at 0.6 THz and become similar at ≈ 1 THz. The oscillatory artefacts above 0.9 THz likely stem from mode-conversions in the circular waveguide curvature. However, the visible but unexpected oscillations in the transmission characteristics of $H2$ are due to the antenna characteristics of the directly-coupled receiver (elaborated in the next chapter). To compare the suppressed mode-conversion in a sine-squared bend compared to a circular curvature, we need significant measurement DNR above 1.2 THz, which is unavailable in the measurement setup shown in Fig. 4.3(a). Additionally, explicit calculation of bend losses per 90° turn (η_{90°) requires a comparison of waveguides with a single bend and multiple bends. In chapter 6, we assemble a semi-integrated PVNA using the demonstrated waveguide architecture with operational range up to ≈ 1.5 THz and conduct these two characterisations. The results are available in appendix A.4.

Although the waveguides $H1$, $H2$, $H3$ and $C1$ have different ROCs, comparing their transmission losses gives an estimate of the power absorption coefficient of the waveguides with HDPE substrate. Between 0.45 – 0.6 THz, the losses in HDPE-supported waveguides significantly reduces to 0.6 – 1.7 dB/cm compared to the 4 – 20 dB/cm losses for the Qz substrate. At higher frequencies, the power absorption coefficient in waveguides featuring both the substrates are similar, as the guided power travelling in

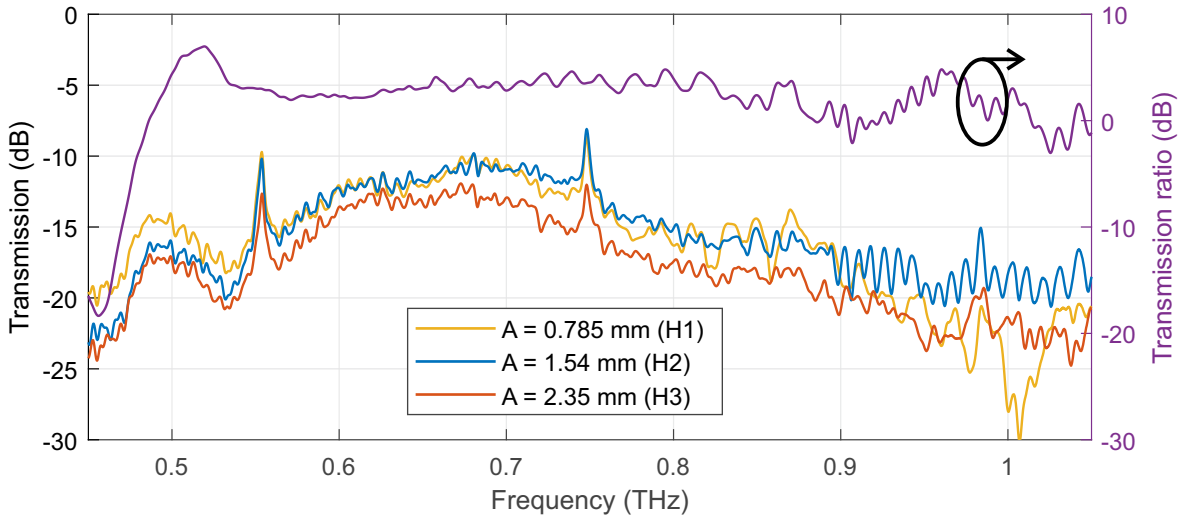


Figure 4.18.: The measured total loss in waveguides with sine-squared bends with scaling factors $A = \pi/4, \pi/2$ and $3\pi/4$ mm, where the waveguides are 16.63, 24.69, 31.26 mm long, respectively, supported by HDPE substrate. The purple plot shows the gain of sine-squared bends over a circular bend of identical effective radii $\tilde{\rho}_{wg} = 1.71$ mm. The peaks in the plots occur at the locations of the waterlines and are normalisation artefacts.

the evanescent fields decreases from $\approx 50\%$ at 0.5 THz to $\approx 8\%$ at 1 THz and is minimally affected by the losses induced by the substrates and adhesives.

4.5.3. Coupling losses

The transmission and bend losses in the waveguide architecture are negligible within the operational bandwidth with respect to the total losses measured in the setup. The mode-mismatch at the two in- and out-coupling end-facets between the guided mode and the free-space Gaussian beam contribute almost entirely to the measured losses. Figure 4.19 shows a comparison of the total expected coupling losses from the simulations with the measured total loss of 19.14 mm long waveguide with 2 mm bend radius (Q2). The total coupling loss at two positions is between 28 – 30 dB over the entire range of 0.4 – 1.05 THz! Using HDPE substrate reduces the coupling losses to 18 – 26 dB (see Fig. 4.17) due to better mode-matching with the Gaussian beam, however, such losses are unacceptable in high DNR systems and significantly limits their operational range. As already mentioned, we show a direct coupling technique using an end-fire VA in the next chapter, which reduces the coupling losses to just ≈ 2 dB at its best operating point.

4.5.4. Dispersion

As discussed in section 2.1.5, the dispersion factor D in eqn. (2.56) reads as

$$D = \frac{f_{THz}^2}{2\pi c_0} \cdot \frac{d^2 \beta_g}{df_{THz}^2}, \quad (4.13)$$

where β_g is the propagation constant of the guided mode, ω is the angular frequency and c_0 is the speed of light in vacuum. The dispersion induced by the HRFZ-Si waveguide of length l_{wg} in the

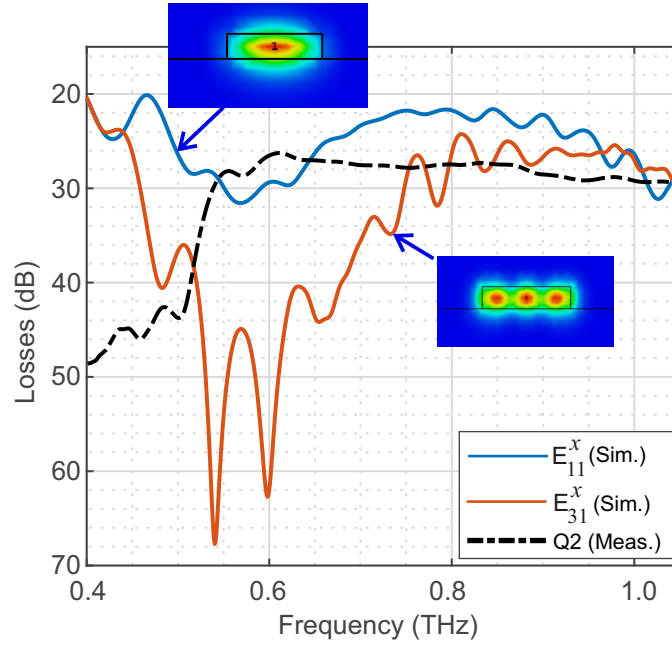


Figure 4.19.: Comparison of the total measured losses in a 19.14 mm long waveguide with the simulated coupling losses between the free-space Gaussian beam to E_{11}^x and E_{31}^x modes at two coupling positions. Almost all of the propagation losses stem from inefficient in- and out-coupling in the waveguides.

measurement setup can be calculated from the phase of the detected THz field Φ at the receiver. The total accumulated phase shift in the setup equates to

$$\Phi = \beta_g l_{wg} + \beta_0 l_{fs} + \beta_{fibre} l_{fibre} + \phi_{ant}(f_{THz}) + \phi_0, \quad (4.14)$$

where $\beta_0 = 2\pi f_{THz}/c_0$ is the free-space propagation constant and l_{fs} is free-space distance travelled by the THz wave, ϕ_{ant} is an additional phase change induced by the emitting and receiving antennas [97] and ϕ_0 is an arbitrary constant. The phase of the reference signal (Φ_{ref}) without the waveguide reads

$$\Phi_{ref} = \beta_0 l'_{fs} + \beta_{fibre} l_{fibre} + \phi_{ant}(f_{THz}) + \phi'_0, \quad (4.15)$$

where ϕ'_0 is another constant and l'_{fs} is the free space propagation length of the reference measurement. Second order derivatives of Φ_{ref} and Φ with respect to frequency f_{THz} read as,

$$\frac{d^2 \Phi_{ref}}{df_{THz}^2} = \frac{d^2 \phi_{ant}}{df_{THz}^2} \text{ and} \quad (4.16)$$

$$\frac{d^2 \Phi}{df_{THz}^2} = \frac{d^2 \beta_g}{df_{THz}^2} l_{wg} + \frac{d^2 \phi_{ant}}{df_{THz}^2}. \quad (4.17)$$

Subtracting eqn. (4.16) from (4.17) removes the dispersion caused by the antennas and subsequently, the dispersion factor in eqn. (4.13) modifies to

$$D = \frac{f_{THz}^2}{2\pi c_0} \cdot \frac{1}{l_{wg}} \frac{\partial^2}{\partial f_{THz}^2} \left(\Phi - \Phi_{ref} \right). \quad (4.18)$$

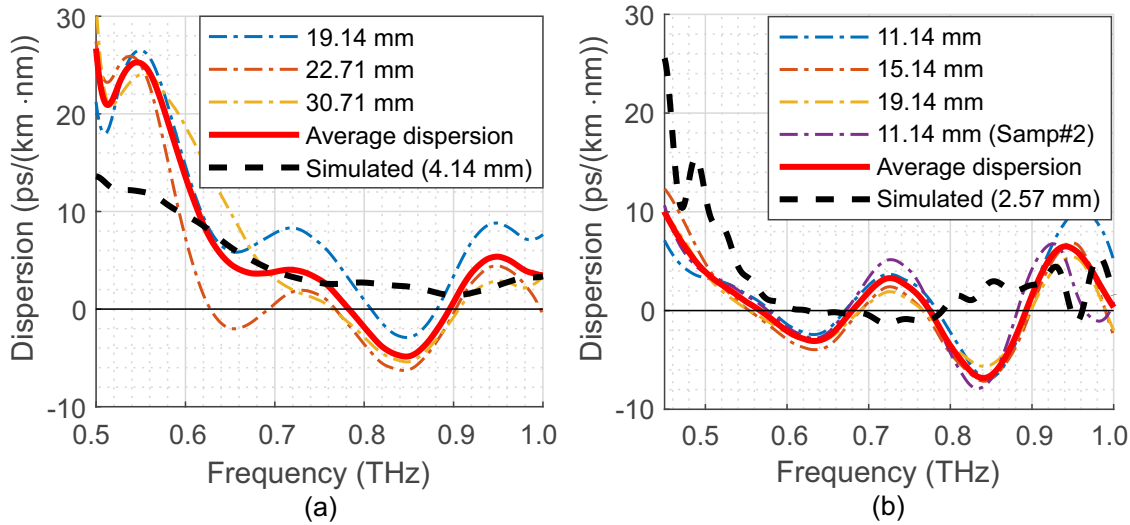


Figure 4.20.: (a) and (b) show measured dispersion in waveguides of different lengths as indicated in the legend but same radius of curvature, placed on Qz and HDPE substrate, respectively. The bends radius of measured and simulated waveguides in (a) is 2 mm. The waveguides in (b) have a bend radius of 1 mm. Adapted from [70].

The measured dispersion factor for waveguides on Qz and HDPE substrates are shown in fig. 4.20(a) and (b), respectively. The dispersion factors are in the same order of magnitude as the expected values from simulation and show the same frequency-dependent trend. The source of the oscillatory pattern in the measured data, present over the whole investigated frequency range, cannot be ascertained. Likely causes can be the standing waves in the waveguides or the temperature-controlled frequency tuning of the DFB lasers, where the offset between the set (read) and the actual frequency is non-uniform throughout the scan. The chromatic dispersion in the presented dielectric waveguides results in undesired pulse broadening when used in pulsed-THz systems. However, dispersion compensation by controlled mode-conversion among the guided modes [73], adding slits into the waveguide (slotted waveguides) [156] or utilising photonic-crystal structures [157], can extend their applicability in pulsed-THz systems. Dispersion effects can be compensated in CW systems by normalizing it to a reference measurement in post-processing.

4.5.5. The splitter/coupler structure

Figure 4.21 shows the measured transmission through the 3-dB coupler/splitter simulated in Fig. 4.14. The effective bend radii of both the circular and the sine-squared bends are 1 mm. The measured splitter is supported by a Qz substrate. The measured data is normalised to those with a waveguide of same length and bend radius to compensate for the transmission and coupling losses. The two arms of the splitter feature similar insertion losses of 4.8 – 6 dB above 0.6 THz, which is in excellent agreement with the simulated transmission losses.

The measured losses below 0.6 THz are lower than the simulated values due to the normalisation methodology. Unlike the simulated data, which is not normalised, the normalising factor of the measured data already incorporates a waveguide bend which cancels out the excess losses at the splitter bends. The undulating transmission characteristics above 0.85 THz is a result of mode-conversion between first two E_{pq}^x modes, enforced by the small ROC of 1 mm. A larger bend radius would suppress

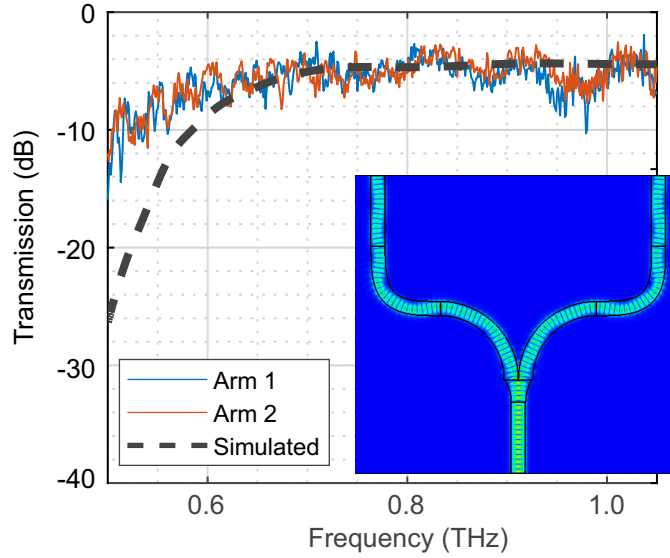


Figure 4.21.: Measured transmission through both the splitter output-arms shows good agreement with the simulated data. The mismatch at the lower frequencies is a normalisation artefact. The oscillatory features at frequencies > 0.85 THz are due to mode-conversion losses, occurring at the waveguide bend because of lower than optimal ROC. Adapted from [70].

such mode conversions. The verification of the simulated isolation is not possible as the system DNR is smaller than the expected isolation between the two arms. We only measure noise in one arm when the other arm is excited by the Gaussian beam, pointing to sufficient isolation between the output arms of the splitter within the available DNR.

4.5.6. Higher order modes and standing waves

We have already established in section 1.1.1 that in a homodyne system, the optical path travelled by a THz signal can be evaluated from the phase of the receiver current. For the waveguide measurement setup in Fig. 4.3(a), the delay at the receiver is only influenced by the velocity of guided modes in the waveguide as the physical path length is constant. This delay t_0 is the sum of the free-space delay t_{FS} and the waveguide delay t_{wg} components and reads

$$t_0 = t_{FS} + t_{wg} = t_{FS} + \frac{l_{wg}}{c_0/\sqrt{\epsilon_{pq}}}, \quad (4.19)$$

where the waveguide is l_{wg} long and ϵ_{pq} is the effective relative permittivity of the pq^{th} propagating mode. The fundamental mode has the largest permittivity amongst all guided modes (see Fig. 4.5). Thus, the power coupled to HOMS will reach the receiver at a smaller delay than the fundamental mode. In contrast, standing waves (SW) are generated due to the repetitive reflections at the waveguide end-facets and these reflected signals reach the receiver after the fundamental mode. Such time delays can be appropriately visualized by transforming the recorded signals into the time-domain.

The plot in Fig. 4.22(a) shows the time-domain plot of the reference signal. Only a clear main peak is visible. Plots 4.22(b-f) correspond to the time-domain signal of waveguides tabulated in Table 4.1, showing much feature-rich traces. We first note that the dispersion of the signal in waveguide is

Table 4.1.: Parameters corresponding to waveguides plotted in Fig. 4.22. The equivalent time-domain THz pulse in Fig. 4.22(a) corresponds to a frequency scan between 0.3 – 1.2 THz.

Notation	W1	W2	W3	W4
Length (mm)	19.14 ± 0.5	19.14 ± 0.5	22.71 ± 0.5	19.14 ± 0.5
ROC (mm)	1.0	2.0	3.0	4.0
$t_{0,FM}$ (ns)	2.435	2.426	2.464	2.426

evident by the broadening of the time-domain pulses compared to the reference pulse in Fig. 4.22(a). Figures 4.22(b) and (d) show first set of measurements using W1 and W2 respectively. The peaks before the main peak, at a delay < 2.43 ns, indicate the presence of HOMs in the received signal. All characterised waveguides with ROC = 1 mm show this feature, indicating that mode conversion occurs at the bent section. A repeated measurement of W2 with better alignment to the Gaussian beam shows an insignificant HOM excitation (cf. Fig 4.22(c)). In waveguides with larger ROC in plots of 4.22(e-f), the power propagating in HOM is significantly smaller than the fundamental mode. However, copies of the signal arrive at the receiver after the main peak. This indicates the presence of standing waves in the waveguide structure.

The optical path length difference Δd_{total} of 11.4 mm is calculated from the excess delay between the main peaks of W3 and W2, whereas the physical length difference is 3.57 mm. Considering the measurement inaccuracies of the physical waveguide lengths, the Δd_{total} corresponds to an effective RI of the E_{11}^x mode of $\sqrt{\epsilon_{11}} = 3.19 \pm 0.4$, averaged over the measurement frequency range. This is slightly higher than the simulated average refractive index of the E_{11}^x mode and most likely caused by the layer of SuperGLUE™. We note that the undesired HOMs or standing waves can be highly attenuated with adequate data-processing demonstrated in section 3.2, however, the power coupled to these artefacts will also be lost, lowering the DNR of the measurement system.

In summary, we designed, simulated and measured the broadband characteristics of the HRFZ-Si-based dielectric waveguide architecture between 0.4 – 1.05 THz in a free-space CW setup. When supported by a Qz substrate, the HRFZ-Si waveguides show very low attenuation constant < 0.4 dB/cm between 0.65 – 0.9 THz. At higher frequencies, HOMs and standing waves reduce the accuracy of measurements, however, a very pessimistic upper limit of 1.7 dB/cm can be ascertained. In comparison, RHM waveguides have losses between 1.35 – 1.92 dB/cm between 0.75 – 1.1 THz [33], dielectric ribbon structures feature 0.087 dB/cm losses between 0.1 – 0.14 THz [53], losses in suspended HRFZ-Si waveguides are 0.04 – 0.1 dB/cm between 0.55 – 0.75 THz [54], [55], waveguides based on photonic crystal structures lose < 0.1 dB/cm between 0.324 – 0.361 THz [158] and 0.05 – 1 dB/cm between 0.08 – 0.15 THz [56], [58], [59] and polymer fibres feature the lowest losses < 0.01 dB/cm over 0.32 – 0.35 THz [159]. A comprehensive review of the other state-of-the-art waveguide architecture for THz operations can be found elsewhere [160]. To my knowledge, most of the waveguide architectures in the literature operate in their single-mode regime, over a bandwidth of 0.2 THz or smaller. In contrast, we have demonstrated the unimpeded functionality of the HRFZ-Si-based waveguides over a frequency range between 0.5 – 1.05 THz here, and upto 1.5 THz in later chapters, albeit in overmoded configuration and with slightly higher propagation losses. The ROC for circular bends must be larger than ≈ 2 mm to fully suppress radiation losses and significantly reduce the mode-conversion losses. Bend radii of 4 mm and above show negligible bend-related loss ($\eta_{90^\circ} \rightarrow 0$). The simulated non-circular, sine-squared bends preserve the mode features better than the circular bends with similar bend radius. HDPE substrates and less SuperGLUE™ reduce the losses significantly compared to the Qz-supported

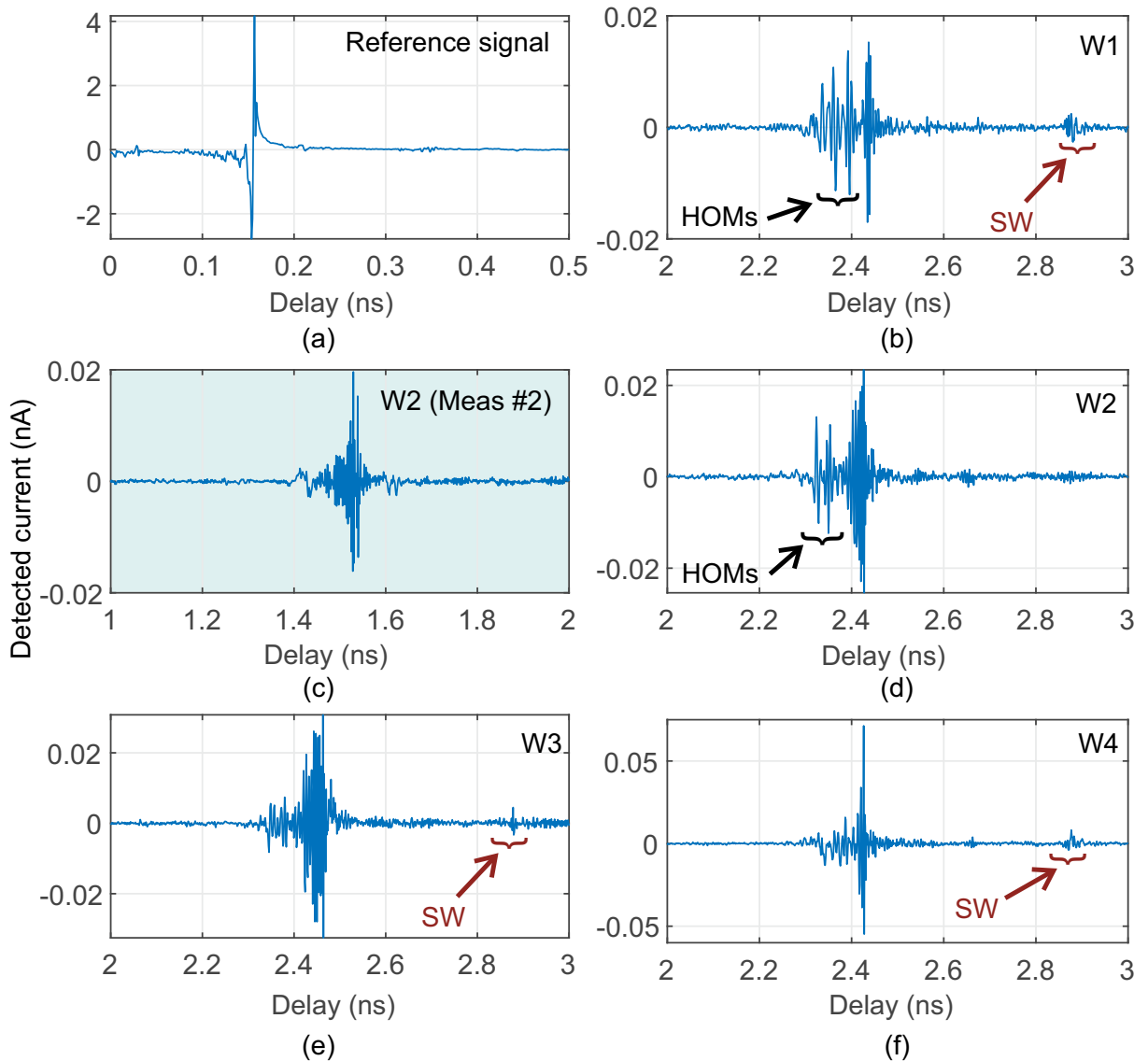


Figure 4.22.: Plot in (a) shows the measured equivalent reference signal in time-domain, plots (b)-(f) show measured time-domain plots of the transmitted signal through the waveguides as described in the text. Measurements shown in Fig. (a)-(b) and (d)-(f) are from the same setup, whereas (c) is measured with an altered optical fibre of the receiver and hence the main peak delay is smaller than the other plots. Adapted from [70].

waveguides and decrease the lower cut-off frequency of E_{11}^x mode to ≈ 0.45 THz and even, significantly lower the attenuation constant to $0.6 - 1.7$ dB/cm between $0.45 - 0.6$ THz. The total free-space in- and out-coupling losses are very high (~ 25 dBs). In the next chapter, we tackle the coupling problem by using an end-fire Vivaldi antenna directly at the end of the waveguide.

5. Active Devices

The realization of low loss transitions between sources, receivers and other electronic integrated circuits and the waveguides presents a significant challenge. In narrow band systems (bandwidths $< 50\%$ of the centre frequency), where insignificant changes in waveguide parameters allow for an almost perfect impedance and mode field diameter matching with losses < 1 dB [161], a plethora of resonant coupling structures are available in the literature. However, a broadband transition/matching structure with bandwidths over several frequency octaves is difficult to achieve. For instance, the guided modes in HRFZ-Si waveguides have frequency-dependent permittivity (see Fig. 4.5), consequently, a frequency-dependent phase velocity. Hence, any broadband topology cannot use low-loss resonant elements. A compromise between acceptable losses and achievable bandwidth is made while designing broadband transitions. DRW antennas, essentially a rectangular waveguide with a sharpened tip (ideally tapered on both axes) [162]–[164], present a broadband solution to the coupling problem. Figure 5.1(a) shows a planar DRW antenna-coupled dielectric waveguide. Although being compatible with the dielectric waveguide topology and possessing a radially symmetric radiated mode, the optimum coupling position is strongly frequency-dependent, i.e., the higher frequencies are emitted at the tip, whereas lower frequencies are radiated rather close to the base of the taper. This complicates in-coupling with fixed lenses as the focus of the free-space Gaussian beam is approximately static and its Rayleigh length is much smaller than taper. On a side note, Axicons can generate Gaussian beams with significantly larger Rayleigh length than typical TPX lenses [165] but these are beyond the scope of this thesis.

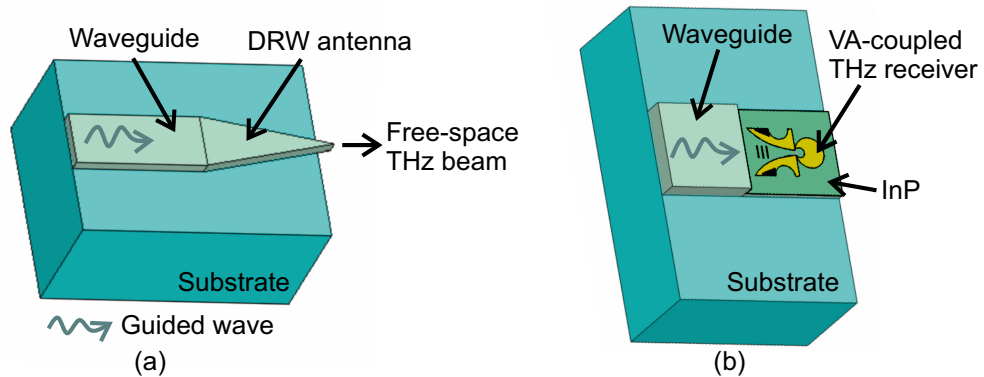


Figure 5.1.: (a) The dielectric waveguide is attached to a DRW antenna for free-space out-coupling to a silicon lens-coupled THz receiver. The DRW antenna is realised by tapering down the waveguide along its horizontal dimension [162]. (b) An endfire Vivaldi antenna-coupled THz receiver is placed directly at the end of the dielectric waveguide for direct out-coupling of the guided power into the active device. The receiver acts as an extension of the waveguide, as the refractive index of its indium phosphide substrate is similar to HRFZ-Si.

In this chapter, we implement a pseudo-near-field coupling scheme at the receiver using planar, endfire VAs. Since the InP substrate of the receivers has similar permittivity ($\epsilon_{r,InP} \approx 12$) as the

silicon waveguides ($\epsilon_{r,Si} \approx 11.7$) in the THz range, we attempt to create an extension of the waveguide using InP with the antenna placed centrally within a high-dielectric material. Figure 5.1(b) shows the coupling scheme using such VAs. Simply put, the antenna is situated within the waveguide and is designed to couple maximum power to the fundamental guided mode of the waveguide. Additionally, this scheme does not necessitate bulky optical components such as lenses, parabolic mirrors and silicon-lenses, typically used in table-top THz sources and receivers. This eases integration and miniaturisation of THz setups, facilitating the assembly of a broadband PVNA. VAs are frequency-independent within the operation range [111], i.e., their beam pattern and impedance theoretically does not alter with frequency and hence, are suitable for broadband operation. The operating frequency range of the VA is altered simply by scaling the antenna dimensions. The ErAs:In(Al)GaAs photoconductor with finger-like electrodes is placed at the base of the antenna. Henceforth, we refer to the entire VA-coupled photoconductor fabricated atop InP substrate as the *active device*. We primarily use these active devices as receivers in this thesis, however, considering the ease of simulation and antenna reciprocity, coupling characteristics to the waveguides are simulated considering the antenna-coupled active devices as THz sources. We have published the antenna designs and characterisations presented in this chapter in [72], [166], whereas the direct coupling mechanism is reported in our publication [70].

5.1. Vivaldi antennas

VAs are travelling-wave antennas of the surface-wave kind [167], i.e., the antennas have endfire characteristics. In contrast, the log-periodic antennas used in THz receivers for free-space PVNA are travelling wave antennas that feature broadside characteristics. Intuitively, travelling-wave antennas can be considered as radiating waveguide structures. The EM power gradually leaks out into the surrounding medium as the wave propagates through the antenna away from the antenna feed and the distance between the antenna arms d_{gap} increases (see Fig. 2.8). For a minuscule gap between the antenna arms ($d_{gap} \ll \lambda/4$), the electric field is well-confined within the antenna structures and guided away from the source. With the increasing gap between the antenna arms, the travelling wave becomes loosely coupled to the antenna and the guided power gradually couples into free-space radiative modes. In a lossless environment, all the guided power is eventually radiated. When $d_{gap} > \lambda$, the antenna structure cannot sustain any guided mode. The *phase-centre* of the antenna is defined as the location where the maximum power is radiated. Usually, for centrosymmetric designs such as log-periodic antennas, the phase centres are located at the geometric centre of the antenna. In contrast, the phase-centre in axially-symmetric VAs lies on the axis of symmetry, usually located when the slot width is $\approx \lambda/2$. However, in VAs, the phase-centres of the radiated electric and magnetic fields do not vary identically with frequency [168]–[170], and hence, the exact location of the phase-centre is disputed in literature.

5.1.1. Base design and endfire characteristics

Figure 5.2(a) shows the base design of a VA, which we use extensively in this thesis for integration of the active devices to the waveguides. The antenna features an exponentially tapered slot which radiates the THz field generated by the ErAs:In(Al)GaAs photoconductor situated at the port. The exponential taper function reads as,

$$y(x) = \pm y_0 \exp(\varsigma x), \quad (5.1)$$

where y_0 is a constant and ς is called the *taper-factor*.

Now, if we change x additively by x_0 , exponential taper changes in eqn. (5.1) to,

$$\begin{aligned} y(x + x_0) &= \pm y_0 \exp(\varsigma[x + x_0]) \\ &= \pm \exp(\varsigma x_0) \cdot y_0 \exp(\varsigma x) \\ &= \pm \exp(\varsigma x_0) \cdot y(x). \end{aligned} \quad (5.2)$$

Comparing with eqn. (2.84), we can write $C = x_0$ and $K = \exp(\varsigma x_0) = \exp(\varsigma C)$. Although K is a function of C , both K and C are independent of absolute dimensions x and y , thus satisfying the necessary *angle principle* for frequency independence (see section 2.3.2). Moreover, the surface current of antenna decays to zero when $x \rightarrow \infty$ [171] and with increment in frequency, the exponential taper approaches a limiting form $y = \pm y_0 \rightarrow 0$, hence also satisfying the *truncation principle*. In practice, the VAs are truncated at a non-zero y_0 corresponding to the quarter wavelength of the maximum design frequency, i.e., $f_{max} = c_0/(4y_0\sqrt{\epsilon_{eff}})$, where $c_0/\sqrt{\epsilon_{eff}}$ is the phase velocity of radiated waves. Similarly, the largest opening taper Y determines the minimum design frequency as $f_{min} = c_0/(4Y\sqrt{\epsilon_{eff}})$.

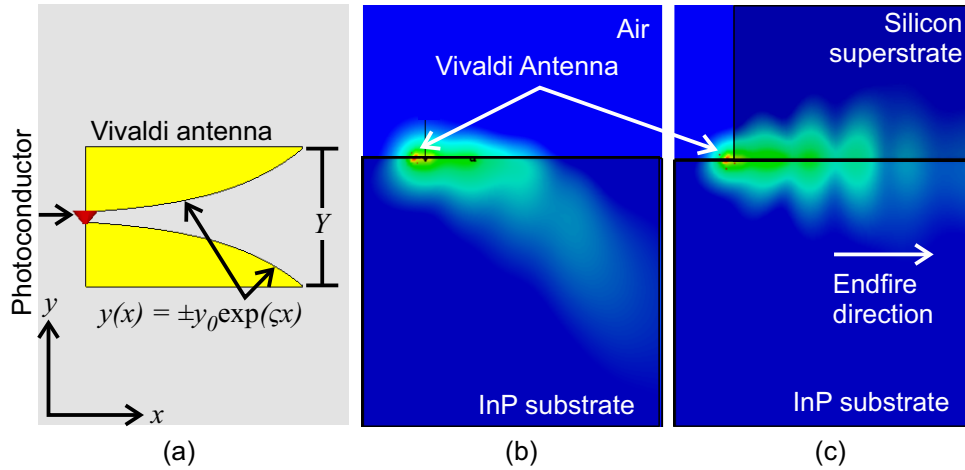


Figure 5.2.: (a) Schematic of the basic design of a VA. The red triangle shows the position of the active device. (b) A CST® microwave studio simulation of power leakage into the InP substrate during the antenna operation due to its lower wave impedance. (c) Simulated endfire characteristics of the VA are restored by adding a HRFZ-Si superstrate atop the antenna. Simulation snapshots are taken at 1 THz.

The taper-factor ς determines the rate of decay of the surface current along the direction of the travelling wave and acts as an optimisation parameter between the broadband radiation characteristics and antenna directivity at a certain design frequency [167]. For $\varsigma \rightarrow 0$, the exponentially-tapered slot approximates to a linear taper $y'(x) \approx \pm[y_0 + y_0x]$ and the slot tapers out gradually. Consequently, the radiative aperture of the VA for the design frequency is elongated, resulting in narrower main-lobe width due to the Fourier relationship between the antenna aperture and farfield distribution. Thus, VAs with linear tapers of lengths $6 - 8\lambda$ are highly directive. However, as $y'(x)$ does not fulfil the angle principle, the antennas are not frequency-independent [167]. In contrast, a large ς results in a comparatively low directivity but a larger radiating bandwidth. P. J. Gibson, in one of the first demonstrations of the exponentially-tapered Vivaldi aerial, showed ≈ 10 dBi gain over a bandwidth of 2 – 40 GHz [172]. The addition of an antenna substrate increases the directivity of the VAs [167]. The substrate thickness must also be smaller than the effective half-wavelength of the design frequency to maintain the endfire characteristics of the antenna.

In this thesis, the ErAs:In(Al)GaAs photoconductor is supported by an InP substrate and the planar VAs are fabricated atop the substrate. Thus, the guided wave from the VA is radiated along the air–InP interface, resulting in a significant power leakage into the substrate as it offers a lower impedance path than air or the air–InP interface. Figure 5.2(b) simulates such a leaky configuration where the endfire characteristic of the antenna is lost. In Fig. 5.2(c), a HRFZ-Si superstrate is employed to equalise the permittivity difference between the top and bottom media of the antenna. Subsequently, the endfire radiation direction is restored.

Figure 5.3(a) plots the performance comparison of the VA with superstrate and log-periodic antennas [97], with and without silicon lenses. The standard THz measurement setup shown in Fig. 1.2 is used. The performance of the log-periodic antenna without a silicon lens (red) is very similar to the VA (green) over the whole frequency range. However, the DNR of silicon lens coupled log-periodic antenna (blue) is ~ 20 dB higher. The reason for an increased directivity by the silicon lens is its hyper-hemisphericity [45]. The radiated beam from the antenna is always incident almost normally at the silicon–air interface of the lens (see Fig. 5.3(c)) and only $\approx 33\%$ power is reflected back due to the RI difference. In contrast, the schematic in Fig. 5.3(b) without the silicon lens shows that the radiated power undergoes refraction at the flat substrate–air interface, which enlarges the main lobe, thus reducing the antenna directivity. Equation (2.81) predicts an ≈ 12 dB loss of directivity just due to the broadening of the 3-dB angular width of the main-lobe (θ_{3dB}). Additionally, the transmitted power from the high dielectric medium to air decreases with an increase of the angle of incidence θ_i . Further losses are attributed to the resulting total-internal reflection of the radiated power for $\theta_i > 17^\circ$. We also note that the measured DNR without the silicon lens shows higher Fabry-Pérot oscillations than the silicon-lens coupled antenna as the dielectric structure with flat facets makes a better cavity resonator.

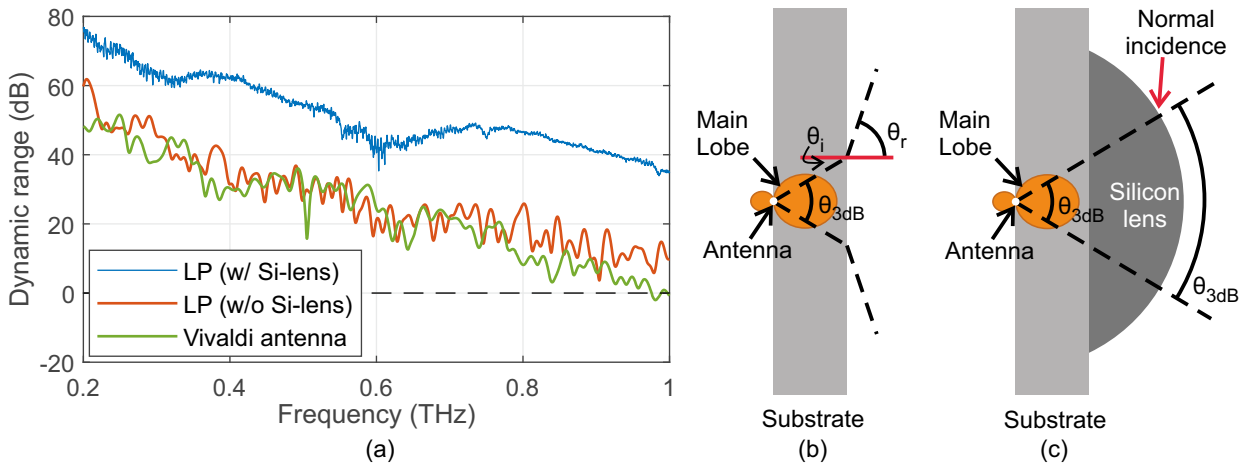


Figure 5.3.: (a) A comparison of THz setup in Fig. 1.2 measured using VA with superstrate and log-periodic antenna without silicon lens show similar DNR [166]. The silicon lens coupled log-periodic antenna shows ≈ 20 dB higher DNR and is comparable to state-of-the-art commercial systems [97]. (b) The 3-dB main lobe width is enlarged for flat substrate-air interface. (c) Hyper-hemispherical silicon lenses help maintain 3-dB bandwidth of the antenna and reduces reflection at the silicon-air interface.

Regardless of the restored endfire characteristics of the VA by adding a superstrate, integrating it with the waveguides is cumbersome. The covered VAs are not visible any more, impeding its proper alignment with the designed waveguides. Moreover, the superstrate must not cover the finger electrodes

over the active area (see Fig. 2.5) as that hinders the optical excitation of the photoconductors. An alternative to using superstrates is to polish the substrate down to $< 30 \mu\text{m}$ to have an end-fire radiation pattern, as depicted in Fig. 5.2(c). However, the devices then become fragile and difficult to handle. Nonetheless, design improvements of the substrate-thinned VAs enhances its power transfer efficiency and integrability with the HRFZ-Si waveguides.

5.1.2. Active devices with improved antennas

The substrate-thinned, antenna-coupled photoconductor is placed directly at an end-facet of the waveguide to excite the E_{11}^x mode in waveguide. Due to antenna reciprocity, the simulated power coupling coefficient between the VA and the waveguide stays the same when the antenna is used as a THz receiver and is excited by the fundamental waveguide mode. To realise this, the width of an individual active device is set to $\sim 200 \mu\text{m}$, matching the width of the HRFZ-Si waveguides and the $\approx 520 \mu\text{m}$ InP substrate thickness is reduced to $\sim 30 \mu\text{m}$. We simulate this direct-coupling mechanism using CST® microwave studio to improve and optimise the antenna designs.

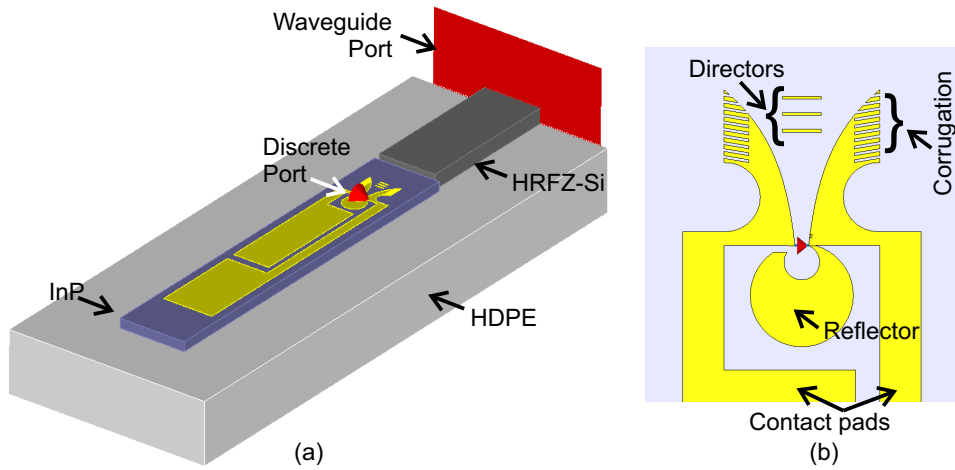


Figure 5.4.: (a) Simulation setup for the VA-coupled photoconductor, placed directly at the end-facet of the HRFZ-Si waveguide. Both the waveguide and active device is supported by a HDPE substrate. (b) An example VA with design improvements.

We use the simulation schematic in Fig. 5.4(a) to estimate the coupling efficiency between the active device and the waveguide. Both the active device and the waveguide are placed on a low-loss HDPE substrate. The discrete port (Port 1) feeding the antenna represents the photoconductor, and the waveguide port (Port 2) absorbs the corresponding power coupled into the waveguide. Apart from the fundamental mode, the waveguide port also supports nine HOMs. The simulated S_{21} parameters provide an estimate of the power coupled from the active device to each of these modes in the waveguide. An exemplary antenna structure is depicted in Fig. 5.4(b). The contact pads are necessary to extract the detector current for further amplification and lock-in demodulation. We analyse the effects of structures added to the basic VA design, such as slot reflectors, directors and the corrugations, on the simulated S_{21} parameter.

Figures 5.5(a–d) show the various stages of the VA design and (e) is the simulated $|S_{21}|$ parameter, where the effects of additional design improvements are plotted. Fig. 5.5(a) is the basic VA design, identical to the design for superstrate-coupled architecture. However, the antenna dimensions are scaled-up according to the diminished effective permittivity of the surrounding media. The blue curve

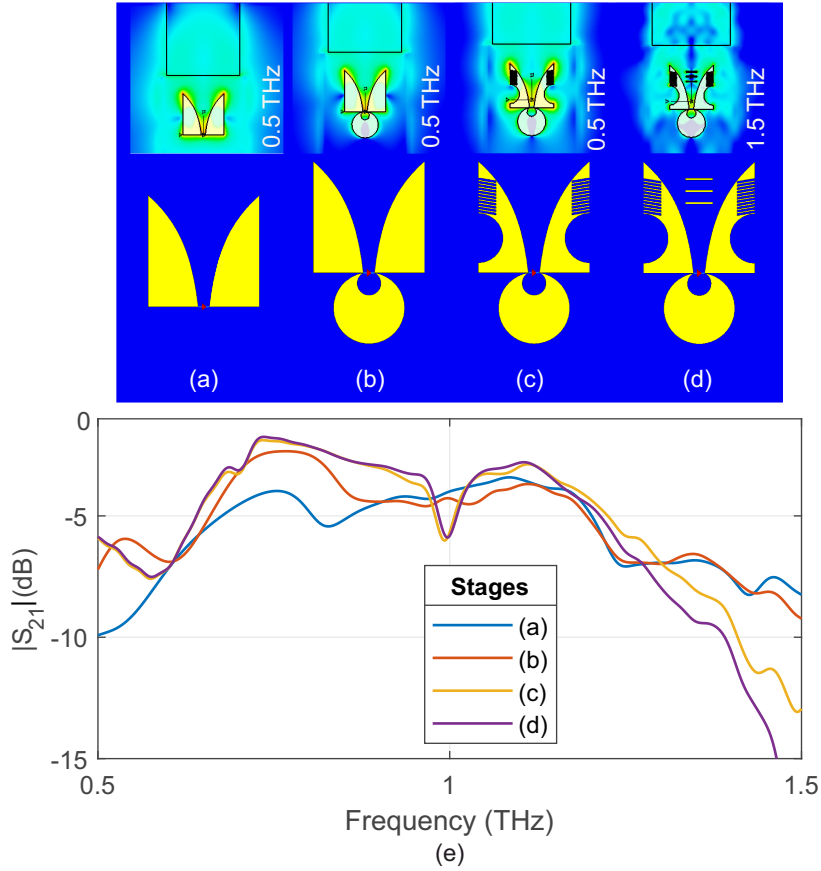


Figure 5.5.: Antenna configuration for the different developmental stages of the VA and the corresponding simulated power flows. (a) The basic VA design. (b) Circular slot reflector added at the antenna base. (c) Symmetrical corrugation slots are added to the antenna blades. (d) Directors are added in front of the VA. (e) The simulated S_{21} parameters between the discrete port and the waveguide port for stages (a-d).

shows the simulated power coupled to the fundamental guided mode E_{11}^x . The best coupling efficiency is ~ -4 dB between 0.75 – 1.12 THz. At higher frequencies, the phase centre lies closer to the discrete port. Therefore, the radiated wave leaks significantly into the InP substrate and does not reach the waveguide. The only way to counter this over a large bandwidth is by further substrate thinning. At lower design frequencies, a considerable fraction of the generated power leaks backwards in the base VA design. We resolve this by placing a circular *slot reflector* behind the antenna (see Fig. 5.5(b)). The circular slot creates an open circuit behind the antenna, which reflects the leaking power back into the tapered slot [173], reducing the back-lobe of the VA. A comparison of simulations of structures (a) and (b) shows the diminished power flow opposite to the endfire direction. We note that if the radius of the circular slot is too small compared to the wavelength, it will result in an electrical short, i.e., its reflectivity will be diminished. Conversely, a too large circular slot radius has no significant effect on the leaky wave. Thus, the slot only improves the low-frequency performance of the antenna. The added reflector enhances $|S_{21}|$ at frequencies between 0.6 – 0.9 THz, shown by the red curve in Fig. 5.5(e).

The *corrugated* outside edges of the antenna blades help to concentrate the surface current on the inner edge of the exponential slot of the VA, and consequently, the antenna directivity improves [167].

The addition of corrugation structures to the VA-blades increase the coupled power to the waveguide between 0.6 – 1.15 THz (yellow curve). However, the high-frequency performance deteriorates as the corrugated structure does not follow the angle principle necessary for broadband performance. In literature, *directors* are further used to enhance the gain of antennas [174], [175]. The directors placed in front of the VA and tangential to the radiated electric field, act as dipole antennas and re-radiate the power travelling in the InP substrate. Although simulations with homogenous and isotropic antenna surroundings show significant gain enhancement at higher THz frequencies, the violet curve shows that the directors only marginally improve the antenna performance below 1.15 THz but degrade the coupling efficiency at higher frequencies significantly. In addition to the non-homogeneity of the VA surroundings, simulation results in Fig. 5.6(a) show that the higher-order E_{21}^y mode is significantly excited at 1.5 THz due to the directors, reducing the power coupled to the fundamental E_{11}^x mode.

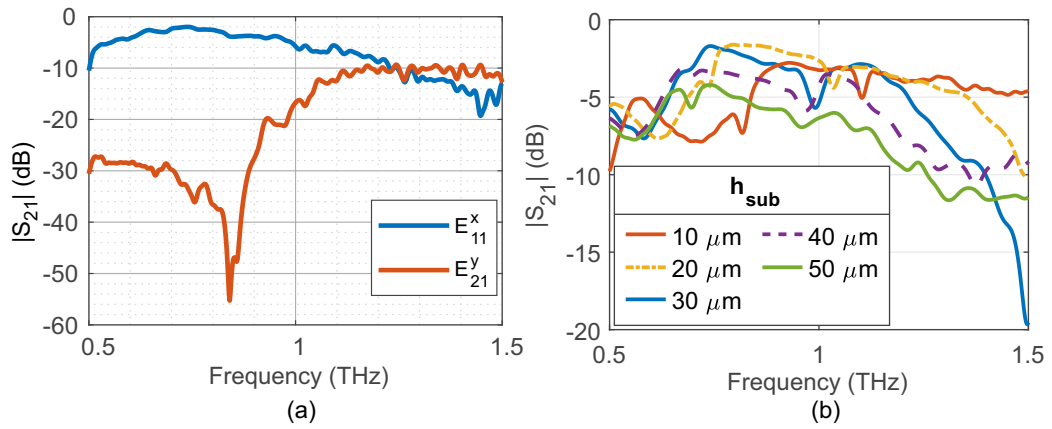


Figure 5.6.: (a) The simulated coupling efficiency between the VA and guided modes in the waveguides. E_{11}^x is the fundamental mode, E_{21}^y is the only significant higher order mode excited by the VA. The coupling efficiency to all other modes is < -20 dB. (b) Simulated change of coupling efficiency with the InP thickness. Active devices with 10 μm substrate thicknesses shows excellent coupling efficiency > -5 dB above 0.7 THz. Higher substrate thicknesses deteriorate the coupling efficiency at higher frequencies.

The thinner the InP substrate of the active device, the main lobe points closer to the endfire direction ($\theta = 90^\circ$, $\phi = 0$). Simulated S_{21} for $h_{sub} = 10 - 50 \mu\text{m}$ in Fig. 5.6(b) show this phenomenon. Figure 5.6(b) confirms that an active device with InP thickness $h_{sub} < 10 \mu\text{m}$ will significantly improved high-frequency performance. However, such small thicknesses are difficult to realise in practice. We could only polish the substrate down to 32 μm in our laboratory. The metallic *contact pads* attached behind the antenna to extract the detected current from the active device, pads modify the S_{21} parameters insignificantly. Figure 5.7 shows the VA-coupled active device as a receiver at 0.875 THz. The fundamental mode is excited at the waveguide port, and the transmitted power to the VA is simulated. The discrete port at A represents the position of the photoconductor. B is the end facet of the waveguide. Simulations show that the discrete port primarily absorbs the THz power. Only an insignificant amount of power (< -18 dB) leaks towards the contact pads.

In addition to the antennas shown in Fig. 5.5(c) and (d), five other antenna designs are fabricated in the scope of this thesis, three of which are depicted in Fig. 5.8(a). The fourth design is the antenna shown in Fig. 5.8(b), but with directors and finally, we also fabricated a log-periodic antenna-coupled photoconductors for comparing the VAs-coupled counterparts with the state-of-the-art.

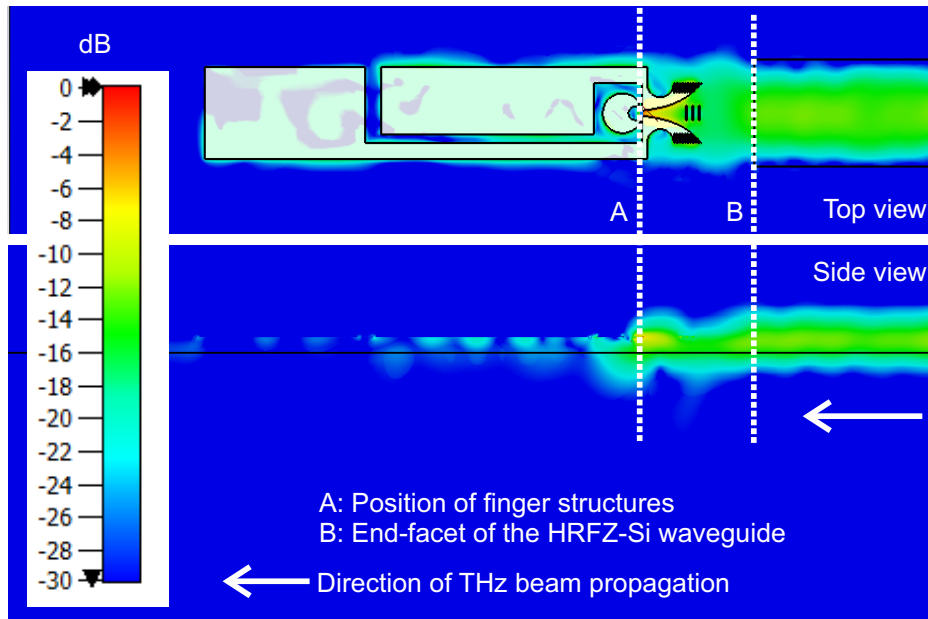


Figure 5.7.: Simulation of the average power flowing from the waveguide into the VA at 0.875 THz. The simulated coupling efficiency of the waveguide-VA interface at 0.875 THz is -4.3 dB. The distance AB is set to ~ 200 μm for the ease of cleaving after fabrication. Adapted from [70].

5.1.3. Fabrication

We fabricated the VA-coupled photoconductors in-house following the standard photolithography-based processes detailed in Appendix A.6. Upon completion, a fabricated sample contains ≈ 50 VA-coupled and 4 log-periodic antenna-coupled photoconductors of various configurations and is 7×8 mm^2 large. The 1.7 μm thick ErAs:In(Al)GaAs photoactive area of the sample is supported by 520 μm thick layer InP substrate (see Fig. 2.5), which is polished down to ~ 30 μm to enhance the endfire characteristics of the VA. Subsequently, individual photoconductors are separated. We note here that the samples after polishing still feature a surface area of 7×8 mm^2 , but only with a thickness of ~ 30 μm . The samples are exceptionally brittle, and it is cumbersome to scratch and cleave them post polishing. Therefore, we scratch the sample with a diamond pen before polishing, and we cleave it afterwards.

The devices are first coated with 1.8 μm thick layer of photoresist to protect the photoconductors and then scratched with a diamond pen in a grid-like form, such that each rectangular space enclosed between the grid-lines contains an active device. The sample edges are not scratched to avoid sample breakage during the chemo-mechanical polishing process. The sample is then attached upside-down on a quartz plate using plasticised bonding wax [176] exposing the InP substrate for polishing. The wax provides additional protection to the active devices. We use a sodium hypochlorite-based polishing suspension with a high pH suitable for polishing semiconductors like InP [176]. Once the InP is polished down to the desired thickness, the quartz plate along with the sample is placed on a 130 $^\circ\text{C}$ hot plate. The liquefied wax expands and exerts pressure on the predefined scratches, eventually cleaving the sample. Figure 5.8(a) shows an image of the cleaved devices. Here we note that the scratched grid must be aligned to the crystal axis and as a precursor, also the fabricated antenna-coupled photoconductors. Misalignment between the scratched lines and the crystal axis may lead to irregular cleaving.

Later, acetone is used to dissolve the wax and the individual VA-coupled photoconductors are “fished

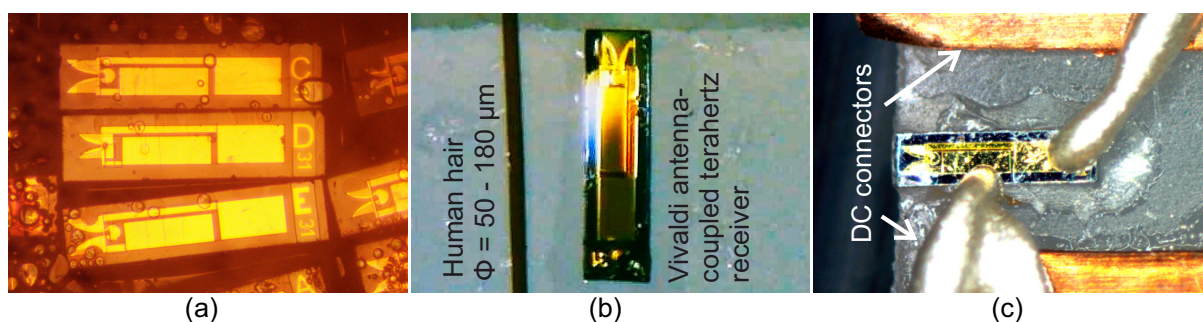


Figure 5.8.: (a) Image of three different VA designs after polishing and cleaving. The bubbles in the image are formed in the melted wax. (b) Individual VAs are separated and placed on a HDPE substrate. The devices are comparable in size to a single strand of human hair. (c) The contact pad of the active device are connected to two metallic strips using conductive epoxy. The metallic strips are later soldered to a Bayonet Neil-Concelman (BNC) connector for extraction of DC detector current. Adapted from [70].

out” with a wooden toothpick using the *Van der Waals forces* of evaporating acetone. Figure 5.8(b) shows one such VA-coupled photoconductor in comparison to a human hair to emphasize the minuscule size of the active devices. The photoconductors are later fixed on a HDPE substrate using low-loss adhesives, such as UV-glue. External electrical connectors are subsequently attached to the contact pads using conductive epoxy resin. Figure 5.8(c) shows such a electrically connected VA-coupled photoconductor.

5.2. Characterisation

We use the semi-free-space measurement setup depicted in Fig. 5.9(a) to characterise two VA designs shown in Fig. 5.9(b) and (c). The measurement setup is a modification of Fig. 4.3(a), where the VA-coupled receiver, directly placed at the waveguide terminal, replaces the lens-coupled free-space receiver. The inset shows a micrograph of an actual VA-coupled, ErAs:In(Al)GaAs-based photoconductor placed in direct contact with the waveguide on a HDPE substrate. VA in Fig. 5.9(b) (Design A) features a circular corrugation near the base of the antenna, i.e., near the location of the finger structures, with additional uniformly spaced rectangular corrugation slots near its tip. The antenna in 5.9(c) (Design B) only contains rectangular slotted corrugations with linearly increasing length throughout the outer edge of the antenna blades. Additionally, metallic directors are used in front of both designs for improved performance at higher frequencies. The relevant antenna dimensions are presented in Table 5.1.

Firstly, a reference measurement of the detected THz current (I_{ref}) is taken in the free-space setup using the log-periodic antenna coupled photoconductor (Fig. 4.3(a)). Then, both the antennas A and B are positioned directly in contact with a silicon waveguide of length 19 mm, comprising a 90° bend with 4 mm radius as shown in Fig. 5.9(a). The other tapered-out end of the waveguide facilitates free-space in-coupling and is placed at the focus of a TPX lens. The total transmission losses (T) in dB for this setup reads as

$$T = 20 \log_{10} \frac{I_{VA}}{I_{ref}}, \quad (5.3)$$

where $I_{VA} \propto E_{THz}^{meas}$ is the detector current corresponding to the THz field E_{THz}^{meas} measured with

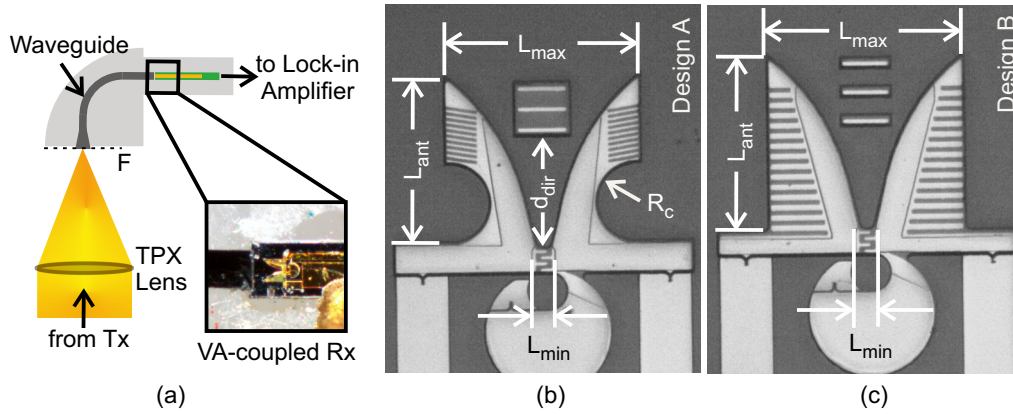


Figure 5.9.: (a) Schematic of a semi-free-space THz setup for characterising VAs. The inset shows a micrograph of an actual fabricated active device placed in direct contact with the HRFZ-Si waveguide. Both the active device and the waveguide are placed on a HDPE substrate (grey background). The 90° waveguide bend avoids line-of-sight coupling between the free-space Gaussian beam and the VA. Images in (b) and (c) show two antenna designs extensively used in PVNA architecture. Adapted from [72] ©2021 IEEE.

Table 5.1.: Design parameters related to the VAs shown in Fig. 5.9. These parameters are obtained via optimisation in CST® microwave studio.

	Parameters	Design A	Design B
Basic	Antenna length (L_{ant})	112.5 μm	135 μm
	Max. tapered slot width (L_{max})	112.5 μm	150 μm
	Min. tapered slot width (L_{min})	10 μm	10 μm
Directors	Width	1 μm	2 μm
	Length	28 μm	28 μm
	Gap	10 μm	10 μm
	Dist. from antenna base (d_{dir})	75 μm	75 μm
Corrugation	Slot length	18.23 μm	12.25 – 33.25 μm
	Slot width	2 μm	3 μm
	Gap btw. slots	1.25 μm	3 μm
	Tilt angle	9°	0°
	Radius of the base semicircle (R_c)	25 μm	–
Other	Reflecting slot radius	12 μm	12 μm
	Gold thickness	≈ 420 nm	≈ 420 nm
	Finger width	1.5 μm	1.5 μm
	Gap btw. fingers	2 μm	2 μm

the VAs. We plot the measured transmission characteristics for antenna designs A and B between 0.5 – 1.2 THz in Fig. 5.10(a) and (b), respectively. The detected THz signal at higher frequencies is indistinguishable from the receiver noise without additional data-processing. The measured losses for both the antennas are in good agreement with the simulated values, however, the antenna B shows 3 – 4 dB higher coupling efficiency than its simulated model at below ≈ 0.75 THz. The losses in T broadly have three different components. Firstly, the in-coupling losses between the free-space beam and the waveguide at point F , which accounts for $\approx 10 - 13$ dB losses (see section 4.5.3). Secondly,

the out-coupling losses between the waveguides and the VAs. Lastly, the transmission losses in the waveguides, which are negligible compared to the other two types of losses at these frequencies [70]. Between 0.6 – 0.9 THz, the simulations predict that the coupling loss between both the antennas and the dielectric waveguide is < 4 dB. The minimum insertion loss for design *B* is ≈ 2 dB at 0.74 THz per VA-waveguide interface and a simulated 3-dB bandwidth of the direct-coupling technique is between 0.55 – 0.99 THz (relative bandwidth = 57.1%). The receiver with the antenna *A* shows a slower frequency-dependent roll-off at higher frequencies. Due to antenna reciprocity, we argue that the total transmission losses are further reduced to 8 – 10 dB below 1.2 THz, if the VA-coupled transmitters are used instead of free-space in-coupling.

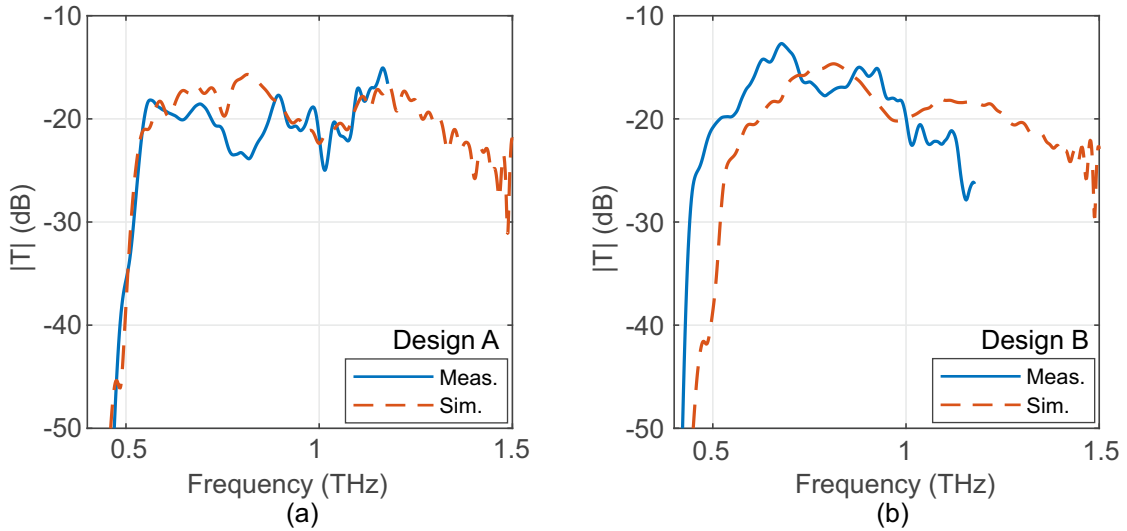


Figure 5.10.: Measured transmission losses ($|T|$) in the semi-free-space measurement setup for antenna design *A* in (a) and design *B* in (b) show good agreement with the expected losses from the simulations. The transmission features of both the antennas are measured till 1.1 THz due the lack of sufficient DNR in the semi-free-space setup. Adapted from [72] ©2021 IEEE.

5.3. Comparison with free-space coupling

Utilising the data post-processing techniques described in section 3.2, we extend the operational bandwidth of the VAs up to ≈ 1.6 THz. Figure 5.11(a) shows the following plots for comparison: the violet plot shows the measured transmission losses through the waveguides with lens-assisted, free-space in- and out-coupling as depicted in Fig. 4.3(a). The total losses are about 22 – 26 dB over 0.4 – 1.2 THz, which agrees with the free-space in-coupling losses discussed previously. The blue curve shows the losses measured in the setup with the VA-coupled receiver shown in Fig. 5.9(a). Compared to the free-space setup, the losses with integrated receivers are 5 – 14 dB smaller between 0.4 – 1.05 THz, with a maximum reduction of ≈ 14 dB at ~ 0.68 THz. The dashed-dotted black plot shows the achievable coupling efficiency simulated with VAs employed for both in- and out-coupling to the waveguides. Note that the simulated coupling losses are higher than the measured losses in free-space and VA setup at frequencies above 1.2 THz. This indicates a lower coupling efficiency at the VA-waveguide interface at higher frequencies than the free-space coupling, and hence, the necessity for further optimization of the VAs at the upper end of the operational band. A VA-coupled transmitter can

also generate higher order vertical modes in the waveguides, however, the height of the waveguides ($50\ \mu\text{m}$) ensures that only the fundamental vertical mode is guided.

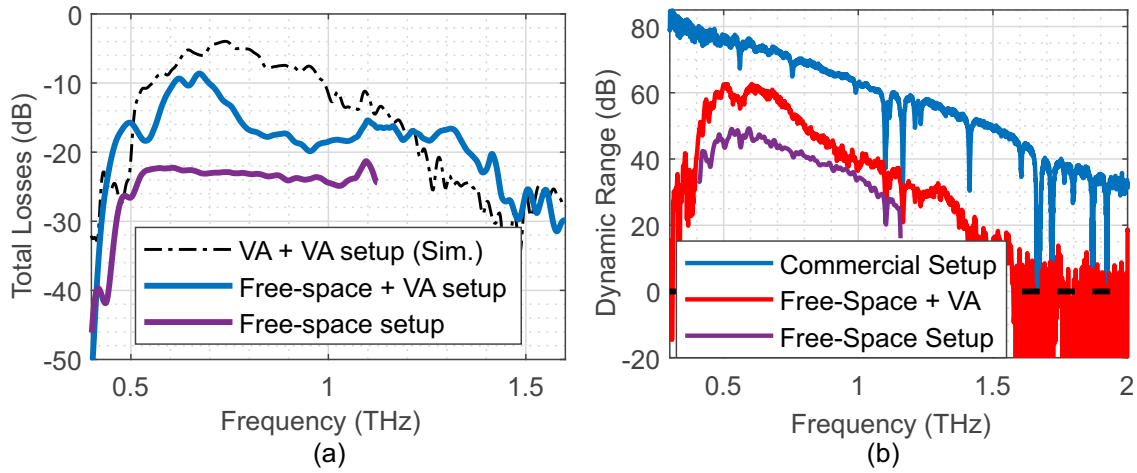


Figure 5.11.: (a) Measured and simulated losses of the semi-free-space measurement setup shown in Figure 5.9(a). Post-processing is employed over the measured dataset to reduce measurement noise. (b) Comparison of measured DNR between the (ideally) lossless commercial setup (Fig. 1.2), the free-space setup using waveguides (Fig. 4.3(a)) and the semi-free-space setup with VA receiver (Fig. 5.9(a)). Adapted from [70].

In summary, the VAs feature a 5 – 14 dB improvement of coupling efficiency per coupling interface above 0.5 THz. Using a lens-coupled commercial p-i-n diode source and data post-processing, the VAs can be used up to 1.6 THz as shown in Figure 5.11(b). With further substrate thinning and replacing the free-space in-coupling by a VA-coupled transmitter, we expect an increase of the operational bandwidth to at least 2 THz. The demonstrated VA-coupled receivers are $\approx 150 \times 220 \times 30\ \mu\text{m}^3$ in dimension, which is ~ 6 orders of magnitude smaller than their free-space counterpart. Additionally, the bulky optical components like the parabolic mirrors and the TPX lenses are no longer necessary enabling miniaturisation of photonic setups. Experimental findings also show reduced reflections by the VA antenna due to improved mode field diameter and impedance matching, reducing the amplitude of undesired standing waves in the waveguide. This justifies the VAs as the antennas of choice for the PVNA, and more generally, broadband integrated THz SOCs.

6. Semi-integrated THz PVNA

With all the necessary data-processing tools from chapter 3 at hand, we now proceed to manufacture the 1.5-port (semi-) integrated PVNA using the waveguides described in chapter 4 and the VAs of chapter 5. Figure 6.1 shows a schematic of the 1.5-port setup. The waveguide-based 3-dB splitter is excited by a free-space THz beam from a commercial P-I-N diode source. The section *AB* represents the DUT. The DFB lasers driving the receivers *Rx1* and *Rx2* are optically aligned atop the active area of the photoconductors using precise 3-D translation stages. The measured current at *Rx1* yields the transmission coefficient S_{21} of the DUT and similarly, the current at *Rx2* yields its the reflection coefficient S_{11} . For symmetric structures, i.e., where $S_{21} = S_{12}$ and $S_{11} = S_{22}$, only the two aforementioned S-parameters are sufficient for a complete device characterisation. The whole setup is supported by a 1.5 mm thick HDPE substrate and a 3 mm thick PVC plate is placed underneath for mechanical support and attenuation of the substrate modes in the HDPE.

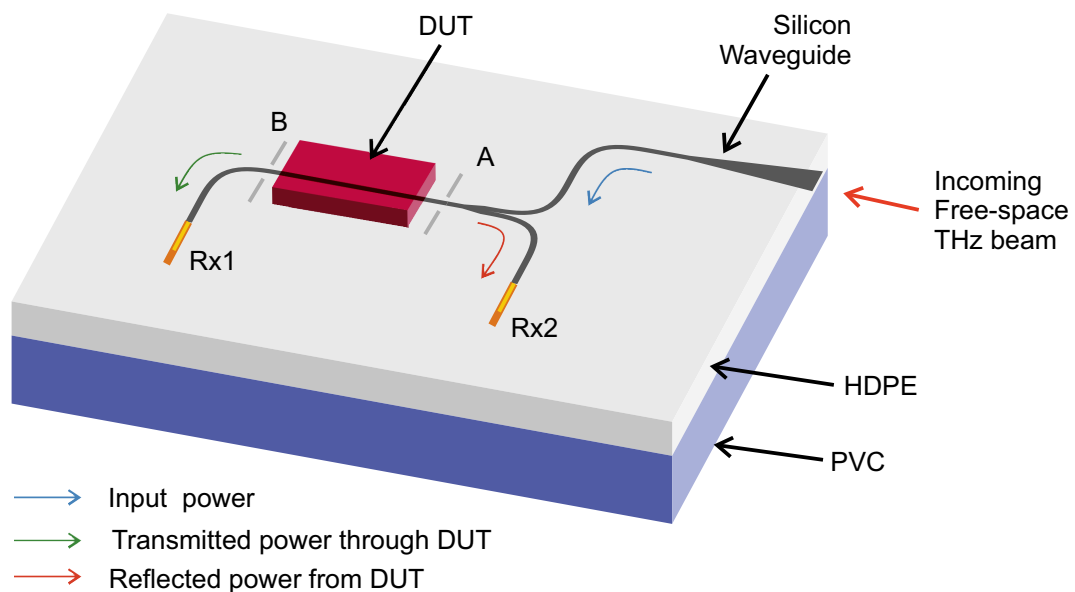


Figure 6.1.: Schematic of the 1.5-port (semi-) integrated PVNA architecture. The waveguide structure is atop a 1.5 mm thick HDPE substrate, supported by a 3 mm PVC plate. The in-coupled THz wave from the free-space port gets partially transmitted through the DUT reaching *Rx1* and is partially reflected back to *Rx2*.

In this chapter, we characterise waveguide-based circuit components, such as WGM and cavity resonators, THz fibre Bragg grating, etc., using two different 1.5-port setups. We start with detailing the digital data-processing techniques from chapter 3 employed to extend the operational bandwidth of the PVNA. Then, we briefly discuss about a coupling mechanism to integrated, metallic electronic circuitry and finally, we propose a 2-port fully integrated PVNA architecture.

6.1. Data acquisition and software setup

The CW Terascan™ system from *Toptica Photonics* has three measurement bands spanning between 0 – 1.15 THz, 0.95 – 2.2 THz and 1.5 – 2.75 THz respectively. Each band uses a different pair of DFB lasers. We utilize the first and the second bands to measure a total bandwidth between 0.3 – 1.6 THz in the PVNA setups. The setup is operated in a homodyne fashion, just like the other free-space counterparts shown in this thesis. Figure 6.2(a-d) shows the following post-processing steps applied to the measured photocurrent at the receivers:

- The alignment of the laser spot on the device causes a variation of the laser power absorbed by the receivers. As the laser serves as a local oscillator (LO), this turns into a responsivity variation. In order to calibrate the effects of unequally absorbed laser power out, we record a DC I-V characteristics under illumination and normalize the measured rectified THz current to the

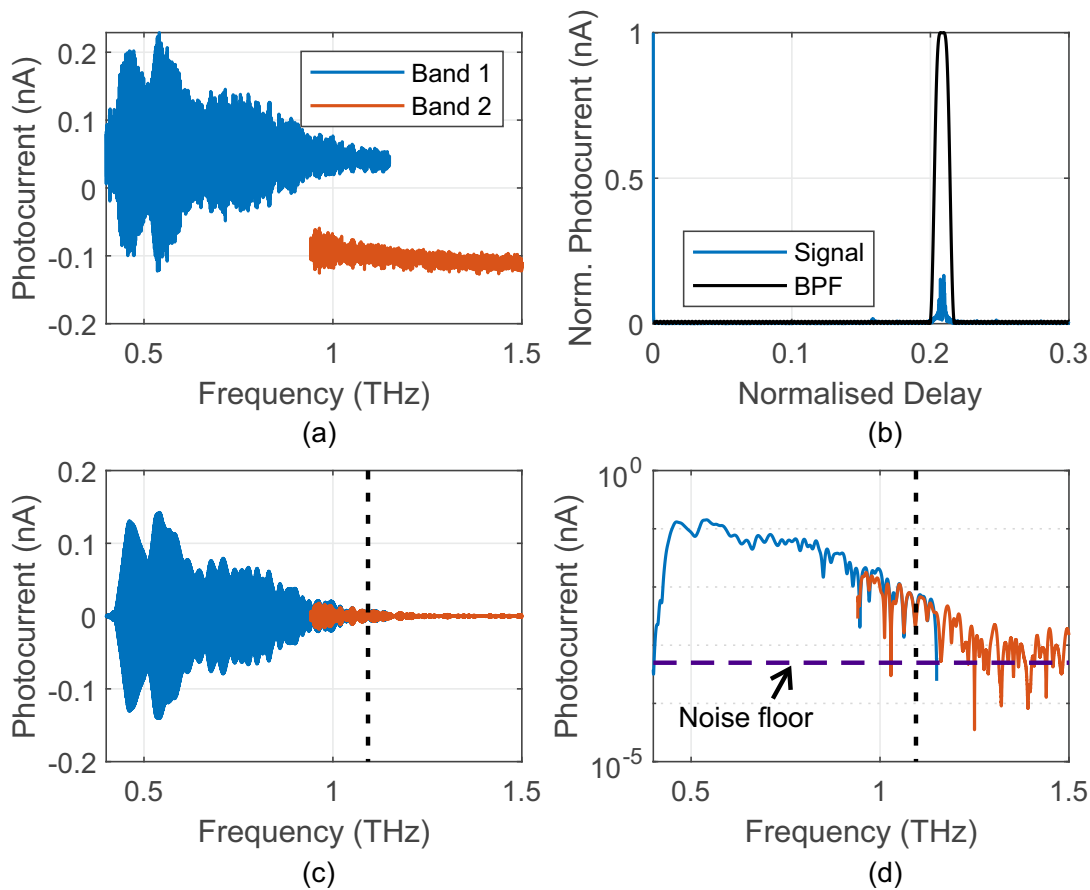


Figure 6.2.: (a) Measured raw data at the receivers has different DC-offsets due to ground loops in the post-detection electronics. (b) A BPF (window in time-domain) filters-out the unwanted DC current and also the stray reflections arriving before or after the main signal. (c) The filtered data can be stitched together to have a continuous homodyne spectrum. We usually combine the data at a waterline to suppress unwanted phase jumps in the cumulative dataset. (d) Hilbert transform of (c) reveals the amplitude (and phase) information of the measured spectrum between 0.45 – 1.5 THz. The dashed vertical line in (c) and (d) marks 1.098 THz where the data-sets are joined together.

DC photocurrent at 0.2 V.

- The normalised receiver current usually has an offset due to ground loops, which is a common feature of the TIAs. Figure 6.2(a) shows two homodyne signals with different (even frequency-dependent) current offsets recorded in the first and the second frequency bands.
- In Fig. 6.2(b), we use an appropriate BPF (equivalent time-window) to remove the current offset and other stray reflections from the data.
- Then, we compensate for the frequency lag between the actual and set frequency of the Terascan system by aligning the waterlines at 0.557 and 1.098 THz. We stitch the data together at the waterline of 1.098 THz to avoid phase jumps at the junction, as shown in Fig. 6.2(c).
- Finally, in Fig. 6.2(d) we compute the Hilbert transform of the measured current to obtain its complex form and subsequently normalise it to the reference setup to calculate the S-parameters. We also estimate the system noise from the scan range between 1.595 – 1.60 THz, where no signal is recorded.

The post-processing of the measured data increases the maximum operational frequency of the PVNA from 1.1 THz to ~ 1.5 THz, i.e., a 36% bandwidth increment. A deep-dive into the impact of data processing on homodyne measurement systems can be found in section 3.2. We have also submitted a patent application to the German Patent Office (DPMA) [69] regarding the bandwidth extension proposition of homodyne THz systems aided by digital signal processing.

Table 6.1 features a comprehensive list of DUTs and their corresponding measurement parameters characterised in this chapter using both the PVNA setups. The measurement band 1 spans between 0.3 – 1.15 THz, whereas the band 2 between 0.95 – 1.6 THz. For confirming the optical alignment of the laser spot, the DC photocurrent is measured across the VA-coupled receivers with four different antenna types (*A*, *B*, *C* and *D*) against a bias of 0.2 V.

Table 6.1.: Comprehensive list of measurement parameters of the DUTs characterised in this chapter.

Setup	DUT	Scattering parameter	Band	VA-type	DC photo-current	Integration time
Additive DUT	WGM resonator	S_{21}	1	<i>A</i>	2.50 μA	30 ms
			2		2.80 μA	
Modular PVNA	Terahertz fibre Bragg grating	S_{21}	1	<i>C</i>	3.45 μA	100 ms
			2	<i>D</i>	3.05 μA 3.10 μA	
	Cavity resonator (3.167 mm)	S_{21}	1	<i>C</i>	3.40 μA	100 ms
			2		3.70 μA	
	Cavity resonator (~ 9 mm)	S_{11}	1	<i>D</i>	3.50 μA	100 ms
			2		3.10 μA	
Cavity resonator (~ 9 mm)	S_{11}	1	<i>D</i>	3.40 μA	100 ms	
		2		3.42 μA		

6.2. 1.5-port setups

Figure 6.3(a) and (b) show the two configurations of the 1.5-port (semi-) integrated PVNA setup. In the first case of Fig. 6.3(a), the DUT interface is a 9 mm long waveguide section, fabricated with the splitter structure on the one end and a 90° bend on the other. This structure is used as reference. DUTs are later added either on top or beside this reference structure, i.e., this setup can characterise only *additive DUTs*. The receivers are modular and coupled to the waveguide end facets.

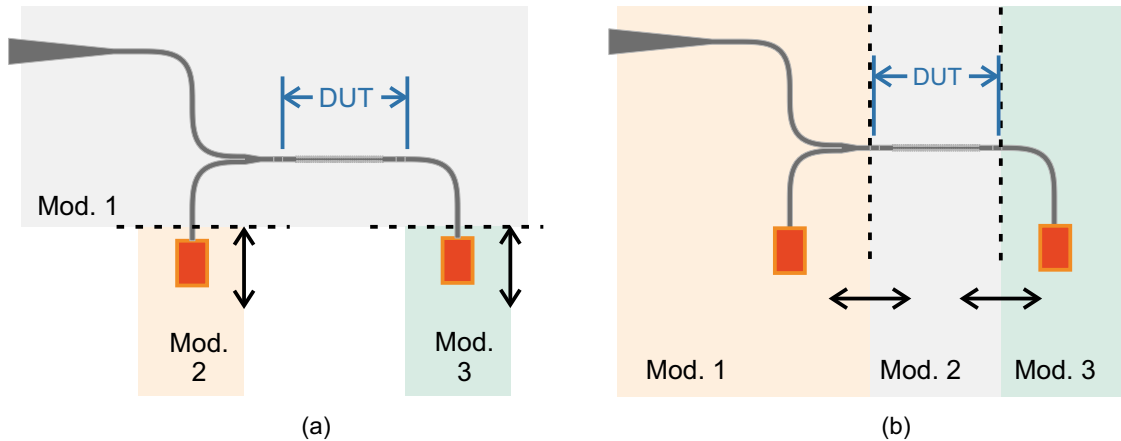


Figure 6.3.: (a) 1.5-port PVNA setup with additive DUTs. Only the receivers are detachable. (b) Schematic of a modular PVNA setup where only the DUT structure can be replaced. The dashed black lines indicate the alignment planes in both the setups.

The second configuration is more modular, where module 1 and 3 hold the waveguide-integrated receivers (PVNA heads) and the module holding the DUT (Module 2) can be altered. Henceforth, we refer to this as the *modular PVNA* setup. For fully integrated setups with THz sources and receivers, each PVNA head can be calibrated just after manufacturing. However, this is not the case for the (semi-) integrated version, as the free-space alignment can vary between measurements. Henceforth, we refer to the waveguide coupled *Rx2* before the DUT as the *reflection port* and waveguide-coupled *Rx1* after the DUT as the *transmission port*.

We use four different antenna-coupled photoconductive receivers in total for all the measurements shown in this chapter (and appendix A.4). The fabricated VAs are fragile and break during disassembly. Therefore, the receivers used in the setup of Fig. 6.3(a) could not be reused in the setup of Fig. 6.3(b). Figure 6.4 shows all the receivers and their corresponding DNRs, used both in the transmission and the reflection ports. The micrographs of each antenna coupled photoconductor are presented above the plots. The setup with additive DUTs used the receiver with antenna *A*, whereas the modular PVNA used receivers with antennas *B* and *C* at the transmission port and with antenna *D* at the reflection port. A few noteworthy observations from Fig. 6.4 are as follows:

1. The measured transmission in the setup with additive DUT shows 5 – 10 dB lower losses than the modular PVNA setup. This is primarily due to the misalignment of the DUT with the PVNA heads. The waveguides are easily aligned along the horizontal plane, however, an uneven HDPE surface makes the vertical alignment cumbersome. We have to use highly-absorptive SuperGLUE™ at the alignment points sparingly to hold the waveguides in place, which increases the transmission losses. The reflection spectra are similar for both the setups as they are measured only from the splitter structure, devoid of any DUT.

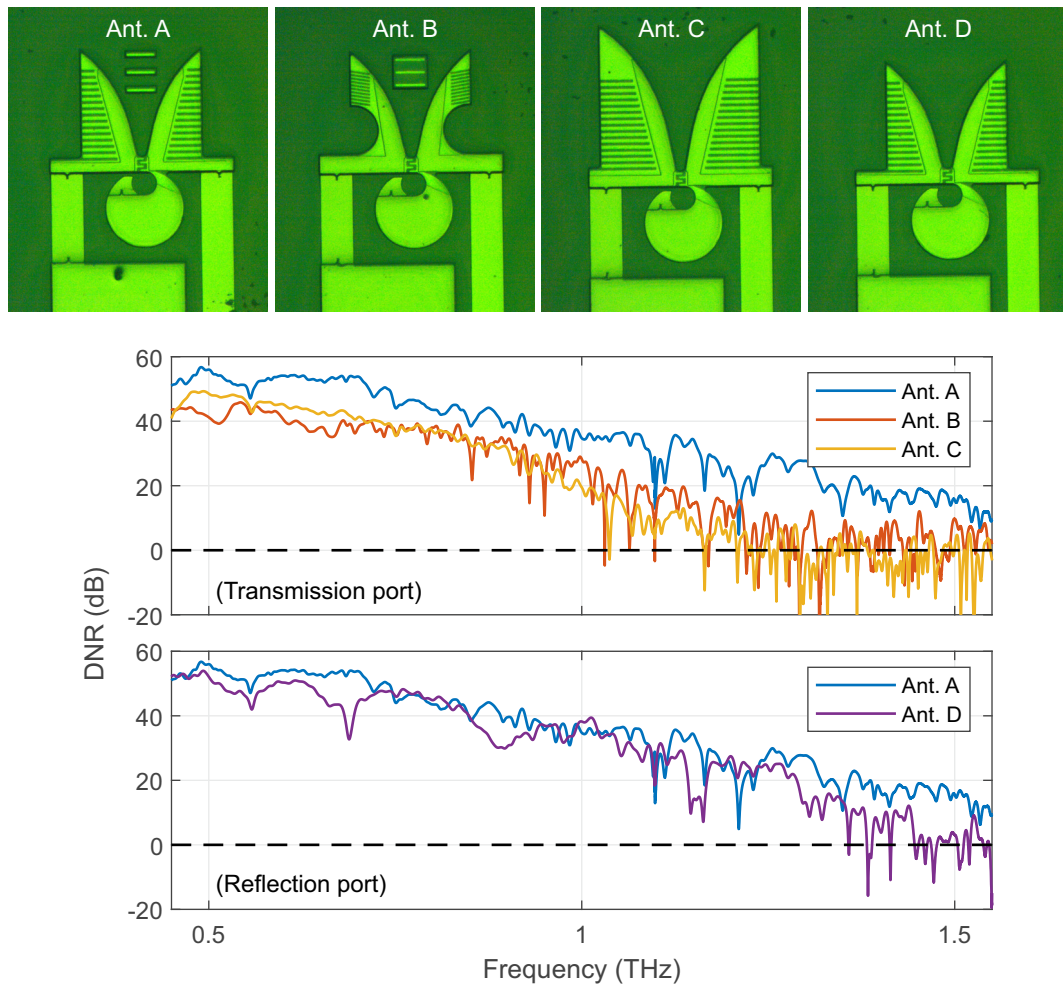


Figure 6.4.: A comparison of measured DNRs of VA-coupled receivers used in the integrated PVNA setup. The worse performance of antennas *B* and *C* is, to a large degree, caused by the modular PVNA. The green microscopic images of the individual antennas are shown on top.

2. Antennas *A* and *D* have similar base structure and the former also features the directors. The high-frequency performance of the VA with directors seem to be better than the one without, contrary to the simulations of chapter 5.
3. Antenna *C* is 1.2 times larger than the other VAs and hence, the receiver has a better low-frequency performance than Antenna *B*. However, the maximum operational frequency of the former receiver is about 100 GHz lower than the receiver with antenna *B*.

The setup with additive DUTs offer a measurement bandwidth beyond 1.5 THz. The waveguides are highly lossy below 0.45 THz and the VAs with 30 μm -thick substrate seize to work above 1.6 THz due to their lower coupling efficiency and the lack of source power. We characterise a WGM resonator using the integrated setup between 0.5 – 1.5 THz and a THz fibre Bragg grating and two cavity resonators using the modular PVNA setup. The operational bandwidth of the modular PVNA is 0.5 – 1.2 THz.

6.3. Whispering gallery mode resonator

The WGM resonators derive its name from the whispering gallery of the St. Paul's Cathedral in London, where the sound wave travels along the curved surface of cathedral's dome, rather than bouncing from the walls. EM waves can be similarly confined within devices with concave boundaries. High RIs facilitate the mode confinement in the resonators. We can intuitively understand the WGM resonators from the conformal-transformed waveguide bends. The smaller the ROC of a dielectric bend with high RI contrast, the more the centre of mass of the mode is shifted to the outer edge (see Fig. 4.7) and consequently, the more power travels grazing the outer edge of the waveguide bend. If either the width of the bend is large or the ROC is small, such that the mode travelling in the bend is not affected by its inner edge, we have a whispering gallery mode propagation. If the bend forms a closed path, it creates a WGM resonator. The resonant features arise from the interference of the wave with itself after one round trip.

When a resonator is placed in proximity to the HRFZ-Si-based waveguides, the evanescent fields of the guided modes couple with the WGMs of the resonator. At resonance, the out-coupled fraction of the field stored in the cavity destructively interferes with the field in the silicon waveguide. Thus, at the resonance frequencies, the transmitted power through the waveguide is stored in the resonator and hence, its transmission characteristics feature sharp peaks. The transmitted power through the waveguide depends upon fraction of power lost per round-trip in the resonator α^2 , and the field coupling coefficient between the WGM resonator and the waveguide κ , and reads [177]

$$P_{tx} = \frac{(\alpha - \sqrt{1 - |\kappa|})^2}{(1 - \alpha\sqrt{1 - |\kappa|})^2}. \quad (6.1)$$

The coupled power to the resonator decreases with increasing frequency as the power guided by the evanescent fields decreases, decreasing κ . This results in three coupling conditions, namely, the *under-critical* coupling, the *critical* coupling and the *over-critical* coupling. Critical-coupling occurs when $\alpha = \sqrt{1 - \kappa}$ and no power is transmitted, i.e., $P_{tx} = 0$. The critical-coupling condition features a $\pm\pi$ phase shift at the resonant frequency. At other resonant frequencies, the resonator is under-critically-coupled when $\alpha < \sqrt{1 - \kappa}$ and are over-critically-coupled if $\alpha > \sqrt{1 - \kappa}$. At these resonances, $P_{tx} > 0$ and the phase-jumps are smaller than $\pm\pi$. Therefore, a frequency-sweep of S_{21} of the WGM resonator-coupled waveguide would show very high losses at multiple, (almost) equispaced resonance frequencies, with the coupling conditions changing from over-critical to critical coupling and further to under-critical coupling condition, accompanied by their corresponding phase jumps. The spacing between two consecutive resonances is called the FSR and it decreases slightly with increasing frequency as the HRFZ-Si-based waveguides and WGM resonators are dispersive.

The shape the resonance peaks define the extent of coupling between the resonator and the waveguide. The Q-factor of such a resonance is defined as the ratio of the energy stored in a resonator to the amount of energy lost per radian of the cycle of oscillation [178]. Alternately, it is formulated as the ratio of the centre frequency of a resonance to its 3-dB bandwidth. Therefore, we can characterise a waveguide-coupled WGM resonator from the measured resonance peaks in the S_{21} parameter. Even though WGM resonators are widely used at optical frequencies, until recently such resonators were rarely characterised at the THz frequencies [179], [180]. In 2018, Vogt *et al.* published a detailed characterisation of a WGM resonator fabricated using a HRFZ-Si sphere, coupled to a silica waveguide [181] and demonstrated Q-factors of the order 1.5×10^4 at 0.63 THz. This is at least an order of magnitude higher than the Q-factors of the other commonly used resonators in the THz domain, such as photonic crystal slabs, parallel plate waveguides, etc. [181].

Setup with additive DUTs

We characterise a planar 180 μm thick circular disk made out of HRFZ-Si, with a 1.007 ± 10 mm radius, placed atop a HRFZ-Si waveguide. The evanescent field along the comparatively wide horizontal waveguide axis vanishes at higher THz frequencies and hence, the “on-top” configuration is preferred rather than placing the resonator beside the waveguide. We have demonstrated the latter configuration

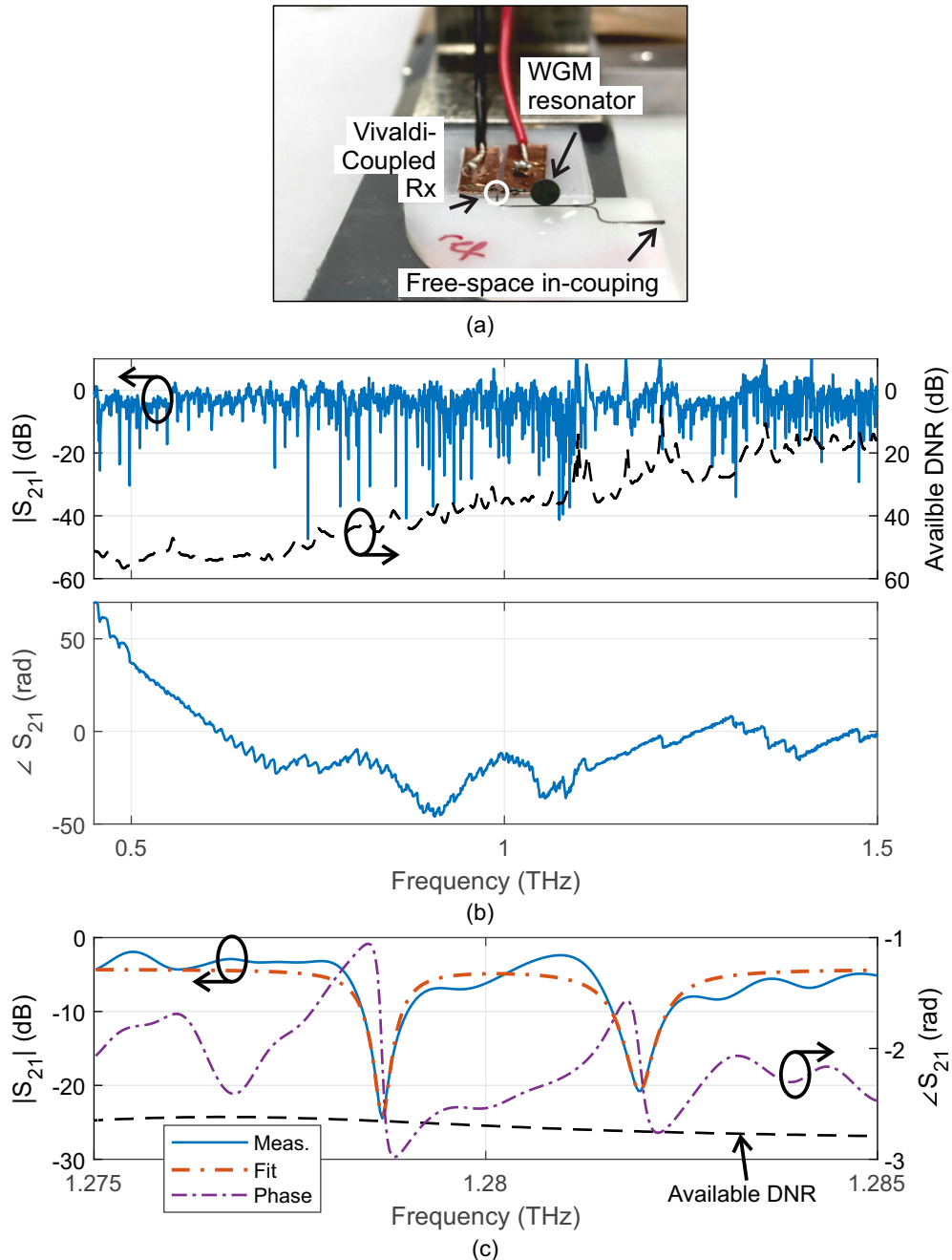


Figure 6.5.: (a) Photograph shows the actual measurement setup. The WGM resonator is placed atop the HRFZ-Si waveguide. (b) The measured complex S_{21} parameter of the WGM resonator. (c) A closer look at two resonances at 1.279 and 1.282 THz.

in [70], but with very little coupling and hence, we do not explore them further in this work. Figure 6.5(a) shows the measurement setup. The entire waveguide structure is etched out of a single piece of silicon wafer. We measure the transmission port first as reference. Then, we fix the HRFZ-Si disk vertically on top of the waveguide using SuperGLUE™. Figure 6.5(b) shows the periodic resonance trenches in measured $|S_{21}|$. Below 0.8 THz, the gap between two consecutive resonances, i.e., its FSR is ≈ 14 GHz. Above, HOMs are excited in the circular disk owing to its small ROC (similar to higher order bend-modes) and we observe more frequent, unequally spaced resonances from different radial resonator modes in S_{21} . The measured phase shows $< \pi$ transitions at over-critical coupling between 0.5 – 0.7 THz to a $\sim \pi$ transition at the critical coupling frequency ~ 0.736 THz, followed by decreasing phase shifts for the under critical coupling at higher frequencies. A simulated radius of 1.004 mm matches the measured resonance features.

In Fig. 6.5(c), we take a closer look at two resonances between 1.275 – 1.285 THz. The FSR of ≈ 3 GHz between the resonances indicates that they occur from different radial resonator modes. We fit the resonant features to a Lorentzian distribution for estimating their 3-dB bandwidth [181] and subsequently calculate their Q-factors. The estimated Q-factor of the resonant feature at 1.279 THz is 1.04×10^4 , which is at least 3 times larger higher than the WGM resonator in [182], comparable to the Q-factors reported in [181], [183] and an order of magnitude larger than the non-WGM resonators at THz range [184]–[186]. The $\approx \pi$ phase jump at the resonance frequency indicate a near-critical coupling condition. Table 6.2 lists Q-factors at other resonance frequencies of the WGM resonator.

Table 6.2.: A list of a few resonances and their corresponding Q-factors. All the listed resonance peaks have lower attenuation than the available DNR.

Frequency	Q-Factors
0.736 THz	5 847
0.905 THz	21 191
1.279 THz	10 437
1.282 THz	5 524

The visibility of the resonances till 1.5 THz and beyond attests to the broad operational bandwidth of the miniaturised PVNA, at least with additive DUTs. However, the available DNR limits the resolvable depth of the resonance feature. Simply speaking, only resonant features with < 15 dB attenuation can be properly characterised above 1.5 THz. The setup with additive DUTs show 5 – 7 dB lower losses than the modular configuration, however, the calibration planes are ill-defined. Furthermore, the setup is convenient for additive structures like the WGM resonators or sub-wavelength grating filters, however, is very inconvenient for waveguide-integrated DUTs or metallic structures like integrated circuits operating at THz frequencies.

6.4. Modular PVNA setup

The modular PVNA setup provides more flexibility and mimics a traditional electronic VNA with two measurement ports. The DUTs are separate and interchangeable without recalibrating the PVNA heads. Figure 6.6 shows the modular version of the assembled (semi-) integrated 1.5-port PVNA. The *reflection port* on the left HDPE plate constitutes the free-space in-coupling port, the splitter structure and the receiver Rx2, which measures the reflected power. The *transmission port* is the rightmost HDPE plate hosting the waveguide-coupled Rx1. The coupled waveguide is made intentionally longer to temporally separate reflections from Rx1 from the reflection from the DUT at Rx2. The section AB contains the DUT

mounted on the centre HDPE piece. Even though the standing waves at the edges of the HDPE plates are significant, large gaps in-between make it easy to remove these stray reflections in post-processing. This configuration adds two more alignment points at *A* and *B* compared to the additive DUTs and results in 5 – 7 dB higher misalignment losses below 1 THz, as is also evident in plot 6.4.

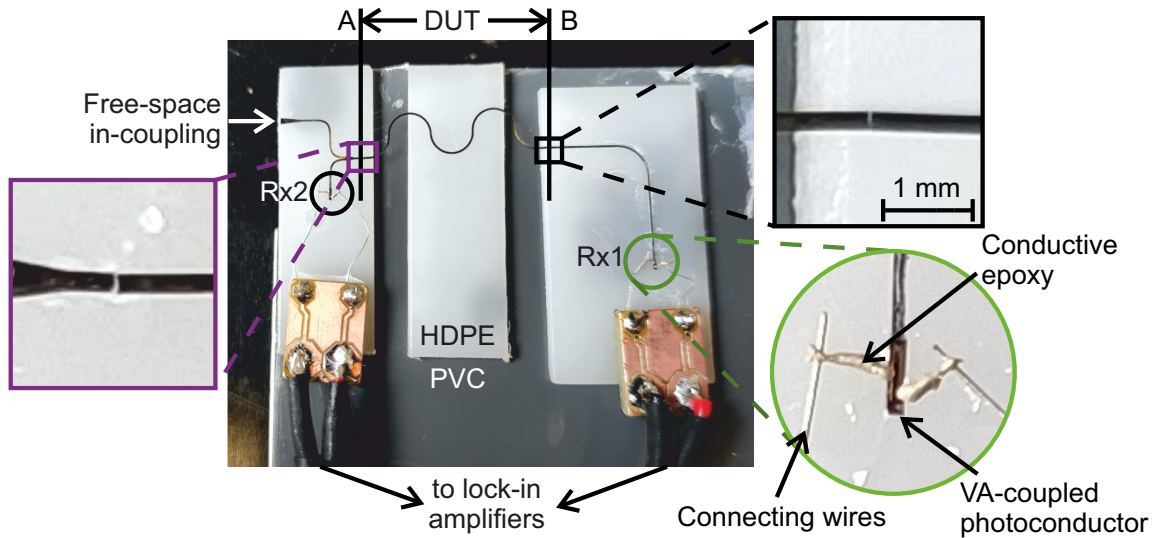


Figure 6.6.: A modular PVNA setup. The misalignments between the DUT and the PVNA heads are visible at locations *A* and *B*, respectively. The gap is in the order of tens of micrometers. The direct coupling between the waveguides and the VA-coupled receiver is magnified in the circular inset.

The transmitted wave through the DUT reaches *Rx1* before any other stray reflections and thus, can be easily time-gated or filtered out using a LPF. The situation is more complex at the reflection port. Figure 6.7 shows the equivalent time-domain plots for the received signal at *Rx2* in the modular PVNA setup. We plot three different measurements, namely,

1. an open at point *A* (black), i.e., the DUT is absent,
2. an open at point *B* (red) implemented attaching an additional 9 mm long waveguide at *A* but the transmission port is disconnected,
3. a cavity resonator as DUT (blue) with a connected transmission port.

The reflections from point *A* arrive the receiver with ≈ 1.5 ns delay, whereas the reflection from point *B* reaches with a 1.75 ns delay. We also see some reflections from *A* for the second case and some additional reflections from the discontinuity in HDPE substrates at 1.65 ns, which are two orders of magnitude smaller. The cavity resonator connected to the transmission port also shows significant reflections from point *A*, i.e., at the beginning of the cavity and at 1.58 ns from the other end of the ~ 3 mm long cavity. The blue plot also shows trailing reflections at regular intervals of 82 ps. This resonator and the other ~ 9 mm long waveguide are characterised later in this chapter, where we revisit this time-domain plot. Here, we conclude that the reflections from the DUT reach the receiver with delays between 1.5 – 1.75 ns and we use time-windows (equivalent to BPFs) to separate the reflections occurring at the DUT from undesired reflections of the setup.

The transmission port is calibrated using the 9 mm waveguide as a through-line. The reflection port is more difficult to calibrate as we need 100% reflection at the point *A*, which is very difficult to

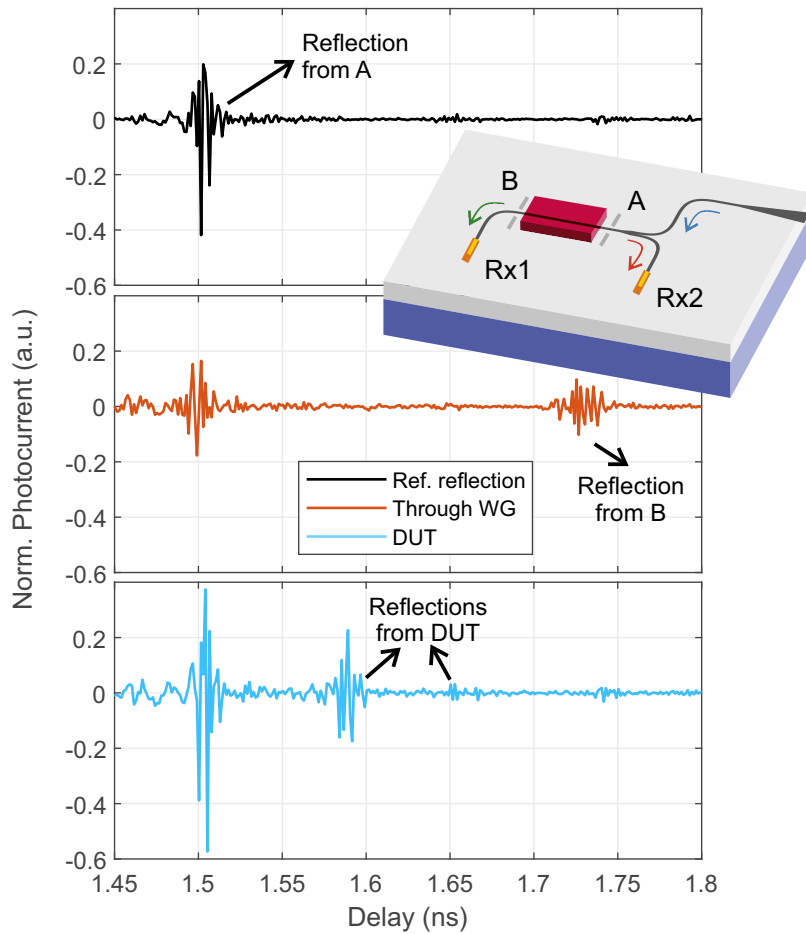


Figure 6.7.: Time-domain plot showing the measured delays in the reflection port. The reflections at 1.58 ns and 1.75 ns occur from the points A and B, respectively. The reflection from an arbitrary DUT placed between AB reaches Rx1 at an intermediate delay.

achieve. Instead, we use reflections from the open at A as reference and scale it with the simulated $|S_{11}|$ values of an abruptly terminated waveguide. To compensate for the inadequate calibration and manufacturing tolerances, we add a constant phase delay $\Delta\phi$ to the measured S-parameters, in the form $S_{ij} \cdot \exp(-j\Delta\phi)$, for an improved phase match with the simulated values. However, these added phase delays cannot appropriately compensate the dispersion in the waveguides. The power at higher frequencies are more confined within the HRFZ-Si guide, have a smaller phase velocity and consequently, arrives at a greater delay than the power travelling at lower frequencies. Despite being unimportant for PVNA calibration, the knowledge of the waveguide dispersion is crucial for an appropriate de-embedding of the measured waveguide-coupled DUTs. At this stage, the measured S-parameters in the integrated PVNA give just a qualitative rather than a quantitative characterisation of any DUT.

6.4.1. Terahertz fibre Bragg grating

Equation (2.43) relates the propagation constant of the guided modes as a function of the waveguide dimensions. Intuitively speaking, the smaller the waveguide cross-section, the higher the fraction of

guided power travelling in the evanescent fields outside the HRFZ-Si waveguide and consequently, the lower the effective RI of the guided mode. The guided wave is partially reflected whenever it experiences a change in its modal RI. We use this phenomenon to create a resonator structure by altering the waveguide width, periodically, between $w_{wg} = 100 \mu\text{m}$ and $250 \mu\text{m}$. Each section is a quarter of the guided wavelength ($\lambda_g/4$) long at the resonance frequency to mimic a DBR. The power reflectivity of such reflectors reads [187]

$$R = \left[\frac{(n_H)^{2(N+1)} - n_{wg}^2 (n_L)^{2N}}{(n_H)^{2(N+1)} + n_{wg}^2 (n_L)^{2N}} \right]^2, \quad (6.2)$$

where, n_L , n_H and n_{wg} are the effective RIs of the propagating modes in the 100, 250 and 200 μm waveguide sections, respectively and N is the number of 100 μm –250 μm section pairs.

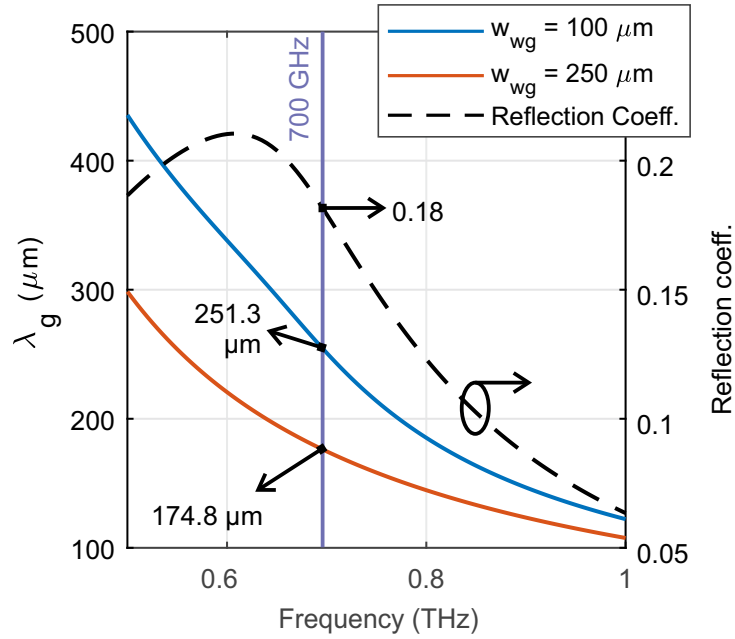


Figure 6.8.: The plot shows the simulated effective wavelength λ_g of the E_{11}^x mode at waveguide widths of 100 and 250 μm . The guided wavelength at 0.7 THz is 251.3 μm and 174.8 μm respectively. The reflection coefficient is 0.18 at 0.7 THz.

Figure 6.8 shows the simulated guided wavelength λ_g of the fundamental E_{11}^x mode for waveguide widths 100 μm and 250 μm , respectively. We designed the THz fibre Bragg grating at 0.7 THz. Correspondingly, the 250 and 100 μm wide sections are 43.7 and 62.825 μm long, respectively. The RIs are $n_{wg} = 2.37$, $n_H = 2.45$ and $n_L = 1.70$. The field reflection coefficient between the 100 and 250 μm sections is only $r = 0.18$. According to eqn. (6.2), the resonator with 61 periods of width variation between 100 and 250 μm should feature a total reflection at 0.7 THz. Simulated values show $|S_{21}| < -30 \text{ dB}$, $|S_{11}| > -0.7 \text{ dB}$ and a reflected bandwidth of $\sim 25 \text{ GHz}$ in $|S_{11}|$ at 0.7 THz. In an ideal DBR, the propagating wave experiences periodic, sharp changes in RI, defined by the physical media, whereas in the waveguide-based periodic structures, the effective RI of the propagating mode does not change abruptly between the 100 and 250 μm wide sections, rather changes smoothly. Hence, the reflectance of the simulated periodic DUT is lower than the analytical values obtained from eqn. (6.2).

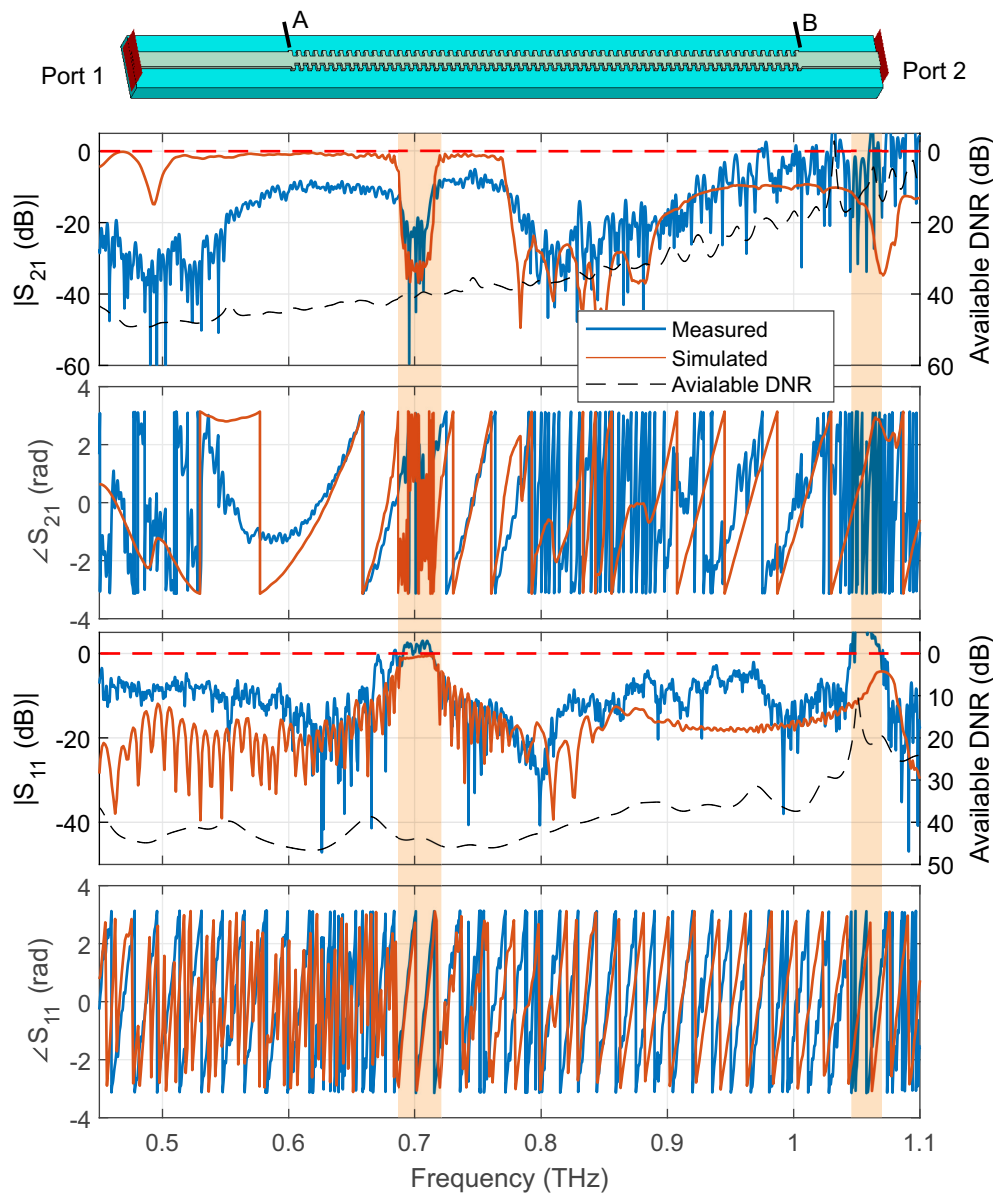


Figure 6.9.: Simulated and measured complex S-parameters of the THz fibre Bragg grating. The dashed black plots shows the available DNR for the measurements and corresponds to the right ordinate. The designed stop-band at 0.7 THz is excellent visible in the measured S_{21} through the fibre Bragg structure. The power is completely reflected by the grating structures and is detected in the S_{11} measurements. The schematic atop the plots shows the simulated THz fibre Bragg grating structure.

The periodic THz fibre Bragg grating is characterised in the modular PVNA. Figure 6.9 shows the complex S-parameter for the structure. The simulated values are added for comparison. The magnitude of the S_{21} parameter shows ≈ 10 dB higher losses than the simulated values at lower frequencies, whereas the losses are similar to the simulated values above 0.8 THz. The DUT features a ≈ 20 dB deep resonance trench around 0.7 THz, matching our design expectations and the simulated characteristics. The measured resonance trench does not feature as steep slopes as in the simulation, which is likely due

to the finite time-window (filter bandwidth) used in post-processing to reduce noise. The measured phase shows similar characteristics to the simulated values after a delay correction of 11.8 ps. The amplitude of measured S_{11} parameter prominently shows the reflected power around 0.7 THz. The measured $|S_{11}|$ goes above 0 dB due to the inaccurate calibration of the reflection port. The stop-band widths of the measured and the simulated peaks are in excellent agreement. At lower frequencies, the measured $|S_{11}|$ is 8 – 10 dB higher than the simulations and accounts for similar losses in the transmission measurements. At higher frequencies, the measured S_{11} differs from the simulated value mostly likely due to the inaccuracies in fabrication and the application of the absorptive SuperGLUE™, which also result in the weaker reflectivity of the stop bands. Regardless, the simulated resonance at 1.08 THz is discernible in both the measured S-parameters, but at ≈ 1.06 THz. The measured phase of the S_{11} parameter also shows excellent match with the simulations without any delay correction. These discrepancies between the measured and simulated S-parameters emphasize the need of appropriate characterisation tools for THz circuit components, such as the demonstrated PVNA as experimental imperfections cannot be simulated appropriately.

In the actual experiment, we measured the section between ports 1 and 2 in Fig. 6.9 as the DUT, where the total distance between the ports is designed to be 9 mm, matching the length of the through waveguide used for calibration. The grating structure (section AB) is not centrally placed and hence, the reflected signal reaches their corresponding ports of origin at different delays, t_1 and t_2 , respectively. Consequently, $\angle S_{11} = \angle S_{22} + \Delta\phi(f)$, where $\Delta\phi(f) = 2\pi f n_{wg}(f)(t_1 - t_2)/c_0$ is the resulting phase difference and c_0 is the speed of light in vacuum. The complex transmission parameters at either ports are identical but, only the magnitudes of the reflection parameters are the same. Thus, the total characterised structure is asymmetric ($S_{11} \neq S_{22}$) and a 2-port measurement is necessary for its full characterisation. Nonetheless, since we know the distance from the ports to A and B , the S-parameters of symmetric section AB can be calculated using de-embedding techniques [188], [189]. A known dispersion correction factor of the 1.5-port PVNA will significantly improve the phase accuracy of the de-embedded data.

6.4.2. Cavity resonator

We take advantage of the ~ 50 μm gap at location A to create a cavity resonator using a slotted HRFZ-Si waveguide. The designed DUT has a 450×150 μm^2 slot etched at B about 3.2 mm away from point A . Figure 6.10 shows the simulated model. The 3.2 mm-long silicon cavity (AB) resonates for both the transmission and reflection measurements. However, the 450 μm long slot reflects most of the power and hence, we see ~ 20 dB losses in the simulated S_{21} parameters.

The measured S_{11} of the cavity resonator show excellent match with the simulated values in Fig. 6.10. The delay is corrected by -4.5 ps. The periodicity of the simulated $|S_{11}|$ matches the measured values for a cavity of length $AB = 3.167$ mm, which is slightly shorter than the physical length of 3.24 ± 0.01 mm measured with the *IC measure* software [190]. The transmission parameters show higher losses than expected, most likely due to misalignment at the transmission port. Additionally, the periodicity of the measured $|S_{21}|$ is almost double that of the simulated values, which indicates larger gap between DUT and the waveguide at A . The phase of the measured S_{21} matches excellently with the simulated values after a delay correction of 1.1 ps.

Figure 6.11(a) compares the measured S_{11} parameters for two resonant cavities, namely the preceding 3.2 mm long cavity *C-3mm* and the 9 mm long cavity *C-9mm* we mentioned in Fig. 6.7. The resonances of *C-9mm* have a FSR of 4.4 GHz, compared to the 12.08 GHz FSR for the shorter resonator. Table 6.3 lists the Q-factors of two resonances for each of the resonant cavities at as high as possible frequency, yet with the resonant peak above the noise floor. The Q-factors of *C-9mm* is almost an order

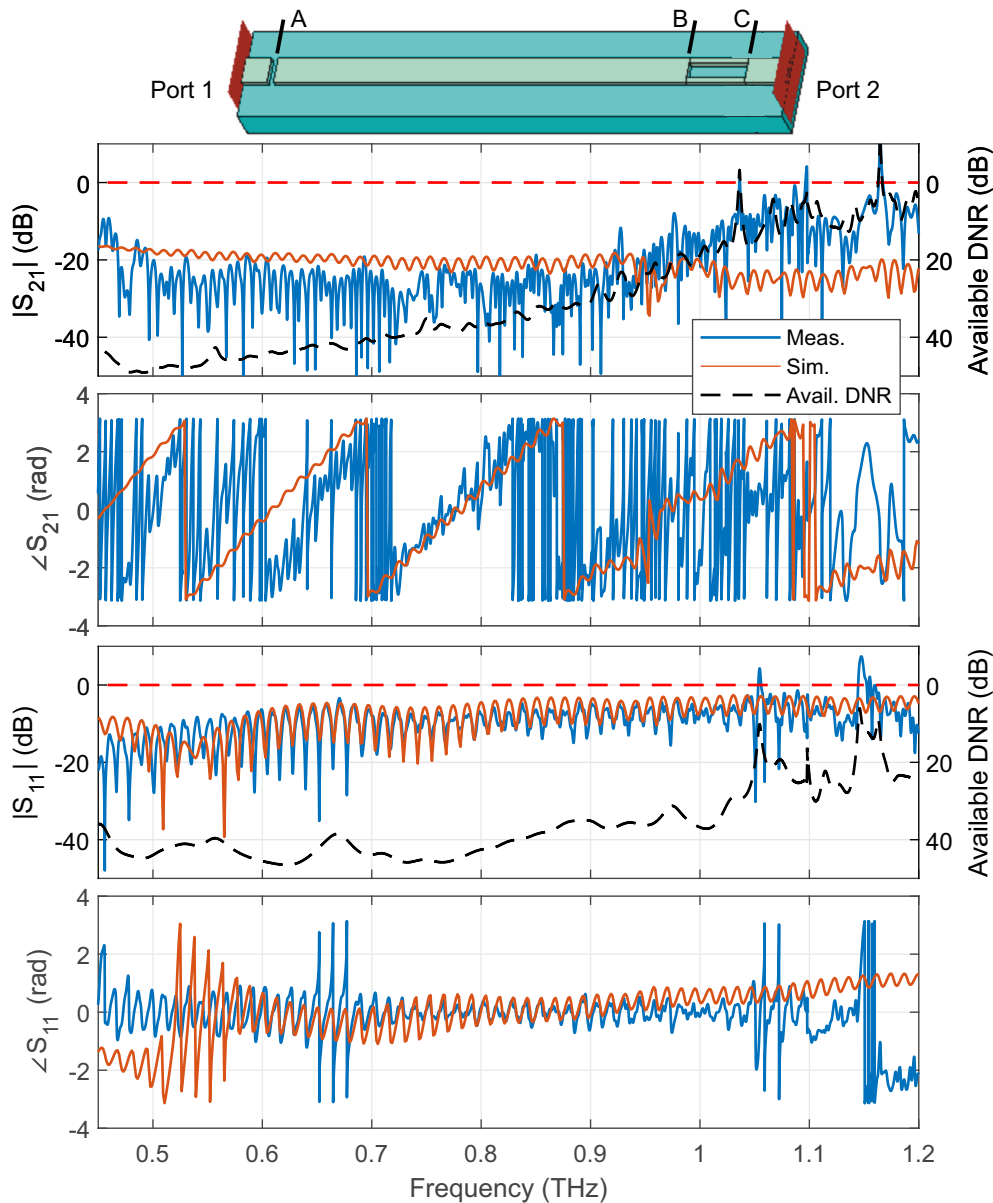


Figure 6.10.: Simulated and measured complex S-parameters of the cavity resonator. The dashed black plots shows the available DNR for the measurements and corresponds to the right ordinate. The designed distance AB is 3.2 mm and BC is 450 μm . The schematic atop the plots shows the simulated resonance cavity AB .

of magnitude larger than $C-3\text{mm}$.

Figure 6.11(b) shows the equivalent time-domain plots for the two resonators. Firstly, the dispersive nature of the waveguide is evident as the trailing pulse of the $C-9\text{mm}$ cavity is $\sim 20\%$ wider that of the $C-3\text{mm}$ resonator. Secondly, the time delay between the subsequent reflections in the former is ~ 223 ps, in contrast to the ~ 82 ps for the latter. Assuming the simulated length of $C-3\text{mm}$ is correct, the estimated length of $C-9\text{mm}$ cavity is ≈ 8.613 mm, about 2% smaller than the physical length of 8.88 ± 0.01 mm measured with the *IC measure* software. The ratio of the FSRs of the two resonators ascertains the actual length of the $C-9\text{mm}$ cavity.

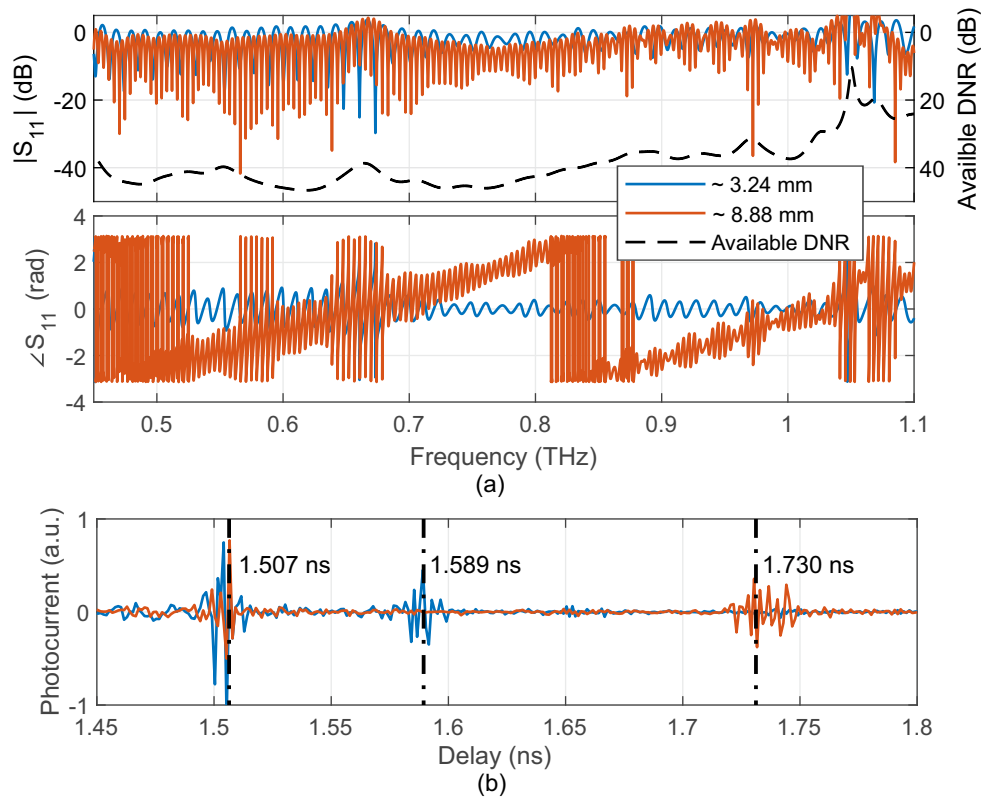


Figure 6.11.: (a) A comparison between the measured complex S_{11} parameters for resonators $C-3mm$ and $C-9mm$ reveals a 2.745-times lower FSR of the latter resonator. The phase jumps in the measured $\angle S_{11}$ plots align excellently well with the resonances. The simulated cavity lengths are $\sim 2\%$ smaller than the measured physical lengths, indicating a slightly smaller effective RI of the actual propagating mode compared to the simulated models. (b) The delays of the trailing reflections also indicate that the $C-9mm$ resonator is ~ 2.712 times larger than the $C-3mm$ one. The dispersion in the waveguide is qualitatively visible.

Table 6.3.: Q-factors and FSR of two resonances at the two cavity resonators of length 3.167 mm and ~ 9 mm. The resonances are selected with close to π phase jumps at as high as possible frequencies. The attenuation at the resonant frequencies is lower than the available measurement DNR.

Cavity length	3.24 \pm 0.01 mm		8.88 \pm 0.01 mm	
FSR	12.08 GHz		4.4 GHz	
Frequency	892.6 GHz	904.73 GHz	1036.8 GHz	1041.2 GHz
Q-factor	401	247	2,451	4,218

6.4.3. Dispersion in the waveguides

Dispersion in the HRFZ-Si waveguides broadens the equivalent pulse shape in time-domain as a function of distance travelled by the wave (see section 4.5.4). To estimate the dispersion, we use the reflections from the $C-9mm$ resonator. There is a ≈ 50 μm gap between DUT and the PVNA head at point A. In a cavity resonator, the multiple trailing reflections propagate different lengths before reaching the

receiver. Filtering the individual reflections out and comparing two successive reflections gives an estimate of the dispersion in the waveguide cavity. Figure 6.12(a) shows the equivalent time-domain pulse at the receiver at the reflection port. Two prominent reflections reach $Rx2$ at delays around 1.51 and 1.75 ns originating from A and B , respectively. We use 2 BPFs (equivalent time-window of 1 ns) $F1$ and $F2$ to segregate the reflected pulses and calculate the dispersion coefficient according to eqn. (4.18). Figure 6.12(b) plots the calculated dispersion in the cavity resonator and it shows good agreement with the measurements in the free-space setup in Fig. 4.20(b). At lower frequencies the resonator shows more dispersion most likely due to the SuperGLUE™, which changes the RI of the fields travelling outside the HRFZ-Si structure. The strong resonances above 0.75 THz occur at the gap at position A , where as the reflected pulse undergoes additional reflections at the gap. The waveguide losses can be similarly characterised, however, we need at least one more reflection to separate the reflection and the attenuation coefficients reliably.

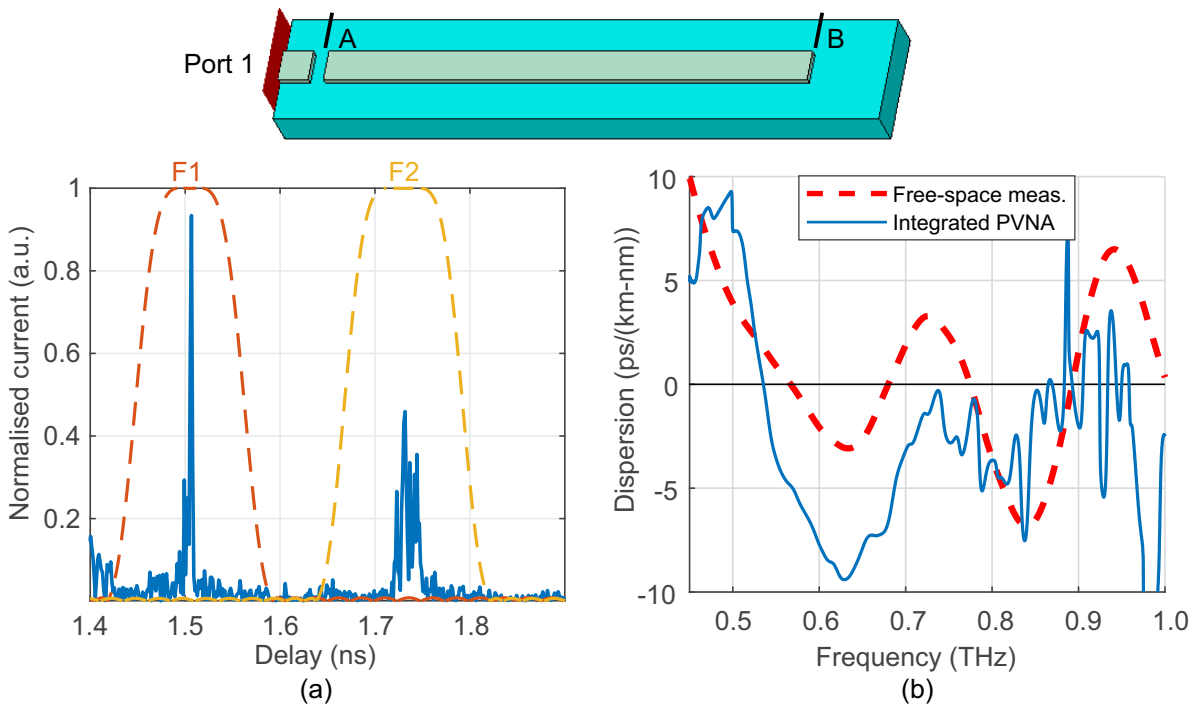


Figure 6.12.: (a) The equivalent delay plots from the frequency scans. Multiple reflections arriving at the receiver can be temporally filtered out by BPFs $F1$ and $F2$ (equivalent to time-domain windows). (b) Measured dispersion (blue) from the 9 mm long resonant cavity. The estimated dispersion of waveguides on HDPE substrate from the free-space measurement setup (red) is added for comparison. The strong oscillations in the blue graph occur as the individual reflected peaks cannot be completely segregated from the neighbouring ones and thus some standing waves leak, especially at higher frequencies. The origin of the overall oscillations with a periodicity of 200 GHz is inconclusive. It is probably a measurement artefact, either originating from standing waves in the setup or occurs due to the non-ideal tuning of the DFB laser frequencies.

6.4.4. Necessary improvements for the modular PVNA

Two aspects of the modular PVNA must be improved for reliable, accurate and repeatable measurements. Firstly, in my opinion, a robust **packaging** is crucial for the repeatability of the measurements. In the presented modular setup, alignment inaccuracies occur at least at five instances, namely, the alignment of the DFB lasers on the two receivers, the free-space alignment of the source and the two ends of the DUT with the PVNA heads. The former two misalignments can be rectified using the corresponding DC photocurrent values, however, the latter three vary between the reference and each DUT measurement. Furthermore, the vertical alignment is excruciatingly difficult without using any adhesive as surface warping of the HDPE substrate is in the order of a few tens of micrometers. Ideally, a robust packaging with an integrated THz source and fixed lenses for the incident lasers over the active devices can reduce the locations of potential misalignment to two. The DUT and the transmission port can be further mounted on a 3-D translation stage with precision micrometer screws to align the waveguide ends as accurately as possible. A gap of $< 10 \mu\text{m}$ is practically invisible to the propagating waves and hence, we need to achieve better than $10 \mu\text{m}$ alignment accuracy.

Secondly, an appropriate **calibration** routine would guarantee proper quantitative analyses of the DUTs. The free-space PVNAs use some variation of the *through-reflect-line* (TRL) calibration routine [34], [35]. Assuming a robust packaging and minimal misalignments, the phase and amplitude of the S_{21} parameter can be calibrated easily with through waveguides of different lengths. The dispersion of the waveguides can also be calibrated by similar methods. However, the dispersion in the waveguides is not an essential calibration parameter, yet it is vital for the phase estimation and subsequent de-embedding of the waveguide-coupled DUTs. Calibrating the reflection port poses a challenge as a broadband $\sim 100\%$ reflection is necessary. A metal mirror at the waveguide end-facet can solve this problem or alternatively, multiple high-reflectivity, THz fibre Bragg grating structures can be employed to attain over 95% reflections.

6.5. 2-port PVNA

Assuming the calibration and packing issues being resolved for the (semi-) integrated modular PVNA, we can extend the setup to manufacture an integrated 2-port PVNA. Figure 6.13 shows the conceptual schematic of such a setup. The waveguide in the transmission port is replaced by another splitter to create the second PVNA input port. Albeit, the transmission losses would increase by 4 – 6 dB, an integrated THz transmitter can compensate for the lost power. The two ports can be simultaneously scanned by biasing the two THz sources at different modulation IFs. The setup also requires two LIAs to simultaneously demodulate the received signal from the two sources.

6.6. Transitions to hollow metallic waveguides

In collaboration with Benedikt Krause, involved in the development of photonic spectrum analysers (PSAs) [191], [192], we have shown that the dielectric waveguides in conjunction with the ErAs:In(Al)GaAs receivers, both developed in this thesis, are well-suited for coupling to RHM waveguide-based sources. We ran a feasibility test using an electronic VNA as the THz source and a VA-coupled ErAs:In(Al)GaAs-based receiver directly coupled to a waveguide with a 90° bend. Figure 6.14(a) shows the measurement schematic. The VNA is set to 0.47 THz and the DFB lasers driving the receiver is swept between 0.47 – 0.471 THz. They act as a LO for the detected signal. Figure 6.14(b) shows the measured power in the waveguide-coupled receiver. The spectral peak is found at ≈ 0.47093 THz, in

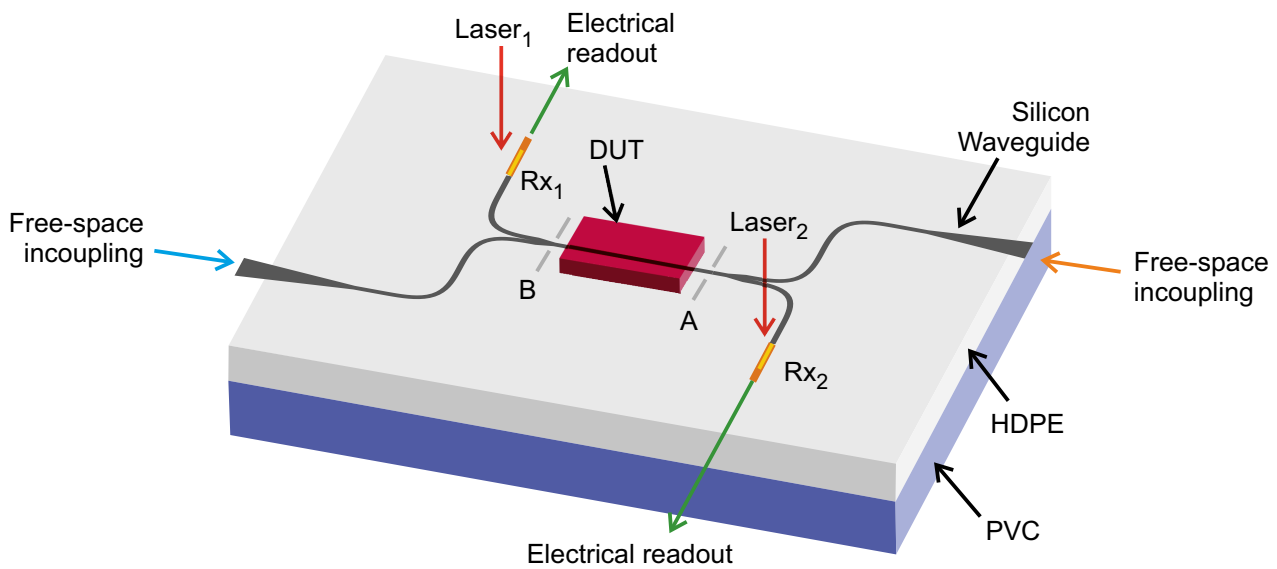


Figure 6.13.: Schematic of a (semi-) integrated 2-port PVNA architecture based on the demonstrated 1.5-port PVNA. Another splitter structures symmetrically replaces the transmission measurement port of the 1.5-port architecture.

agreement with the offset caused by the uncalibrated look-up table of the optical LO. Further details about the PSA for waveguide-coupled sources can be found in [192]. Above ≈ 0.52 THz, the simulated coupling losses between the designed HRFZ-Si-based waveguides and RHM waveguides (*WR-1.0* and *WR-1.5*) are lower than 1 dB. Thus, this scheme can be reverted to probe integrated metallic electronic circuits using RHM waveguide-coupled *ground-signal-ground* (G-S-G) probes, such as the commercially available T-wave probes, capable of measuring up to 1.1 THz [193]. This enables the on-chip measurement capability of the (semi-) integrated PVNA.

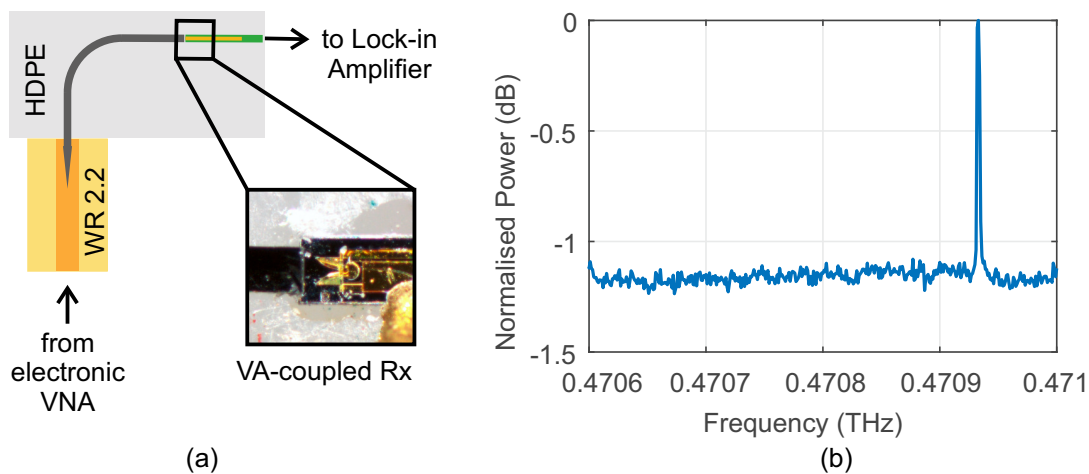


Figure 6.14.: (a) The schematic of a waveguide-coupled PSA. The waveguide is inserted in a *WR 2.2* RHM waveguide excited by an electronic VNA at 0.47 THz. (b) The resonance peak is recorded in the PSA scanned with 1 MHz step and with an integration time of $\tau = 200$ ms. The plot is adapted from [192].

In summary, we have demonstrated a prototype of the (semi-) integrated PVNA supported by the waveguide architecture developed in this thesis. We characterised a WGM resonator up to 1.5 THz and multiple resonator structures between 0.45 – 1.2 THz using the modular version of the PVNA. In this chapter, we also briefly looked at the current pitfalls of the PVNA architecture and discussed possible remedies. In essence, we successfully demonstrated a miniaturised and nearly-integrated CW, free-space PVNA setup using a waveguide-based platform in this chapter. The (semi-) integrated PVNA is indeed a broadband characterisation tool for the THz range.

7. Summary and Outlook

Using the photonic vector network analyser (PVNA) demonstrated by Fernandez Olvera *et al.* [35] as the base-design, we transformed the free-space transmission media to a HRFZ-Si waveguide-based architecture, supported by high density polyethylene (HDPE) and crystalline quartz (Qz) substrates. For the ease of integration, we changed the broadside, log-periodic antenna-coupled ErAs:In(Al)GaAs-based photoconductive receivers to end-fire Vivaldi antenna (VA)-coupled variants and directly coupled them to the waveguides. We further demonstrated a functional semi-integrated 1.5-port PVNA and characterised exemplary dielectric waveguide components. We also presented multiple data and image processing algorithms and an optimisation technique, useful for bandwidth extension of both the free-space and integrated PVNAs. The data-processing and imaging techniques can be extended to multitude of other measurement systems, irrespective of their frequency regime of operation.

7.1. Synopsis

The goal of this thesis was the miniaturisation the continuous-wave (CW), free-space PVNA operating at THz frequencies. i.e., to manufacture an integrated THz-system-on-chip (SOC). After providing the necessary theoretical background on dielectric waveguides, photomixing and antennas, we start chapter 3 with a brief analysis of the free-space PVNA design and detail several of its applications in material characterisation and imaging. We estimated the refractive index (RI) and thickness of single layered, lossless, dielectric structures using Fabry-Pérot resonances in planar devices under test (DUTs). We showed two different algorithms for optical thickness estimation using the amplitude and phase of the measured Fabry-Pérot transmission coefficient in S_{21} . We developed a scattering transfer parameter (T-parameter)-based modelling technique for multilayered structures and proposed a vectorial optimisation method to determine thicknesses and RIs of the individual layers from the measured S-parameters. Initial tests show that the vectorial optimisation has comparable accuracy, but better convergence with respect to the widely used Nelder-Mead simplex algorithm (NMA) (see Appendix A.2), however, an extensive comparison of the algorithms is yet to be done. Furthermore, we were able to image structures as small as 50 nm thick using the phase of the measured S_{21} parameter. The thickness corresponds to $\lambda/10,000$ in the farfield, with a precision of $\lambda/15,000$ [66]. We also put forward an imaging technique using zero-padding which emulates large bandwidth scans and does not necessitate a thick substrate for imaging thin, low RI films. We successfully imaged a relative thickness difference of 350 nm using only a 10 GHz frequency scan, i.e., ~ 5 orders of magnitude lower than the Fourier-transformed delay resolution. We additionally demonstrated data processing techniques which can improve the operational range of the free-space PVNAs, and more generally, of any homodyne CW system, by $\approx 30\%$ and improve the system dynamic range (DNR) by ~ 20 dB, without any significant increment of measurement time. We have submitted a patent regarding the digital post-processing techniques [69].

As a next step, we designed the overmoded dielectric waveguides architecture necessary to miniaturise the free-space PVNA. The employed deep reactive-ion etching (DRIE) process etches 50 μm thick HRFZ-Si wafer within half an hour and features a side-wall undulation in the order of 10 nm. The HDPE or

Qz substrates support the $50 \times 200 \mu\text{m}^2$ waveguides. The single mode bandwidth of the waveguides is between 0.5 – 0.75 THz, however, with appropriate design and excitation, they can be operated in the fundamental mode up to as high as 1.5 THz. Circular bends with radii ≥ 4 mm suppress mode conversion and facilitate broadband operation. Sine-squared bends with non-linearly increasing curvature reduce the required bend radii (see section 4.3.3) to ≈ 2.4 mm. The waveguides are characterised in a free-space setup, where a Gaussian THz beam excited the waveguides. The total incurred in- and out-coupling losses are between 28 – 30 dB for Qz substrate and 18 – 26 dB for HDPE substrate. In comparison, the transmission losses in the guides are between 0.4 – 1 dB/cm, increased significantly due to the presence of cyanoacrylate adhesives underneath. We also fabricated and measured a 3-dB splitter structure, which eventually replaces the polariser-based splitters employed in the free-space PVNA.

To reduce the coupling losses to the waveguides, we demonstrated a direct-coupling mechanism for the active devices, especially the ErAs:In(Al)GaAs-based photoconductive receiver. We designed and simulated end-fire VAs using CST® microwave studio and fabricated them in-house. We further characterised two specific designs in conjunction with the waveguides, which are later extensively used in the integrated PVNA setup. The VAs show similar performance as commonly used log-periodic antennas without the silicon lens. Directly coupling the VAs to the waveguides lowers the coupling losses by 8 – 12 dB per coupling interface and extends the operation bandwidth of the semi-integrated PVNA to ≈ 1.5 THz. The coupling losses between the end-fire antenna and the waveguide are < 5 dB between 0.6 – 0.9 THz. However, the losses become comparable to free-space coupling above 1 THz. Hence, a thinner VA substrate and further design improvements are necessary.

With the waveguide architecture and the active elements at hand, we assemble a 1.5-port semi-integrated PVNA in chapter 6. We demonstrated its functionality by characterising symmetric dielectric structures. The 1.5-port measurements are sufficient for a full characterisation of the DUT [34] as $S_{11} = S_{22}$ and $S_{12} = S_{21}$. We lack a powerful integrable THz source and hence, we resorted to free-space in-coupling from a commercial P-I-N diode-based transmitter. The data-processing techniques developed in chapter 3 are extensively used during the estimation of S-parameters, to compensate for the free-space in-coupling losses and for extending the measurement bandwidth till 1.5 THz. Some important results of DUT characterisation using the semi-integrated PVNA are as follows:

- We measured quality factors (Q-factors) up to 20,000 at 0.9 THz of resonances from a HRFZ-Si-based planar whispering gallery mode (WGM) resonator demonstrating sufficient dynamic range and resolution even for such high-Q resonances.
- We characterise a THz fibre Bragg grating structure which shows $> 95\%$ reflections over a bandwidth of 20 GHz. In the future, it can be utilised for calibrating the integrated PVNA.
- A 9 mm long cavity resonator features resonances of Q-factors $> 4,000$ at 1.04 THz.
- We show that the mode conversion is suppressed in sine-squared bends by at least 1 dB per 90° bend as compared to the circular ones above 1.35 THz for effective bend radii of 2.4 mm. However, this result is inconclusive and hence, is presented in appendix A.4.

Expectedly, we also face some calibration hurdles arising from varying DUT sizes and misalignment with the free-space Gaussian THz beam. This emphasises the necessity of a directly-coupled THz source for a robust operation of the PVNA. Regardless, we show DUT characterisation between 0.5 – 1.5 THz using the same waveguide and the VA-coupled ErAs:In(Al)GaAs-based receivers. This operational bandwidth can be further extended up to 2 THz and beyond, with the availability of a powerful, integrable THz source and a receiver with thinner substrate. With the exception of the source, we

miniaturise the free-space CW PVNA to a THz-photonic integrated circuit (THz-PIC) and extend its operational bandwidth up to 1.5 THz. The presented semi-integrated PVNA architecture provides a feasible alternative to highly expensive and comparatively narrowband electronic vector network analyser (VNA) extenders, at least for dielectric component characterisation. The demonstrated hollow metallic waveguide transition in section 6.6 presents a promising scheme of its integration with the commercially available *ground-signal-ground* (G-S-G) probes to characterise integrated electronics circuitry.

7.2. Outlook

Upgrading the 1.5-port PVNA to a 2-port system just requires changing the waveguide bend at the second port by a splitter. However, this would result in an additional 4 – 6 dB losses at the receiver of the second port (c.f section 4.5.5). The exemplary PVNA shown in this thesis is a proof-of-concept. For a commercially viable product, it lacks robustness and repeatability. In addition to an improvement in VA design, we suggest four-fold follow-up work as an outlook.

1. Most measurement inconsistencies arise from misalignments either at the free-space in-coupling port or at the waveguide-DUT junction (positions *A* and *B* in Fig. 6.1). A robust packaging with integrated optical and electrical connections will reduce these alignment errors significantly. Additionally, mounting the DUT and the PVNA-head of at least one port on 3-D translation stages with micrometre precision will increase the flexibility and scalability of the integrated PVNA.
2. Assuming a robust packaging, an accurate calibration of the PVNA heads is necessary to characterise DUTs both qualitatively and quantitatively. In this regard, the *through-reflect-line* (TRL) calibration technique can be exploited. A set of sub-wavelength periodic structures together can induce very high reflections (> 95%) over a large bandwidth, adequate to appropriately calibrate the reflection measurements. However, in such cases, a proper calibration mechanism for the reflected phase must be devised.
3. Electronic VNAs feature power monitors in order to compensate for drifts in the system. Power monitors, like Schottky-based direct detectors can easily be integrated in the PVNA by tapping off a small fraction of power from each source using the coupler structures developed in this thesis, redesigned to achieve 10 : 90 splitting ratio or similar.
4. Finally, a mechanism to measure metallic transmission line-coupled structures will make the integrated PVNA viable and affordable alternative to its electrical counter part. A coplanar striplines (CPS) line in *ground-signal* (G-S) or G-S-G configuration can be attached to VAs to transfer the guided power in the waveguides to metallic electrical networks. Alternatively, the dielectric waveguides can be directly coupled to rectangular hollow metallic (RHM) waveguide-coupled commercial G-S-G probes as shown in section 6.6.

A. Appendices

A.1. Lock-in detection

The *Toptica source control* biases the transmitter (Tx) at a modulation frequency f_{mod}^{Tx} to aid in lock-in detection. The output of the receiver (Rx) reads as

$$i_{det}(f_{THz}) = i_{THz}(f_{THz}) \cos(2\pi f_{mod}^{Tx} t), \quad (A.1)$$

where i_{THz} is given by eqn. (1.1) and $f_{mod}^{Tx} \ll f_{THz}$. Since the same pair of distributed feedback (DFB) lasers are used for both Tx and Rx, the detection mechanism is homodyne. See Fig. 1.2 for reference.

The lock-in amplifier (LIA) located in the *Toptica source control* first demodulates the amplified i_{THz} and then, averages it over an integration time (or time constant) of τ to reduce the measured noise even further. A 10-fold increment in τ results in ~ 10 dB reduction in the measured noise power. Mathematically, the operation of an (ideal) LIA with an integration time τ reads

$$i_{LIA}(f_{THz}, \tau) = \frac{2}{\tau} \int_{t-\tau}^t i_{TIA}(f_{THz}, t) \cdot r(t) dt, \quad (A.2)$$

where, $i_{LIA}(f_{THz}, \tau)$ is output current of the LIA, i_{TIA} is the output current from the transimpedance amplifier (TIA) and $r(t) = \cos(2\pi f_{mod}^{Rx} t)$ is the normalized demodulation signal. Assuming additive noise at the detector and an amplification factor of A_{TIA} at the TIA, i_{TIA} reads

$$\begin{aligned} i_{TIA}(f_{THz}, t) &= A_{TIA} \cdot i_{det}(f_{THz}) \\ &= A_{TIA} \cdot [i_{THz} \cos(2\pi f_{mod}^{Tx} t) + i_N(f_{THz}, t)] \end{aligned} \quad (A.3)$$

Using eqn. (A.3) in (A.2), the output current of the LIA alternatively reads as

$$\begin{aligned} i_{LIA}(f_{THz}, \tau) &= \frac{A_{TIA}}{\tau} \int_{t-\tau}^t i_{THz}(f_{THz}) \cos(2\pi [f_{mod}^{Tx} - f_{mod}^{Rx}] t) dt \\ &\quad + \frac{A_{TIA}}{\tau} \int_{t-\tau}^t i_{THz}(f_{THz}) \cos(2\pi [f_{mod}^{Tx} + f_{mod}^{Rx}] t) dt \\ &\quad + \frac{2A_{TIA}}{\tau} \int_{t-\tau}^t I_N(f_{THz}, t) \cos(2\pi f_{mod}^{Rx} t) dt. \end{aligned} \quad (A.4)$$

Since the usual integration time $\tau \gg 1/f_{mod}^{Tx(Rx)}$, the second term equates to zero. The first term is essentially the amplified detector current. Ideally, the modulation frequency at the transmitter and at the receiver is identical, however, in practice, the modulation frequency feature a non-zero bandwidth. When $f_{mod}^{Tx} - f_{mod}^{Rx} \neq 0$, the integral decays to zero as $\text{sinc}(2\pi [f_{mod}^{Tx} - f_{mod}^{Rx}])\tau$ and consequently, some noise components leaks through the LIA. The *sinc* decay in the time domain corresponds to a boxcar function in the frequency domain

$$I_{LIA}(f_{THz}) = \frac{1}{2\pi} \int_{-\infty}^{\infty} i_{TIA}([f_{mod}^{Tx} - f_{mod}^{Rx}]) \cdot \tau \cdot \Pi(2\pi f\tau/2) df, \quad (A.5)$$

where $\Pi(t)$ is a normalised boxcar function and $i_{TIA}(f)$ is the frequency spectrum of the detected current.

A.2. Performance of the vectorial error minimisation

The vectorial minimisation technique is compared with `fminsearch`, the Matlab implementation of the commonly used NMA. A distributed Bragg reflector (DBR) [35] with three layers of HRFZ-Si ($n_{Si} = 3.416$, $d_{Si} = 520 \pm 25 \mu\text{m}$), separated by two air-gaps ($d_{air} \approx 150 \mu\text{m}$) is measured with a fast CW system [27] between 0 – 1.314 THz. Three separate fitting cases are considered, namely

- Case I: Parameters \hat{n}_{Si} , \hat{d}_{Si} and \hat{d}_{air} are optimised, where \hat{n}_{Si} is the estimated refractive index of the silicon layer. Estimated thicknesses of all silicon layers and air gaps are considered to be \hat{d}_{Si} and \hat{d}_{air} respectively.
- Case II: Parameters $\hat{d}_{Si,1}$, $\hat{d}_{air,1}$, $\hat{d}_{Si,2}$, $\hat{d}_{air,2}$ and $\hat{d}_{Si,3}$ are optimised, where $n_{Si} = 3.416$ is assumed.
- Case III: Parameters \hat{n}_{Si} , $\hat{d}_{Si,1}$, $\hat{d}_{air,1}$, $\hat{d}_{Si,2}$, $\hat{d}_{air,2}$ and $\hat{d}_{Si,3}$, where the refractive index of silicon and individual layer thicknesses are estimated.

The results and performance metrics are tabulated in Table A.1. We tested both the algorithms based on the same error calculating function. The optimisation accuracy for the vectorial error minimisation is comparable to the NMA for the optimisation of three and five parameters, even though the latter is faster. The performance the former is significantly improves as the complexity of the model and number of parameters to be optimised increases. The convergence of NMA for higher order optimisations highly depends on the initial simplex and it does not converge for different sets of initial values in case II. The said algorithm fails to find the optimal set of parameters for case III. A more constrained implementation of NMA, `fmincon`, performs better than the vectorial optimisation in this case, given an appropriate initial simplex is set. Vectorial optimiser shows similar residual errors as `fmincon` if higher estimation accuracy is set, albeit at an expense of longer optimisation time.

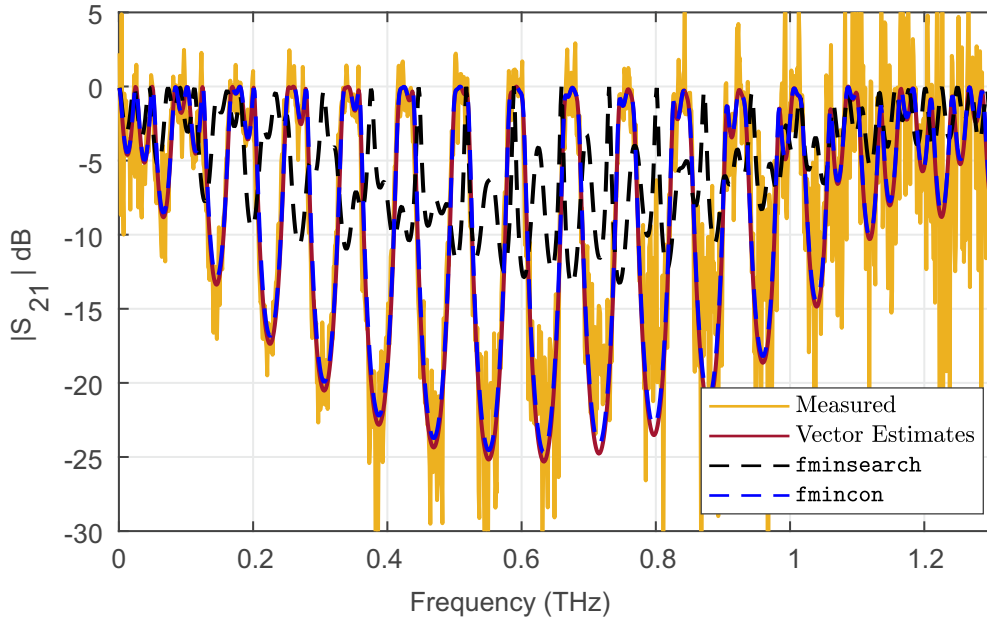


Figure A.1.: Plot shows the comparison of measured data and estimated data using vector-based approach and NMAs, both unconstrained and constrained variant, for case III.

Table A.1.: Comparison of residual errors and optimisation time between vectorial minimisation and NMAs in Matlab (fminsearch and fmincon). Asterisked estimates are obtained in the best case scenario, where the algorithm converges towards the actual values.

Algorithm	Case I		Case II		Case III	
	Time (s)	Res. error	Time (s)	Res. error	Time (s)	Res. error
fminsearch	4.01	11.21	7.13*	10.97*	25.23	16.32
fmincon	–	–	–	–	9.88*	10.94*
Vectorial optimiser	15.70	11.21	8.33	10.97	17.30	10.96
Optimised Params.	3		5		6	

Fig. A.1 plots the measurement and fitted data for case III. In contrast to the NMA estimates, the parameters found using vectorial optimisation regenerates the measurement curve excellently. The estimated thicknesses of silicon wafers are $520.95 \mu\text{m}$, $519.93 \mu\text{m}$ and $517.93 \mu\text{m}$ in order, whereas, the estimated air-gaps between them are $129.38 \mu\text{m}$ and $114.09 \mu\text{m}$ respectively. The estimations are in good agreement with the actual values [35].

A.3. Gaussian beam diameter

The electric field distribution of a radially symmetric Gaussian beam propagating along positive z -direction reads as [142],

$$E_s(r, z) = E_0 \exp \left[-\frac{r^2}{\rho(z)^2} \right], \quad (\text{A.6})$$

where r is the radial distance from the centre of the beam and $\rho(z) = \rho_0 \sqrt{1 - (z/z_R)^2}$ is the transversal location where $E_s = E_0/e$ at any longitudinal position z , E_0 being the maximum field intensity occurring at $r = 0$, ρ_0 is radius of Gaussian beam at its focus and $z_R = \pi \rho_0^2 / \lambda$ is the Rayleigh distance. Thus, transmitted power P_ρ through any circular aperture of radius ρ_{ap} concentric to the Gaussian beam equates to

$$\begin{aligned} P_\rho &= P_{\rho \rightarrow \infty} \int_0^{\rho_{ap}} \exp \left[-\frac{2r^2}{\rho(z)^2} \right] dr \\ &= P_{\rho \rightarrow \infty} \left[1 - \exp \left\{ \frac{-2\rho_{ap}^2}{\rho(z)^2} \right\} \right]. \end{aligned} \quad (\text{A.7})$$

Thus the transmission coefficient through the aperture T is given by

$$T = \frac{P_\rho}{P_{\rho \rightarrow \infty}} = 1 - \exp \left[-2 \frac{\rho_{ap}^2}{\rho^2(z)} \right]. \quad (\text{A.8})$$

To estimate the Gaussian beam radius at the focus F in the THz setup shown in Fig. 1.2, we place an circular iris diaphragm between lens $L1$ and F at longitudinal distances z_1 , z_2 and z_3 from the focus and measure the corresponding transmission coefficient T_1 , T_2 and T_3 . We note that the absolute positions of the iris are insignificant, however, the relative displacements, i.e., $(z_2 - z_1)$ and $(z_3 - z_1)$, are important to derive Gaussian beam width at the focus. Additionally, the radius of the iris must be comparable or smaller than the Gaussian beam at these longitudinal positions and hence, having them closer to the lens results in better estimates. The diffraction caused by the iris aperture is negligible as the aperture is much larger than the wavelength of the THz beam.

Using eqn. (A.8), we can write

$$\ln(1 - T_1) = \frac{2\rho_{ap}^2}{\rho^2(z_1)} \quad (\text{A.9})$$

$$\ln(1 - T_2) = \frac{2\rho_{ap}^2}{\rho^2(z_2)} \quad (\text{A.10})$$

$$\ln(1 - T_3) = \frac{2\rho_{ap}^2}{\rho^2(z_3)}. \quad (\text{A.11})$$

Using values of $\rho(z)$ in equations (A.9) and (A.10) result in

$$\frac{\ln(1 - T_1)}{\ln(1 - T_2)} = 1 + \frac{2z_1(z_2 - z_1) + (z_2 - z_1)^2}{z_R^2 + z_1^2} = B. \quad (\text{A.12})$$

Similarly, dividing eqn. (A.11) by (A.9) result in

$$\frac{\ln(1 - T_1)}{\ln(1 - T_3)} = 1 + \frac{2z_1(z_3 - z_1) + (z_3 - z_1)^2}{z_R^2 + z_1^2} = A. \quad (\text{A.13})$$

Dividing (A.12) by (A.13), we get

$$\frac{A-1}{B-1} = \frac{2z_1(z_2 - z_1) + (z_2 - z_1)^2}{2z_1(z_3 - z_1) + (z_3 - z_1)^2} \quad (\text{A.14})$$

Solving eqn. (A.14) we obtain z_1 as

$$z_1 = -\frac{(A-1)(z_3 - z_1)^2 - (B-1)(z_2 - z_1)^2}{2[(A-1)(z_3 - z_1) - (B-1)(z_2 - z_1)]}. \quad (\text{A.15})$$

Thus, the absolute distance z_1 is obtained from the relative displacement of the iris diaphragm and the corresponding transmission coefficients. Subsequently, the values of z_2 and z_3 are calculated from the known relative displacements of the iris.

Again diving eqn. (A.9) by (A.10), we get

$$A = \frac{\ln(1 - T_1)}{\ln(1 - T_2)} = \frac{z_R^2 + z_2^2}{z_R^2 + z_1^2}, \text{ and hence,}$$

$$z_R^2 = \frac{z_2^2 - Az_1^2}{A-1} = \frac{\pi^2 \rho_0^4}{\lambda^2} \quad (\text{A.16})$$

Manipulating eqn. (A.16), we obtain the $1/e^2$ Gaussian beam radius at its focus (ρ_0) for the THz setup as

$$\rho_0 = \left(\frac{\lambda^2}{\pi^2} \frac{z_2^2 - Az_1^2}{A-1} \right)^{1/4}. \quad (\text{A.17})$$

A.4. Characterisation of waveguide bends using modular PVNA

We use the modular PVNA (c.f. section 6.4) to do the pending characterisations from chapter 4 and measure the transmitted power through waveguides with multiple 90° bends. Table A.2 lists the dimensions and the measurement parameters of 4 measured waveguides. We have used *Antenna B* (see Fig. 6.4) to characterise these waveguides.

Table A.2.: Nomenclature of the measured bends with an effective bend radius of 2.4 mm. In total, three waveguides with circular curvatures and a waveguide with sine-squared curvature are characterised. Comprehensive list of other measurement parameters are also listed.

Setup	DUT	Total length	Band	DC photo-current	Integration time
Modular PVNA	<i>C04</i> – Waveguide with 360° circular bend	16.91 mm	1 2	3.10 μA 2.80 μA	100 ms
	<i>C08</i> – Waveguide with 720° circular bend	30.16 mm	1 2	3.80 μA 3.90 μA	100 ms
	<i>C16</i> – Waveguide with 1440° circular bend	60.32 mm	1 2	3.60 μA 4.00 μA	100 ms
	<i>S10</i> – Waveguide with 90° sine-squared bend	44.10 mm	1 2	3.70 μA 3.80 μA	100 ms

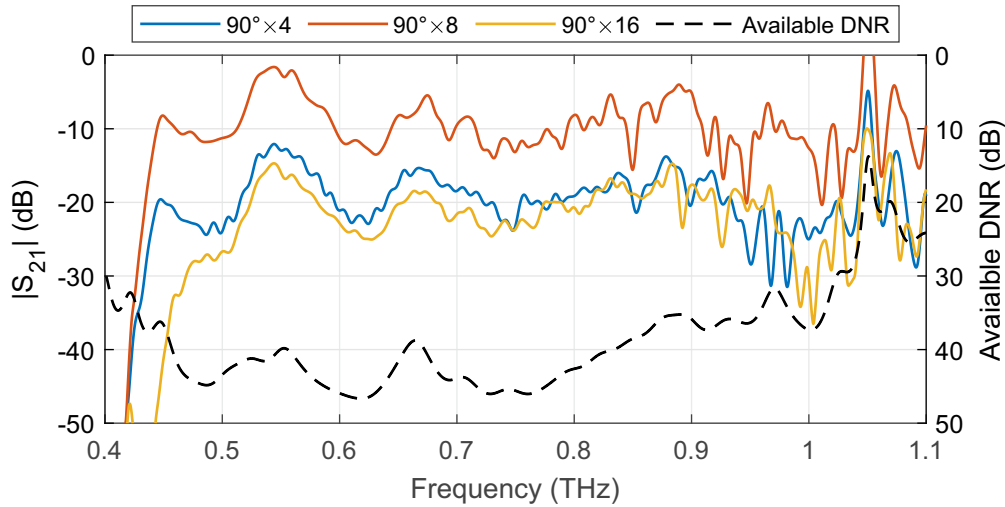


Figure A.2.: Comparison of $|S_{21}|$ between waveguides with circular bends with total curvature of 360°, 720° and 1440°. Misalignment reduces the measured $|S_{21}|$ of the waveguides with minimum and maximum curvatures by $\sim 7 - 10$ dB respectively with respect to the waveguides with 720° total bends. The length of the waveguides can in found in Table A.2.

We plot the measured $|S_{21}|$ in figures A.2 and A.3, normalised to a 9 mm long straight waveguide used in calibrating the transmission port. Figure A.2 shows a comparison of waveguides with circular bends. The measured $|S_{21}|$ is highest through *C08*, whereas the $|S_{21}|$ of *C04* and *C16* are comparable. There is an ≈ 10 dB difference between *C04* and *C08* over the whole frequency range, which indicates severe misalignment within the PVNA system or at the free-space in-coupling. The $|S_{21}|$ of *C16* decreases

severely above 1 THz, which results from the power coupling to the higher-order modes (HOMs). The decrement is subtler for *C04* and *C08*, waveguides with lower total curvature. At frequencies < 0.5 THz, losses of *C16* is significantly higher than the other two owing to the its larger length.

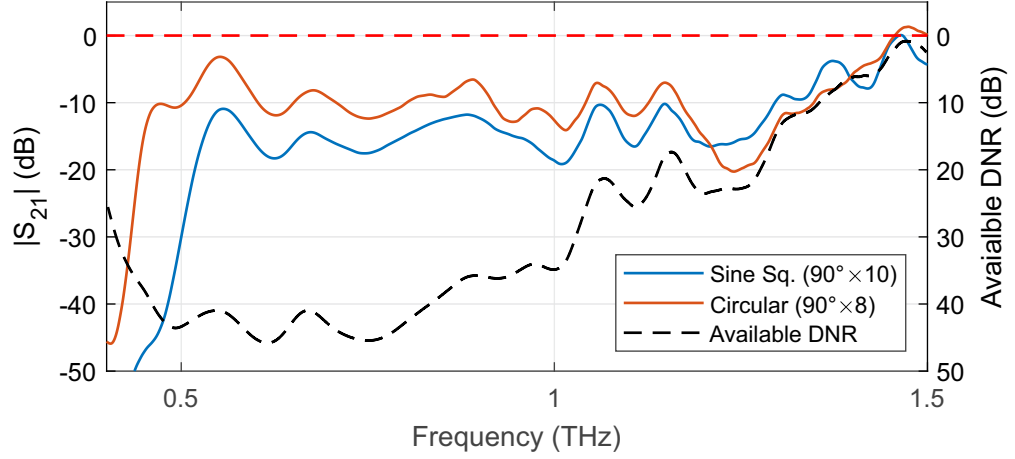


Figure A.3.: $|S_{21}|$ comparison between waveguides *S10* and *C08*. Despite of being shorter and featuring less curvature, the losses in *C08* are significantly higher at frequencies > 1.2 THz than the former owing to mode conversion. The plot is smoothed over 25 GHz to remove the effects of waterlines and VA resonances.

Figure A.3 shows a DNR-comparison between a sine-squared bend (*S10*) of length 44.10 mm, with a total bend of 90° and *C08*, a 30.16 mm long waveguide with 720° of circular curvature. The measured $|S_{21}|$ of the sine-squared bend is ~ 5 dB lower than the circular curvature between 0.55 – 1 THz due to alignment inaccuracies. Two further discrepancies between the measured DNR over 0.4 – 1.6 THz are immediately noticeable:

1. The losses at frequencies < 0.5 THz are higher in the sine-squared bend than the circular bend. The maximum curvature of the sine-squared bend exceeds the constant curvature of the circular bends, resulting in higher radiation losses at lower frequencies. A comparison of figures 4.9(b) and (e) explains this behaviour. The boundary of ρ_{lim} , beyond which all the travelling power is radiated, comes much closer to the waveguide in the case of sine-squared bends compared to the circular ones. The evanescent fields at lower frequencies extend more outside the waveguide and hence, suffer more radiation losses than at higher frequencies.
2. The losses in *C08* are visibly larger than that of *S10* above 1.2 THz, which indicates the advent of mode conversion in the former structure. Extrapolated to 1.35 THz after being adjusted for the misalignments, the sine-squared bend shows ≈ 10 dB DNR lower losses than the circular, despite of being 14 mm shorter and having 180° less curvature. Numerically calculated, the sine-squared curvatures suppresses power conversion to HOMs by at least 0.97 dB per $/90^\circ$ above 1.35 THz compared to a circular curvature with the same radius of 2.4 mm.

Furthermore, the difference of $|S_{21}|$ between both the bends is practically constant between 0.5 – 1 THz despite of the difference in the waveguide lengths. This asserts that the propagation losses in the designed waveguides are negligible in this frequency range. At higher frequencies, the attenuation constant is expected to be even lower, as more power travels within the HRFZ-Si structure. A comparison of waveguides with sine-squared bends, but with varying length can help estimate the

attenuation constant at higher frequencies. At this juncture, the *Rx1* with antenna *B* broke down during measurements and the measurements could not be repeated with better alignment. We replaced it by another receiver with antenna *C*. All the subsequent measurements in this thesis use a receiver coupled to antenna *C* at the transmission port and another receiver coupled to antenna *D* at the reflection port. Therefore, we cannot present an appropriate comparison between waveguides of different lengths above 1 THz.

A.5. Deep reactive-ion etching

DRIE is a process of anisotropic etching comprised alternating etching and deposition steps, each lasting only for a few seconds. Each individual etching step is isotropic, followed by the deposition of a chemically inert passivation layer, which protects the overall substrate from the getting further attacked by the etchant. In the following etching step, the passivation layer at the bottom of the etched trench is removed by the sputtering of the directional etchant ions and further chemical etching of the exposed substrate occurs. However, the side walls of the trench is protected by the passivation layer from this chemical etching process. This etching-deposition cycle is repeated several times to achieve a quasi-anisotropic deep-etch of the substrate. Figure A.4 shows the DRIE process used for etching silicon. Usually, sulphur hexafluoride (SF_6) is used as the etchant and Octafluorocyclobutane (C_4F_8) is used to create the passivation layer. The process was patented in 1996 by *Robert Bosch GmbH* and is, thus, also commonly known as *Bosch process*. We carried out the DRIE of silicon wafers used in this thesis out at the group for Nanofabrication (TDSU1) of the Max Planck Institute for the Science of Light (MPL) in Erlangen, Germany using a “Plasmalab System 100” from *Oxford Instruments*.

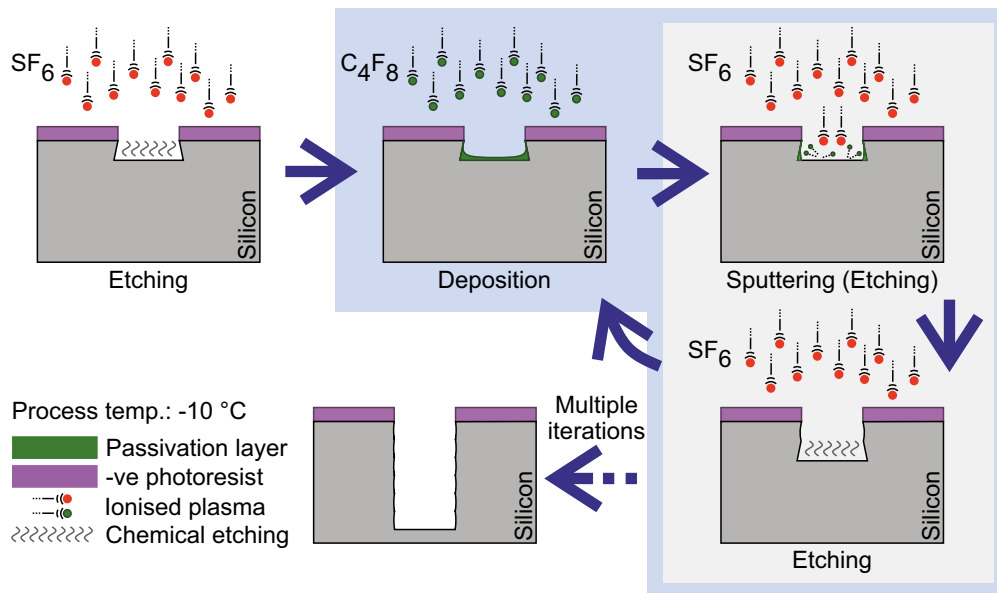


Figure A.4.: Schematic showing the alternating etching and deposition processes during DRIE of silicon.

Etching steps and process parameters

The silicon wafers are first glued to quartz substrates using cyanoacrylate adhesive (SuperGLUE™) for mechanical support during processing. Thereafter, a photolithography step is carried out to create a protective layer atop the waveguide structures. A high selectivity between the silicon wafer and the protective photoresist layer is necessary to achieve deep etching and a $3\text{ }\mu\text{m}$ -thick hard-baked photoresist AZ *nLof 2035* is used for a silicon wafer thickness of $50\text{ }\mu\text{m}$. The samples are kept under white light for 1 – 2 days and finally baked at $110\text{ }^\circ\text{C}$ for 10 minutes.

The complete etching process is an iteration of the 3 distinct steps, namely etching, deposition and cooling down. The etching-deposition cycle is repeated M times before running a sample cooling down phase. The etching rate decreases as the sample heats up and thus, M is kept in the range

of 10 – 12. Each etching-deposition cycle removes $\approx 750 - 800$ nm of silicon and thus the whole etching-deposition-cool down cycle is repeated for $N = 5$ times for a 50 μm etch depth. For etching an depth 180 μm , a total of $N \times M = 19 \times 12$ iterations are needed, however etching rate also deteriorates with increased iterations as the purity of the etching chamber is compromised. The detailed recipe used for the DRIE of silicon is as follows:

- Repeat N times
 - Cool down
 - Etching (*hold*)
 - Repeat M times
 - * Deposition (*hold*)
 - * Etching (*hold*)
 - Deposition
- Pump Down

The steps with *hold* in parenthesis signify steps where plasma is not shutdown after the step is completed. Process parameters are tabulated in Table A.3.

Table A.3.: Process parameters for the etching and deposition steps

Step	C_4F_8	SF_6	Pressure	RF power	ICP power	Duration
Cool down	0 sccm	0 sccm	0 mT	0 W	0 W	120 s
Etching	10 sccm	120 sccm	30 mT	25 W	700 W	8 s
Deposition	100 sccm	5 sccm	20 mT	4 W	700 W	5 s
Pump down	0 sccm	0 sccm	0 mT	0 W	0 W	30 s

Characteristic features of an etched sample

Micrographs in figure A.5 show scanning electron microscope (SEM) images of an etched silicon wafer using DRIE. Figure A.5(a) shows a partially etched waveguide structure with a layer of photoresist on top. Lateral imperfections in the range of 0.1 – 0.5 μm of the waveguide side-walls occur due to the limited pixel resolution of the photolithographic mask, which, in this case, is ≈ 6 μm . Figure A.5(b) shows the vertical stepped profile of the waveguide side-walls. Shorter etching-deposition steps and a fast switching time in-between results in smaller undulation structures. In this work the vertical undulations are in the order of a few nanometres. Thus, the waveguides etched out of a double-side-polished silicon wafer have optically smooth top and bottom surfaces, however, inaccuracies in the photolithographic mask significantly contributes to roughness of the side-walls.

If the photoresist layer is not optimally hard-baked, the SF_6 ions sputters fragments of the photoresist, which are subsequently redeposited in the areas to be etched resulting in needle like structures on the etched surface as depicted in Figure A.5(c). This is not critical for the waveguide fabrication process as the silicon between the waveguides are completely etched through. Additionally, larger etching depth also necessitates an optimal ratio between the duration of the etching and deposition steps. Figure A.5(d) shows a non-ideally etched sample where an etch depth of 130 μm results in retrograde side-walls.

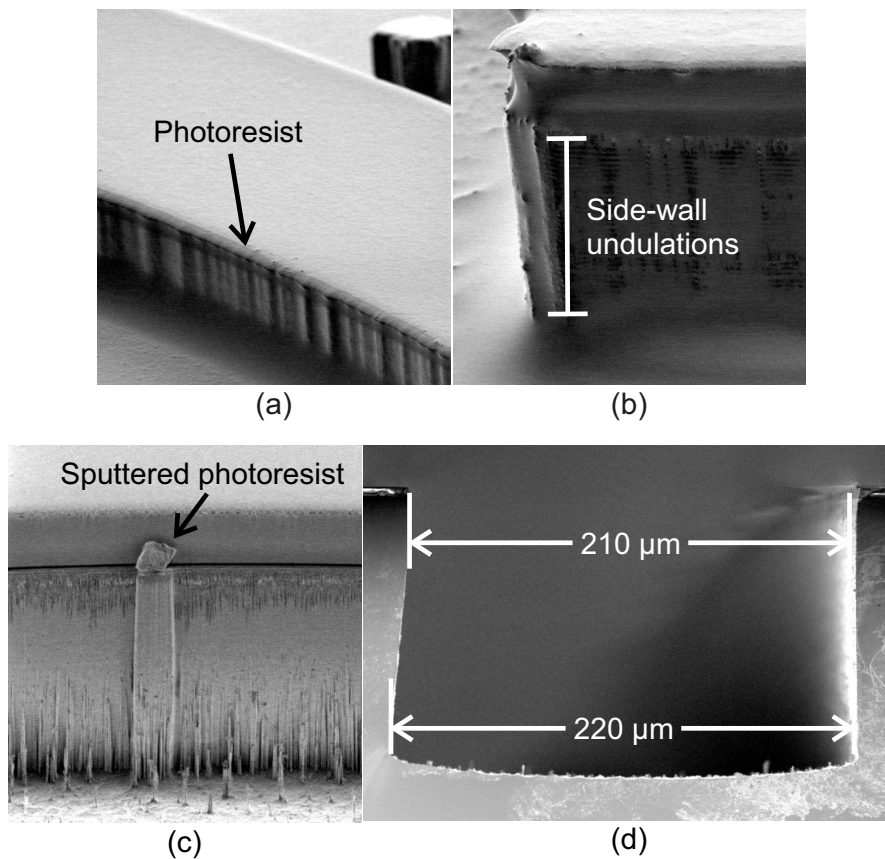


Figure A.5.: Micrograph using a SEM of an etched silicon wafer. Figure (a) shows an etched silicon waveguide with a thin layer of photoresist on top. (b) shows the undulations of the vertical wall after etching. (c) shows needles like structures formed due to the re-deposition of photoresist particulates while etching on the exposed surface. (d) shows concave etching profiles due to longer etching than deposition step.

Substrates and adhesives

Since the DRIE is conducted at $-10\text{ }^{\circ}\text{C}$, it is imperative to have a good thermally conductive substrate. Thick and physically rigid silicon wafers are fixed on a polished alumina wafer using thermally conductive lubricant called Fomblin®. However, $50\text{ }\mu\text{m}$ -thick silicon wafers need to be supported by Qz wafers and are then placed on the alumina wafer using Fomblin®. Substrates with lower thermal conductivity such as HDPE or Teflon result in a rapid removal of the protective photoresist layer and over-etching of the silicon wafer, along with substantial substrate damage due to excessive heat of the ionised plasma.

Post DRIE the waveguides are transferred on to HDPE substrates and that necessitates an adhesive which can be easily removed after etching, preferably with minimal physical force. Cyanoacrylate adhesives are found to be apt for this purpose and thus, are used to stick thin silicon wafers on Qz substrate before etching. Other removable adhesives like a thin photoresist layer or First Contact™ cleaning solutions cannot tolerate the heat from ionised plasma and readily burn in the etching chamber. Alternatively, Cyclotene™ Advanced Electronic Resin (BCB) can be used as an adhesive due to its high thermal stability and low losses in terahertz frequencies, however its applicability was not tested in scope of this thesis.

A.6. Photoconductor fabrication

The fabrication the ErAs:In(Al)GaAs photoconductive receivers follows the following six steps:

1. **Deposition of the metal electrodes:** The finger structures of the VA-coupled photoconductors can be as small as 1 – 1.5 μm wide and this necessitates a very thin photoresist layer for contact lithography. We deposit a 1.4 μm thick layer of AZ 5214E by spin-coating our $7 \times 8 \text{ mm}^2$ sample. We then expose the photoresist layer under 365 nm ultra-violet (UV) light and use AZ MIF 726 developer to create electrode patterns on the sample surface.
2. **Gold deposition:** We first evaporate 40 nm of titanium using electron-beam evaporation for better adhesion of the evaporated 220 nm of gold on the sample surface featuring a lithographically defined protective mask. We *lift-off* the unnecessary metals from the sample surface using acetone. Then, the samples are annealed at 420 $^{\circ}\text{C}$ for 30 s to diffuse the gold into the semiconductor and form an ohmic contact.
3. **Mesa etching:** The photoactive ErAs:In(Al)GaAs layer is 1.7 μm thick. We remove all but the ErAs:In(Al)GaAs layer between the metal electrodes from the sample surface using a solution of $\text{H}_2\text{SO}_4:\text{H}_2\text{O}_2$, leaving just the semi-insulating indium phosphide (InP) substrate. The photoactive

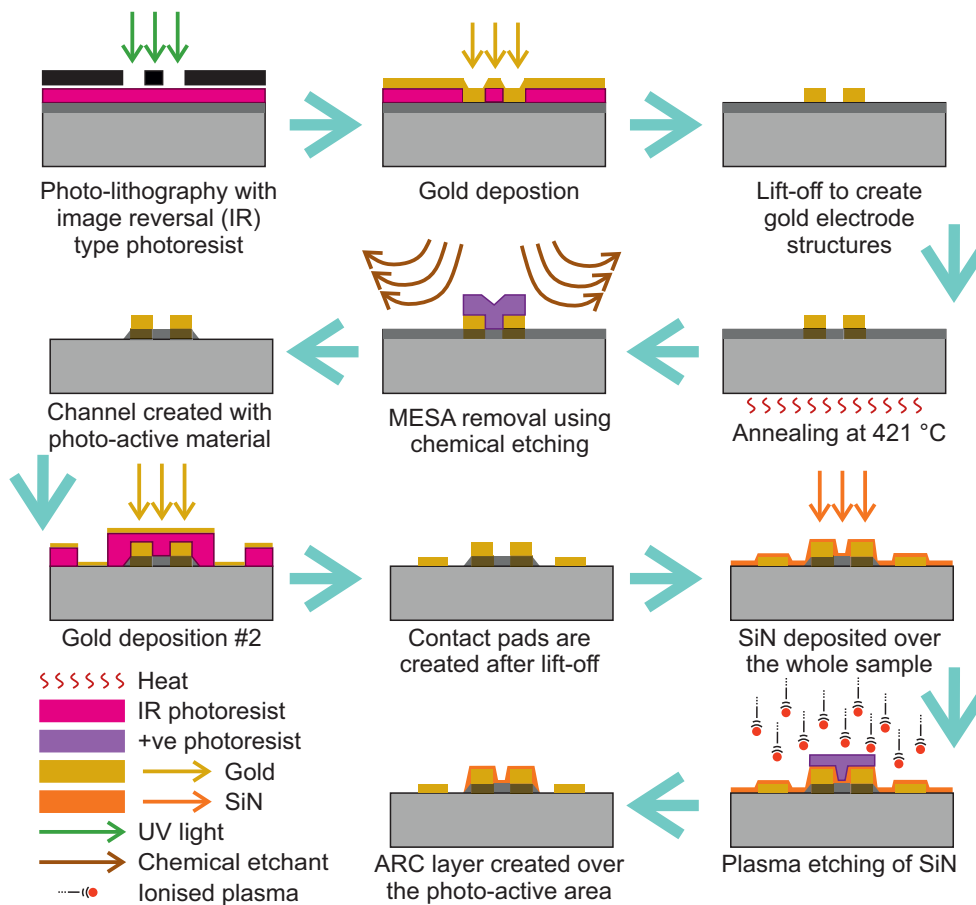


Figure A.6.: Steps in fabricating ErAs:In(Al)GaAs receivers using photolithographic masks.

layer has the dimensions ($l \times w \times h$) of $12 \times 10 \times 1.7 \mu\text{m}^3$. We use $1.8 \mu\text{m}$ thick *AZ 1518* photoresist mask for the chemical etching process.

4. **Deposition of metallic antennas:** The lithography process for the metallic antennas is the same as in step 1. We evaporate 420 nm of gold to fabricate the antennas. The devices are placed on a tilted rotating holder whilst the evaporation process, as discontinuities may arise at the $1.7 \mu\text{m}$ step between the photoactive layer and the InP substrate.
5. **Anti-reflection coating (ARC):** We finally deposit a silicon nitride (SiN) layer to suppress the reflection of the exciting laser signal off the device surface. The thickness of the ARC layer is determined by the wavelength of the laser used to drive the devices. The SiN layer is first deposited using chemical vapour deposition (CVD). We just keep the ARC layer atop the photoactive areas and etch the rest using CF_4 plasma in a reactive ion etching chamber. Photoresist *AZ 1518* is used as the protective mask.
6. **Polishing, cleaving and packaging:** The devices are polished, cleaved and package to be finally used as receivers in the (semi-)integrated PVNA architecture. We have detailed these processes in section 5.1.3.

The detailed data-sheet of the photoresists are on the website of MicroChemicals [194].

A.7. Codes and application

Codes used for data analysis in this thesis are available upon request from the author. All Matlab™ codes are uploaded either in the shared file-server of institute or on Gitlab of Terahertz Devices and Systems group hosted by RWTH Aachen. The work in this thesis has also led to the development of five Matlab™- and Python-based standalone applications for signal processing, imaging, material characterisation and modelling multi-layered structures. This appendix briefly describes each of these applications.

Bandwidth extension

Section 3.2 details signal processing techniques to extend measurement bandwidth of a homodyne CW system. Screenshot in Fig. A.7 shows an application, developed in Python, that can communicate with the *Toptica Terascan* system, fetch data from the instrument and modularly add filters to extend the system bandwidth. The application provides users the opportunity to interactively move and change the filter bandwidths and find the best settings for the use-case. The application is also capable of communicating to *Toptica TSweeper* systems. Two simulators are also available in the application for demonstration purposes. Miss Alina Weber designed the user interface of this application. *Toptica Photonics* displayed this application on their company portfolio during the 47th International Conference on Infrared, Millimetre, and Terahertz Waves (IRMMW-THz) in 2022.

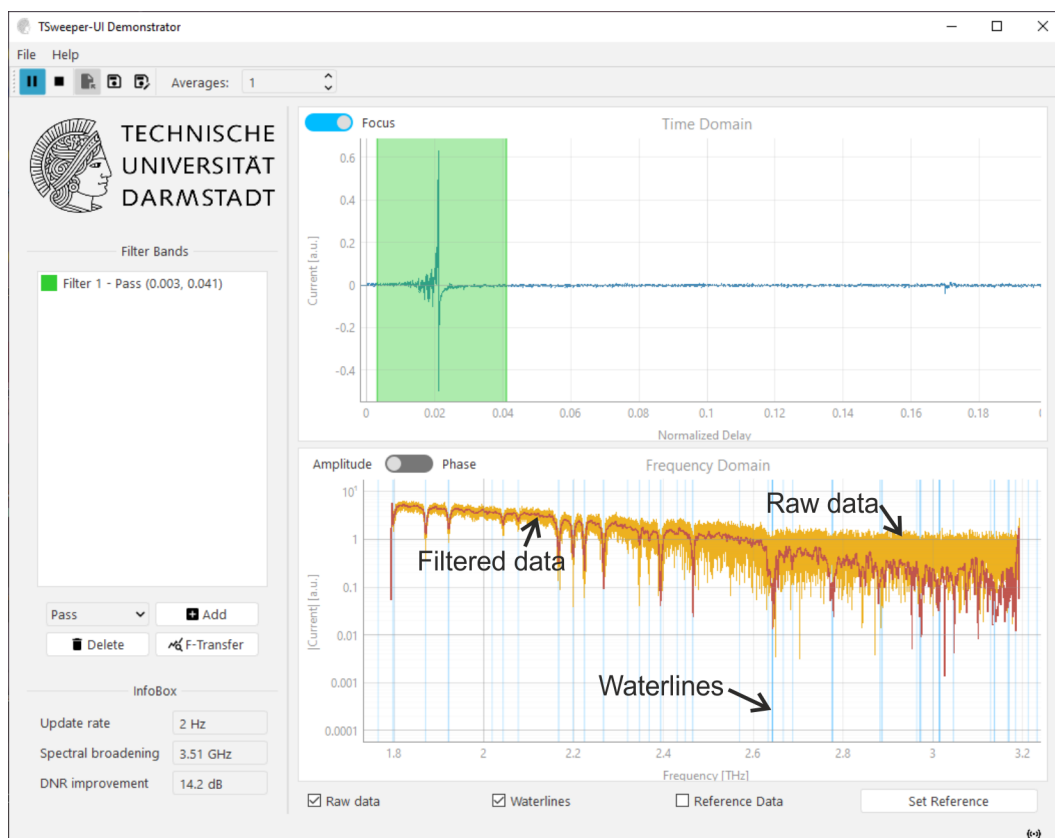


Figure A.7.: Screenshot of the bandwidth extender application for CW systems coded in Python.

Multilayer modelling

The application calculates the analytical S-parameters of a multilayered sample using Fabry-Pérot transmission and reflection coefficients and transfer matrices (T-matrixs). The model is described in section 3.3.2. This application is developed using Matlab™. A limitation of T-matrix-calculation in Matlab™ is that the maximum number of samples is limited to 1,000. Figure A.8 shows a screenshot of the application.

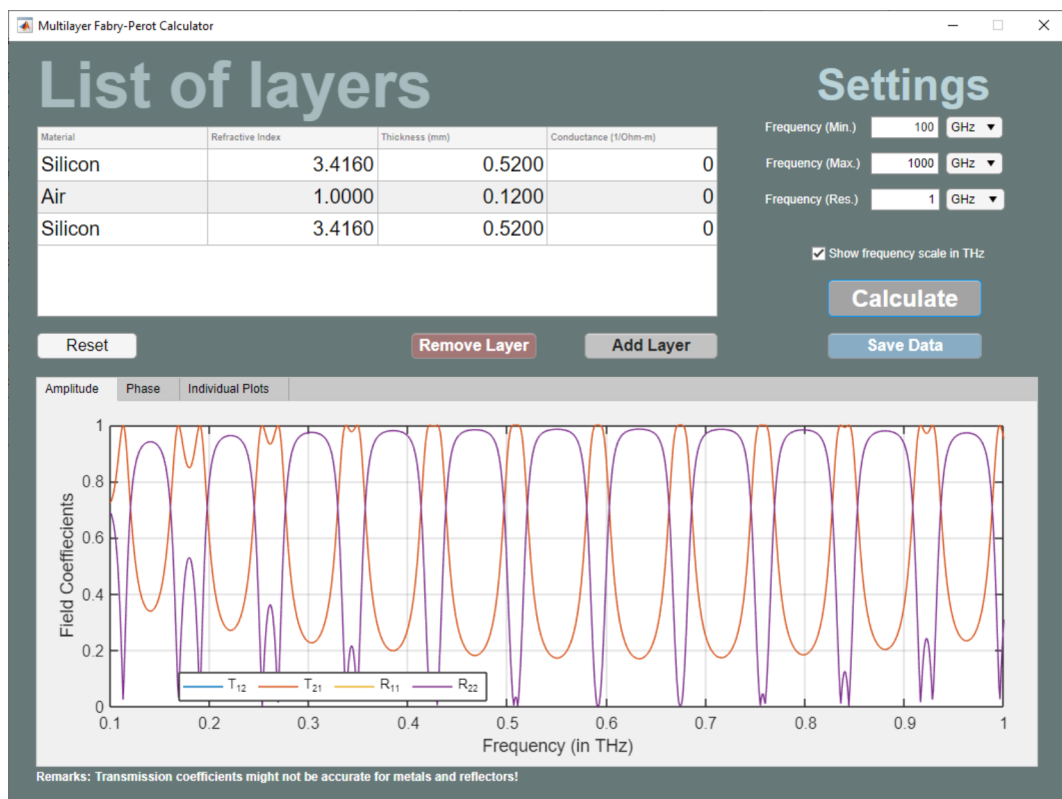


Figure A.8.: Screenshot of the Matlab™-based application to calculated S-parameters of planar, multi-layered structures.

Gaussian beam propagation

This Matlab™-based application calculates details of a propagating Gaussian beam through free-space optical components, especially dielectric lenses. Multiple spherical or cylindrical lenses can be added to the propagation path and the application calculates the effective focal length of the lens-system and Gaussian beam radius at any distance from the lenses. Figure A.9 shows a screenshot of the application.

Material characterisation from free-space PVNA

Figure A.10 shows the screenshot the material characterisation application used in conjunction with the free-space PVNA to estimate the RI and thickness of planar dielectric DUTs. The estimation algorithm is detailed in section 3.3.1. In free-space measurements, often the measured transmission and reflection coefficients exceed unity. The transmission measurements are more robust than the reflection ones and

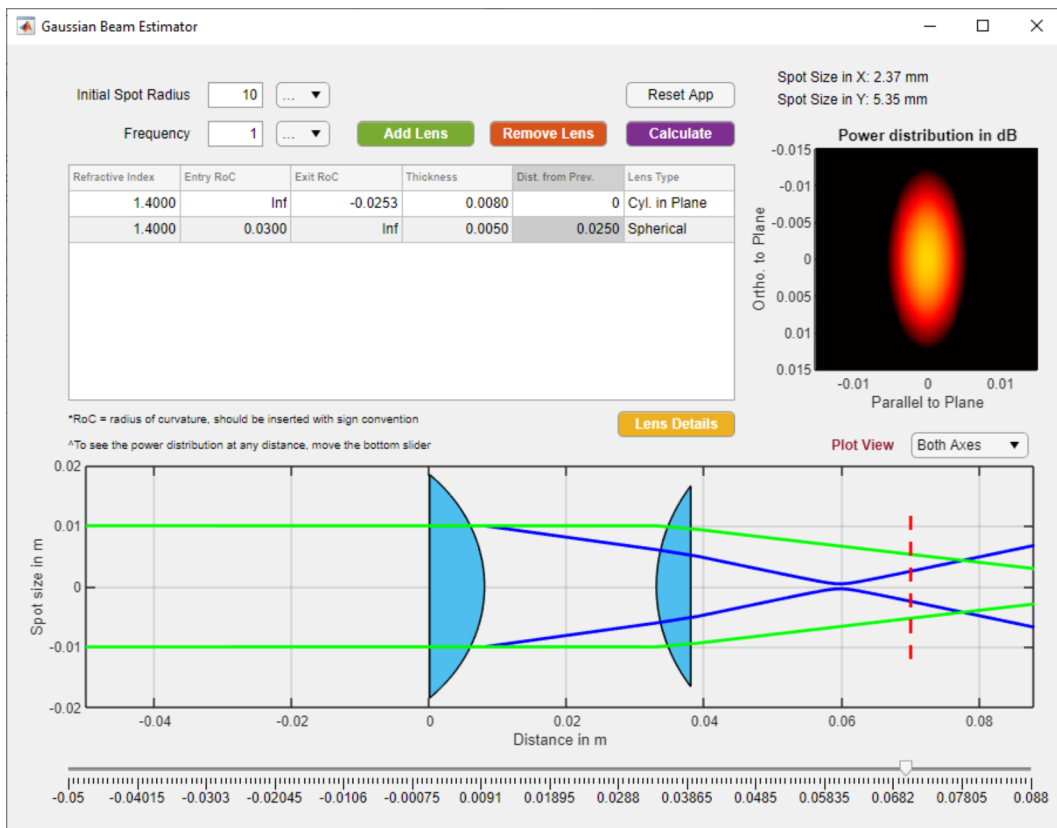


Figure A.9.: Screenshot of the application to calculate Gaussian beam characteristics in a lens-coupled free-space system.

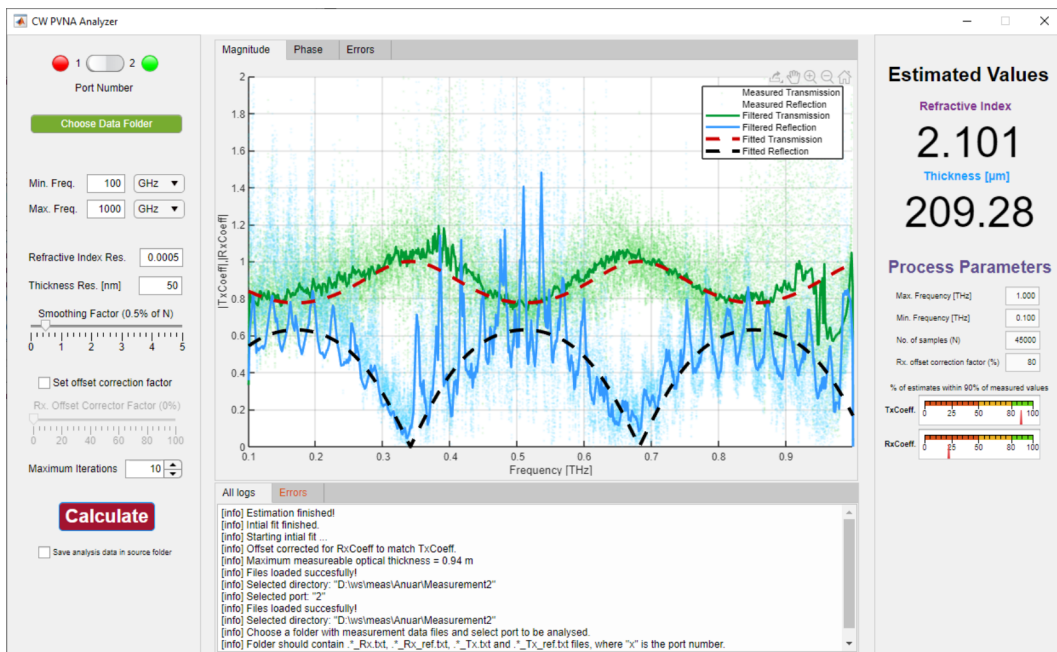


Figure A.10.: Screenshot of the material characterisation application for the free-space PVNA.

hence, the application provides an offset correction factor to correct for these error. This application is developed using Matlab™.

2-D scanner for imaging application

Figure A.11 shows a Matlab™ application to integrate the *Toptica Terascan* system with an *OWIS translation stage* for imaging using CW THz systems (see Fig. 3.13). The application is capable of meandering or raster scans both for the frequency and spatial parameters. The lag between the set and the actual frequency of the *Terascan* system varies over the scan duration and requires a short-term Fourier transform-based homodyne fringe correction technique for appropriate imaging. This feature is yet to be implemented. Nonetheless, the application now records scanned data without generating an image of the sample.

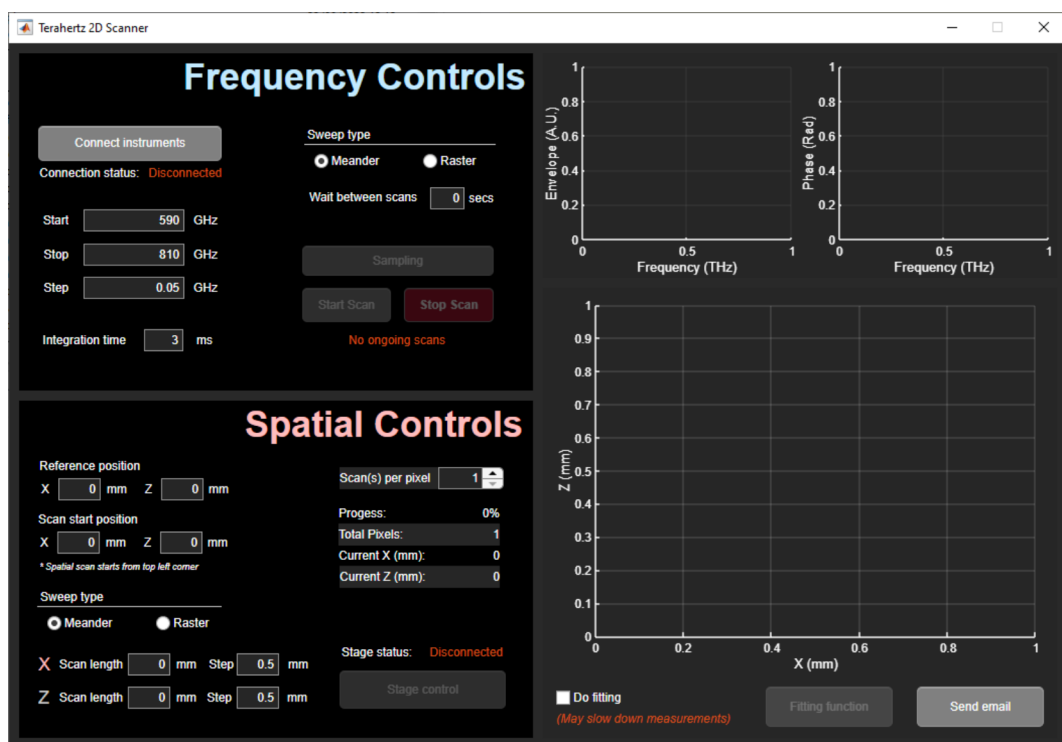


Figure A.11.: Screenshot of the 2-D scanning application for the CW system.

Bibliography

- [1] G. J. Stacey, "THz Low Resolution Spectroscopy for Astronomy," *IEEE Transactions on Terahertz Science and Technology*, vol. 1, no. 1, pp. 241–255, 2011. DOI: 10.1109/TTHZ.2011.2159649.
- [2] G. Bubnov *et al.*, "Development and research of sub-terahertz astronomy and telecommunication equipment," *AIP Conference Proceedings*, vol. 2300, no. 1, p. 020013, 2020. DOI: 10.1063/5.0032083.
- [3] Y. Peng *et al.*, "Terahertz spectroscopy in biomedical field: A review on signal-to-noise ratio improvement," *Photonix*, vol. 1, no. 1, p. 12, Apr. 2020, ISSN: 2662-1991. DOI: 10.1186/s43074-020-00011-z.
- [4] M. C. Beard, G. M. Turner, and C. A. Schmuttenmaer, "Terahertz Spectroscopy," *The Journal of Physical Chemistry B*, vol. 106, no. 29, pp. 7146–7159, Jul. 2002, ISSN: 1520-6106. DOI: 10.1021/jp020579i.
- [5] E. Castro-Camus, M. Koch, and D. M. Mittleman, "Recent advances in terahertz imaging: 1999 to 2021," *Applied Physics B*, vol. 128, no. 1, p. 12, Dec. 2021, ISSN: 1432-0649. DOI: 10.1007/s00340-021-07732-4.
- [6] P. Hillger *et al.*, "Terahertz Imaging and Sensing Applications With Silicon-Based Technologies," *IEEE Transactions on Terahertz Science and Technology*, vol. 9, no. 1, pp. 1–19, 2019. DOI: 10.1109/TTHZ.2018.2884852.
- [7] D. Molter *et al.*, "Multilayer terahertz thickness imaging at 1.6-kHz pixel rate," in *Terahertz, RF, Millimeter, and Submillimeter-Wave Technology and Applications XV*, L. P. Sadwick and T. Yang, Eds., International Society for Optics and Photonics, vol. PC12000, SPIE, 2022, PC120000H. DOI: 10.1117/12.2615320.
- [8] D. Nuessler and J. Jonuscheit, "Terahertz based non-destructive testing (ndt)," *tm - Technisches Messen*, vol. 88, Apr. 2020. DOI: 10.1515/teme-2019-0100.
- [9] A. de Jesus Fernandez Olvera, "ErAs:In(Al)GaAs Photoconductive Mixers as Continuous-Wave Terahertz Detectors: Modelling and Applications," Ph.D. dissertation, Technische Universität, Darmstadt, 2022, pp. 1–137. DOI: <https://doi.org/10.26083/tuprints-00021340>.
- [10] T. Crowe *et al.*, "Terahertz sources and detectors and their application to biological sensing," *Philosophical transactions. Series A, Mathematical, physical, and engineering sciences*, vol. 362, 365–74, discussion 374, Mar. 2004. DOI: 10.1098/rsta.2003.1327.
- [11] S. Preu *et al.*, "Principles of THz Generation," in *Semiconductor Terahertz Technology*. John Wiley and Sons, Ltd, 2015, ch. 2, pp. 3–68, ISBN: 9781118920411. DOI: 10.1002/9781118920411.ch2.
- [12] E. Peytavit *et al.*, "CW Source Based on Photomixing With Output Power Reaching 1.8 mW at 250 GHz," *IEEE Electron Device Letters*, vol. 34, no. 10, pp. 1277–1279, 2013. DOI: 10.1109/LED.2013.2277574.

-
- [13] A. Al-Khalidi *et al.*, “Resonant Tunneling Diode Terahertz Sources With up to 1 mW Output Power in the J-Band,” *IEEE Transactions on Terahertz Science and Technology*, vol. 10, no. 2, pp. 150–157, 2020. DOI: 10.1109/TTHZ.2019.2959210.
- [14] *Frequency Multipliers (WR and D series)*, <https://www.vadiodes.com/en/frequency-multipliers>, Accessed: 2021-01-26.
- [15] P.-K. Lu, D. Turan, and M. Jarrahi, “High-sensitivity telecommunication-compatible photoconductive terahertz detection through carrier transit time reduction,” *Optics Express*, vol. 28, no. 18, pp. 26 324–26 335, 2020.
- [16] *N5291a 900 Hz to 120 GHz pna mm-wave system*, <https://www.keysight.com/de/pdx-2817990-pn-N5291A/900-hz-to-120-ghz-pna-mm-wave-system>, Accessed: 2021-11-05.
- [17] Y. H. Tao, A. J. Fitzgerald, and V. P. Wallace, “Non-Contact, Non-Destructive Testing in Various Industrial Sectors with Terahertz Technology,” *Sensors*, vol. 20, no. 3, 2020, ISSN: 1424-8220. DOI: 10.3390/s20030712.
- [18] K. Humphreys *et al.*, “Medical applications of terahertz imaging: A review of current technology and potential applications in biomedical engineering,” in *The 26th Annual International Conference of the IEEE Engineering in Medicine and Biology Society*, vol. 1, 2004, pp. 1302–1305. DOI: 10.1109/IEMBS.2004.1403410.
- [19] N. Rothbart *et al.*, “Millimeter-wave gas spectroscopy for breath analysis of COPD patients in comparison to GC-MS,” *Journal of Breath Research*, vol. 16, no. 4, p. 046 001, Jun. 2022. DOI: 10.1088/1752-7163/ac77aa.
- [20] E. A. A. Pogna *et al.*, “Terahertz near-field nanoscopy based on detectorless laser feedback interferometry under different feedback regimes,” *APL Photonics*, vol. 6, no. 6, p. 061 302, 2021. DOI: 10.1063/5.0048099.
- [21] T. Cocker *et al.*, “Nanoscale terahertz scanning probe microscopy,” *Nature Photonics*, vol. 15, no. 8, pp. 558–569, 2021.
- [22] I. F. Akyildiz *et al.*, “Terahertz Band Communication: An Old Problem Revisited and Research Directions for the Next Decade,” *IEEE Transactions on Communications*, vol. 70, no. 6, pp. 4250–4285, 2022. DOI: 10.1109/TCOMM.2022.3171800.
- [23] H. Elayan *et al.*, “Terahertz communication: The opportunities of wireless technology beyond 5G,” in *2018 International Conference on Advanced Communication Technologies and Networking (CommNet)*, 2018, pp. 1–5. DOI: 10.1109/COMMNET.2018.8360286.
- [24] *TeraScan: Frequency-Domain Terahertz Platform*, <https://www.toptica.com/products/terahertz-systems/frequency-domain/terascan>, Accessed: 2021-11-05.
- [25] A. F. Olvera *et al.*, “Continuous-wave 1550 nm operated terahertz system using ErAs:In(Al)GaAs photo-conductors with 52 dB dynamic range at 1 THz,” *Opt. Express*, vol. 25, no. 23, pp. 29 492–29 500, Sep. 2017. DOI: 10.1364/OE.25.029492.
- [26] *TeraFlash pro: Versatile time-domain terahertz platform*, <https://www.toptica.com/products/terahertz-systems/time-domain/teraflash-pro>, Accessed: 2022-09-20.
- [27] L. Liebermeister *et al.*, “Optoelectronic frequency-modulated continuous-wave terahertz spectroscopy with 4 THz bandwidth,” *Nature Communications*, vol. 12, no. 1, p. 1071, 2021, ISSN: 2041-1723. DOI: 10.1038/s41467-021-21260-x.

-
- [28] R. Safian, G. Ghazi, and N. Mohammadian, "Review of photomixing continuous-wave terahertz systems and current application trends in terahertz domain," *Optical Engineering*, vol. 58, no. 11, pp. 1–28, 2019. DOI: 10.1117/1.OE.58.11.110901.
- [29] P. Penfield, "Noise in Negative-Resistance Amplifiers," *IRE Transactions on Circuit Theory*, vol. 7, no. 2, pp. 166–170, 1960. DOI: 10.1109/TCT.1960.1086655.
- [30] K. Kurokawa, "Power Waves and the Scattering Matrix," *IEEE Transactions on Microwave Theory and Techniques*, vol. 13, no. 2, pp. 194–202, 1965. DOI: 10.1109/TMTT.1965.1125964.
- [31] *ENA Vector Network Analyzers*, <https://www.keysight.com/us/en/products/network-analyzers/ena-vector-network-analyzers.html>, Accessed: 2022-09-19.
- [32] *Vector Network Analyzer Extenders*, <https://www.vadiodes.com/en/products/vector-network-analyzer-extension-modules>, Accessed: 2022-09-19.
- [33] *Waveguide Band Designations*, <https://vadiodes.com/VDI/pdf/waveguidechart200908.pdf>, Accessed: 2020-09-04.
- [34] F. R. Faridi and S. Preu, "Pulsed free space two-port photonic vector network analyzer with up to 2 THz bandwidth," *Opt. Express*, vol. 29, no. 8, pp. 12 278–12 291, Apr. 2021. DOI: 10.1364/OE.418120.
- [35] A. D. J. F. Olvera, A. k. Mukherjee, and S. Preu, "A Fully Optoelectronic Continuous-Wave 2-Port Vector Network Analyzer Operating From 0.1 THz to 1 THz," *IEEE Journal of Microwaves*, pp. 1–8, 2021. DOI: 10.1109/JMW.2021.3107472.
- [36] S. Preu, *Terahertz Photonic integrated circuit*, German patent application DE 10 2019 104 982 A1 (2019).
- [37] T. H. Lee and S. S. Wong, "CMOS RF integrated circuits at 5 GHz and beyond," *Proceedings of the IEEE*, vol. 88, no. 10, pp. 1560–1571, 2000. DOI: 10.1109/5.888995.
- [38] O. Daulay, R. Botter, and D. Marpaung, "On-chip programmable microwave photonic filter with an integrated optical carrier processor," *OSA Continuum*, vol. 3, no. 8, pp. 2166–2174, Aug. 2020. DOI: 10.1364/OSAC.400037.
- [39] M. Hossain *et al.*, "Efficient active multiplier-based signal source for >300 GHz system applications," *Electronics Letters*, vol. 55, no. 23, pp. 1220–1221, 2019. DOI: <https://doi.org/10.1049/el.2019.2387>.
- [40] N. Ranjkesh *et al.*, "1.1 THz U-Silicon-On-Glass (U-SOG) Waveguide: A Low-Loss Platform for THz High-Density Integrated Circuits," *IEEE Transactions on Terahertz Science and Technology*, vol. 8, no. 6, pp. 702–709, 2018. DOI: 10.1109/TTHZ.2018.2868462.
- [41] H. Amarloo, N. Ranjkesh, and S. Safavi-Naeini, "Terahertz Silicon-BCB-Quartz Dielectric Waveguide: An Efficient Platform for Compact THz Systems," *IEEE Transactions on Terahertz Science and Technology*, vol. 8, no. 2, pp. 201–208, 2018. DOI: 10.1109/TTHZ.2017.2788202.
- [42] H. Amarloo and S. Safavi-Naeini, "Terahertz Slot Dielectric Waveguide Implemented on the Silicon-BCB-Quartz Platform," *IEEE Transactions on Terahertz Science and Technology*, vol. 11, no. 3, pp. 310–317, 2021. DOI: 10.1109/TTHZ.2021.3049650.
- [43] T. W. Crowe *et al.*, "Vna frequency extenders to 1.1 THz," in *2011 International Conference on Infrared, Millimeter, and Terahertz Waves*, 2011, pp. 1–1. DOI: 10.1109/irmmw-THz.2011.6105028.

-
- [44] K. Sengupta, T. Nagatsuma, and D. M. Mittleman, "Terahertz integrated electronic and hybrid electronic–photonic systems," *Nature Electronics*, vol. 1, no. 12, pp. 622–635, 2018, ISSN: 2520-1131. DOI: 10.1038/s41928-018-0173-2.
- [45] L. E. G. Muñoz *et al.*, "Principles of Emission of THz Waves," in *Semiconductor Terahertz Technology*. John Wiley and Sons, Ltd, 2015, ch. 3, pp. 69–159, ISBN: 9781118920411. DOI: <https://doi.org/10.1002/9781118920411.ch3>.
- [46] H. Han *et al.*, "Terahertz pulse propagation in a plastic photonic crystal fiber," *Applied Physics Letters*, vol. 80, no. 15, pp. 2634–2636, 2002. DOI: 10.1063/1.1468897.
- [47] D. Chen and H. Chen, "A novel low-loss terahertz waveguide: Polymer tube," *Opt. Express*, vol. 18, no. 4, pp. 3762–3767, Feb. 2010. DOI: 10.1364/OE.18.003762.
- [48] J. Champion *et al.*, "Toward Industrial Exploitation of THz Frequencies: Integration of SiGe MMICs in Silicon-Micromachined Waveguide Systems," *IEEE Transactions on Terahertz Science and Technology*, vol. 9, no. 6, pp. 624–636, 2019, ISSN: 21563446. DOI: 10.1109/TTHZ.2019.2943572.
- [49] D. Headland *et al.*, "Unclad Microphotronics for Terahertz Waveguides and Systems," *J. Lightwave Technol.*, vol. 38, no. 24, pp. 6853–6862, Dec. 2020.
- [50] H. Zhu *et al.*, "Design, Fabrication, and Measurement of the Low-Loss SOI-Based Dielectric Microstrip Line and its Components," *IEEE Transactions on Terahertz Science and Technology*, vol. 6, no. 5, pp. 696–705, 2016. DOI: 10.1109/TTHZ.2016.2585345.
- [51] J. Xie *et al.*, "Terahertz integrated device: High-Q silicon dielectric resonators," *Opt. Mater. Express*, vol. 8, no. 1, pp. 50–58, Jan. 2018. DOI: 10.1364/OME.8.000050.
- [52] Z. Wang *et al.*, "Voltage-actuated thermally tunable on-chip terahertz filters based on a whispering gallery mode resonator," *Opt. Lett.*, vol. 44, no. 19, pp. 4670–4673, Oct. 2019. DOI: 10.1364/OL.44.004670.
- [53] N. Ranjkesh *et al.*, "Silicon-on-Glass Dielectric Waveguide—Part ii: For THz Applications," *IEEE Transactions on Terahertz Science and Technology*, vol. 5, no. 2, pp. 280–287, 2015. DOI: 10.1109/TTHZ.2015.2397279.
- [54] N. Ranjkesh *et al.*, "Broadband Single-Mode THz Suspended Silicon-On-Glass Waveguide," *IEEE Microwave and Wireless Components Letters*, vol. 28, no. 3, pp. 185–187, 2018. DOI: 10.1109/LMWC.2018.2797524.
- [55] E. Akiki *et al.*, "Low Loss Suspended Silicon Waveguide and Photonic Crystal for THz Regime," in *2019 Conference on Lasers and Electro-Optics Europe European Quantum Electronics Conference (CLEO/Europe-EQEC)*, 2019, pp. 1–1. DOI: 10.1109/CLEOE-EQEC.2019.8872554.
- [56] A. L. Bingham and D. R. Grischkowsky, "Terahertz 2-D Photonic Crystal Waveguides," *IEEE Microwave and Wireless Components Letters*, vol. 18, no. 7, pp. 428–430, 2008. DOI: 10.1109/LMWC.2008.924906.
- [57] H. Amarloo and S. Safavi-Naeini, "Terahertz Line Defect Waveguide Based on Silicon-on-Glass Technology," *IEEE Transactions on Terahertz Science and Technology*, vol. 7, no. 4, pp. 433–439, 2017. DOI: 10.1109/TTHZ.2017.2708505.
- [58] W. Withayachumnankul, M. Fujita, and T. Nagatsuma, "Integrated Silicon Photonic Crystals Toward Terahertz Communications," *Advanced Optical Materials*, vol. 6, no. 16, p. 1800401, 2018. DOI: <https://doi.org/10.1002/adom.201800401>.

-
- [59] X. Yu *et al.*, “Simultaneous low-loss and low-dispersion in a photonic-crystal waveguide for terahertz communications,” *Applied Physics Express*, vol. 12, no. 1, p. 012005, 2019.
- [60] W. Gao *et al.*, “Effective-medium-cladded dielectric waveguides for terahertz waves,” *Opt. Express*, vol. 27, no. 26, pp. 38721–38734, Dec. 2019. DOI: 10.1364/OE.382181.
- [61] T. Seifert *et al.*, “Efficient metallic spintronic emitters of ultrabroadband terahertz radiation,” *Nature Photonics*, vol. 10, no. 7, pp. 483–488, 2016, ISSN: 1749-4893. DOI: 10.1038/nphoton.2016.91.
- [62] A. F. Olvera *et al.*, “Architecture and Component Characterization of a High-Resolution Free-Space Vector Network Analyzer for the Terahertz Range,” in *2019 European Microwave Conference in Central Europe (EuMCE)*, 2019, pp. 257–260. DOI: 10.25534/tuprints-00011365.
- [63] U. Nandi *et al.*, “ErAs:In(Al)GaAs photoconductor-based time domain system with 4.5 THz single shot bandwidth and emitted terahertz power of 164 μ W,” *Opt. Lett.*, vol. 45, no. 10, pp. 2812–2815, May 2020. DOI: 10.1364/OL.388870.
- [64] L. Liebermeister *et al.*, “Ultra-fast, High-Bandwidth Coherent CW THz Spectrometer for Non-destructive Testing,” *Journal of Infrared, Millimeter, and Terahertz Waves*, vol. 40, no. 3, pp. 288–296, 2019, ISSN: 1866-6906. DOI: 10.1007/s10762-018-0563-6.
- [65] H. Amarloo and S. Safavi-Naeini, “Slot plasmonic waveguide based on doped-GaAs for terahertz deep-subwavelength applications,” *J. Opt. Soc. Am. A*, vol. 32, no. 11, pp. 2189–2194, Nov. 2015. DOI: 10.1364/JOSAA.32.002189.
- [66] A. Ingar Romero *et al.*, “Visualizing nanometric structures with sub-millimeter waves,” *Nature Communications*, vol. 12, no. 1, p. 7091, 2021, ISSN: 2041-1723. DOI: 10.1038/s41467-021-27264-x.
- [67] A. k. Mukherjee and S. Preu, “Emulating a broadband frequency sweep for Terahertz thin-film imaging,” in *2022 47th International Conference on Infrared, Millimeter and Terahertz Waves (IRMMW-THz)*, 2022, pp. 1–4. DOI: 10.1109/IRMMW-THz50927.2022.9895797.
- [68] A. k. Mukherjee, S. Wassmann, and S. Preu, “Operational bandwidth extension in continuous-wave terahertz systems by digital post-processing,” *IEEE Transactions on Terahertz Science and Technology*, pp. 1–8, 2022. DOI: 10.1109/TTHz.2022.3230924.
- [69] A. k. Mukherjee and S. Preu, *Bandbreitenerweiterung von THz Photomischersystemen mittels Rauschunterdrückung*, German patent application DE 10 2022 115 387.8, Jun 2022.
- [70] A. k. Mukherjee, M. Xiang, and S. Preu, “Broadband Terahertz Photonic Integrated Circuit with Integrated Active Photonic Devices,” *Photonics*, vol. 8, no. 11, 2021, ISSN: 2304-6732. DOI: 10.3390/photonics8110492.
- [71] A. k. Mukherjee, M. Xiang, and S. Preu, “Broadband Dielectric Waveguides for 0.5–1.1 THz Operation,” in *2020 45th International Conference on Infrared, Millimeter, and Terahertz Waves (IRMMW-THz)*, 2020, pp. 1–2. DOI: 10.1109/IRMMW-THz46771.2020.9370829.
- [72] A. k. Mukherjee, M. Xiang, and S. Preu, “Antenna designs for near field waveguide coupling between 0.6 – 0.9 THz,” in *2021 46th International Conference on Infrared, Millimeter and Terahertz Waves (IRMMW-THz)*, 2021, pp. 1–2. DOI: 10.1109/IRMMW-THz50926.2021.9567575.
- [73] C. Yeh and F. I. Shimabukuro, “Propagation Characteristics of Guided Waves Along a Dielectric Guide,” in *The Essence of Dielectric Waveguides*. Boston, MA: Springer US, 2008, pp. 55–98, ISBN: 978-0-387-49799-0. DOI: 10.1007/978-0-387-49799-0_3.

-
- [74] J. C. Maxwell, *A treatise on electricity and magnetism* (Clarendon Press series), eng. Oxford: At the Clarendon Press, 1873.
- [75] “Green’s Functions,” in *Electromagnetic Wave Propagation, Radiation, and Scattering*. John Wiley and Sons, Ltd, 2017, ch. 5, pp. 137–168, ISBN: 9781119079699. DOI: <https://doi.org/10.1002/9781119079699.ch5>.
- [76] C. Yeh and F. I. Shimabukuro, “Fundamental Electromagnetic Field Equations,” in *The Essence of Dielectric Waveguides*. Boston, MA: Springer US, 2008, pp. 11–53, ISBN: 978-0-387-49799-0. DOI: [10.1007/978-0-387-49799-0_2](https://doi.org/10.1007/978-0-387-49799-0_2).
- [77] C. Yeh, “Boundary conditions in electromagnetics,” *Phys. Rev. E*, vol. 48, pp. 1426–1427, 2 Aug. 1993. DOI: [10.1103/PhysRevE.48.1426](https://doi.org/10.1103/PhysRevE.48.1426).
- [78] A. Sommerfeld, “Über die Ausbreitung der Wellen in der drahtlosen Telegraphie,” *Annalen der Physik*, vol. 333, no. 4, pp. 665–736, 1909. DOI: <https://doi.org/10.1002/andp.19093330402>.
- [79] C. Bouwkamp, “A note on singularities occurring at sharp edges in electromagnetic diffraction theory,” *Physica*, vol. 12, no. 7, pp. 467–474, 1946, ISSN: 0031-8914. DOI: [https://doi.org/10.1016/S0031-8914\(46\)80061-2](https://doi.org/10.1016/S0031-8914(46)80061-2).
- [80] E. A. J. Marcatili, “Dielectric rectangular waveguide and directional coupler for integrated optics,” *The Bell System Technical Journal*, vol. 48, no. 7, pp. 2071–2102, 1969. DOI: [10.1002/j.1538-7305.1969.tb01166.x](https://doi.org/10.1002/j.1538-7305.1969.tb01166.x).
- [81] C. Yeh and F. I. Shimabukuro, “Approximate Methods,” in *The Essence of Dielectric Waveguides*. Boston, MA: Springer US, 2008, pp. 221–240, ISBN: 978-0-387-49799-0. DOI: [10.1007/978-0-387-49799-0_7](https://doi.org/10.1007/978-0-387-49799-0_7).
- [82] C. Yeh and F. I. Shimabukuro, “Planar Dielectric Waveguides,” in *The Essence of Dielectric Waveguides*. Boston, MA: Springer US, 2008, pp. 99–135, ISBN: 978-0-387-49799-0. DOI: [10.1007/978-0-387-49799-0_4](https://doi.org/10.1007/978-0-387-49799-0_4).
- [83] R. E. Collin, “Surface waveguides,” in *Field Theory of Guided Waves*. 1991, pp. 697–748. DOI: [10.1109/9780470544648.ch11](https://doi.org/10.1109/9780470544648.ch11).
- [84] C. Xu, W. Huang, and S. Chaudhuri, “Efficient and accurate vector mode calculations by beam propagation method,” *Journal of Lightwave Technology*, vol. 11, no. 7, pp. 1209–1215, 1993. DOI: [10.1109/50.238083](https://doi.org/10.1109/50.238083).
- [85] J. E. Goell, “A Circular-Harmonic Computer Analysis of Rectangular Dielectric Waveguides,” *Bell System Technical Journal*, vol. 48, no. 7, pp. 2133–2160, 1969. DOI: <https://doi.org/10.1002/j.1538-7305.1969.tb01168.x>.
- [86] W. J. Westerveld *et al.*, “Extension of Marcatili’s Analytical Approach for Rectangular Silicon Optical Waveguides,” *Journal of Lightwave Technology*, vol. 30, no. 14, pp. 2388–2401, 2012. DOI: [10.1109/JLT.2012.2199464](https://doi.org/10.1109/JLT.2012.2199464).
- [87] N. S. Kapany, J. J. Burke, and T. Sawatari, “Fiber Optics. XII. A Technique for Launching an Arbitrary Mode on an Optical Dielectric Waveguide,” *J. Opt. Soc. Am.*, vol. 60, no. 9, pp. 1178–1185, Sep. 1970. DOI: [10.1364/JOSA.60.001178](https://doi.org/10.1364/JOSA.60.001178).
- [88] C. Yeh, F. Shimabukuro, and P. H. Siegel, “Low-loss terahertz ribbon waveguides,” *Appl. Opt.*, vol. 44, no. 28, pp. 5937–5946, Oct. 2005. DOI: [10.1364/AO.44.005937](https://doi.org/10.1364/AO.44.005937).
- [89] A. W. Snyder, “Coupled-Mode Theory for Optical Fibers,” *J. Opt. Soc. Am.*, vol. 62, no. 11, pp. 1267–1277, Nov. 1972. DOI: [10.1364/JOSA.62.001267](https://doi.org/10.1364/JOSA.62.001267).

-
- [90] A. V. Räisänen *et al.*, “Dielectric rod waveguide as an enabling technology for THz frequencies,” in *The 8th European Conference on Antennas and Propagation (EuCAP 2014)*, 2014, pp. 2638–2639. DOI: 10.1109/EuCAP.2014.6902364.
- [91] M. Smit, E. Pennings, and H. Blok, “A normalized approach to the design of low-loss optical waveguide bends,” *Journal of Lightwave Technology*, vol. 11, no. 11, pp. 1737–1742, 1993. DOI: 10.1109/50.251169.
- [92] R. N. Sheehan, S. Horne, and F. H. Peters, “The design of low-loss curved waveguides,” *Optical and Quantum Electronics*, vol. 40, no. 14, pp. 1211–1218, Nov. 2008, ISSN: 1572-817X. DOI: 10.1007/s11082-009-9329-7.
- [93] S. Ramo, J. R. Whinnery, and T. V. Duzer., *Fields and waves in communication electronics*. J. Wiley, 1965, ISBN: 9780471707202.
- [94] W. Imbriale, T. Otsoshi, and C. Yeh, “Power loss for multimode waveguides and its application to beam-waveguide system,” *IEEE Transactions on Microwave Theory and Techniques*, vol. 46, no. 5, pp. 523–529, 1998. DOI: 10.1109/22.668651.
- [95] R. Ramaswami, K. Sivarajan, and G. Sasaki, *Optical networks: a practical perspective*. Morgan Kaufmann, 2009.
- [96] S. Preu *et al.*, “Tunable, continuous-wave terahertz photomixer sources and applications,” *Journal of Applied Physics*, vol. 109, no. 6, p. 061301, 2011. DOI: 10.1063/1.3552291.
- [97] A. D. J. Fernandez Olvera *et al.*, “Dispersive properties of self-complementary log-periodic antennas in pulsed THz systems,” in *2017 42nd International Conference on Infrared, Millimeter, and Terahertz Waves (IRMMW-THz)*, 2017, pp. 1–2. DOI: 10.1109/IRMMW-THz.2017.8067069.
- [98] S. Gupta *et al.*, “Subpicosecond carrier lifetime in GaAs grown by molecular beam epitaxy at low temperatures,” *Applied Physics Letters*, vol. 59, no. 25, pp. 3276–3278, 1991. DOI: 10.1063/1.105729.
- [99] M. Griebel *et al.*, “Tunable subpicosecond optoelectronic transduction in superlattices of self-assembled ErAs nanoislands,” *Nature Materials*, vol. 2, no. 2, pp. 122–126, Feb. 2003, ISSN: 1476-4660. DOI: 10.1038/nmat819.
- [100] S. Preu *et al.*, “Tunable, continuous-wave Terahertz photomixer sources and applications,” *Journal of Applied Physics*, vol. 109, no. 6, p. 061301, 2011. DOI: 10.1063/1.3552291.
- [101] T. Göbel *et al.*, “Telecom technology based continuous wave terahertz photomixing system with 105 decibel signal-to-noise ratio and 3.5 terahertz bandwidth,” *Opt. Lett.*, vol. 38, no. 20, pp. 4197–4199, Oct. 2013. DOI: 10.1364/OL.38.004197.
- [102] S. Preu *et al.*, “1550 nm ErAs:In(Al)GaAs large area photoconductive emitters,” *Applied Physics Letters*, vol. 101, no. 10, p. 101105, 2012. DOI: 10.1063/1.4750244.
- [103] H. Ito *et al.*, “Continuous THz-wave generation using antenna-integrated uni-travelling-carrier photodiodes,” *Semiconductor Science and Technology*, vol. 20, no. 7, S191–S198, Jun. 2005. DOI: 10.1088/0268-1242/20/7/008.
- [104] A. d. J. Fernandez Olvera *et al.*, “International System of Units (SI) Traceable Noise-Equivalent Power and Responsivity Characterization of Continuous Wave ErAs:InGaAs Photoconductive Terahertz Detectors,” *Photonics*, vol. 6, no. 1, 2019, ISSN: 2304-6732. DOI: 10.3390/photonics6010015.

-
- [105] U. Nandi *et al.*, “Bias-dependent carrier dynamics and terahertz performance of ErAs:In(Al)GaAs photoconductors,” *IEEE Transactions on Terahertz Science and Technology*, pp. 1–1, 2022. DOI: 10.1109/TTHZ.2022.3170523.
- [106] U. Nandi *et al.*, “Material properties and performance of ErAs:In(Al)GaAs photoconductors for 1550 nm laser operation,” *Journal of Vacuum Science & Technology A*, vol. 39, no. 2, p. 023 407, 2021. DOI: 10.1116/6.0000773.
- [107] *GaAs and InGaAs Photomixers*, <https://www.toptica.com/products/terahertz-systems/frequency-domain/gaas-and-ingaas-photomixers>, Accessed: 2022-07-03.
- [108] D. Turan, N. T. Yardimci, and M. Jarrahi, “Plasmonics-enhanced photoconductive terahertz detector pumped by Ytterbium-doped fiber laser,” *Opt. Express*, vol. 28, no. 3, pp. 3835–3845, Feb. 2020. DOI: 10.1364/OE.386368.
- [109] B. Globisch *et al.*, “Iron doped InGaAs: Competitive THz emitters and detectors fabricated from the same photoconductor,” *Journal of Applied Physics*, vol. 121, no. 5, p. 053 102, 2017. DOI: 10.1063/1.4975039.
- [110] D. W. Vogt and R. Leonhardt, “High resolution terahertz spectroscopy of a whispering gallery mode bubble resonator using hilbert analysis,” *Opt. Express*, vol. 25, no. 14, pp. 16 860–16 866, Jul. 2017. DOI: 10.1364/OE.25.016860.
- [111] V. Rumsey, H. Booker, and N. Declaris, *Frequency Independent Antennas* (Electrical science series). Elsevier Science, 2014, ISBN: 9781483282220.
- [112] R. Hansen, “CHAPTER 1 - Aperture Theory,” in *Apertures*, R. Hansen, Ed., Academic Press, 1964, pp. 1–105, ISBN: 978-0-12-323901-3. DOI: <https://doi.org/10.1016/B978-0-12-323901-3.50008-5>.
- [113] R. Johnson and H. Jasik, “Introduction to antennas,” in *Antenna Engineering Handbook* (McGraw-Hill handbook v. 2), McGraw-Hill handbook v. 2. McGraw-Hill, 1984, ch. 1, ISBN: 9780070322912.
- [114] S. Silver, *Microwave Antenna Theory and Design* (IEE electromagnetic waves series). P. Peregrinus, 1984, ISBN: 9780863410178.
- [115] D. Paris, “Digital computer analysis of aperture antennas,” *IEEE Transactions on Antennas and Propagation*, vol. 16, no. 2, pp. 262–264, 1968. DOI: 10.1109/TAP.1968.1139151.
- [116] R. Johnson, H. Ecker, and J. Hollis, “Determination of far-field antenna patterns from near-field measurements,” *Proceedings of the IEEE*, vol. 61, no. 12, pp. 1668–1694, 1973. DOI: 10.1109/PROC.1973.9358.
- [117] C. Balanis, *Antenna Theory: Analysis and Design*. Wiley, 2012, ISBN: 9781118585733.
- [118] B. Will and I. Rolfes, “The TTN-method - A phase shift calibration technique for vector network analyzers,” in *Asia-Pacific Microwave Conference 2011*, 2011, pp. 697–700.
- [119] S. Regensburger *et al.*, “Broadband THz detection from 0.1 to 22 THz with large area field-effect transistors,” *Opt. Express*, vol. 23, no. 16, pp. 20 732–20 742, Aug. 2015. DOI: 10.1364/OE.23.020732.
- [120] *filtfilt: Zero-phase digital filtering*, <https://de.mathworks.com/help/signal/ref/filtfilt.html>, Accessed: 2021-11-05.
- [121] J. O. Smith, *Introduction to Digital Filters with Audio Applications*. W3K Publishing, 2007, ISBN: 978-0-9745607-1-7.

-
- [122] I. E. Gordon *et al.*, “The HITRAN2020 molecular spectroscopic database,” *Journal of Quantitative Spectroscopy and Radiative Transfer*, vol. 277, p. 107 949, 2022. DOI: 10.1016/j.jqsrt.2021.107949.
- [123] D. W. Vogt, M. Erkintalo, and R. Leonhardt, “Coherent Continuous Wave Terahertz Spectroscopy Using Hilbert Transform,” *Journal of Infrared, Millimeter, and Terahertz Waves*, vol. 40, no. 5, pp. 524–534, May 2019, ISSN: 1866-6906. DOI: 10.1007/s10762-019-00583-3.
- [124] S. E. Tavares, “A Comparison of Integration and Low-Pass Filtering,” *IEEE Transactions on Instrumentation and Measurement*, vol. 15, no. 1/2, pp. 33–38, 1966. DOI: 10.1109/TIM.1966.4313498.
- [125] W. Davenport and W. Root, *An Introduction to the Theory of Random Signals and Noise* (International student edition). McGraw-Hill, 1958, ch. 11, ISBN: 9780879422356.
- [126] C. Caglayan and K. Sertel, “Noncontact On-Wafer Characterization of Differential-Mode Millimeter- and Submillimeter-Wave Devices and Integrated Circuits,” *IEEE Transactions on Microwave Theory and Techniques*, vol. 64, no. 11, pp. 3911–3917, 2016. DOI: 10.1109/TMTT.2016.2606412.
- [127] Y. Karisan *et al.*, “Lumped-Element Equivalent-Circuit Modeling of Millimeter-Wave HEMT Parasitics Through Full-Wave Electromagnetic Analysis,” *IEEE Transactions on Microwave Theory and Techniques*, vol. 64, no. 5, pp. 1419–1430, 2016. DOI: 10.1109/TMTT.2016.2549520.
- [128] G. Hernández, *Fabry-Pérot interferometers*. Cambridge University Press, 1988. DOI: doi : 10.1017/S0263034600001919.
- [129] B. S. Everitt and A. Skrondal, *The Cambridge Dictionary of Statistics*. Cambridge University Press, Aug. 2010. DOI: 10.1111/j.1751-5823.2011.00149_2.x.
- [130] C. L. Davies *et al.*, “Temperature-Dependent Refractive Index of Quartz at Terahertz Frequencies,” *Journal of Infrared, Millimeter, and Terahertz Waves*, vol. 39, no. 12, pp. 1236–1248, Dec. 2018, ISSN: 1866-6906. DOI: 10.1007/s10762-018-0538-7.
- [131] C. C. Katsidis and D. I. Siapkas, “General transfer-matrix method for optical multilayer systems with coherent, partially coherent, and incoherent interference,” *Appl. Opt.*, vol. 41, no. 19, pp. 3978–3987, Jul. 2002. DOI: 10.1364/AO.41.003978.
- [132] D. Pozar, *Microwave Engineering, 4th Edition*. Wiley, 2011, ISBN: 9781118213636.
- [133] J. A. Nelder and R. Mead, “A Simplex Method for Function Minimization,” *The Computer Journal*, vol. 7, no. 4, pp. 308–313, Jan. 1965, ISSN: 0010-4620. DOI: 10.1093/comjnl/7.4.308.
- [134] P. Lounesto, “Clifford Algebras and Spinors,” in *Clifford Algebras and Their Applications in Mathematical Physics*, J. S. R. Chisholm and A. K. Common, Eds. Dordrecht: Springer Netherlands, 1986, pp. 25–37, ISBN: 978-94-009-4728-3. DOI: 10.1007/978-94-009-4728-3_2.
- [135] H. Grassmann, *Die Lineale Ausdehnungslehre ein neuer Zweig der Mathematik: Dargestellt und durch Anwendungen auf die übrigen Zweige der Mathematik, wie auch auf die Statik, Mechanik, die Lehre vom Magnetismus und die Krystallonomie erläutert* (Cambridge Library Collection - Mathematics). Cambridge University Press, 2012. DOI: 10.1017/CB09781139237352.
- [136] D.-M. Chiu and R. Jain, “Analysis of the increase and decrease algorithms for congestion avoidance in computer networks,” *Computer Networks and ISDN Systems*, vol. 17, no. 1, pp. 1–14, 1989, ISSN: 0169-7552. DOI: 10.1016/0169-7552(89)90019-6.
- [137] G. Cataldo *et al.*, “Infrared dielectric properties of low-stress silicon nitride,” *Opt. Lett.*, vol. 37, no. 20, pp. 4200–4202, Oct. 2012. DOI: 10.1364/OL.37.004200.

-
- [138] D. Molter *et al.*, “Two decades of terahertz cross-correlation spectroscopy,” *Applied Physics Reviews*, vol. 8, no. 2, p. 021311, 2021. DOI: 10.1063/5.0037395.
- [139] *Undoped / Intrinsic Float Zone Silicon Wafers for Researcher*, <https://www.universitywafer.com/undoped-silicon-wafers.html>, Accessed: 2022-08-21.
- [140] R. Baets and H. Thienpont, *Dielectric waveguides*, <http://fotonica.intec.ugent.be/download/ocs131.pdf>, Sep. 2009.
- [141] M. A. de Araújo *et al.*, “Measurement of Gaussian laser beam radius using the knife-edge technique: Improvement on data analysis,” *Appl. Opt.*, vol. 48, no. 2, pp. 393–396, Jan. 2009. DOI: 10.1364/AO.48.000393.
- [142] *Gaussian Beam Optics*, <https://www.newport.com/n/gaussian-beam-optics>, Accessed: 2022-08-23.
- [143] O. Mitrofanov and J. A. Harrington, “Dielectric-lined cylindrical metallic THz waveguides: Mode structure and dispersion,” *Opt. Express*, vol. 18, no. 3, pp. 1898–1903, Feb. 2010. DOI: 10.1364/OE.18.001898.
- [144] O. Mitrofanov *et al.*, “Reducing Transmission Losses in Hollow THz Waveguides,” *IEEE Transactions on Terahertz Science and Technology*, vol. 1, no. 1, pp. 124–132, 2011. DOI: 10.1109/TTHZ.2011.2159547.
- [145] E. A. J. Marcatili, “Bends in Optical Dielectric Guides,” *Bell System Technical Journal*, vol. 48, no. 7, pp. 2103–2132, 1969. DOI: <https://doi.org/10.1002/j.1538-7305.1969.tb01167.x>.
- [146] M. Schottenloher, “Conformal Transformation and Conformal Killing Fields,” in *A Mathematical Introduction to Conformal Field Theory: Based on a Series of Lectures given at the Mathematisches Institut der Universität Hamburg*. Springer Berlin Heidelberg, 1997, pp. 3–19, ISBN: 978-3-540-70690-8. DOI: 10.1007/978-3-540-70690-8_2.
- [147] M. Heiblum and J. Harris, “Analysis of curved optical waveguides by conformal transformation,” *IEEE Journal of Quantum Electronics*, vol. 11, no. 2, pp. 75–83, 1975. DOI: 10.1109/JQE.1975.1068563.
- [148] A. Melloni *et al.*, “Determination of bend mode characteristics in dielectric waveguides,” *Journal of Lightwave Technology*, vol. 19, no. 4, pp. 571–577, 2001, ISSN: 07338724. DOI: 10.1109/50.920856.
- [149] R. G. Hunsperger, “Losses in Optical Waveguides,” in *Integrated Optics: Theory and Technology*. Springer Berlin Heidelberg, 2002, pp. 93–111, ISBN: 978-3-540-38843-2. DOI: 10.1007/978-3-540-38843-2_6.
- [150] A. Melloni *et al.*, “An effective method for the analysis of bent dielectric waveguides,” in *1999 IEEE LEOS Annual Meeting Conference Proceedings. LEOS’99. 12th Annual Meeting. IEEE Lasers and Electro-Optics Society 1999 Annual Meeting (Cat. No.99CH37009)*, vol. 2, 1999, 641–642 vol.2. DOI: 10.1109/LEOS.1999.811891.
- [151] *Curvature and Radius of Curvature*, <https://math24.net/curvature-radius.html>, Accessed: 2021-12-14.
- [152] *Arc length*, https://en.wikipedia.org/wiki/Arc_length, Accessed: 2022-08-27.
- [153] A. Maese-Novo *et al.*, “Wavelength independent multimode interference coupler,” *Opt. Express*, vol. 21, no. 6, pp. 7033–7040, Mar. 2013. DOI: 10.1364/OE.21.007033.

-
- [154] R. Hui and M. O'Sullivan, "Chapter 4 - Optical Fiber Measurement," in *Fiber Optic Measurement Techniques*, R. Hui and M. O'Sullivan, Eds., Boston: Academic Press, 2009, pp. 365–479, ISBN: 978-0-12-373865-3. DOI: <https://doi.org/10.1016/B978-0-12-373865-3.00004-5>.
- [155] C. Jansen *et al.*, "Terahertz spectroscopy on adhesive bonds," *Polymer Testing*, vol. 30, no. 1, pp. 150–154, 2011, ISSN: 0142-9418. DOI: <https://doi.org/10.1016/j.polymeresting.2010.11.005>.
- [156] M. M. Aller and S. Preu, "Quasi-Analytical Description of a Double Slit Planar Dielectric Waveguide as Broadband Dispersion Compensating Element," in *2019 44th International Conference on Infrared, Millimeter, and Terahertz Waves (IRMMW-THz)*, 2019, pp. 1–2. DOI: [10.1109/IRMMW-THz.2019.8874529](https://doi.org/10.1109/IRMMW-THz.2019.8874529).
- [157] P. Colman *et al.*, "Control of dispersion in photonic crystal waveguides using group symmetry theory," *Opt. Express*, vol. 20, no. 12, pp. 13 108–13 114, Jun. 2012. DOI: [10.1364/OE.20.013108](https://doi.org/10.1364/OE.20.013108).
- [158] K. Tsuruda, M. Fujita, and T. Nagatsuma, "Extremely low-loss terahertz waveguide based on silicon photonic-crystal slab," *Opt. Express*, vol. 23, no. 25, pp. 31 977–31 990, Dec. 2015. DOI: [10.1364/OE.23.031977](https://doi.org/10.1364/OE.23.031977).
- [159] L.-J. Chen *et al.*, "Low-loss subwavelength plastic fiber for terahertz waveguiding," *Opt. Lett.*, vol. 31, no. 3, pp. 308–310, Feb. 2006. DOI: [10.1364/OL.31.000308](https://doi.org/10.1364/OL.31.000308).
- [160] R. A. S. D. Koala, M. Fujita, and T. Nagatsuma, *Nanophotonics*, vol. 11, no. 9, pp. 1741–1759, 2022. DOI: [doi:10.1515/nanoph-2021-0673](https://doi.org/10.1515/nanoph-2021-0673).
- [161] M. Navarro-Cía *et al.*, "Generation of radially-polarized terahertz pulses for coupling into coaxial waveguides," *Scientific Reports*, vol. 6, no. 1, p. 38 926, 2016, ISSN: 2045-2322. DOI: [10.1038/srep38926](https://doi.org/10.1038/srep38926).
- [162] A. Rivera-Lavado *et al.*, "Dielectric Rod Waveguide Antenna as THz Emitter for Photomixing Devices," *IEEE Transactions on Antennas and Propagation*, vol. 63, no. 3, pp. 882–890, 2015. DOI: [10.1109/TAP.2014.2387419](https://doi.org/10.1109/TAP.2014.2387419).
- [163] A. Rivera-Lavado *et al.*, "Design of a Dielectric Rod Waveguide Antenna Array for Millimeter Waves," *Journal of infrared, millimeter and terahertz waves*, vol. 38, pp. 33–46, Jan. 2017. DOI: [10.1007/s10762-016-0310-9](https://doi.org/10.1007/s10762-016-0310-9).
- [164] A. Rivera-Lavado *et al.*, "Planar Lens-Based Ultra-Wideband Dielectric Rod Waveguide Antenna for Tunable THz and Sub-THz Photomixer Sources," *Journal of Infrared, Millimeter, and Terahertz Waves*, vol. 40, no. 8, pp. 838–855, 2019, ISSN: 1866-6906. DOI: [10.1007/s10762-019-00612-1](https://doi.org/10.1007/s10762-019-00612-1).
- [165] A. I. Hernandez-Serrano and E. Pickwell-MacPherson, "Low cost and long-focal-depth metallic axicon for terahertz frequencies based on parallel-plate-waveguides," *Scientific Reports*, vol. 11, no. 1, p. 3005, 2021, ISSN: 2045-2322. DOI: [10.1038/s41598-021-82503-x](https://doi.org/10.1038/s41598-021-82503-x).
- [166] M. F. Abdullah *et al.*, "Vivaldi End-Fire Antenna for THz Photomixers," *Journal of Infrared, Millimeter, and Terahertz Waves*, vol. 41, no. 6, pp. 728–739, Jun. 2020, ISSN: 1866-6906. DOI: [10.1007/s10762-020-00679-1](https://doi.org/10.1007/s10762-020-00679-1).
- [167] D. Schaubert *et al.*, "Endfire tapered slot antennas on dielectric substrates," *IEEE Transactions on Antennas and Propagation*, vol. 33, no. 12, pp. 1392–1400, 1985. DOI: [10.1109/TAP.1985.1143542](https://doi.org/10.1109/TAP.1985.1143542).

-
- [168] D. Burrell and J. Aberle, "Characterization of Vivaldi antennas utilizing a microstrip-to-slotline transition," in *Proceedings of IEEE Antennas and Propagation Society International Symposium*, 1993, 1212–1215 vol.3. DOI: 10.1109/APS.1993.385130.
- [169] W. Qun *et al.*, "An approach to the determination of the phase center of Vivaldi-based UWB antenna," in *2006 IEEE Antennas and Propagation Society International Symposium*, 2006, pp. 563–566. DOI: 10.1109/APS.2006.1710585.
- [170] X. Yin *et al.*, "An ultra wideband tapered slot antenna," in *2005 IEEE Antennas and Propagation Society International Symposium*, vol. 2A, 2005, 516–519 vol. 2A. DOI: 10.1109/APS.2005.1551859.
- [171] M. Chiappe and G. L. Gragnani, "Theoretical and numerical analysis of the self-scaling properties of the exponentially tapered slot-line antenna," *Microwave and Optical Technology Letters*, vol. 45, no. 6, pp. 485–491, 2005. DOI: <https://doi.org/10.1002/mop.20860>.
- [172] P. Gibson, "The Vivaldi Aerial," in *1979 9th European Microwave Conference*, 1979, pp. 101–105. DOI: 10.1109/EUMA.1979.332681.
- [173] Y. Cao and G. Wei, "Circular Slot Vivaldi Antenna with Low Backlobe," in *2018 Cross Strait Quad-Regional Radio Science and Wireless Technology Conference (CSQRWC)*, 2018, pp. 1–3. DOI: 10.1109/CSQRWC.2018.8455216.
- [174] R. Kazemi, A. E. Fathy, and R. A. Sadeghzadeh, "Dielectric Rod Antenna Array With Substrate Integrated Waveguide Planar Feed Network for Wideband Applications," *IEEE Transactions on Antennas and Propagation*, vol. 60, no. 3, pp. 1312–1319, 2012. DOI: 10.1109/TAP.2011.2182489.
- [175] G. Zhai *et al.*, "Gain Enhancement of Printed Log-Periodic Dipole Array Antenna Using Director Cell," *IEEE Transactions on Antennas and Propagation*, vol. 62, no. 11, pp. 5915–5919, 2014. DOI: 10.1109/TAP.2014.2355851.
- [176] *Consumable Product Catalogue*, <https://logitech.com/wp-content/uploads/Consumables-Web.pdf>, Accessed: 2022-07-11.
- [177] A. Yariv, "Critical coupling and its control in optical waveguide-ring resonator systems," *IEEE Photonics Technology Letters*, vol. 14, no. 4, pp. 483–485, 2002. DOI: 10.1109/68.992585.
- [178] I. Hickman, *Analog Electronics: Analog Circuitry Explained*. Elsevier Science, 2013, ISBN: 9781483162287.
- [179] S. Preu *et al.*, "Dielectric microcavities for THz radiation: Identical mode spectrum and coupling in poly-ethylene disks," in *Conference on Lasers and Electro-Optics/Quantum Electronics and Laser Science Conference and Photonic Applications Systems Technologies*, Optica Publishing Group, 2008, JTua131.
- [180] S. Preu *et al.*, "Coupled whispering gallery mode resonators in the Terahertz frequency range," *Opt. Express*, vol. 16, no. 10, pp. 7336–7343, May 2008. DOI: 10.1364/OE.16.007336.
- [181] D. W. Vogt and R. Leonhardt, "Ultra-high Q terahertz whispering-gallery modes in a silicon resonator," *APL Photonics*, vol. 3, no. 5, p. 051702, 2018. DOI: 10.1063/1.5010364.
- [182] G. Annino *et al.*, "Whispering gallery modes in a dielectric resonator: Characterization at millimeter wavelength," *IEEE Transactions on Microwave Theory and Techniques*, vol. 45, no. 11, pp. 2025–2034, 1997. DOI: 10.1109/22.644226.

-
- [183] D. W. Vogt, A. H. Jones, and R. Leonhardt, "Free-space coupling to symmetric high-Q terahertz whispering-gallery mode resonators," *Opt. Lett.*, vol. 44, no. 9, pp. 2220–2223, May 2019. DOI: 10.1364/OL.44.002220.
- [184] M. Nagel, M. Först, and H. Kurz, "THz biosensing devices: Fundamentals and technology," *Journal of Physics: Condensed Matter*, vol. 18, no. 18, S601–S618, Apr. 2006. DOI: 10.1088/0953-8984/18/18/s07.
- [185] W. Cao *et al.*, "Low-loss ultra-high-Q dark mode plasmonic Fano metamaterials," *Opt. Lett.*, vol. 37, no. 16, pp. 3366–3368, Aug. 2012. DOI: 10.1364/OL.37.003366.
- [186] Y. Zhao *et al.*, "Photonic Crystal Resonator in the Millimeter/Terahertz Range as a Thin Film Sensor for Future Biosensor Applications," *Journal of Infrared, Millimeter, and Terahertz Waves*, vol. 43, no. 5, pp. 426–444, Jun. 2022.
- [187] C. J. R. Sheppard, "Approximate calculation of the reflection coefficient from a stratified medium," *Pure and Applied Optics: Journal of the European Optical Society Part A*, vol. 4, no. 5, pp. 665–669, Sep. 1995. DOI: 10.1088/0963-9659/4/5/018.
- [188] T. Kolding, "A four-step method for de-embedding gigahertz on-wafer CMOS measurements," *IEEE Transactions on Electron Devices*, vol. 47, no. 4, pp. 734–740, 2000. DOI: 10.1109/16.830987.
- [189] E. Vandamme, D.-P. Schreurs, and G. Van Dinther, "Improved three-step de-embedding method to accurately account for the influence of pad parasitics in silicon on-wafer RF test-structures," *IEEE Transactions on Electron Devices*, vol. 48, no. 4, pp. 737–742, 2001. DOI: 10.1109/16.915712.
- [190] *IC Measure: On-Screen Vermessung von Längen, Winkeln, Kreisen und Vielecken, sowie Bilderfassung*, <https://www.theimagingsource.de/produkte/software/end-anwender-software/ic-measure>, Accessed: 2022-10-08.
- [191] B. L. Krause, A. D. J. F. Olvera, and S. Preu, "Photonic Spectrum Analyzer for Wireless Signals in the THz Range," *IEEE Access*, vol. 10, pp. 42 047–42 054, 2022. DOI: 10.1109/ACCESS.2022.3168162.
- [192] B. L. Krause, A. k. Mukherjee, and S. Preu, "A Photonic Spectrum Analyzer for Waveguide-Coupled Sources in the Terahertz Range," *IEEE Journal of Selected Topics in Quantum Electronics*, pp. 1–6, 2023. DOI: 10.1109/JSTQE.2023.3241017.
- [193] *Cascade T-Wave Probe*, <https://www.formfactor.com/product/probes/t-wave/t-wave-probe>, Accessed: 2022-09-28.
- [194] *Photoresists*, <https://www.microchemicals.com/products/photoresists>, Accessed: 2022-09-25.
- [195] A. k. Mukherjee *et al.*, "Characterisation of multi-layered structures using a vector-based gradient descent algorithm at terahertz frequencies," Manuscript submitted for publication, 2023.
- [196] F. R. Faridi *et al.*, "A Comparison of Continuous-Wave and Pulsed Free Space 2-Port Photonic Vector Network Analyzers for Terahertz Characterization," in *2022 47th International Conference on Infrared, Millimeter and Terahertz Waves (IRMMW-THz)*, 2022, pp. 1–2. DOI: 10.1109/IRMMW-THz50927.2022.9895486.

Acronyms

- AC** alternating current.
AlO_x Alumina.
ARC anti-reflection coating.
ARMA auto-regressive-moving-average.
BCB Cyclotene™ Advanced Electronic Resin.
BNC Bayonet Neil-Concelman.
BPF band-pass filter.
CPS coplanar striplines.
CVD chemical vapour deposition.
CW continuous-wave.
DBR distributed Bragg reflector.
DC direct current.
DFB distributed feedback.
DNR dynamic range.
DRIE deep reactive-ion etching.
DRW dielectric rod waveguide.
DUT device under test.
EDFA Erbium-doped fibre amplifier.
EM electro-magnetic.
ENBW equivalent noise bandwidth.
ErAs:In(Al)GaAs erbium arsenide/indium (aluminium) gallium arsenide.
FIR finite impulse response.
FPGA field programmable gate array.
FSR free spectral range.
G-S-G *ground-signal-ground*.
HDPE high density polyethelene.
HOM higher-order mode.
HRFZ-Si highly-resistive float-zone silicon.
ICP inductively coupled plasma.
IF intermediate frequency.
IFT inverse Fourier transform.
IIR infinite impulse response.
InGaAs indium gallium arsenide.
InP indium phosphide.
LIA lock-in amplifier.
LO local oscillator.
LPF low-pass filter.
MMI multimode interference.
MMIC monolithic microwave integrated circuit.
MPL Max Planck Institute for the Science of Light.
NEP noise equivalent power.
NMA Nelder-Mead simplex algorithm.
PIC photonic integrated circuit.
PSA photonic spectrum analyser.
PVC Polyvinyl Chloride.
PVNA photonic vector network analyser.
Q-factor quality factor.
Qz crystalline quartz.
RF radio frequency.
RHM rectangular hollow metallic.
RI refractive index.
ROC radius of curvature.
S-parameter scattering parameter.
SEM scanning electron microscope.
SiC silicon carbide.
SiN silicon nitride.
SNR signal-to-noise ratio.
SOC system-on-chip.
SoI silicon-on-insulator.
T-matrix transfer matrix.
T-parameter scattering transfer parameter.
TCP Transfer control protocol.
TDS time-domain spectroscopy.
TEM transverse electro-magnetic.
THz Terahertz.

THz-PIC THz-photonic integrated circuit.

TIA transimpedance amplifier.

TPX Polymethylpentene.

TRL *through-reflect-line*.

UV ultra-violet.

VA Vivaldi antenna.

VNA vector network analyser.

VSWR voltage standing wave ratio.

WGM whispering gallery mode.

List of Publications

In journals

1. A. k. Mukherjee, S. Wassmann, and S. Preu, "Operational bandwidth extension in continuous-wave terahertz systems by digital post-processing," *IEEE Transactions on Terahertz Science and Technology*, pp. 1–8, 2022. DOI: 10.1109/TTHZ.2022.3230924
2. A. k. Mukherjee, M. Xiang, and S. Preu, "Broadband Terahertz Photonic Integrated Circuit with Integrated Active Photonic Devices," *Photonics*, vol. 8, no. 11, 2021, ISSN: 2304-6732. DOI: 10.3390/photonics8110492
3. B. L. Krause, A. k. Mukherjee, and S. Preu, "A Photonic Spectrum Analyzer for Waveguide-Coupled Sources in the Terahertz Range," *IEEE Journal of Selected Topics in Quantum Electronics*, pp. 1–6, 2023. DOI: 10.1109/JSTQE.2023.3241017
4. A. Ingar Romero, A. k. Mukherjee, A. Fernandez Olvera, M. Méndez Aller, and S. Preu, "Visualizing nanometric structures with sub-millimeter waves," *Nature Communications*, vol. 12, no. 1, p. 7091, 2021, ISSN: 2041-1723. DOI: 10.1038/s41467-021-27264-x
5. A. D. J. F. Olvera, A. k. Mukherjee, and S. Preu, "A Fully Optoelectronic Continuous-Wave 2-Port Vector Network Analyzer Operating From 0.1 THz to 1 THz," *IEEE Journal of Microwaves*, pp. 1–8, 2021. DOI: 10.1109/JMW.2021.3107472
6. M. F. Abdullah, A. k. Mukherjee, R. Kumar, and S. Preu, "Vivaldi End-Fire Antenna for THz Photomixers," *Journal of Infrared, Millimeter, and Terahertz Waves*, vol. 41, no. 6, pp. 728–739, Jun. 2020, ISSN: 1866-6906. DOI: 10.1007/s10762-020-00679-1

Submitted manuscripts

1. A. k. Mukherjee, S. Wassmann, K. Wenzel, B. G. Globlich, R. Kohlhaas, L. Liebermeister, and S. Preu, "Characterisation of multi-layered structures using a vector-based gradient descent algorithm at terahertz frequencies," Manuscript submitted for publication, 2023

Conference contributions

1. A. k. Mukherjee and S. Preu, "Emulating a broadband frequency sweep for Terahertz thin-film imaging," in *2022 47th International Conference on Infrared, Millimeter and Terahertz Waves (IRMMW-THz)*, 2022, pp. 1–4. DOI: 10.1109/IRMMW-THz50927.2022.9895797
2. F. R. Faridi, A. D. J. Fernandez Olvera, A. k. Mukherjee, and S. Preu, "A Comparison of Continuous-Wave and Pulsed Free Space 2-Port Photonic Vector Network Analyzers for Terahertz Characterization," in *2022 47th International Conference on Infrared, Millimeter and Terahertz Waves (IRMMW-THz)*, 2022, pp. 1–2. DOI: 10.1109/IRMMW-THz50927.2022.9895486

-
3. A. k. Mukherjee, M. Xiang, and S. Preu, "Antenna designs for near field waveguide coupling between 0.6 – 0.9 THz," in *2021 46th International Conference on Infrared, Millimeter and Terahertz Waves (IRMMW-THz)*, 2021, pp. 1–2. DOI: 10.1109/IRMMW-THz50926.2021.9567575
 4. A. k. Mukherjee, M. Xiang, and S. Preu, "Broadband Dielectric Waveguides for 0.5–1.1 THz Operation," in *2020 45th International Conference on Infrared, Millimeter, and Terahertz Waves (IRMMW-THz)*, 2020, pp. 1–2. DOI: 10.1109/IRMMW-THz46771.2020.9370829

Workshop contributions

1. A. k. Mukherjee and S. Preu, "Broadband characterisation of a high-Q resonator using a 1.5-port photonic vector network analyser," in *10th International Workshop on Terahertz Technology and Applications (IWTTA'22)*, Kaiserslautern, Germany, May 2022

Patent Application

1. A. k. Mukherjee and S. Preu, *Bandbreitenerweiterung von THz Photomischersystemen mittels Rauschunterdrückung*, German patent application DE 10 2022 115 387.8, Jun 2022

Acknowledgements

I have spent the first 24 years of my life in India, a country where, among many other things, gratitude is implied rather than expressed in words. However, and I quote Victor H. Rumsey from the preface of his book *Frequency Independent Antennas* [111],

“... it would be a pity not to support the custom of expressing gratitude to those who have helped the author. But one hardly knows where to stop, for on reflection, one is struck by how completely indebted he is not only to his teachers, colleagues and students, but to the previous generation who taught them, and so on.”

I express my enormous gratitude to many professors, colleagues, students and friends at the Technical University of Darmstadt, with whom I had the pleasure of working. I consider myself extremely fortunate to have some of the most intelligent, curious, patient and kindest colleagues, who guided me through the thick and thin of my doctoral studies. However, it would be quite unfair if I do not explicitly thank three individuals for their enormous contribution to this thesis work.

I am indebted to Sascha (**Prof. Dr. rer. nat. Sascha Preu**) for the opportunity to work towards integrating the free-space terahertz systems. I thank him for his constant guidance and supervision, starting with my master thesis and during my doctoral studies. I also apologise in advance for my version of gratitude which follows. Working with him, we enjoyed “den Tag der offenen Tür” essentially every day. He answered all but one of million questions I asked him, ranging from dental insurance schemes to quantum tunnelling effects (the zero-padded resolution is still unresolved). Contrastingly, his self-proclaimed “stupid” questions have upended my understanding of many scientific phenomena and things I had long hold as truths. Among many of his enviable qualities, his ability to maintain a straight face in the terahertz oral exams has baffled me the most. His patience, persistence and willingness to help everyone are like Buddhism, astonishing but difficult to replicate. I have learned a great deal from him and will continue to do so in future.

I am also indebted to **Dr. Irina Harder** for her expertise and guidance during the DRIE runs at MPL. Some conversations we had changed my perspective about many hurdles of this thesis work. She was always available for my questions, at times even irrelevant ones, and gracefully guided me through all the bureaucratic hassles, safety trainings and much more. I have tested random adhesives in the RIE chamber, ranging from superglue to cyclo-olefin copolymers and I would like to take this opportunity to apologise for all the scrubbing and cleaning of the said chamber she had to do after the processing runs.

During her master thesis, **Mingjun Xiang** helped me design, fabricate and characterise the Vivaldi antennas. Her relative inexperience, but out-of-the-box thinking made the direct-coupling between the waveguides and the antennas possible. She also contributed one strand of her hair to science (see Fig. 5.8), which is also immortalised in Fig. 5(b) of [70]. I wish her all the best for her doctoral studies and all future endeavours.

This work was funded by *European Research Council* under the ERC Starting grant *Pho-T-Lyze*, grant agreement No. 713780. I thank the *Group for Nanofabrication TDSU1* from the MPL, Erlangen for providing access to the MPL cleanroom and dry etching facilities. I also thank *3D Micromac AG* for the laser ablation processing.



Curriculum Vitae

Name: Amlan kusum Mukherjee
Date of birth: 15.07.1991
Place of birth: Bankura, WB, India

Academic Qualifications

07.2009 – 05.2013 Electronics and Communication Engineering
Bachelor of Technology *National Institute of Technology, Durgapur*
Durgapur, West Bengal, India

10.2015 – 12.2017 Information and Communication Engineering
Master of Science *Technische Universität Darmstadt*
Darmstadt, Germany

03.2018 – 01.2023 Department of Electrical Engineering and Information Technology
Doctor of Engineering *Technische Universität Darmstadt*
(*Dr.-Ing.*) Darmstadt, Germany

Professional Experience

09.2013 – 09.2015 Associate Applications Developer
Oracle Financial Software Services
Mumbai, MH, India

01.2016 – 09.2016 Web Developer (Freelance)
Icecream Cloud UG
Darmstadt, Germany

10.2016 – 04.2017 Applications Engineer (Intern)
Qualcomm CDMA GmbH
Sulzbach, Germany

03.2017 – Present System Design Engineer
Robert Bosch GmbH
Reutlingen, Germany

Erklärungen laut Promotionsordnung

§8 Abs. 1 lit. c PromO

Ich versichere hiermit, dass die elektronische Version meiner Dissertation mit der schriftlichen Version übereinstimmt.

§8 Abs. 1 lit. d PromO

Ich versichere hiermit, dass zu einem vorherigen Zeitpunkt noch keine Promotion versucht wurde. In diesem Fall sind nähere Angaben über Zeitpunkt, Hochschule, Dissertationsthema und Ergebnis dieses Versuchs mitzuteilen.


§9 Abs. 1 PromO

Ich versichere hiermit, dass die vorliegende Dissertation selbstständig und nur unter Verwendung der angegebenen Quellen verfasst wurde.

§9 Abs. 2 PromO

Die Arbeit hat bisher noch nicht zu Prüfungszwecken gedient.

Darmstadt, 13.10.2022


Amlan kusum Mukherjee